Instabilities in High Reynolds Number Flows.

A thesis presented for the degree of

Doctor of Philosophy of the University of London

and the

Diploma of Imperial College

by

Curtis Alwyn Banks

Department of Mathematics

Imperial College

180 Queen's Gate, London SW7 2BZ

SEPTEMBER 30, 2015

I certify that this thesis, and the research to which it refers, are the product of my own work, and that any ideas or quotations from the work of other people, published or otherwise, are fully acknowledged in accordance with the standard referencing practices of the discipline.

Signed:

Copyright

I would like to thank Professor Philip Hall for the supervision this project. I would like to acknowledge the financial support of EPSRC and Airbus UK. Many thanks to my collaborators Dr Alex White, Dr Shahid Mughal, Dr Christian Thomas and Dr Ubaid Qadri. I would like to give lots of appreciation and thanks to all my friends at Imperial College London who have supported and aided me throughout this process, notably, Jamie Nutter, David Pryce, Liam Dempsey, Joseph Maestri, Jamie Nutter, Thomas deCointet, Elizaveta Dubrovina, Gianmarco Mengaldo, Daniele De Grazia and Florencia Tettamanti. And lastly I would to thank my family and my girlfriend Emma Lewis for their support throughout the years.

This research was conducted in the Laminar Flow Control centre at Imperial College London. With the financial support of Airbus UK, EPSRC and EADS Innovation Works.

Abstract

An asymptotic theory for predicting stability characteristics, both stationary and travelling crossflow vortices, over a variety of surface variations was formulated. These include flat, convex and concave curved surfaces. Comparisons were made with two different numerical methods (Parabolised Stability Equations and Velocity-Vorticity) and good agreement, to within 5% of the numerical value of the crossflow mode streamwise growth rate was met for both stationary and travelling modes initially for a flat surface. An additional comparison was made with the streamwise growth rates to observe the impact of including curvature and a small convex curvature surface variation was used. Similar results were achieved for this study also. Likewise, results for travelling crossflow modes were in accordance with the numerical values.

Receptivity analysis was developed to analyse various mechanisms in the production of crossflow vortices. A response function was established from the receptivity analysis to calculate the efficiency of this process. The response function is largest near the leading edge, meaning the disturbance is most effective at propagating into the boundary layer there. The results we obtain via this approach qualitatively agree with other research methods. This is true for all surface curvatures and both crossflow modes. There is an intriguing behaviour that the response function exhibits for both convex and concave curvature with travelling modes at a high frequency. When we consider moderate spanwise wavenumber ($\gamma = 0.4$), the response function is much larger than other modes or for a flat surface and this could have repercussions for experiments. Careful consideration is needed for this case and can be avoided with the aid of this research.

Finally, an asymptotic theory was created to analyse two-dimensional closed streamlines for secondary instabilities. The first instability analysed was the elliptical instability, due to the links to turbulence and it was the initial interest to these types

of problems. The method anticipates the existence of short-wave three-dimensional disturbances on a streamline at a distance away from the centre of the vortex of this secondary instability. There was no limitation in the study for symmetrical known streamlines and the analysis can be extended further to analyse any two-dimensional closed streamline such as separation bubbles. With this in mind an observation was required to test this hypothesis and the approach was tested on the structure inside a cavity, from which the location and behaviour of the disturbance was correctly predicted.

List of Figures

1.1 Numerical Simulation of NACA airfoil. 29
1.2 Overview of different plasma actuator arrangements. 30

2.1 Schematic of 3-D swept wing with roughness. 43
2.2 Flow against a solid wedge. 46
2.3 Similarity streamfunction with different values of m. 47
2.4 Streamwise velocity with different values of m. 47
2.5 Spanwise similarity solution with different values of m. 48
2.6 Swept Hiemenz base flow functions with changing wall normal coordinate. 51
2.7 Dispersion relation for α_{0i} and γ_0. 57
2.8 An example of a normalised eigenfunction of v_0 with x=1.0 and $\gamma_0 = 1.0$. 57
2.9 Dispersion relation for α_{0i} and θ_{sw} at $x = 1.0$ and for $\gamma = 0.4$. 58
2.10 Dispersion relation for α_{0i} and γ_0 at $x = 0.25$, 1.0 and 4.0. 59
2.11 Normalised eigenfunction $|v_0(\zeta)|$ at $x = 0.25$, 1.0 and 4.0. 59
2.12 Comparison between α_{0i}, α_{1i} and α_i 66
2.13 A comparison between VV, PSE and asymptotic theory at $Re = 500$, $\gamma_0 = 0.4$. 67
2.14 A comparison between VV, PSE and asymptotic theory at $Re = 750$, $\gamma_0 = 0.4$. 68
2.15 Growth rate comparison between different values of spanwise wavenumber at $Re = 500$ calculated using the asymptotic approach. 69
2.16 Dispersion relation between α_{0i} and γ_0 for different ω_0. 70
2.17 Dispersion relation between α_{0i} ω_0 for γ_0=0.5. 71
2.18 A comparison between α_{0i} with varying ω_0 for $\gamma_0 = 0.4$. 71
2.19 A comparison between VV, PSE and asymptotic theory for $Re = 500$,$\gamma = 0.4$,$\omega_0 = 7.5 \times 10^{-4}$ 72
2.20 Dispersion relation between α_{0i} and γ_0 for various curvature orientations. 74
2.21 Normalised eigenfunction (v_0) with $x = 1.0$, $\gamma_0 = 0.6$ with various curvature orientations. 75
2.22 Dispersion relation between α_{0i} and ω_0 for $\gamma_0 = 0.5$ with varying κ_C, for $\kappa_C \ll 1$. 76
2.23 Dispersion relation between α_{0i} and ω_0 for $\gamma_0 = 0.5$ with varying κ_C, for $\kappa_C \sim O(1)$. 76
2.24 Dispersion relation between α_{0i} and γ_0 for ω_0=0.05 with varying κ_C. . 78

2.25 Dispersion relation between α_{0i} and γ_0 for ω_0=0.1 with varying κ_C. . 78
2.26 Dispersion relation comparison γ_0 and $-\alpha_i$ between inviscid theory and two-term correction X=1.0, $\overline{(\zeta)}$=1.0 and at various κ_C. 82
2.27 Comparison between PSE and 2-term curvature method for $-\alpha$ with $\gamma_0 = 0.8$. 83
2.28 Comparison between PSE and 3-term viscous method for $-\alpha$ with $\gamma_0 = 0.8$. 84
2.29 Comparison between 3-term theory and inviscid growth rate at $\gamma_0 = 0.5$ for $\omega_0 = 0.05$ and $\omega_0 = 0.1$ 85

3.1 93
3.2 Behaviour of $|K_R|$ over x for a stationary mode with $\gamma = 0.4$. 99
3.3 Behaviour of $|K_R|$ with varying γ_0 for a stationary mode with $x = 1.0$. 100
3.4 Behaviour of $|K_R|$ over x for stationary a crossflow mode for flat and convex curvature surface with $\gamma = 0.4$ 103
3.5 Behaviour of $|K_R|$ with varying γ for stationary crossflow modes for flat and convex surface with $x = 1.0$. 103
3.6 Comparison of the $|K_R|$ over x for stationary crossflow vortices with small convex and concave curvature for $\gamma = 0.4$. 105
3.7 A comparison of the receptivity response function, $|K_R|$, across the spanwise wavenumber, γ, for stationary crossflow vortices for small convex and concave curvature for a streamwise coordinate of $x = 1.0$. 106
3.8 A comparison of the receptivity response function, $|K_R|$, across a reduced range of spanwise wavenumber, γ - for stationary crossflow vortices for small convex and concave curvature for a streamwise coordinate of $x = 1.0$. 106
3.9 Behaviour of $|K_R|$ over x for stationary and travelling crossflow modes with $\gamma = 0.4$. 107
3.10 Variation of $|K_R|$ with γ for stationary and travelling modes with $x = 1.0$. 108
3.11 Variation of $|K_R|$ with varying γ for stationary and travelling crossflow modes for a convex surface with $x = 1.0$. 109
3.12 Variation of $|K_R|$ with varying γ for two different travelling crossflow modes with and without curvature with $x = 1.0$. 110
3.13 Variation of $|K_R|$ over ω with and without curvature for x=1.0 and γ=0.4 111
3.14 Variation of $|K_R|$ with varying γ for travelling modes for a flat and convex surface with $x = 1.0$. 112
3.15 Variation of $|K_R|$ with x for travelling modes comparing with convex and concave curvature with $\gamma = 0.4$. 113
3.16 Behaviour of $|K_R|$ with varying γ for travelling modes comparing with convex and concave curvature with $x = 1.0$. 114
3.17 Schematic of an asymmetric single dielectric barrier plasma. 115
3.18 Boundary conditions for the 2D plasma actuator 121
3.19 Initial electric fields for parametric study. 123
3.20 Initial species densities. 124

3.21 Electric field for various initial conditions. 125
3.22 Electron density for various initial conditions. 126
3.23 Ion density for various initial conditions. 127
3.24 Electric field at t=5.0×10^{-5} for various initial conditions shown in figure 3.19. 128
3.25 Electron density at t=5.0×10^{-5} for various initial conditions shown in figure 3.19. 129
3.26 Ion density at t=5.0×10^{-5} for various initial conditions shown in figure 3.19. 130
3.27 Electric field at t=1.0×10^{-3}. 131
3.28 Two cases for different widths of the ion density. 132
3.29 Progression of plasma boundary through time. 133
3.30 Plasma boundary with various different frequencies for a fixed power, $\phi_0 = 1.0$. 133
3.31 Plasma boundary with various different applied power for a fixed frequency, $f = 100$. 134
3.32 Plasma boundary with various different frequencies. 135
3.33 Variation of $|K_R|$ over x with $\gamma = 0.4$ with various frequencies for a plasma actuator. 136
3.34 Plasma boundary with various different voltages. 136
3.35 Variation of $|K_R|$ over x with $\gamma = 0.4$ with various voltages for a plasma actuator. 137

4.1 Schematic of closed 2D streamline. 145
4.2 The variation of $\overline{u}$ and κ with S for $a = 2.0, b = 1.9, K = 1.0$ 147
4.3 Temporal leading order growth rate, σ_{0r}, for a fixed value of $b = 1.0$ with varying a. 152
4.4 The value of the integral condition I_N with varying K for $a = 0.7$ and $b = 1.0$. 154
4.5 Real part of d_0 with η for d $a = 2.0$ and $b = 1.0$. 161
4.6 Imaginary part of d_0 with η for d $a = 2.0$ and $b = 1.0$. 161
4.7 The value of the integral I_N with varying K for $a = 2.0$ and $b = 2.0$. . 162
4.8 Location of the disturbance for a circle. 163
4.9 The value of the integral I_N with varying K for $a = 2.0$ and $b = 1.15$. 164
4.10 Location of the disturbance for an ellipses. 165
4.11 Relationship between a^* and b^* for the condition of $I_N = 0$ with $a^* = aK^{1/2}$ and $b^* = bK^{1/2}$. 166
4.12 Next order growth rate, σ_{2r}, with the major axis, a^*. 167
4.13 Behaviour of $\overline{\sigma}$ with varying E. 168
4.14 2D symmetrical streamlines with the corresponding growth rates. . . . 170
4.15 2D non-symmetrical streamlines with the corresponding growth rates. 170
4.16 Schematic of an open cavity. 172
4.17 Streamlines within a square cavity. The DNS data was provided by Qadri [74] at $Re = 787$. 173
4.18 The value of the integral I_N with varying K_C for closed square cavity. 173

4.19 The value of the integral I_N with varying K_C for closed square cavity for a smaller range of K_C. 174
4.20 The predicted location of the instability in a square cavity. 174
4.21 The temporal growth rate σ_r with different streamlines. 175
4.22 Behaviour of $|\hat{V}_0|$ over S for $K_c = 0.1$. 176
4.23 Behaviour of $|\hat{V}_0|$ over S for $K_c = 0.4$. 176
4.24 Behaviour of $|\hat{V}_0|$ over S for $K_c = 0.414$. 177
4.25 Absolute value of the eigenfunction in y for the square cavity with superimposed basic flow streamlines in the cavity from DNS results. . 177
4.26 Absolute value of the amplitude function, d_0, along the normal coordinate to the streamline. 178
4.27 Basic flow streamlines within a rectangular cavity at $Re = 289$ with $L/D = 4$. The DNS results were provided Qadri [74]. 179
4.28 The value of the integral I_N with varying K_C for a rectangular cavity for a smaller range 179
4.29 The analysed streamlines in blue (.....) lines with the location of the instability as the red (_____) line for the rectangular cavity streamlines. 180
4.30 Absolute value of the eigenfunction in y for the rectangular cavity with superimposed basic flow streamlines in the cavity from DNS results. . 180
4.31 The temporal growth rate, σ_r, with different streamlines. 181
4.32 Streamlines within an open cavity at $Re = 1500$. The DNS data was provided by Qadri [74]. 182
4.33 The value of the integral I_N with varying K_C for an open cavity for a smaller range 182
4.34 The analysed streamlines in blue (.....) lines with the location of the instability as the red (_____) line for the open cavity streamlines. . . . 183
4.35 Absolute value of the eigenfunction in y for the open cavity with superimposed basic flow streamlines in the cavity from DNS results. . . 183
4.36 The temporal growth rate (σ_r) with different streamlines. 184

C.1 Dispersion relation for streamwise wavenumber, α_0, and spanwise wavenumber, γ_0, with $\gamma_0 \ll 1$. 211

G.1 The points used for the streamlines with a thickness of $\tau = 0.002$. . . 217
G.2 First spline example. 218
G.3 Second spline example. 218

H.1 Absolute value of the eigenfunction in x for the square cavity with superimposed basic flow streamlines in the cavity from DNS results. . 219
H.2 Absolute value of the eigenfunction in x for the rectangular cavity with superimposed basic flow streamlines in the cavity from DNS results. . 220
H.3 Absolute value of the eigenfunction in x for the open cavity with superimposed basic flow in the cavity from DNS results. 220

Table of contents

Abstract **5**

1 Introduction **14**
1.1 History of Flying . . . 14
1.2 Fluid Dynamics . . . 17
1.3 The Road to Transition. . . . 18
1.4 Stability Analysis . . . 19
1.5 Boundary-Layers . . . 21
1.6 Types of Disturbances . . . 22
1.6.1 Attachment-line instability . . . 22
1.6.2 Tollmien-Schlichting waves . . . 22
1.6.3 Görtler Vortices . . . 23
1.7 Crossflow Instability . . . 23
1.8 Receptivity . . . 25
1.9 Control Techniques . . . 27
1.10 Plasma Actuators . . . 28
1.10.1 Examples of Plasma Actuator Impact . . . 28
1.10.2 Operating Conditions for DBD Plasma Actuator . . . 31
1.11 Electromagnetism . . . 32
1.12 Secondary Instabilities . . . 32
1.13 Elliptical Instability . . . 33
1.14 Cavity Flow . . . 34
1.15 Base Profile of Swept Wings . . . 34
1.15.1 Falkner-Skan Profile . . . 34
1.15.2 Swept Hiemenz Flow . . . 35
1.16 Scope of Thesis . . . 35

2 An Asymptotic Approach for Predicting Streamwise Behaviour of Crossflow Vortices with Various Surface Curvatures. **40**
2.1 Introduction . . . 40
2.2 Formulation . . . 41
2.3 Base Profile . . . 42
2.4 Stationary and Travelling Crossflow Vortices on a Flat Plate . . . 52
2.4.1 Disturbance Equations . . . 52

2.4.2 Inviscid Modes . . . 52
2.4.3 Inviscid Results . . . 56
2.4.4 Viscous Correction Results . . . 60
2.4.5 Numerical Comparison . . . 65
2.4.6 Travelling Crossflow Vortices . . . 70
2.5 The Effects of Curvature on the Stability of Crossflow Vortices . . . 73
2.5.1 Results . . . 73
2.5.2 Numerical Comparison with PSE . . . 83
2.6 Conclusion . . . 86

3 Receptivity Theory of Crossflow Vortices with Surface Curvature Variations and Plasma Actuators. 89
3.1 Introduction . . . 89
3.2 Formulation . . . 90
3.3 Viscous Sublayer . . . 93
3.4 Receptivity Analysis . . . 95
3.5 Receptivity on a Flat Surface . . . 98
3.6 Influence of surface curvature on the boundary-layer receptivity. . . . 100
3.6.1 Convex Curvature . . . 102
3.6.2 Concave Curvature . . . 105
3.7 Receptivity of Surface Vibrations. . . . 107
3.8 Plasma Actuators . . . 115
3.8.1 Fluid-Plasma Interaction . . . 115
3.8.2 Formulation of DBD model . . . 118
3.8.3 FTCS Discretisation and Implementation . . . 120
3.8.4 Receptivity Analysis for Plasma Actuators . . . 135
3.9 Conclusion . . . 138

4 Three-dimensional short-wave instabilities developing on general two-dimensional closed streamlines 143
4.1 Introduction . . . 143
4.2 Formulation . . . 144
4.2.1 Flow Configuration . . . 144
4.2.2 Leading Order Problem . . . 150
4.2.3 Determination of Instability Location. . . . 152
4.2.4 Next Order Eigenvalue Problem . . . 155
4.3 Localised Streamlines . . . 162
4.3.1 Circular streamlines . . . 162
4.3.2 Elliptical streamlines . . . 164
4.4 Elliptical Instability . . . 167
4.5 Generalised Two-Dimensional Closed Streamlines . . . 169
4.5.1 Symmetrical Two-Dimensional Closed Streamlines . . . 169
4.5.2 Non-symmetrical Two-Dimensional Closed Streamlines . . . 170
4.6 Flow inside a Cavity. . . . 172
4.7 Conclusion . . . 185

5 Conclusion **188**

References **202**

A Boundary-layer equations **203**

B Shooting Method **205**

C Long-wave Approximation **207**

D Hadamard Finite Part Integral. **212**

E Secant Method. **213**

F Variables for Weber differential equation **214**

G Cavity Spline Examples **216**

H DNS eigenfunctions in x for a variety of cavities **219**

Chapter 1

Introduction

1.1 History of Flying

Ever since the dawn of time, mankind has had an obsession with the phenomenon of flight. The first known attempt at human flight was in 863 BC. Creating wings made of feathers, Bladud the 10th king of England jumped from a tower in order to fly. However, this approached failed and he died of a broken neck [55]. Bladud was probably inspired by the Greek myth of Icarus and Daedalus [2], who created wax wings and flew too close to the sun. Early ideas consisted of imitating flight in nature, in particular, birds. This is the main reason why most of the early attempts at flying involved attaching feathered wings to human arms and flapping zealously. People soon realised this idea would not work and it was replaced by mechanical objects. In the 1480s, Leonardo da Vinci came up with the concept of vibrating mechanical parts which were human-powered by arms or legs. These machines were called ornithopters. No evidence has be found to indicate whether or not these devices could fly or if they were even tested. Many years later the first human flight was achieved in 1783 in Paris [2] by Joseph and Etienne Montgolfier, who created a large balloon attached to a basket and used hot air to obtain lift. The idea came around because scientists knew at the time that hot air rises, so they used this concept.

Towards the end of that century, many revolutionary ideas came around, most notably by George Cayley. In 1799, he conceived the original design for the modern aircraft [2]. There were many concepts that were introduced by Cayley, such as separating the ideas of lift and propulsion. A fixed wing was used to generate a lift force and paddles

to produce drive. Other concepts incorporated were vertical and horizontal tails for stability during flight. Altogether these new ideas led to the development of the modern aircraft. He also created the first experiments to analyse the wings by fixing them to a whirling arm and seeing the impact of the lift force. However, this was not an accurate method, since vortices were produced and interfered with the experiment after a few rotations [12]. Cayley noted that the use of a fixed wing generated lift force and that force was enough to support the weight of the flying machine. Increasing the wing angle of attack and having a convex curved wing surface created a larger lift force. Cayley was the first person to state that the lift was generated from low pressure - this was a key discovery in aerodynamic history. Nonetheless, he was obsessed with an engine configuration that flapped like a bird to create the speed needed to fly. Another major notion that he suggested for plane design was to include multiple wings on top of each other, known as biplanes for two wings and triplanes for three wings. In the design, the structural integrity of his flying machine could not handle its own weight to sustain flight, but the multiple wings would share the load force. He went on to build the first human carrying glider in 1853, however this was not successful attempt at human flight.

The field of aerodynamics remained stagnant for a number of years, since many pioneers did not consider Cayley's contributions as progress on the journey to human flight. The flying enthusiasts were interested in building the best glider and flying from a large hill or building. A breakthrough was made in 1891 by Otto Lilienthal [2], who designed and flew the first successful glider. Lilienthal made over 2500 attempts at flight, but he was to die during one of these tests.

However most of the advancement came from America in the 1890s. Major developments in the creation of powered aircraft were made by Samual Pierpont Langley. He built several powered aircrafts and piloted two flights, but he was not successful and a few weeks later the Wright brothers achieved what Langley couldn't - human flight. On December 17th 1903 at Kill Devil Hills in North Carolina, Wilbur and Orville Wright produced the first manned, controlled powered flight in history. The new subject of aerodynamics grew vastly and research was undertaken into building faster and better machines, with the experiments of Cayley being revisited.

Phenomenal improvements were made mostly due to the First and Second World Wars.

In the First War, the design of the biplane aircraft had adopted multiple engines, a larger frame and heavier materials. It had a complete steel framework and improved piston engines. Airline companies were created after the First World War. During this time a slightly different design was used - a single - wing design called a monoplane instead of the multi-plane of the previous generation. In the Second World War new technologies were introduced, such as turbocharged radial engines, radar and navigation equipment. At the end of the war a new engine was introduced, the jet engine. However this was not a very successful transition, due to increased cost and weight compared to propellers [102]. The next innovation came after the Second World War - the transition from straight wings to swept ones. The idea was to reduce the drag caused by the wing due to compressible effects and structural integrity. This new approach changed the understanding of forces and stability on the aircraft. From here, commercial aircraft were developed and planes have been getting bigger ever since. Research on the stability properties of wing design and structure of the aircraft aided future designs and improvements. This is where the area of fluid dynamics comes into play. If we want to understand the behaviour of the flow around a plane, we need to understand the physics of the fluid motion. We are interested in reducing the drag of an aircraft and increasing the region where the air is laminar. We will discuss the advancements in this field in the following sections.

1.2 Fluid Dynamics

The field of fluid mechanics has been around since Ancient Greece. Archimedes discovered that if an object is placed in a liquid then there will be a displacement of this fluid due to the buoyancy force from the objects weight [50], and hence the idea of fluid mechanics was born. Later, during numerous observations (whilst considering a duct for example) Leonardo da Vinci found a relationship between the cross-sectional area of a duct (A) and the velocity of the fluid (V)

$$AV = \text{constant}.$$

This was known as the continuity equation. Hundreds of years later fluid dynamics developed further with the aid of Euler, who derived differential equations representing the motion of an incompressible fluid but with frictional forces neglected and they are given by

$$\rho_t + \nabla \cdot (\rho \mathbf{u}) = \mathbf{0}, \tag{1.1}$$

$$\mathbf{u_t} + (\mathbf{u} \cdot \nabla)\mathbf{u} + \frac{\mathbf{1}}{\rho}\nabla \mathbf{p} = \mathbf{0}, \tag{1.2}$$

where ρ is the density of the fluid, $\mathbf{u}$= (u, v, w) is the velocity of the fluid, t denotes the time, p is the pressure of the fluid and $\nabla = (\partial/\partial x, \partial/\partial y, \partial/\partial z)$. The continuity equation is described as (1.1) and the motion of the fluid, momentum equations, are represented by (1.2). The key result from Euler was that the pressure forces act inside a moving fluid. Later internal viscous forces were included in the Euler equations by Navier (1827) and Stokes (1845) to produce the well known Navier-Stokes equations

$$\frac{\partial \mathbf{u}}{\partial t} + (\mathbf{u} \cdot \nabla)\mathbf{u} = -\frac{\mathbf{1}}{\rho}\nabla \mathbf{p} + \nu \nabla^{\mathbf{2}}\mathbf{u}, \tag{1.3}$$

where ν is the viscosity coefficient and with the continuity equation given by

$$\nabla \cdot \mathbf{u} = \mathbf{0}. \tag{1.4}$$

with $\rho =$ constant. These are the governing equations for fluid dynamics.

1.3 The Road to Transition.

Understanding the flow dynamics of an aircraft in flight conditions is a very difficult task. The process that the flow undergoes is complicated and many factors are involved. An important part of this process is that it undergoes a transition from laminar flow (parallel streamlines) to turbulent (chaotic, mixed) one. The region where this changes is called laminar-turbulent transition. It is important to understand the characteristics of the flow for prediction of this transition location. Laminar flows are sensitive to adverse pressure gradients and are inclined to separate, whereas turbulent flows create larger wall friction. For more details see [87].

Reynolds [80] assessed this laminar-turbulent transition by performing experiments in a pipe. He did this by injecting ink into a pipe with a water flow and observing the results. He noted that there were different regimes based on the speed of the flow, laminar and turbulent regions. A parameter, which is named after him, quantified this different behaviour of the fluid. The Reynolds number is the ratio of the inertia forces over the viscous ones and it dictates the transition process. We are interested in what caused this transition to occur.

In aerodynamics many factors exist that contribute to the triggering of turbulence. In a three-dimensional boundary-layer on a swept wing, various instabilities are observed, such as crossflow vortices and Görtler vortices. In a two-dimensional environment the instability takes the form of Tollmien-Schlichting (T-S) waves. These are primary instabilities and research has developed to focus mostly on them. If there is nonlinear breakdown of these instabilities, a secondary instability can occur. For example, a T-S wave will develop spanwise variations the further downstream it propagates. These cause a three-dimensional structure, which develops a vortical structure and the generation of this can be analysed by secondary stability theory. Understanding the behaviour of secondary stabilities is helpful for predicting where the transition region is. The primary linear theory is simply not enough to accurately predict this. Other phenomena can also occur, e.g. turbulent spots can occur within the disturbances, causing fluctuations of laminar and turbulent regions - this development is called indeterminacy. The disturbances discussed thus far have small amplitudes (natural transition). If we were to consider larger amplitudes (higher levels of free-stream turbulence) there will not exist any linearly growing disturbance modes. A turbulence intensity level of 0.5% or

more will cause this bypass transition to occur. For more details see [86].

1.4 Stability Analysis

Researchers have become intrigued by perturbations to the mean flow for various fluid dynamical systems and hence, the research area of stability analysis has arisen. One of the first of these studies was performed by Lord Rayleigh in 1887. Rayleigh derived the inflexion point criterion. This governs if there exists an inflexion point within a velocity profile then there exists an unstable inviscid perturbations within the fluid [78]. Some of these perturbations will grow and might eventually become turbulent.
To analyse this system from a mathematical point of view the idea was to consider time stability characteristics of dynamical systems within rigid bodies. A base solution to the Navier-Stokes equations was perturbed by a small variation and evolved in time as $e^{\omega t}$. For a perturbation to be considered growing, in this situation, they had real and positive ω values with this evolution of the perturbation. In general this is not true and ω is normally complex for global stability analysis. However this would be the opposite for decaying or stable solutions since they had negative ω. The main interest is in small perturbations, such that quadratic terms are ignored, for a linearised set of equations (linearised with respect to the small perturbation). To understand the early development of stability analysis we consider the following example of perturbation into the linearised Navier-Stokes equation (this will become useful later for our stability analysis)

$$\vec{u} = (u_b(y) + U(x, y, t), V(x, y, t), 0). \tag{1.5}$$

With $u_b(y)$ denoted as the basic flow from which it is steady and parallel. The velocity perturbations, U and V, are normal to the wall and streamwise direction respectively. This is a solution for boundary-layer and pipe flow. For the continuity equation to be satisfied, the stream function $\Psi(x, y, t)$ is introduced and such that

$$U = \frac{\partial \Psi}{\partial y}, \quad V = -\frac{\partial \Psi}{\partial x}. \tag{1.6}$$

Hence, following the work of Rayleigh [78] we represent the perturbation in the normal-mode form

$$\Psi(x, y, t) = \Phi(y) e^{i(\alpha x - \omega t)}, \tag{1.7}$$

where $\Phi(y)$ is an eigenfunction and either α or ω is an eigenvalue depending on whether analysing spatial or temporal stability. For temporal stability α is a real quantity and is consider given, ω is complex eigenvalue to be found, and an instability arises when $\omega_i > 0$. Since ω is complex, $\omega = \omega_r + i\omega_i$ with ω_r described as the frequency and ω_i is known as the amplification factor. For convenience, with temporal stability, a new parameter c is introduced and characterises the phase velocity (c_r) of the wave with $c = \omega/\alpha = c_r + ic_i$. However, for spatial stability, ω is a given real quantity and α is complex, and the condition for the disturbance to become unstable is $\alpha_i < 0$. The streamwise wavenumber, α, is complex, therefore $\alpha = \alpha_r + i\alpha_i$ where α_r describes the oscillation and α_i is the growth rate of the disturbance mode. The evolution of both of these disturbances is the same - either can be studied for stability analysis. Gaster [30] showed that the amplification rates are the same for both spatial and temporal, to some high order correction. In particular, for small amplification rates the frequencies are related to the spatial growth rate by the group velocity. Linearising the Navier-Stokes equation with respect to the disturbance and substituting (1.5), (1.7) into (1.3) yields

$$(u_b - c)(\Phi'' - \alpha^2\Phi) - u_b''\Phi = \frac{-i}{\alpha Re}(\Phi'''' - 2\alpha^2\Phi'' + \alpha^4\Phi), \tag{1.8}$$

where the prime denotes derivatives with respect to y and Re is the Reynolds number which is given by $Re = u_e d/\nu$, u_e is a reference velocity far away from the fluctuations and d is the reference length scale of the system. This is the Orr-Sommerfeld equation derived by Orr (1907) [68] and Sommerfeld (1908) [93]. For a boundary-layer there is a no-slip condition at the wall and disturbances decay far away from the wall

$$\Phi(0) = \Phi'(0) = 0, \quad \Phi(\infty) = \Phi'(\infty) = 0.$$

For laminar parallel flow the stability characteristics are described by the Orr-Sommerfeld equation. This is an eigenvalue problem for c, Re and α are consider given, $c = c_r + ic_i$ is an eigenvalue with eigenfunction $\Phi(y)$ and needs to be solved to find the stability properties.

Rayleigh was interested in the inviscid temporal stability. By taking the limit where

the Reynolds number is large in the Orr-Sommerfeld equation reduces to

$$(u_b - c)(\Phi'' - \alpha^2\Phi) - u_b{}''\Phi = 0. \tag{1.9}$$

This is known as the Rayleigh equation and is reference to Lord Rayleigh's work in 1879. This equation will appear in Chapter 2 in the context of analysis of crossflow vortices. An analytical study of the Orr-Sommerfeld equation was performed by Tollmien [97] and Schlichting [88], and this is the link to modern boundary-layer theory. We are interested in disturbances that occur in a swept wing. The idea of boundary-layers was first introduced by Prandtl.

1.5 Boundary-Layers

The concept of boundary-layers was first thought of in the early 1900s by Ludwig Prandtl. He presented a paper in Germany in 1904 which outlined a slightly viscous fluid near a solid boundary [72]. In this paper certain assumptions were made. Firstly the Reynolds number is large, so the viscous terms can be neglected far away from the solid boundary. Then there exists a thin layer of fluid near the solid boundary and this fluid is known as a boundary-layer. Outside this viscous flow is an inviscid flow region, which gives rises to a two-deck structure. This boundary layer has a thickness of δ and is is given by $\delta/L \propto Re^{-1/2}$, where L is the characteristic length scale of the solid boundary. The pressure from outside the boundary-layer is not significantly different from the pressure inside the boundary-layer. The boundary condition for pressure can be approximated by the value of upper boundary in the inviscid region. Rescaling the wall normal coordinate y by the boundary-layer thickness $Re^{-1/2}$ implies that we are located within the boundary-layer and this retains some viscous terms. The following scalings are introduced to perform analysis within a boundary-layer

$$x^* = xL, \quad y^* = \delta yL, \quad z^* = zL, \quad p^* = p_\infty + \rho {U_\infty}^2 p, \tag{1.10}$$

$$u^* = U_\infty u, \quad v^* = \epsilon U_\infty v, \quad w^* = U_\infty w. \tag{1.11}$$

The thickness of the boundary layer, δ, can be determined by balancing the viscous term with the inertial terms. For instance considering the x-momentum equation in the

Navier-Stokes equations we observe the following balancing between the inertia and viscous terms,

$$u\frac{\partial u}{\partial x} \sim \nu\frac{\partial^2 u}{\partial y^2} \implies \frac{U_\infty^2}{L} \sim \frac{\nu U_\infty L^2}{\delta^2} \implies \delta = Re^{-1/2}. \tag{1.12}$$

1.6 Types of Disturbances

In a three-dimensional boundary-layer on a swept wing, various instabilities are introduced, such as T-S waves, crossflow vortices and Görtler vortices. Tollmien-Schlichting [97, 88] waves enter into the boundary-layer with variations in the curvature of the surface being receptive to acoustic disturbances. Similarly, Görtler vortices can be generated by the concavity of a surface [37] and crossflow vortices are introduced by surface roughness and sweep angle [38].

1.6.1 Attachment-line instability

In a swept wing, the first instability to occur is the attachment-line instability. The attachment-line instability can be eliminated by either a Gaster bump [31] added at the leading edge or suction of the boundary-layer. The idea is to exclude any turbulent flow and not inject turbulence into the boundary-layer. Otherwise, the boundary-layer will be contaminated and the transition to turbulence will occur at the leading edge.

1.6.2 Tollmien-Schlichting waves

T-S waves are generated by some external disturbance, such as acoustic noise or sound waves interacting with the surface roughness via a process known as receptivity. It is a streamwise disturbance that emerges in a viscous boundary-layer and is dominant in two-dimensional and swept-wing transition. As these waves propagate downstream, they slowly amplify until nonlinear effects take action and the flow eventually becomes turbulent.

1.6.3 Görtler Vortices

In 1941, Görtler [35] showed solutions of the disturbance equation to counter-rotating structures that were streamwise orientated. The pressure fluctuations occur when the boundary-layer thickness is comparable to the radius of curvature and thus creates centrifugal instability. This centrifugal-type instability is named the Görtler instability which is a consequence of the formation of Görtler vortices. One can predict the onset of Görtler vortices by using a dimensionless number called the Görtler number (G). The Görtler number [36] is defined as mentioned earlier $G = 2Re^{1/2}l/a$, where a is the radius of curvature, Re is the Reynolds number and l is the typical length scale along the wing. The instability is not just limited to concave geometry - it can also be applied to convex geometry.
These vortices are very similar to the Taylor vortices [94] produced in Taylor-Couette flow. This flow arises amidst of two concentric cylinders where an array of vortices are generated. For more details about these two flows, see Rosenhead [82].

1.7 Crossflow Instability

In 1952, Gray [38] recognised that the transition of a swept wing occurred much earlier than the transition of an unswept wing. In observing the flow, he noticed that stationary vortices were close to the leading edge. The sweep of the wing coupled with a pressure gradient produces curved streamlines in the inviscid region. The pressure gradient remains the same in the boundary-layer (compared to outside the boundary-layer) but the streamwise velocity decreases, inducing a secondary flow perpendicular to the streamlines. There is no imbalance between the pressure gradient and the centripetal acceleration [101]. This traverse flow is called a crossflow. We are concerned with three-dimensional boundary-layers in the modelling of this instability. Further investigations into crossflow vortices have been made since Gray's investigation with the application of a rotating disk. Gregory, Stuart and Walker [39] investigated and found (experimentally and via asymptotic analysis) that the production of crossflow vortices occurred in a three-dimensional boundary-layer on a rotating disk. This work was developed further by Hall [42] and can be applied to swept-wing cases. Since then, more detailed studies have been performed analytically. They give insight into the stability

of crossflow vortices, since the velocity profiles demonstrate a basic state and stability analysis similar to a swept wing. Rotating disks are easier to analyse because there are some well known similarity solutions [79]. Nonlinear effects are still currently being investigated.

Crossflow vortices are an inviscid instability since the vortices must vanish at the wall and also decay away from the boundary-layer, therefore there must be an inflexion point in the basic flow (the combination of $\alpha u + \gamma w$). The appearance of crossflow vortices at the beginning of the boundary-layer means that they lie within a few degrees of the inviscid streamline. Visually, crossflow vortices appear to be co-rotating structures.

Stationary crossflow vortices are produced in quiet freestream (low levels of turbulence) flight conditions, near the leading edge of a swept wing. Quiet freestream conditions mean that the environment has very low levels of turbulence. Whereas in high levels of freestream turbulence, the travelling crossflow modes dominate over the stationary one. Understanding the behaviour of these disturbances is very important for transition prediction, since eventually, due to non-linear processes they break down into turbulence. Both stationary and travelling crossflow vortices have been shown to appear in experiments for three-dimensional boundary-layers of swept wings. These were performed by Müller & Bippes [64], Poll [71], Dagenhart & Saric [24] and Arnal *et al.* [3]. Instabilities arise because of the favourable pressure gradient and inflexion in the mean velocity profile. Müller & Bippes used a swept flat plate inside a wind tunnel and discovered the existence of regular patterns of crossflow vortices. Several external disturbances were investigated but in their experiment they showed that freestream turbulence was the most effective in producing the largest disturbances. A different experiment by Radezsky *et al* [77] found that the transition location of a crossflow disturbance was not effected by acoustic noise. A connection between very low freestream turbulence and surface roughness for stationary crossflow vortices was first made by Müller & Bippes. In their wind tunnel experiments they noticed that regular patterns of stationary crossflow vortices were connected to the swept wing test section.

It is important to understand the impact of surface roughness on transition for this receptivity mechanism. Many studies in the 1990s have looked at different roughnesses,

such as natural roughness and Direct Roughness Elements (DRE) [85], [77],[14]. Radezsky [77] showed that the most amplified stationary crossflow vortices were most effective when a surface roughness was placed near the neutral stability point. The neutral stability point is the location where the crossflow mode growth rate first becomes positive and therefore the disturbance grows from this point. Research has shown that the periodic placement of DRE has some control, reducing the crossflow amplitudes over which instability waves are being propagated downstream. Distributed roughness studies have been performed by Radezsky, Reibert & Saric [76]. From their experiments they showed that a certain wavelength (λ) spacing of the DRE could delay transition by reducing the amplitudes of the crossflow modes. This is related to the wavelengths of the crossflow modes. The optimal spacing of the DRE was a wavenumber spacing of $k = 2\pi/\lambda$ and only integer multiples of the spanwise wavenumber can produce instability waves [86]. Suppression of the most unstable waves can be achieved through this mechanism, aiding transition control. Interestingly, Saric *et al* [85] found that an unpolished swept wing had lower initial disturbance amplitudes than a polished one. This seems to also suggest that randomised roughness may aid control for crossflow vortices.

The effects of convex surface curvature on the stability characterisation were examined by Malik *et al* [56], [58], [57]. They used perturbation theory and PSE (Parabolized Stability Equations) to model the boundary-layer over a swept cylinder. The results showed that convex curvature has a stabilising effect on crossflow modes.

1.8 Receptivity

We are interested in receptivity, a term first coined by Morkovin [62] in 1969. It concerns the initial stage of the transition process consisting of a progression of external disturbances, such as surface roughness, acoustic noise or free-stream turbulence, into internal instability waves within the boundary-layer. A wide range of disturbances can occur upon penetration of the boundary-layer. Many of these disturbances decay and only a few amplify downstream. These grow linearly until the amplitudes of the disturbances become large enough to introduce non-linear effects, which breakdown and then eventually the transition to turbulence occurs. This is why understanding of the problem of receptivity is very important and the mechanisms involved in this

transition process. Ruban [84] and Goldstein [34] investigated the receptivity of a two-dimensional boundary-layer over a flat plate with the influence of an acoustic disturbance. They found that streamwise variations in surface geometry, coupled with the external acoustic waves, produced a T-S instability wave. This was the first theoretical study of receptivity. Since then an abundance of work has been done by numerous authors to try and understand the different mechanisms involved.

However, the receptivity mechanisms are different for a three-dimensional disturbances such as crossflow vortices, which are produced by external disturbances interacting with imperfections on the swept wing. One of the first attempts to understand crossflow receptivity was undertaken by Choudhari & Streett [16]. They suggest in their report that the travelling crossflow modes have larger growth rates than their stationary counterpart, but the receptivity mechanism tends to excite the stationary crossflow vortices. This statement has been verified independently by Crouch [21] and Choudhari [17] for swept wedge flow with a basic profile of the Falkner-Skan-Cooke equations. The receptivity theory of Ruban and Goldstein was extended to analyse the crossflow disturbance by Crouch [21], Streett & Choudhari [17],[16] in the same classical manner. They created a method for solving the receptivity problem by using quasi-parallel approximation within the vicinity of the surface. Rather than the more classical approach, the reduction of the Navier-Stokes equation using asymptotic analysis. The method was called Finite Reynolds Number Theory (FRNT). The idea first came from Zavol'skii *et al.*[104], who looked at non-localized acoustic receptivity over a wavy wall within a two-dimensional boundary-layer. There are numerous applications for FRNT which have been summarised in the review articles of Crouch [22] and Streett & Choudhari [17]. Solutions can be obtained with ease by using the FRNT for a vast number of receptivity problems involving curvature, localised surface roughness and vortical disturbances [19],[22], [89]. By using FRNT, Crouch [21] and Choudhari [17] showed that initially the stationary crossflow mode amplitudes are much larger than the travelling crossflow modes. The stationary crossflow vortices were created via the basic flow interaction with the surface roughness by a direct scattering mechanism whereas the travelling crossflow vortex was generated via free-steam acoustic wave interaction with the surface roughness. This result actually validates experimental data and what we observe in flight conditions is that the initial amplitudes of the travelling

crossflow modes are very small. This is consistent with the experiments of Deyle & Bippes [27]. They discovered that stationary crossflow modes have a higher amplitude at low turbulence levels, due to the number of factors involved. Another experiment by Radeztsky [75] showed that the transition location of the crossflow vortices was unaffected by acoustic waves and also verified the results of Deyle & Bippes. These experiments by Radeztsky, predict that the largest crossflow mode amplitude occurs just upstream from the neutral stability point of the roughness. It is known that the receptivity is most effective near the leading edge but within this region the growth rates are damped and hence the disturbance will be reduced [89]. A major point made by Choudhari [17] was that non-parallel effects are key near the neutral stability point. We must also mention that a practical application of this theory would place the neutral stability point within the vicinity of the leading edge of a swept wing, which has a large surface curvature, hence the curvature effects are key to understanding the receptivity of crossflow vortices.

A study on the effect of convex curvature and non-parallelism on the receptivity of crossflow vortices was performed by Collis & Lele [19]. From this study they discovered that convex curvature enhanced the receptivity response coefficient.

1.9 Control Techniques

The interest in new technology for laminar-turbulent control is expanding research sector. An abundance of research already exists for passive control techniques such as randomized roughness elements, direct roughness element (DRE) and porous holes. As mentioned earlier in the introduction, DRE are used for control because a certain spacing of the elements in the spanwise direction can eliminate the most dangerous modes. A certain spanwise wavenumber give rise to a particular streamwise growth rate. These elements are micron sized and aid transition by increasing the transition point. We are interested in active flow control techniques, such as suction, heat spots and plasma actuators.

1.10 Plasma Actuators

One of the most intriguing control techniques is the plasma actuator, since the plasma can form a force similar to that of a micron-sized element on the air fluid particles. The idea is to replace the DRE with a micron-sized plasma. The plasma actuators are non-thermal so they do not cause a reaction with the neutral oxygen/nitrogen in the air. No mechanical moving parts are needed for the plasma actuator, which is only powered by the electrodes that are situated on and within the surface. Due to the high frequency response of the plasma, the fluid (air) feels the plasma as a solid surface bump, due to the time scales of the recombination rates of the plasma [67]. The plasma length scales can be changed by the electric potential, which modifies the electrodynamic force and hence is very useful for flow control because the width and height of the plasma can be modified. These devices have been used in numerous ways for unmanned aerial Vehicles, as an example of this can be used for flow control of separation reduction by creating a body force that accelerates the air surrounding it and this interacts with the turbulent region. Plasma actuators cover a variety of different devices that utilise electrical discharge in various ways such as arc discharge, dielectric barrier discharge (DBD), glow discharge and corona discharge. However we will not delve into too much detail about these devices other than the DBD actuator.

1.10.1 Examples of Plasma Actuator Impact

As mentioned in the introduction previously, plasma actuators are used for various flow controls in an aircraft. Examples of these controls are hypersonic flow control, vortex generator and turbulent wakes active noise control, and T-S wave cancellation. The following figure shows an example of the impact the plasma actuators have on the flow around aerofoil. We have the situation where turbulence has fully developed and a DBD plasma actuator is placed near the leading edge of an aeroplane wing.

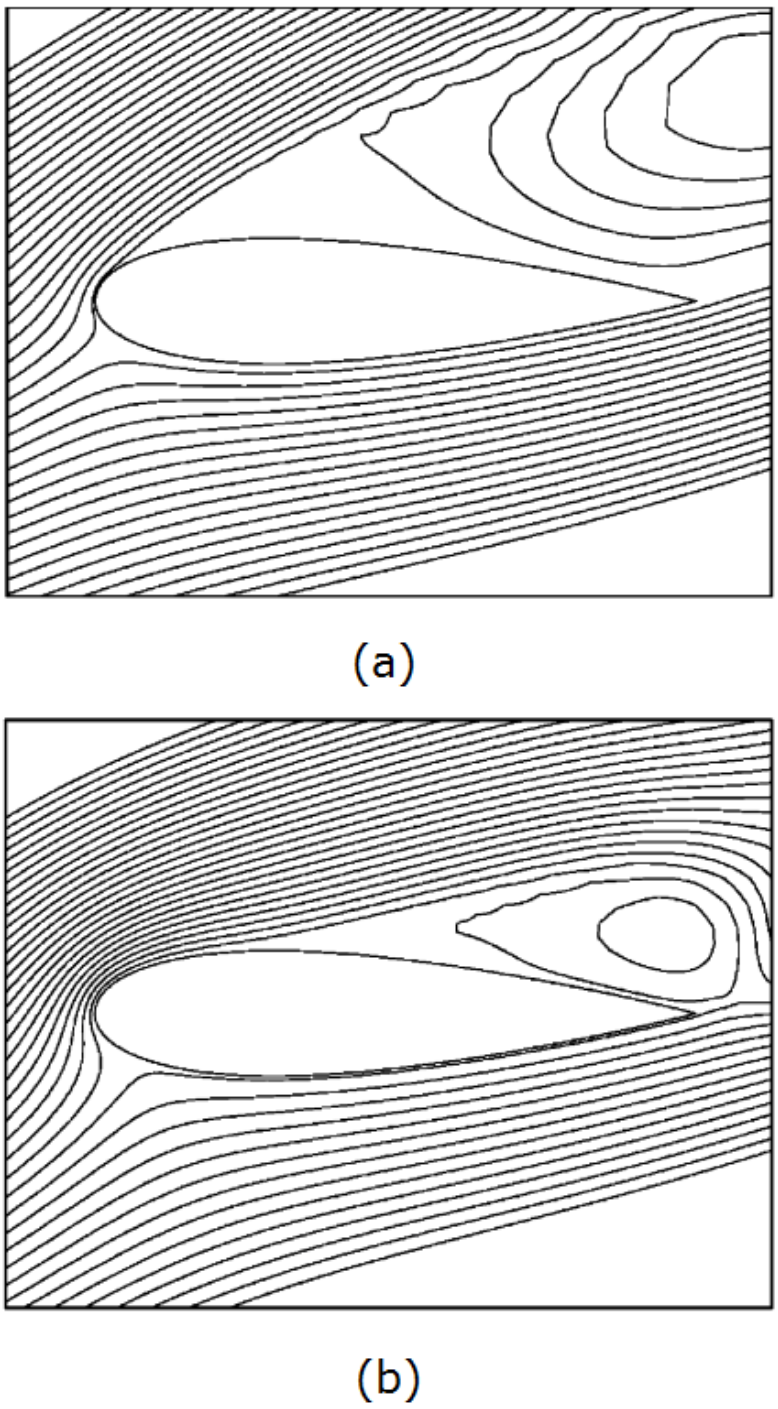

Figure 1.1: Stream functions from numerical simulation (DNS) for flow around NACA 0021 airfoil at a 23° angle of attack. Left plot is baseline. Right plot corresponds to plasma actuator operating at leading edge [67].

In figure 1.1(b) we notice with the addition of the plasma actuator at the trailing edge there is an increase in the number of streamlines. There appear to be more straight streamlines corresponding to laminar flow. There is less turbulence in the system with this introduction of the plasma actuator due to the additional straight streamlines appearing. The plasma actuators can be used to control many disturbances on the aeroplane wing. Experiments have been performed on the control of T-S waves by Grundmann *et al.* [40]. A similar impact occurs when the plasma is introduced for T-S waves - the amplitudes of the disturbance have been reduced.

Thus far we have only discussed the single plasma DBD. We have discussed DRE and its effects but could plasma be arranged in this way? There are various ways to arrange the electrodes to produce the plasma. This is useful, as we have seen, for the crossflow instability.

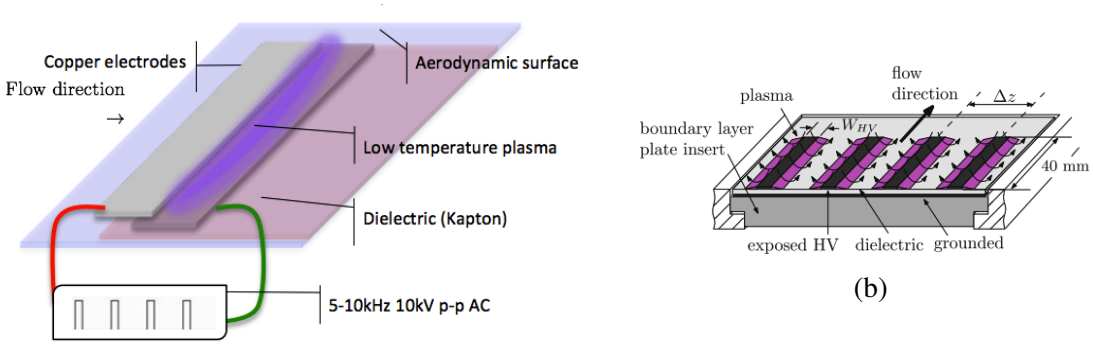

Figure 1.2: Outline configuration for (a) a continuous strip of electrode along the spanwise direction (figure from a report by Alonso & Chirayath [1]) (b) isolated electrodes periodically placed in the spanwise direction (figure from a study by Ronald [81]).

Experiments by Alonso & Chirayath [1] showed the first real world application of plasma actuator control on an unmanned aerial vehicle (UAV). By including the plasma on the wing of the UAV a lot of improvements were made to the efficiencies of weight, power and response time compared to more traditional electrical and mechanical controls. Ronald demonstrated in the figure 1.2(b) that it is possible to have a spanwise array of these micron sized plasmas [81].

1.10.2 Operating Conditions for DBD Plasma Actuator

We will now summarise the operating conditions and improvements to the DBD plasma actuator. We shall mention the efficiency of the actuator. With regards to efficiency, there are typically two types components of the actuator (either mechanical or electrical) and air flow control. Electrical improvements include optimising electrodes, capacitors and circuits, whereas mechanical optimisation includes understanding the induced body force, kinetics power and electric winds that arise. All of these components and physical phenomena combine together to improve the efficiency of the plasma actuator, which for these case studies are usually in free air or with no free flow induced [61]. There has been an abundance of research into air flow control, especially for velocities of around $30m/s$. There have been some significant results for larger velocities of around $110m/s$. However, these results are far from cruise conditions though where commercial aircraft typically fly around $450-500kn$, or in standard units $240 - 260m/s$. The conditions for the electrode that are typically selected have the following ranges and values;

- frequency: 100-500 kHz
- voltage: 5-50 kV
- width: 10-20cm
- height: 5-20mm
- gap: 0-5mm

The weight requirements are very small - the main concern is the power consumption. Grundmann *et al.* showed that there was an increase of efficiency with pulsed ($8.1W/m$) and non-pulsed electrodes ($68.3W/m$) [40]. Interestingly enough, Kriegseis [52] found that there was a linear relation between the plasma forcing and power, length of the plasma, voltage and consumed power. There has been an abundance of research regarding improving the plasma actuator and implementing it for commercial use. The plasma height is typically a few millimetres, whereas, with natural surface roughness on swept wings typically has a height of a few microns. This could be a problem from a practical point of view, since separation would occur at the leading edge.

1.11 Electromagnetism

We are considering a plasma actuator in place of a roughness bump for the production of crossflow vortices. Plasma is one of the four natural fundamental states and is formed when gas is ionised. This ionisation occurs when the gas is exposed to electromagnetic forces. Electromagnetism is one of the four fundamental forces and is described by an electromagnetic field. It concerns the interaction between charged particles with force fields. The mathematical description of the generation of electric and magnetic fields can be modelled by the Maxwell equations and Lorentz law [54]. For more information please refer to this reference [54].

1.12 Secondary Instabilities

Thus far we have only discussed primary instabilities near the leading edge of the swept wing, as mentioned (in the road to transition section) secondary instabilities can be generated further downstream. Secondary instabilities are of great importance in various areas of interest within the field of fluid dynamics. Modelling the behaviour of these is important for aerodynamic applications, where these secondary flows appear in various regions. They can be produced from secondary mechanisms such as nonlinear interactions, separation or vortex-wave interactions. This is also of great interest to the turbulence community. We are interested in the secondary instability denoted the elliptical instability. As the name states, the mechanism is governed by elliptical streamlines where three-dimensional flows can be formed via an instability of two-dimensional streamlines. The elliptical streamline is undistorted such that the normal modes produced in the three-dimensional mechanism align with the corresponding strain field. The associated growth rates, which initially are linear, have a relationship to rate of strain. The instability in question is very sensitive to initial conditions due to the breakdown of small scales and this makes modelling turbulence very difficult. For the three-dimensional instability there is a balance between the vorticity perturbation generation via tilting of the base flow and the stretching of the vorticity. This mathematical and numerical pursuit shows the failure of classical theory but does not account for the three-dimensional instability occurrence. There seems to be an appearance of a generic mechanism from the justification of insensitivity of the two-dimensional in-

stability. Considering most two-dimensional flows, the occurrence of the tilting and stretching combination is likely, henceforth the arise of elliptical streamlines. This led to the hypothesis that "the three-dimensional stability exists due to the ellipticity of these domains" [70]. For a general two-dimensional instability in shear flows, this supplies a general mechanism.

1.13 Elliptical Instability

In 1970 Crow [23] studied a vortex pair subject to a three-dimensional instability and discovered that they were susceptible to long-wave instabilities relating to the vortex separation. This was one of the early results indicating this elliptical mechanism. At a similar time, but using a different formulation and understanding, Obukhov [66] found highly nonlinear effects when investigating the impact of a rotating triaxial ellipsoid submerged within fluid. Similar dynamics were noticed in this experiment, where three-dimensional flows can be generated from two-dimensional elliptical streamlines. Related to this work, a study performed by Gledzer [32] in an elliptical cylinder with rotating fluid within. Saffman & Moore [60] provided further evidence of the existence of the elliptical streamlines with an external straining force applied to an antisymmetric vortex.

Several years later this instability re-emerged for a strained vortex, which was uniform and unbounded [70]. The motivation was the turbulence studies of Brown and Roshko [11] and Townsend [98] in the 1970s when there was deep underlying intrigue in the stability of large scale turbulent eddies. Pierrehumbert [70]stated that both the strain force and the vorticity were constant (spatial direction) with a quadratic flow formed of elliptical streamlines. The temporal growth rate had a strain rate dependence as shown in previous studies. Bayly [5] verified this with the use of Floquet modal analysis. This theory was extended and generalized to the elliptical cylinder of the experiments of Gledzer [32],[33] by Waleffe [99], who used a weakly nonlinear assumption and predicted the existence of elliptical instability in the experiment.

1.14 Cavity Flow

Thus far we have discussed bumps and rivets on a swept wing, but what about the other surface imperfections such as indentations and gaps? The fuselage has instruments to measure various pressures and temperatures - these sensors are implemented in such a way that cavities exist. Cavities also appear within landing gear wheel wells, weapon bays and other sensors. This equipment is needed for monitoring and therefore cannot be ignored. The flow in and around these cavities needs to be understood to reduce fuel load and increase efficiency. Modelling the flow inside and outside the cavity has proved a challenge over the years. From a simple geometrical cavity arises an abundance of interesting phenomena, such as convoluted wave interactions, resonant tones and acoustic instability waves. The following fluid dynamical processes occur around the cavity; vortical disturbance amplification via the shear layer, vortex-surface interaction producing pressure waves, acoustic waves travelling upstream and the conversion of pressure waves into vortical modes via a receptivity process at the cavity's edge.

Academic interest arose in the 1950s - the first researcher to address this issue was Krishnamurty [53], who was interested in aeronautical applications and impacts such as structural fatigue. This led to the idea of controlling the resonant tones occurring around the cavity. This is of great importance when considering fuel efficiency and structural effects with the sparse pressure waves and large disturbance amplitudes produced. Practical solutions are non-trivial for suppressing the resonant waves. Several control techniques exist that are passive, active/closed-loop systems. The control techniques all have advantages and disadvantages, which have been considered over years of research. For more details about the progress and advancements for open cavity flow, please refer to the review paper of Rowley & Williams [83].

1.15 Base Profile of Swept Wings

1.15.1 Falkner-Skan Profile

A possible solution for a pressure gradient driven boundary-layer in a two-dimensional framework was proposed by Falkner and Skan in 1931 [29]. In their analysis they re-

duced partial differential equation into a system of ordinary differential equation. They approach the solution via a method called a similarity solution. This method implies that for the coordinate(s) involved are indistinguishable. They have the same form for all time or length scales. For two different positions in the streamwise direction (x), the streamwise velocity ($u(x, y)$) change by a scale factor in the wall normal direction (y). Therefore, the old velocity and the new rescaled velocity will have a similar profile. The dimensionless coordinates will be the same as they were before.

1.15.2 Swept Hiemenz Flow

The theoretical description of the attachment-line boundary-layer was proposed by Hiemenz [46] in 1911. He found a solution to the plane viscous stagnation point flow, which is known as plane Hiemenz flow. The stability was first studied by Görtler [36] and Hämmerlin [44] in 1955. They thought a centrifugal-type instability would cause the flow to become unstable. By adding sweep to the plane Hiemenz flow, performing any stability analysis proved difficult. The classical way of solving fluid dynamics problems was an Orr-Sommerfeld approach to an eigenvalue problem. This was very different from parallel flows, which were widely studied during the period of time. However, Hämmerlin [44] found a spectrum of continuous stationary perturbations that consisted of real spanwise wavenumbers. Wilson and Gladwell [103] confirmed this and also found that two types of disturbances exist, one which decays algebraically (they neglected this solution deeming it to be unphysical) and the other which decays exponentially (but this was always stable). Later a connection between plane Hiemenz flow and attachment-line flow of swept wings was made by the research of Dallman [25] and Hall, Malik & Poll [43]. By introducing crossflow in the plane Hiemnez flow a three-dimensional attachment-line boundary-layer can be obtained.

1.16 Scope of Thesis

The mathematical analysis is separated into three parts. Firstly in Chapter 2, we consider the stability characteristics of crossflow vortices with curvature variations. In Chapter 3, will deal with the issue of what impact small deviations in curvature will

have on the receptivity of crossflow vortices. Lastly, Chapter 4 will construct short-wave three-dimensional instabilities from a general closed two-dimensional streamline.

We begin with Chapter 2, which describes the linear development of both stationary and travelling crossflow vortices with small curvature variations, including convex and concave surfaces. This chapter is split into two parts. The first part concerns linear stability analysis without any curvature, i.e. a flat plate, and the second part will discuss the effect of the curvature. We formulate the general problem in §2.2, in which we derive a framework to include curvature variations and therefore transform into body-fitted coordinates. In §2.3 we introduce the basic flow that we will use throughout Chapters 2 & 3, which is a swept Hiemenz flow and is a standard base flow for problems concerning a three-dimensional swept wing.

We concentrate only a flat surface for our initial development of the asymptotic approach for calculating characteristics of crossflow vortices in §2.4. We develop an asymptotic theory to predict the stability behaviour of stationary crossflow vortices, initially. In §2.4.3 our inviscid analysis provides us with the leading order growth rate of the stationary crossflow mode and a dispersion relation between this growth rate and the spanwise wavenumber of the vortex. The theory was developed further by analysing the viscous sub-layer of the boundary-layer. This produced a correction term to the growth rate, which depends on information about roughness shape, to the leading order inviscid growth rate. The development of the viscous analysis can be seen in §2.4.3. With this in mind we compared the theoretical approach with two different numerical techniques of PSE and VV which can be found in §2.4.5. The PSE results were provided by Mughal [63] and Masad & Malik [59], whereas the VV results were provided by Thomas [95]. Finally, this method can be extended further to include travelling crossflow vortices. The developments are examined in §2.4.6.

The initial development of this theory ignored the curvature changes - a parameter which defined the curvature was set to zero. With this control parameter set to a non-zero value, a similar analysis can be performed to observe changes in the stability theory in §2.4. For a convex surface the parameter is set to a small positive value, whereas for a concave surface it is a small negative value. A small value was used because, realistically, near the leading edge (the initial location of where crossflow

disturbance propagates), the radius of curvature is large, meaning the curvature of the surface is small. This curvature term introduces a third term in the asymptotic theory and can have a stabilising or destabilising impact depending on the curvature variation. As with §2.3, a comparison with PSE was made. The PSE results were provided by Mughal [63].

The second part of the section §2.5 considers the problem of crossflow vortex receptivity with small curvature variations. The idea is to observe how effective disturbances are at penetrating the boundary-layer and efficiency of this process with the new additional curvature changes. This is discussed in §3.2. There are three main parts of this problem - similar to the linear stability theory in §2, we look at flat surface receptivity, then include curvature in our receptivity in the second part and finally surface vibrations.

We start with the formulation of receptivity analysis without curvature - this can be seen in §3.3. Due to a decomposition of the perturbation when transforming from Fourier to real space, a singular solution arises and therefore we need to expand the velocity component with Laurent expansion. This complex analysis gives rise to a response function, which describes the efficiency of the receptivity process.

The next section includes the analysis of the curvature in §3.4. A similar approach is taken to §3.3 but a different Laurent expansion is needed. The receptivity analysis is split into two sections due to the various curvature mechanisms involved when considering either convex or concave surface. The first segment examines the convex curvature and this is compared to the flat surface response function for both stationary and travelling crossflow vortices. The objective was to show a qualitative agreement for the comparison between stationary crossflow vortices, since solutions for this problem are well understood. The second section of this receptivity analysis considered the other curvature surface and comparisons with the convex surface were made in §3.5.

A comparison between stationary and travelling crossflow modes was made. The response function for the stationary mode was larger than any travelling mode for any streamwise location or spanwise wavenumber. An investigation of the response function for both flat and convex surfaces at a high frequency for travelling modes was also considered. Several different modes were considered and comparisons in the absence of curvature were also made. There were some interesting results involving moderate

frequencies for travelling crossflow vortices and the concave response function, which is discussed in §3.6.

The last part of this chapter, §3.7, includes the derivation and construction of a plasma actuator in place of a roughness bump. A Forward Time Central Scheme (FTCS) is used to solve the Maxwell equations to find a steady state solution for the plasma. We are only interested in the shape the plasma produces and will use this information for the receptivity analysis. Highlights of the progress in the plasma actuator field and the model used can be seen in §3.7.1. The formulation of this problem can be seen in §3.7.2. In §3.7.3, the numerical procedure is defined. Finally, we create a plasma receptivity theory which is very similar to §3.2 but there is a different shape function for plasma. We are only interested in a basic case when considering this analysis, therefore we only analyse stationary crossflow vortices on a flat surface. For this study we observe the effect on the plasma by changing the voltage and frequency of the electrode - the details are highlighted in §3.7.

Chapter 4 is divided into three sections. The first segment consists of generating a general framework for analysing three-dimensional short-wave instabilities from two-dimensional flows. The basis of the problem comes from the research of Bayly [6], who analysed simple two-dimensional flows in Cartesian coordinates and used Floquet analysis. The framework was developed with White [100], in §4.2, we provide a general curvilinear coordinate system situated on the streamline of this two-dimensional flow with an asymptotic approach. A qualitative agreement was found and this work could be extended to more general two-dimensional flows.

In the second part, with our general theoretical methods in mind, we compare with existing studies. First we tested our model with a well known example of circular streamlines which results obtained were satisfactory with previous studies. We then expanded one of the axis and witnessed the impact. The results can be seen in §4.3. From this comparison to Bayly's [6] was achieved and found the location of the temporal disturbance, as he mentions in his analysis. Other studies were considered in §4.4 with slightly different models and linked to the work performed in the turbulence community. An elliptical instability that has been studied in many different research areas. The emphasis of this study was to observe how the eccentricity of the streamline (E) affects the temporal growth rate of the disturbance. The theory was then generalised to

incorporate any two-dimensional streamlines since the studies thus far have only concerned symmetrical streamlines. Remarks on how the stability properties can be seen in §4.5. The final part of the chapter, §4.6, addressed the issue of how to apply this theory to different applications. This method was applied to various closed and open cavities of different lengths which was compared to DNS results. These were provided by Qadri [74]. The results were able to predict where the disturbance lies within the cavity and this solution was then compared to DNS. More details can be found in §4.7. The last chapter draws final conclusions of the three problems and how they were addressed, and it summarises any closing remarks.

Chapter 2

An Asymptotic Approach for Predicting Streamwise Behaviour of Crossflow Vortices with Various Surface Curvatures.

2.1 Introduction

Gregory, Stuart and Walker (GSW) [39] found an inviscid instability mode corresponding to stationary crossflow vortices in a boundary-layer of a rotating disc. The results indicate a good approximation to the orientation of the crossflow modes and agree with the experiments they made. Viscous terms were included in the analysis of GSW by Hall [42]. This modification changed the asymptotic structure and non-parallel effects were considered. The inviscid approach was not a good approximation for the prediction of the wavenumber of this crossflow mode, however this expansion procedure developed by Hall [42] provided the correct results. Due to the analogies between the rotating disc and swept wing because of a similar basic velocity profile, the same theory and a similar expansion can be applied. With these ideas in mind we modify this theory to include curvature variations of the aircraft wing. We will try and understand the effects of wall curvature on the stability arising in the three-dimensional boundary-layer over an infinitely swept wing.

2.2 Formulation

The purpose of this Chapter is to consider a three-dimensional boundary-layer over a swept wing with direct roughness elements situated on the surface of the wing. We start with a simpler model. We assume that the flow is incompressible and the roughness elements are arranged in a regular arrays of isolated sites in along the span of the wing. Similar analysis and methods from the rotating disk problem can be applied here. We are interested in the linear stability theory of crossflow vortices over a swept wing because initially this disturbance grows linearly near the leading edge. Therefore we are only interested in spatial instabilities. The roughness is modelled by,

$$y^* = \Delta h(x^*, z^*) = \Delta h^*(x^*) e^{i\gamma z^*} + c.c, \tag{2.1}$$

were Δ isolated roughness sites of height, x^* is the streamwise coordinate, y^* is the normal to the wing, z^* is the spanwise coordinate γ is the spanwise wavenumber and $h^*(x^*)$ is the shape function of the roughness. The roughness given in equation (2.1) is periodic in the spanwise direction. We model the roughness shape as a Gaussian bump. We now introduce non-dimensional variables $\mathbf{u}$, x, y, z, p, t such that

$$\begin{aligned} x^* = xl, \quad y^* = ylRe^{-1/2}, \quad z^* = zl, \\ p^* = p_\infty + \rho {U_\infty}^2 p, \quad u^* = U_\infty u, \\ v^* = U_\infty v \quad w^* = W_\infty w \quad t^* = \frac{tl}{U_\infty}, \end{aligned} \tag{2.2}$$

where U_∞ is the freestream velocity, $W_\infty = U_\infty \sin(\theta_{sw})$, l is the characteristic length scale of the system and ν is the viscosity of the air. The Reynolds number is defined as the ratio of the freestream velocity with the characteristic length scale over the viscosity, such that $Re = U_\infty l/\nu$.

For a more realistic analytical approach the effects of curvature need to be considered since aerofoils are not completely flat, especially near the leading edge. We need to model the different surface variations, such as the convex and concave curvature parts of the aerofoil. Since the leading edge can be modelled like a cylinder we model the aerofoil in a similar fashion, see Hall *et al.* [43]. A transformation into body-fitted coordinates is needed to analyse the surface curvature effects on the linear stability of

crossflow vortices. For three-dimensional disturbances the momentum and continuity equation can be written as,

$$\frac{\partial u}{\partial t}+\frac{u}{\mathcal{C}}\frac{\partial u}{\partial x}+v\frac{\partial u}{\partial y}+\frac{\kappa uv}{\mathcal{C}}+w\frac{\partial u}{\partial z}=-\frac{1}{\mathcal{C}}\frac{\partial p}{\partial x}+\frac{1}{Re}\left[\frac{1}{\mathcal{C}}\frac{\partial}{\partial x}\left(\frac{1}{\mathcal{C}}\frac{\partial u}{\partial x}\right)+\frac{\partial^2 u}{\partial y^2}+\kappa\frac{\partial}{\partial y}\left(\frac{u}{\mathcal{C}}\right)+\frac{\kappa}{\mathcal{C}^2}\frac{\partial v}{\partial x}+\frac{1}{\mathcal{C}}\frac{\partial}{\partial x}\left(\kappa\frac{v}{\mathcal{C}}\right)+\frac{\partial^2 u}{\partial z^2}\right], \quad (2.3a)$$

$$\frac{\partial v}{\partial t}+\frac{u}{\mathcal{C}}\frac{\partial v}{\partial x}+v\frac{\partial v}{\partial y}-\frac{\kappa u^2}{\mathcal{C}}+w\frac{\partial v}{\partial z}=-\frac{\partial p}{\partial y}+\frac{1}{Re}\left[\frac{1}{\mathcal{C}}\frac{\partial}{\partial x}\left(\frac{1}{\mathcal{C}}\frac{\partial v}{\partial x}\right)+\frac{\partial^2 v}{\partial y^2}+\kappa\frac{\partial}{\partial y}\left(\frac{v}{\mathcal{C}}\right)-\frac{\kappa}{\mathcal{C}^2}\frac{\partial v}{\partial x}-\frac{1}{\mathcal{C}}\frac{\partial}{\partial x}\left(\kappa\frac{u}{\mathcal{C}}\right)++\frac{\partial^2 v}{\partial z^2}\right], \quad (2.3b)$$

$$\frac{\partial w}{\partial t}+\frac{u}{\mathcal{C}}\frac{\partial w}{\partial x}+v\frac{\partial v}{\partial y}+w\frac{\partial w}{\partial z}=-\frac{\partial p}{\partial z}+\frac{1}{Re}\left[\frac{1}{\mathcal{C}}\frac{\partial}{\partial x}\left(\frac{1}{\mathcal{C}}\frac{\partial w}{\partial x}\right)+\frac{\partial^2 w}{\partial y^2}+\kappa\frac{\partial}{\partial y}\left(\frac{w}{\mathcal{C}}\right)+\frac{\partial^2 w}{\partial z^2}\right], \quad (2.3c)$$

$$\frac{1}{\mathcal{C}}\frac{\partial u}{\partial x}+\frac{\partial v}{\partial y}+\kappa\frac{v}{\mathcal{C}}+\frac{\partial w}{\partial z}=0, \quad (2.3d)$$

where κ is the local curvature of the body and the Lamè coefficient $\mathcal{C}=1+\kappa(x)y$. We note that the local curvature is scaled as $\kappa\sim Re^{-1/2}x$. Since $\kappa\ll 1$ for a surface of an aeroplane wing, the boundary-layer equations are modified. To begin with we shall analyse the crossflow disturbances for a flat surface and then apply the same techniques to study the effects of surface curvature.

2.3 Base Profile

We will now turn our attention to the base flow of a three-dimensional swept wing. First we shall discuss the two-dimensional form of the basic flow. We will then extend to the three-dimensional framework.

Falkner-Skan Profile

Falkner-Skan showed that the problem reduces to a similarity solution by introducing two new variables

$$\eta=\frac{y}{L}\frac{Re^{-1/2}}{n(x)}, \quad \xi=\frac{x}{L}, \quad (2.4)$$

Figure 2.1: An overview schematic diagram of a three-dimensional swept wing with isolated roughness sites of height Δ, sweep angle θ_{sw} and velocity far from the body U_∞. A side view is also displayed to show a two-dimensional slice of the three-dimensional swept wing with the same scales and variables as the overview with isolated roughness sites (modelled as an inhomogeneous boundary condition).

where L is the characteristic length scale of the system, $n(x)$ is an unknown dimensionless scale function in y representing the dependence on x and is to be determined. For a flat plate we have a scale function of $n(x) = \sqrt{(2x/L)}$ and a freestream velocity of $u_e(x) = U_\infty$ (with $U_\infty =$ constant). For a more general case the freestream velocity is a function of x, $u_e = u_e(x)$. The following streamfunction is proposed

$$\Psi = \frac{Lu_e(x)n(x)}{Re^{-1/2}} f(\eta, \xi), \tag{2.5}$$

and the streamwise and wall normal velocities can be found by

$$u = \frac{\partial \Psi}{\partial y}, \quad v = -\frac{\partial \Psi}{\partial x}, \tag{2.6}$$

where $f(\eta, \xi)$ is the non-dimensional streamfunction. Substituting (2.6) and applying a change of variables to equation (A.11) (this is the x-momentum equation in (2.3)) we obtain the following

$$f''' + \left(\frac{Ln^2}{u_e}\frac{du_e}{dx}\right)(1 - f'^2) + \left(\frac{Ln}{u_e}\frac{d}{dx}(nu_e)\right) ff'' - n^2\left(f'\frac{\partial f'}{\partial \xi} - f\frac{\partial f''}{\partial \xi}\right) = 0. \tag{2.7}$$

where the prime refers to derivatives with respect to η. For the similarity solution to be valid, there must be no dependency on x and ξ for the similarity stream function must disappear. Hence we now have

$$f''' + \alpha_H(1 - f'^2) + \beta_H f f'' = 0, \tag{2.8}$$

where the parameters are given by

$$\alpha_H = \frac{Ln^2}{u_e}\frac{du_e}{dx} \quad \text{and} \quad \beta_H = \frac{Ln}{u_e}\frac{d}{dx}(nu_e), \tag{2.9}$$

with the following boundary conditions

$$f(0) = f'(0) = 0, \quad f'(\infty) = 1. \tag{2.10}$$

We want the velocities to be zero at the wall, hence the first we need the first two boundary conditions. The last boundary condition comes from the streamwise velocity needs to be constant at a large wall normal coordinate. Whilst we now have a similarity

solution there might yet be constraints on α_H and β_H. Linear combinations of α_H and β_H can be determined by the certain constraints of the dimensionless scale factor and the freestream velocity. By integrating equation (2.8) we can obtain a relation between α_H and β_H [87]. We have the following relations for u_e and n in terms of α_H and β_H

$$u_e(x)/U_\infty = \mathcal{I}^{\left(\frac{2}{2\alpha_H-\beta_H}\right)}\left[(2\alpha_H-\beta_H)\frac{x}{L}\right]^{\frac{2\alpha_H-\beta_H}{2}}, \tag{2.11}$$

$$n(x) = \sqrt{(2\alpha_H-\beta_H)\frac{x}{L}\frac{u_e}{U_\infty}}, \tag{2.12}$$

where $\mathcal{I}$ is an integration constant. This implies that we require $2\alpha_H \neq \beta_H$ as this would cause the new scaled normal variable to have a singularity. Also, we note that $\alpha_H = 0$ would imply that $n(x)$ is complex. The normal coordinate would be complex and this would not be physical. Since we have the factor $(2\alpha_H - \beta_H)$ in $n(x)$, we can set α_H arbitrarily and vice versa β_H. The dimensionless scale factor can be rescaled and thus we can set trivially $\alpha_H = 1$. Commonly a new parameter is introduced

$$m = \frac{\beta_H}{(2-\beta_H)} \quad \Longrightarrow \quad \beta_H = \frac{2m}{m+1}, \tag{2.13}$$

with m known as the acceleration parameter and can be thought of dimensionless pressure since $m > 0$ refers to acceleration and $m < 0$ refers to deceleration. We show later that for the decelerating flow will have some connection with separation. If we substitute (2.13) into (2.11) we obtain

$$\frac{u_e(x)}{U_\infty} = \mathcal{I}^{m+1}\left[\frac{2}{m+1}\frac{x}{L}\right]^{\frac{1}{m+1}}, \tag{2.14}$$

$$n(x) = \sqrt{\frac{2}{m+1}\frac{x}{L}\frac{U_\infty}{u_e}}, \tag{2.15}$$

the streamfunction (2.5) becomes

$$\Psi = \sqrt{\left(\frac{2}{m+1}\nu u_e\right)}f(\eta). \tag{2.16}$$

The normal coordinate now transforms to

$$\eta = y\sqrt{\frac{m+1}{2}\frac{u_e}{\nu x}} = {Re_x}^{1/2}\frac{y}{x}\sqrt{\frac{m+1}{2}} \quad \text{with} \quad Re_x = \frac{u_e x}{\nu}. \tag{2.17}$$

For an outer flow $u_e(x) \sim x^m$ [13] and we have the similarity variable η. The scaled stream function $f(\eta)$ then obeys the ordinary differential equation

$$f''' + ff'' + \beta_H(1 - f'^2) = 0, \tag{2.18}$$

with β_H known as the Hartree parameter and

$$f(0) = f'(0) = 0, f'(\infty) = 1. \tag{2.19}$$

Equation (2.18) is the Falkner-Skan equation, which is a self-similar solution to the boundary layer equations [29]. There are two special cases. The first when $m = 0$,

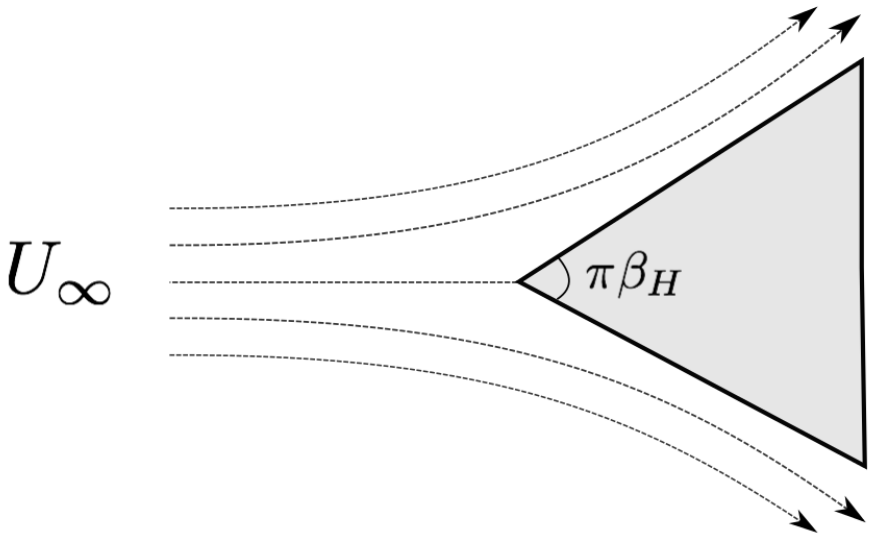

Figure 2.2: Flow against a solid wedge boundary with an angle of $\pi\beta_H$.

corresponds to Blasius flow on a flat plate. The second, when $m = 1$, corresponds to two-dimensional stagnation flow.

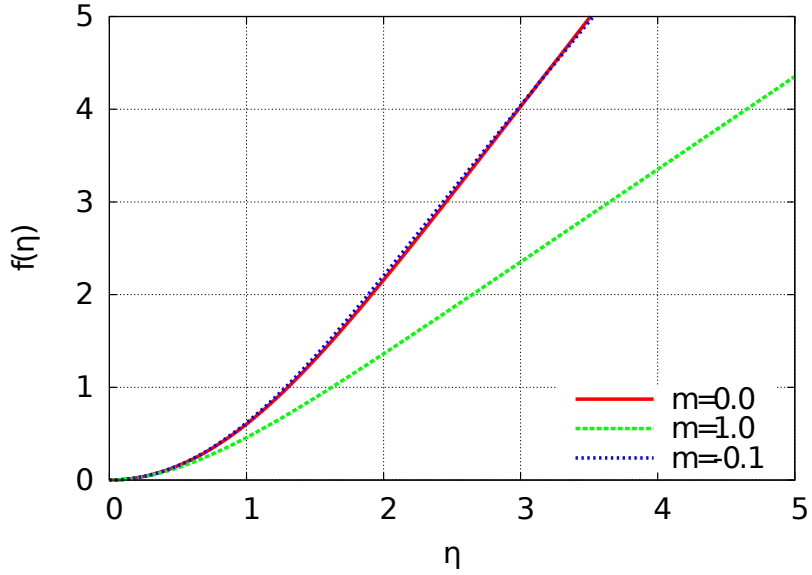

Figure 2.3: Similarity streamfunction with different values of m corresponding to no acceleration (—), acceleration (- - -) and deceleration (.....).

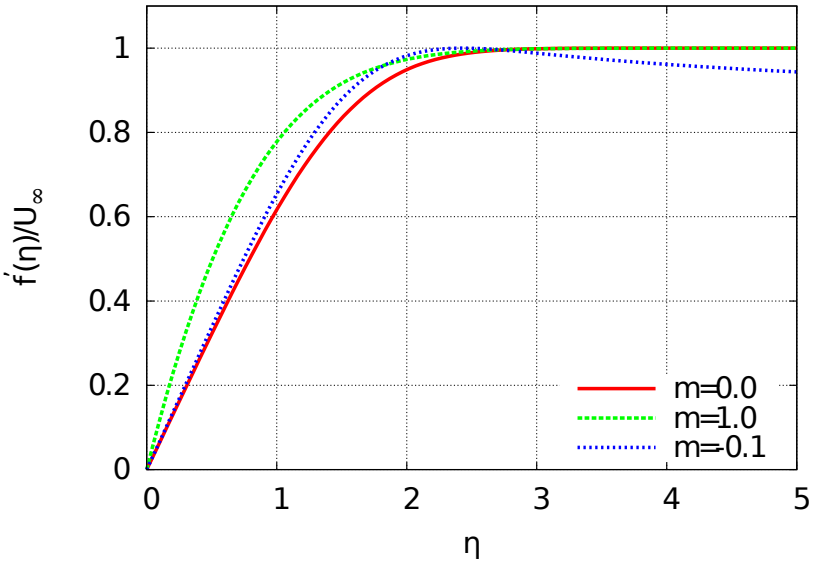

Figure 2.4: Streamwise velocity with different values of m corresponding to no acceleration (—), acceleration (- -) and deceleration (.....).

.

Falkner-Skan-Cooke Profile

In addition to a streamwise (x) and normal component (y), boundary-layers over a swept wing have a component in the spanwise direction (z) so that the flow is three-dimensional. Accordingly, the Falkner-Skan solution needs to be modified to allow for the spanwise velocity [20]. Following the work of Cooke [20] we write the spanwise velocity as

$$w = w_e g(\eta), \tag{2.20}$$

where g is a non dimensional similarity solution in the spanwise direction. We can substitute (2.20) into (2.3c) to obtain the following ordinary differential equation

$$g'' + \alpha_H f g' + n^2 g' \frac{\partial f}{\partial \xi} = 0 \implies g'' + f g' = 0. \tag{2.21}$$

The primes denote derivatives with respect to η. The same arguments apply here, as for the Falkner-Skan solution and we have the following boundary conditions

$$g(0) = 0, \quad g(\infty) = 1. \tag{2.22}$$

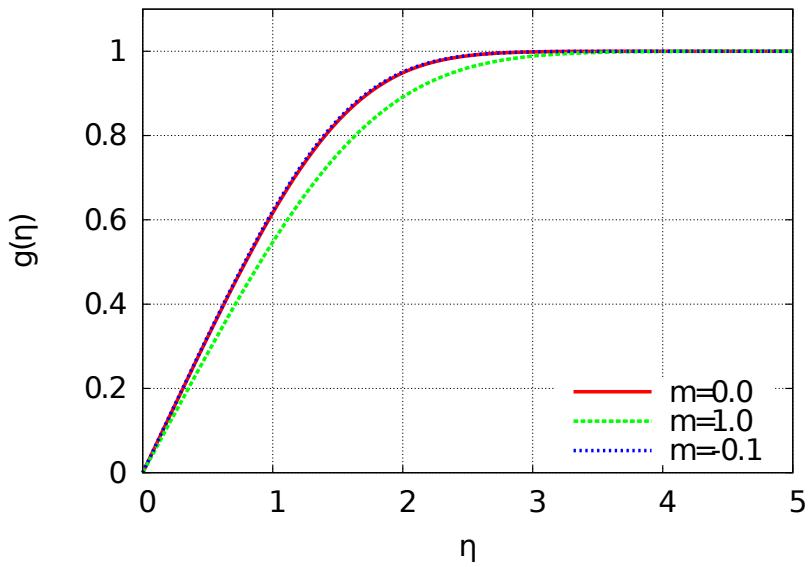

Figure 2.5: Spanwise similarity solution with different values of m corresponding to no acceleration (___), acceleration (..) and deceleration (.....).

Swept Hiemenz Flow

Here we shall formulate the swept Hiemenz base flow because it describes a realistic base flow for the leading edge of a swept wing. Note that the wall normal coordinate y is scaled by the boundary thickness $Re^{-1/2}$. By substituting the non-dimensional quantities of (2.2) into (2.3) and set $\kappa = 0$ we obtain the following set of equations

$$\begin{aligned} u_t + uu_x + Re^{1/2}vu_y + wu_z &= -p_x + Re^{-1}(u_{xx} + u_{zz}) + u_{yy}, && \text{(2.23a)} \\ v_t + uv_x + Re^{1/2}vv_y + wv_z &= -Re^{1/2}p_y + Re^{-1}(v_{xx} + v_{zz}) + v_{yy}, && \text{(2.23b)} \\ w_t + uw_x + Re^{1/2}vw_y + ww_z &= -p_z + Re^{-1}(w_{xx} + w_{zz}) + w_{yy}, && \text{(2.23c)} \\ u_x + Re^{1/2}v_y + w_z &= 0. && \text{(2.23d)} \end{aligned}$$

The subscripts refer to derivatives with respect to the given coordinate. Note that we have dropped the asterisk notation for convenience. We rescale the wall normal coordinate within the boundary layer such that $\zeta = Re^{-1/2}y$. It is time independent, two-dimensional and only the u-component depends on x and ζ. We define the base flow as follows

$$\boldsymbol{u} = \boldsymbol{u}_b = (u_b(x,\zeta), Re^{-1/2}v_b(\zeta), w_b(\zeta)) \quad \text{and} \quad p = p_b(\zeta). \tag{2.24}$$

The subscript b indicates the basic flow for the velocity and pressure. This is a swept Hiemenz base flow and the additional velocity situated in the spanwise direction. Since the boundary-layer is in the wall normal direction, this implies that the wall normal velocity must be scaled with $Re^{-1/2}$. Substituting (2.24) into (2.23) and collecting the highest order terms yields

$$\begin{aligned} u_b u_{bx} + v_b u_{b\zeta} &= -p_{bx} + u_{b\zeta\zeta}, && \text{(2.25a)} \\ p_{b\zeta} &= 0, && \text{(2.25b)} \\ u_b w_{bx} + v_b w_{b\zeta} &= w_{b\zeta\zeta}, && \text{(2.25c)} \\ u_{bx} + v_{b\zeta} &= 0. && \text{(2.25d)} \end{aligned}$$

With the following set of boundary conditions

$$u_b = v_b = w_b = v_b' = 0 \qquad \text{at } \zeta = 0, \tag{2.26a}$$

$$u_b = x,\ v_b' = -1,\ w_b = \sin\theta_{sw} \quad \text{as } \zeta \to \infty. \tag{2.26b}$$

The wall normal momentum equation of (2.25b) implies that the wall normal pressure derivative is zero. This implies that either p_b is a constant or p_b must be a function of x.

Since the problem is a swept wing, the region at the leading edge must resemble that of a flow against a wall, see figure 2.3 for more details. Therefore the stream function of streamwise and wall normal velocities are $u_b = \partial\psi/\partial\zeta$ and $v_b = -\partial\psi/\partial x$, with $\psi = x\zeta$. By using the stream function of u_b, v_b and (2.25a) we obtain the following

$$p_b' = -x \to p_b(x) = -x^2/2 + c.$$

So p_b is only a function of x and c is an arbitrary constant. With this in mind we let

$$u_b(x,\zeta) = xf'(\zeta), \quad v_b(x,\zeta) = -f(\zeta), \quad w_b(x,\zeta) = g(\zeta),$$

then (2.25a), (2.25b) and (2.25d) become

$$f'^2 - ff'' = 1 + f''', \quad -fg' = g''. \tag{2.27}$$

with $f(0) = f'(0) = 0$ and $f'(\infty) = 1$ from (2.26). This can be solved using a standard fourth order Runge-Kutta method with a shooting technique. See appendix A for more details about this method. Since $f''(0)$ and $g'(0)$ are not known, we fix $f''(0) = A$ and $g'(0) = B$. We then use a Newton-Raphson iteration technique until the boundary conditions are satisfied. Other root finding techniques could work but there might be issues with the initial estimate.

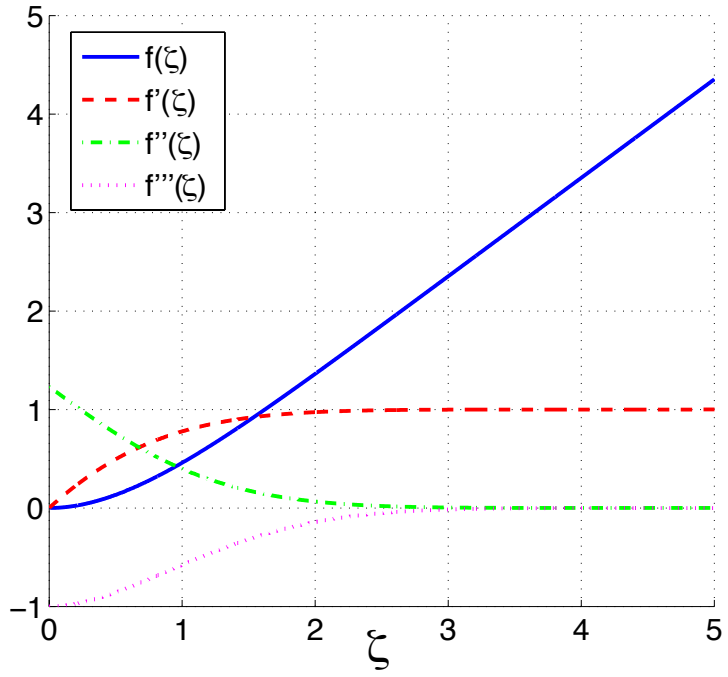

(a)

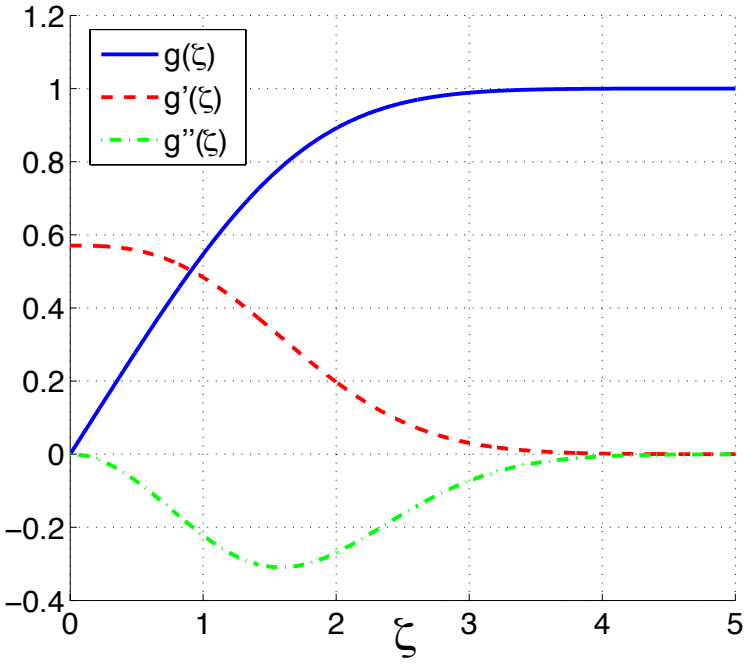

(b)

Figure 2.6: Swept Hiemenz base flow functions with changing wall normal coordinate.

Therefore u_b, v_b, w_b and p_b can be obtained through functions f and g.

2.4 Stationary and Travelling Crossflow Vortices on a Flat Plate

2.4.1 Disturbance Equations

We will now perturb the base flow (swept Hiemenz) by

$$\boldsymbol{u} = \boldsymbol{u}_b + (\Delta/\delta)(U(x,y,z,t), V(x,y,z,t), W(x,y,z,t)). \tag{2.28}$$

The dimensionless height of the roughness bump is presumed to be small ($\Delta/\delta \ll 1$, where $\delta = Re^{-1/2}$ is the thickness of the boundary-layer and Δ is a small parameter which characterises the height of the roughness) such that the disturbances are linear. Substituting (2.28) into (2.3) and performing linearisation around the roughness height yields

$$\begin{aligned} U_t + u_b U_x + U u_{bx} + Re^{-1/2} v_b U_y + Re^{1/2} V u_{by} + w_b U_z = \\ -P_x + Re^{-1}(U_{xx} + U_{zz}) + U_{yy}, \end{aligned} \tag{2.29a}$$

$$\begin{aligned} V_t + u_b V_x + Re^{-1/2} U v_{bx} + Re^{-1/2} v_b V_y + V v_{by} + w_b V_z = \\ -Re^{1/2} P_y + Re^{-1}(V_{xx} + V_{zz}) + V_{yy}, \end{aligned} \tag{2.29b}$$

$$\begin{aligned} W_t + u_b W_x + U w_{bx} + Re^{-1/2} v_b W_y + Re^{1/2} V w_{by} + w_b W_z = \\ -P_z + Re^{-1}(W_{xx} + W_{zz}) + W_{yy}, \end{aligned} \tag{2.29c}$$

$$U_x + Re^{1/2} V_y + W_z = 0. \tag{2.29d}$$

Since we are interested in roughness elements to produce the crossflow instability we have the following boundary condition

$$\vec{u} = 0 \quad \text{at} \quad y = \Delta h(x,z), \tag{2.30}$$

In this model x_0 is the placement of the roughness location and $h(x - x_0, z)$ is the shape function of the roughness.

2.4.2 Inviscid Modes

Initially we are interested in the inviscid modes, since the crossflow vortex is a form of inviscid instability. We need to determine the instability modes and so we assume

that $h = 0$. Using the same scalings from the inviscid theory of Gregory, Stuart and Walker (G.S.W) [39], the wavelengths scale to the boundary-layer thickness. We want to scale the streamwise (x) and spanwise (z) directions to wavelengths of order $Re^{-1/2}$. For simplicity we restrict our disturbance in z by enforcing periodicity in the spanwise direction,

$$Q(x, y, z) = \hat{Q}(x, y)e^{i\gamma z} + c.c, \tag{2.31}$$

with $Q = (U, V, W, P)$ and we seek solutions of the form

$$Q(x, y) = Q_0(x, y) + \epsilon Q_1(x, y) + \cdots , \tag{2.32}$$

with the small parameter $\epsilon = Re^{-1/6}$, as seen in [42]. Since we are dealing with a wave-like disturbance we can use a WKB (Wentzel Kramers Brillouin) approximation of

$$Q(x, y, z) = q(y) \exp\left(\frac{i}{\epsilon^3}\int_0^x \alpha(\hat{x}, \epsilon)d\hat{x} + z\gamma - \omega t\right). \tag{2.33}$$

The streamwise wavenumber α can be found from the perturbation parameter ϵ, spanwise wavenumber γ and the frequency ω. In spatial stability, α and γ are assumed to be complex whereas ω is real. In this situation we want γ to be real, as we are only interested in the streamwise growth rates and direct roughness element placement in z. For spatial theory, we have a dispersion relation of the form;

$$\alpha = F(\gamma, \omega, Re), \tag{2.34}$$

with unknown (α_r, α_i), where γ, ω and Re need to be defined. In general α is complex so we define for convenience $\alpha = \alpha_r + i\alpha_i$. Our aim is to find the streamwise growth rate. Which is determined by the imaginary part of α, α_i. Following the work of Hall [42] we expand the streamwise wavenumber, α, as

$$\alpha \;\; = \;\; \alpha_0 + \epsilon\alpha_1 + \cdots . \tag{2.35}$$

There is an inviscid region with depth $O(\epsilon^3)$ from G.S.W. analysis and to satisfy the no-slip condition at the wall a viscous sub layer of thickness $O(\epsilon^4)$ must exist. For the

inviscid zone within the boundary layer we can expand u, v, w, p as

$$u = u_0(\zeta) + \epsilon u_1(\zeta) + \cdots, \quad v = v_0(\zeta) + \epsilon u_1(\zeta) + \cdots, \tag{2.36}$$

$$w = w_0(\zeta) + \epsilon u_1(\zeta) + \cdots, \quad p = p_0(\zeta) + \epsilon u_1(\zeta) + \cdots, \tag{2.37}$$

with $\zeta = \epsilon^{-3} y$ since our analysis applies within the boundary layer and this is the same scaling as our baseflow. We transform the streamwise, spanwise and time derivatives as

$$\frac{\partial}{\partial x} \to (i/\epsilon^3)(\alpha_0 + \epsilon\alpha_1 + \cdots), \quad \frac{\partial}{\partial z} \to (i/\epsilon^3)\gamma, \quad \frac{\partial}{\partial t} \to (i/\epsilon^3)\omega_0. \tag{2.38}$$

Considering only dominant first order terms in (2.29) and these transformations we obtain at leading order

$$i\overline{U}_{0B} u_0 + v_0 {u_b}' = -i\alpha_0 p_0, \tag{2.39a}$$

$$i\overline{U}_{0B} v_0 = -{p_0}', \tag{2.39b}$$

$$i\overline{U}_{0B} w_0 + v_0 {w_b}' = -i\gamma_0 p_0, \tag{2.39c}$$

$$i\alpha_0 u_0 + {v_0}' + i\gamma_0 w_0 = 0, \tag{2.39d}$$

where prime denotes the derivative with respect to ζ and with 'effective' base flow defined as

$$\overline{U}_{0B} = -\omega_0 + \alpha_0 u_b + \gamma_0 w_b. \tag{2.40}$$

These are the inviscid equations and the disturbance velocity has to be zero at the wall because it has an impermeability condition. Hence, when eliminating the pressure (p_0) and rearranging for wall normal velocity (v_0), we obtain

$$\overline{U}_{0B}[v_0'' - {\beta_0}^2 v_0] - \overline{U}_{0B}'' v_0 = 0. \tag{2.41}$$

where ${\beta_0}^2 = {\alpha_0}^2 + {\gamma_0}^2$ is the 'effective' wavenumber. We have the following boundary conditions

$$v_0(0) = 0 \quad \text{and} \quad v_0(\infty) = 0. \tag{2.42}$$

Equation (2.41) is known as the Rayleigh stability equation. The combination of $\alpha_0 u_b + \gamma_0 w_b$ in (2.40) could produce an inflexion point within the domain because of the boundary conditions of (2.42), they must disappear at the wall and vanish far away from the boundary-layer. There must be an inflexion point in the velocity profile $\overline{U}_{0B}$. This implies that $\overline{U}_{0B}{}'' = 0$ somewhere within the domain of ζ. First we will start by investigating stationary modes so the frequency will be set to zero ($\omega_0 = 0$). We rewrite equation (2.41) in the form

$$v_0'' - \left[{\beta_0}^2 + \frac{\overline{U}_{0B}''}{\overline{U}_{0B}} \right] v_0 = 0. \tag{2.43}$$

For a critical layer to appear with the flow we must have $\overline{U}_{0B}(\zeta_c) = 0$, where ζ_c is the location of the critical layer, then (2.43) would be singular. From the definition of the effective base flow,

$$\overline{U}_{0B}(\zeta_c) = \alpha_0 u_b(\zeta_c) + \gamma_0 w_b(\zeta_c) = 0. \tag{2.44}$$

Since we are only considering purely real spanwise wavenumbers then

$$(\alpha_{0r} + i\alpha_{0i}) u_b(\zeta_c) + \gamma_0 w_b(\zeta_c) = 0. \tag{2.45}$$

For this to hold we must satisfy two constraints:

1. $\alpha_{0r} u_b(\zeta_c) + \gamma_0 w_b(\zeta_c) = 0$,
2. $i\alpha_{0i} u_b(\zeta_c) = 0$.

Satisfying the second condition implies $\alpha_{0i} = 0$ which would correspond to a neutrally stable disturbance. This is not relevant for the crossflow modes since we are only interested in spatially growing modes, $\alpha_i < 0$. It follows from the boundary conditions that $\zeta_c = 0$ as

$$\alpha_0 u_b(x, 0) = x\alpha_0 f'(0) = 0. \tag{2.46}$$

Therefore since u_b, w_b are real functions and $\alpha_{0r} > 0$, there is no critical layer for $\zeta_c > 0$. Consequently, the critical layer at $\zeta_c = 0$ would be absorbed into the wall, to satisfy the boundary condition of (2.42) at the critical point $\zeta = \zeta_c$ [39]. Therefore the profile of $\overline{U}_{0B}$ must behave in such a way that an inflexion point lies within the zero

velocity of the flow, so there exists

$$\overline{U}''_{0B}(\zeta_c) = 0, \tag{2.47}$$

and we have a regular critical layer. Note that the derivative of the wall normal velocity $(v_0{}'(0))$ becomes $-i[\alpha_0 u_0 + \gamma_0 w_0]$ as ζ approaches zero.

2.4.3 Inviscid Results

The first analytical solution to the Rayleigh stability equation was found by Heisenberg in 1924 [45]. Later, a well known solution to the Orr-Sommerfeld equation was proposed by Tollmien [97] from which a solution to the Rayleigh stability equation could be found by taking the limit as the Reynolds number tends to infinity. Here, we solve the Rayleigh stability equation numerically. We solve (2.41) (and the boundary conditions of (2.42)) using a fourth order Runge-Kutta shooting technique. By performing this calculation we obtain a dispersion relation between the streamwise and spanwise wavenumbers.

In figure 2.7 we compare the numerical results with the high wavenumber approximation. A high wavenumber approximation is needed due to the breakdown of the Newton technique as α_0 and γ_0 approach zero. We have discussed how to solve this Rayleigh stability equation already by imposing a far field condition of

$$v_0(\zeta) \sim e^{-\beta_0 \zeta} \to 0 \quad \text{as} \quad \zeta \to \infty.$$

where $\beta_0 = \sqrt{{\alpha_0}^2 + {\gamma_0}^2}$. Problems arise when β_0 becomes small, which occurs when α_0 and γ_0 become small. We define ζ_∞ as a large value that works as the numerical infinity value for our calculation. As β_0 approaches zero ζ_∞ needs to be increased to satisfy the far field boundary condition. Therefore we will either need to increase the value of ζ at ∞, as $\beta_0 \to 0$ or use long wave analysis. The procedure we used is discussed in appendix C and is similar to the methods prescribed by Drazin & Reid [28]. Figure 2.7 displays the dispersion relation between the streamwise growth rate and varying spanwise wavenumber.

The dispersion relation describes the stability characteristics of the crossflow vortex since $\alpha_{0i} < 0$, then the disturbance is unstable because we have a the disturbance in the

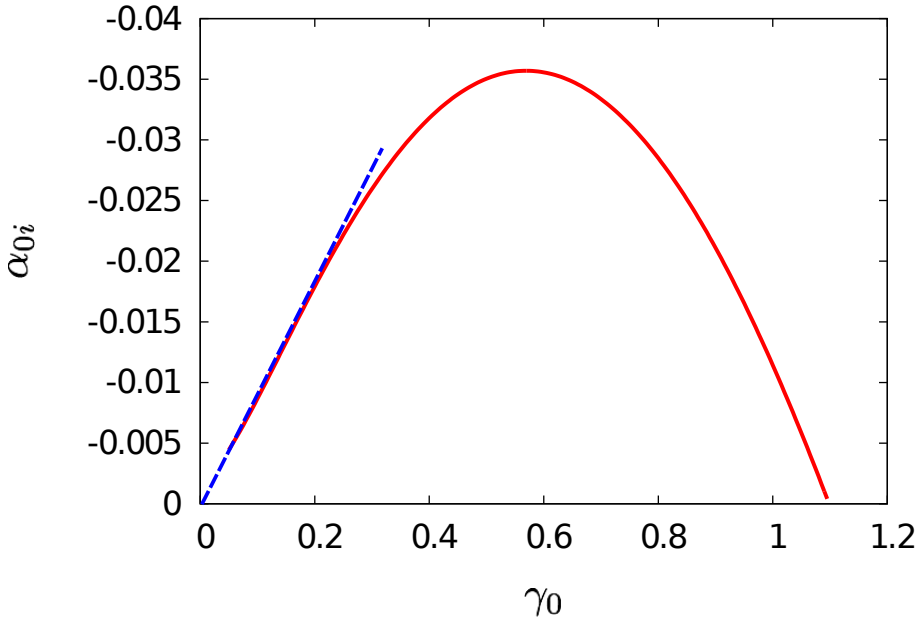

Figure 2.7: Dispersion relation between inviscid streamwise growth rate (-α_{0i}) and spanwise wavenumber (γ_0) corresponding to the solution (_____) and the long wavelength limit which is derived in appendix C (------) with a sweep angle of θ_{sw} at the streamwise location of $x = 1.0$.

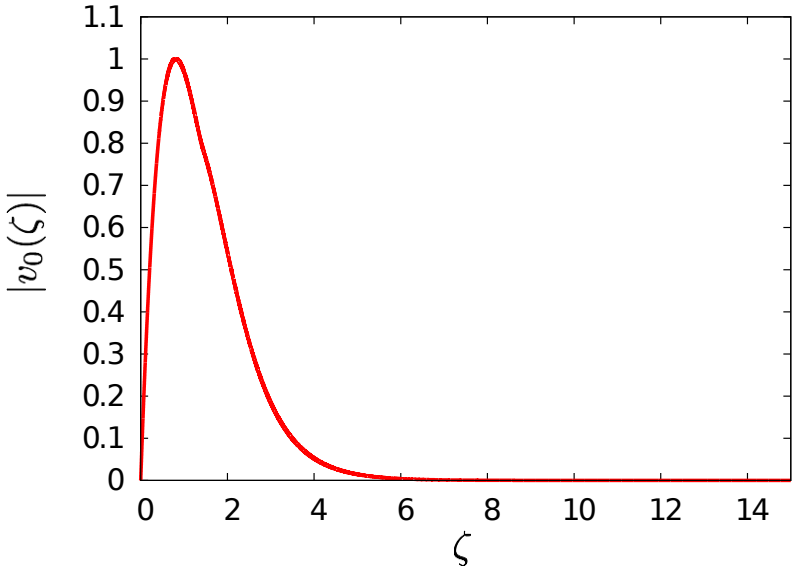

Figure 2.8: An example of a normalised eigenfunction of v_0 with x=1.0 and $\gamma_0 = 1.0$.

form of $U \sim e^{i\alpha x}$. In this situation for $x = 0.4$ between $0 < \gamma_0 < 1.1$ the disturbance is unstable. The most dangerous mode is the spanwise wavenumber corresponding to the largest streamwise growth rate, which is for a spanwise wavenumber around $\gamma_0 = 0.6$. The dispersion relation in figure 2.7 satisfies the conditions of $\overline{U}''_{0B}(\zeta_c) = \overline{U}_{0B}(\zeta_c) = 0$ and can be referred to as the GSW mode. As shown in figure 2.8, the eigenfunction satisfies both boundary conditions of (2.42). We can see the impact that the sweep angle has on the growth rate.

We notice in figure (2.9) that the maximum growth rate is at a sweep angle of $57°$. As

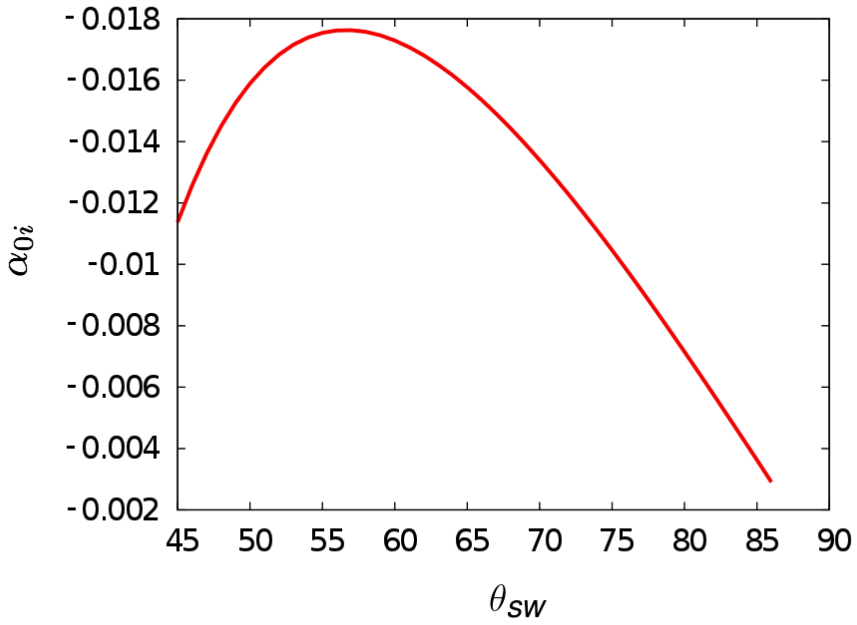

Figure 2.9: Dispersion relation between streamwise growth rate (α_{0i}) and the angel of sweep (θ_{sw}) at a spanwise wavenumber of γ_0=0.4 and a streamwise location of $x = 0.25$.

we increase this angle the growth rate almost decreases at a linear rate until eventually the growth rate is zero at $88°$.

Thus far we have only selected a particular crossflow region ($x = 1$), next we shall study the impact of the crossflow with the dispersion relation. In figure 2.10 we have a dispersion relation for three different crossflow strengths. Firstly we note that as the crossflow strength increases the extent of unstable spanwise wavenumbers decreases. Therefore the higher the crossflow the fewer spanwise wavenumbers corresponding to unstable streamwise wavenumbers. The most dangerous crossflow mode occurs

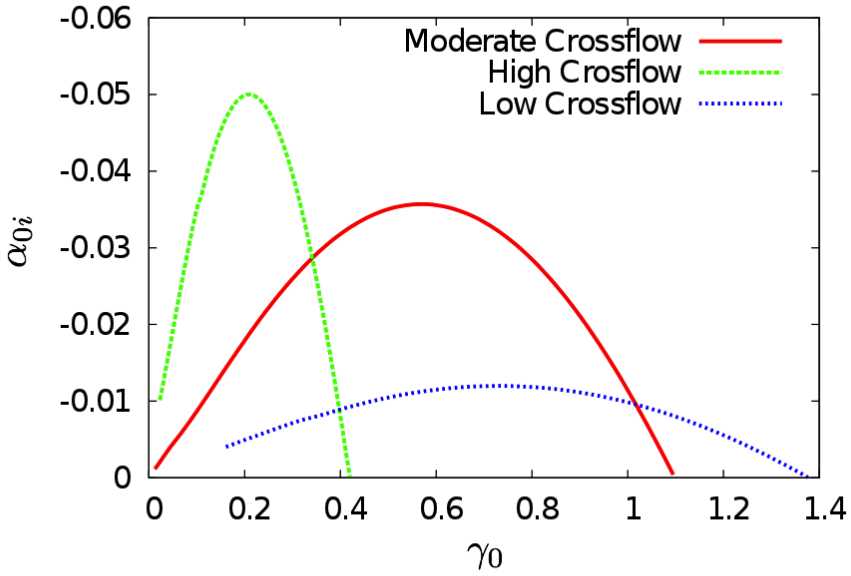

Figure 2.10: Dispersion relation between streamwise growth rate (α_{0i}) and spanwise wavenumber (γ_0) at $x = 0.25$, 1.0 and 4.0 corresponding to high (.....) , moderate (_____) and low (.....) crossflow respectively at a sweep angle of $\theta_{sw} = 45°$.

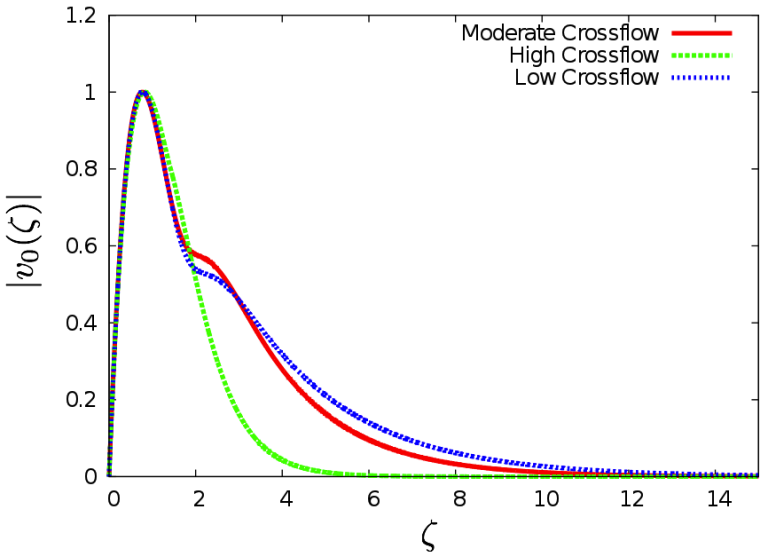

Figure 2.11: Absolute value of normalised eigenfunction $|v_0(\zeta)|$ with respect to $v_{0\{MAX\}}$ at $x = 0.25$, 1.0 and 4.0 corresponding to high (.....) , moderate (_____) and low (.....) crossflow.

when the crossflow strength is largest. Near the neutral stability point the crossflow mode is largest and this corresponds to high crossflow. Also note that in figure 2.11,

the eigenfunction satisfies both boundary conditions $v_0(0) = v_0(\infty) = 0$. We have noticed that an inflexion point arises because of the combination of $\alpha_0 u_b + \gamma_0 w_b$. The kink in the eigenfunction for both low and moderate crossflow occurs since we have taken the absolute value of the eigenfunction.

2.4.4 Viscous Correction Results

We are interested in the correction term from the viscous sublayer. We shall follow the work of Hall [42], who performed similar analysis for a rotating disc. We have solved (2.41) - we now know the boundary condition at the wall and the upper boundary condition in the viscous wall layer. We observe that we must rescale the normal coordinate to analyse within the viscous layer, the convection and diffusion terms need to balance in the disturbance equations (2.29a)-(2.29d), hence the thickness of the viscous wall layer must be of $\mathcal{O}(\epsilon^4)$. The idea is to include the viscous terms within this layer. Rescaling by $\xi = \epsilon^{-4} y$, the base flow within the wall layer can be expanded as

$$u_b = \epsilon \overline{u_0} \xi + \cdots, \quad w_b = \epsilon \overline{w_0} \xi + \cdots \tag{2.48}$$

where

$$\overline{u}_0 = \frac{du_b}{d\xi}(\xi = 0) \text{ and } \overline{w}_0 = \frac{dw_b}{d\xi}(\xi = 0) \tag{2.49}$$

are the slopes at the wall of the velocity profiles of the boundary-layer flow as it approaches the hump and this is calculated via a Taylor expansion. The disturbance velocities and pressure are formulated by

$$U = U_0(\xi) + \epsilon U_1(\xi) + \cdots, \quad V = \epsilon V_0(\xi) + \epsilon^2 V_1(\xi) + \cdots, \tag{2.50}$$

$$V = W_0(\xi) + \epsilon W_1(\xi) + \cdots, \quad P = \epsilon P_0(\xi) + \epsilon^2 P_1(\xi) + \cdots. \tag{2.51}$$

Within the viscous wall layer the pressure and wall normal velocity are an order of ϵ smaller than the streamwise and spanwise velocity components because they have a smaller influence. Substituting all of the new scaled disturbance velocities and pres-

sures, and also using the rescaled base flow expansion yields

$$i\overline{U}_{BV}U_0 + V_0\overline{u_0}' = -i\alpha_0 P_0 + U_0'', \tag{2.52a}$$

$$0 = -iP_0', \tag{2.52b}$$

$$i\overline{U}_{BV}W_0 + V_0\overline{w_0}' = -i\gamma_0 P_0 + W_0'', \tag{2.52c}$$

$$i\alpha_0 U_0 + V_0' + i\gamma_0 W_0 = 0, \tag{2.52d}$$

with $\overline{U}_{BV} = \alpha_0\overline{u}_0 + \gamma_0\overline{w}_0$. Eliminating P_0 and using (2.52d) we obtain

$$[\alpha_0 U_0 + \gamma_0 W_0]''' - i\xi\overline{U}_{BV}[\alpha_0 U_0 + \gamma_0 W_0]' = 0. \tag{2.53}$$

We notice that (2.53) has the same form as an Airy equation. Indeed if we introduce

$$\chi = \phi\xi, \partial/\partial\chi = (1/\phi)\partial/\partial\xi \rightarrow \phi^2\partial^2/\partial^2\chi = \partial^2/\partial^2\xi, \mathcal{V} = (\alpha_0 U_0 + \gamma_0 W_0)', \tag{2.54}$$

where $\phi = [i(\alpha_0\overline{u_0} + \gamma_0\overline{w_0})]^{1/3}$ then (2.53) becomes

$$\phi^2\partial^2\mathcal{V}/\partial^2 - \xi\phi^3\mathcal{V} = 0, \tag{2.55}$$

with $\chi = \phi\xi$ then $\mathcal{V}'' - \chi\mathcal{V} = 0$, which is Airy's differential equation. Accordingly,

$$[\alpha_0 U_0 + \gamma_0 W_0]' = c_1 Ai(\phi\chi) + c_2 Bi(\phi\chi). \tag{2.56}$$

Therefore for the flow to be bounded we set $c_2 = 0$. Thus

$$[\alpha_0 U_0 + \gamma_0 W_0] = c_1 \int_0^{\chi} Ai(\phi\chi^*)d\chi^*. \tag{2.57}$$

From inviscid results we know that as $\zeta \rightarrow 0$

$$i[\alpha_0 u_0(0) + \gamma_0 w_0(0)] \rightarrow -v_0'(0). \tag{2.58}$$

Using this and normalising such that the matching condition is satisfied we find

$$c_1 = \frac{-v_0'(0)}{\int_0^{\infty} Ai(\phi\chi^*)d\chi^*}. \tag{2.59}$$

Therefore we get,

$$[\alpha_0 U_0 + \gamma_0 W_0] = \frac{-{v_0}'(0)\int_0^{\chi} Ai(\phi\chi^*)d\chi^*}{\int_0^{\infty} Ai(\phi\chi^*)d\chi^*}. \tag{2.60}$$

From the continuity equation (2.52d), (2.60) becomes

$${V_0}' = \frac{-{v_0}'(0)\int_0^{\chi} Ai(\phi\chi^*)d\chi^*}{\int_0^{\infty} Ai(\phi\chi^*)d\chi^*}, \tag{2.61}$$

which implies

$$V_0 = \frac{-{v_0}'(0)\int_0^{\chi}\int_0^{\chi} Ai(\phi\chi^*)d\chi^* d\chi^{\dagger}}{\int_0^{\infty} Ai(\phi\chi^*)d\chi^*}. \tag{2.62}$$

We can solve (2.62) by integration by parts to obtain

$$\int_0^{\chi}\int_0^{\chi} Ai(\phi\chi^*)d\chi^* d\chi^{\dagger} = \chi\int_0^{\chi} Ai(\phi\chi^*)d\chi^*\Big|_0^{\chi} - \phi\int_0^{\chi}\chi^* Ai(\phi\chi^*)d\chi^*. \tag{2.63}$$

Let $\overline{\chi} = \phi\chi^*$ therefore

$$\int_0^{\chi}\int_0^{\chi} Ai(\phi\chi^*)d\chi^* d\chi^{\dagger} = \chi\int_0^{\chi} Ai(\overline{\chi})d\overline{\chi}\Big|_0^{\chi} - \phi\cdot\frac{1}{\phi^2}\int_0^{\chi}\overline{\chi}Ai(\overline{\chi})d\overline{\chi}. \tag{2.64}$$

The second integral in (2.64) can be expressed as

$$\int_0^{\chi}\overline{\chi}Ai(\overline{\chi})d\overline{\chi} = Ai'(\overline{\chi})\Big|_0^{\chi}, \tag{2.65}$$

therefore using (2.65), (2.64) becomes

$$\int_0^{\chi}\int_0^{\chi} Ai(\phi\chi^*)d\chi^* d\chi^{\dagger} = \chi\int_0^{\chi} Ai(\overline{\chi})d\overline{\chi}\Big|_0^{\chi} - \frac{1}{\phi}Ai'(\overline{\chi})\Big|_0^{\chi}.$$

Since we want to find large χ then (2.62) becomes

$$V_0 = \lim_{\chi\to+\infty}\chi\int_0^{\chi} Ai(\overline{\chi})d\overline{\chi}\Big|_0^{\chi} - \frac{1}{\phi}Ai'(\overline{\chi})\Big|_0^{\chi} = \chi{v_0}'(0) + \frac{{v_0}'(0)Ai'(0)}{\phi\int_0^{\infty} Ai(\overline{\chi})d\overline{\chi}}.$$

This implies that the next order in the inviscid zone must satisfy

$$v_1(0) = \frac{{v_0}'(0)Ai'(0)}{\phi\int_0^{\infty} Ai(\overline{\chi})d\overline{\chi}}. \tag{2.66}$$

This agrees with the result of Hall [42] (3.13). We now consider the next order in the inviscid region:

$$i\overline{U}_{0B}u_1 + i\overline{U}_{1B}u_0 + v_1 u_b{}' = -i\alpha_0 p_1 - i\alpha_1 p_0, \tag{2.67a}$$

$$i\overline{U}_{0B}v_1 + i\overline{U}_{1B}v_0 = -p_1{}', \tag{2.67b}$$

$$i\overline{U}_{0B}w_1 + i\overline{U}_{1B}w_0 + v_1 w_b{}' = -i\gamma_0 p, \tag{2.67c}$$

$$i\alpha_0 u_1 + i\alpha_1 u_0 + v_0{}' + i\gamma_0 w_1 = 0, \tag{2.67d}$$

with $\overline{U}_{0B}$=$\alpha_0 u_b + \gamma_0 w_b$ and $\overline{U}_{1B}$=$\alpha_1 u_b$. We have set $\gamma_1 = 0$ because we are initially only interested in the streamwise growth rates. Carrying out the same manipulation as we did for equations (2.39a)-(2.39d) we find

$$\overline{U}_{0B}[v_1'' - {\beta_0}^2 v_1] - \overline{U}_{0B}'' v_1 = 2\alpha_0\alpha_1\overline{U}_{0B}v_0 + \alpha_1 u_b{}'' v_0 - \alpha_1 u_b \frac{\overline{U}_{0B}''}{\overline{U}_{0B}} v_0. \tag{2.68}$$

By dividing through by $\overline{U}_{0B}$ we obtain an inhomogeneous Rayleigh equation in self-adjoint form

$$v_1{}'' - \left[{\beta_0}^2 + \frac{\overline{U}_{0B}''}{\overline{U}_{0B}}\right] v_1 = 2\alpha_0\alpha_1 v_0 + \alpha_1 \left[\frac{u_b{}''\overline{U}_{0B} - u_b\overline{U}_{0B}''}{{\overline{U}_{0B}}^2}\right] v_0. \tag{2.69}$$

Multiplying (2.69) by the adjoint of v_0 ($v_0^\dagger$) and integrating over the domain we obtain

$$\begin{aligned}\int_0^\infty v_1{}'' v_0^\dagger - \left[{\beta_0}^2 + \frac{\overline{U}_{0B}''}{\overline{U}_{0B}}\right] v_1 v_0^\dagger d\zeta &= \int_0^\infty 2\alpha_0\alpha_1 {v_0}^2 d\zeta \\ &+ \int_0^\infty \alpha_1 \left[\frac{u_b{}''\overline{U}_{0B} - u_b\overline{U}_{0B}''}{{\overline{U}_{0B}}^2}\right] {v_0}^2 d\zeta.\end{aligned} \tag{2.70}$$

Using integration by parts on the first term we get,

$$\int_0^\infty v_1{}'' v_0^\dagger d\zeta = [v_1{}' v_0^\dagger]_0^\infty - \int_0^\infty v_1{}' (v_0^\dagger)' d\zeta.$$

Choose

$$v_0^\dagger(0) = v_0^\dagger(\infty) = 0 \rightarrow [v_1{}' v_0]_0^\infty = 0.$$

Therefore

$$-\int_0^\infty {v_1}' {v_0^\dagger}' d\zeta = -[v_1 {v_0^\dagger}']_0^\infty + \int_0^\infty v_1 {v_0^\dagger}'' d\zeta.$$

As shown earlier $v_1(\infty) = 0$,

$$\int_0^\infty {v_1}'' v_0 d\zeta = -v_1(0) {v_0^\dagger}'(0) + \int_0^\infty v_1 {v_0}'' d\zeta.$$

Now (2.70) has become:

$$-v_1(0) {v_0^\dagger}'(0) = \alpha_1 \left[\int_0^\infty 2\alpha_0 {v_0}^2 d\zeta + \int_0^\infty (x/R) \left[\frac{{u_b}'' \overline{U}_{0B} - u_b \overline{U}''_{0B}}{{\overline{U}_{0B}}^2} \right] {v_0}^2 d\zeta \right].$$

Hence,

$$\alpha_1 = \frac{-v_1(0) {v_0^\dagger}'(0)}{\int_0^\infty 2\alpha_0 {v_0}^2 d\zeta + \int_0^\infty \left[\frac{{u_b}'' \overline{U}_{0B} - u_b \overline{U}''_{0B}}{{\overline{U}_{0B}}^2} \right] {v_0}^2 d\zeta}.$$

Therefore,

$$\alpha_1 = \frac{\frac{{v_0}'(0)^2 Ai'(0)}{\phi \int_0^\infty Ai(\overline{\chi}) d\overline{\chi}}}{2\alpha_0 I_1 + I_2},$$

using the known value for $Ai'(0)$ and $\int_0^\infty Ai(\chi) d\chi$ we get

$$\alpha_1 = \frac{3[{v_0}'(0)^2 Ai'(0)]/\phi}{2\alpha_0 I_1 + I_2}, \tag{2.71}$$

with

$$I_1 = \int_0^\infty {v_0}^2(\zeta) d\zeta, \quad I_2 = \int_0^\infty \left[\frac{{u_b}''(\zeta) \overline{U}_{0B}(\zeta) - u_b(\zeta) \overline{U}''_{0B}(\zeta)}{{\overline{U}_{0B}}^2(\zeta)} \right] {v_0}^2 d\zeta.$$

At the origin $\overline{U}_{0B}(0) = 0$, and so I_2 is singular there. As the wall normal coordinate approaches zero the baseflow components behave as

$$u_b \sim (X/R)\zeta, \; w_b \sim \zeta \quad \text{and} \quad {u_b}'' \text{ and } {w_b}'' \sim \text{constant}.$$

Therefore the singularity must behave like $1/\zeta$ near the origin. For convenience we define $\overline{F}(\zeta)$ as

$$\overline{F}(\zeta) = \left[\frac{\overline{u}''(\zeta) \overline{U}_{0B}(\zeta) - \overline{u}(\zeta) \overline{U}''_{0B}(\zeta)}{{\overline{U}_{0B}}^2(\zeta)} \right].$$

Since the integral is divergent, we need to find a method to evaluate this integral. For this we will use the Hadamard Finite Part Integral which can be located in the appendix. First we split the integral into two parts,

$$I_2 = \int_0^\infty \overline{F}(\zeta){v_0}^2 d\zeta = \int_0^1 \overline{F}(\zeta){v_0}^2 d\zeta + \int_1^\infty \overline{F}(\zeta){v_0}^2 d\zeta. \tag{2.72}$$

We notice that the second integral is valid across the domain. However, the first integral is not and we have to calculate it by the Hadamard Finite Part Theorem. By applying this theorem we can neglect the infinite part $\left(\int_0^1 \frac{1}{\zeta}{v_0}^2 d\zeta\right)$ and keep the finite part such that

$$\int_0^1 \overline{F}(\zeta){v_0}^2 d\zeta = \underbrace{\int_0^1 \left[\overline{F}(\zeta)| + \frac{1}{\zeta}\right] {v_0}^2 d\zeta}_{\text{finite}} - \underbrace{\int_0^1 \frac{1}{\zeta}{v_0}^2 d\zeta}_{\text{undefined}}.$$

Hence we can state,

$$\int_0^1 \overline{F}(\zeta){v_0}^2 d\zeta = \text{⨍}_0^1 \left[\overline{F}(\zeta) + \frac{1}{\zeta}\right] {v_0}^2 d\zeta.$$

Thus have found a correction to the inviscid growth rate, in the expansion of $\alpha = \alpha_0 + \epsilon\alpha_1$. We can now see the behaviour of the new growth rate $(-\alpha_i)$ downstream. We notice that $\alpha_{0i} < 0$ is the inviscid streamwise growth rate but the viscous correction term $\alpha_{1i} > 0$ has a stabilising effect from equation (2.71).

2.4.5 Numerical Comparison

From our asymptotic approach we have formulated a two-term growth rate prediction method. We now compare these with numerical schemes of Parabolised Stability Equations (PSE) [58] and Vorticity-Velocity equations (VV) [26] to verify the validity and accuracy of our prediction method. The PSE originated from the work of Dallmann & Simen [90],[91] and Herbert & Bertolotti [9] who were inspired by the work of Hall [41]. Due to the Görtler vortices satisfying a parabolic system this gave rise to a parabolic marching algorithm. They can be solved very efficiently due to the marching procedure. The formulation was originally only intended for the description linear development of the modal disturbances. However in recent years this theory has extended for non-linear evolution and for the non-modal disturbance evolution. The VV is a re-

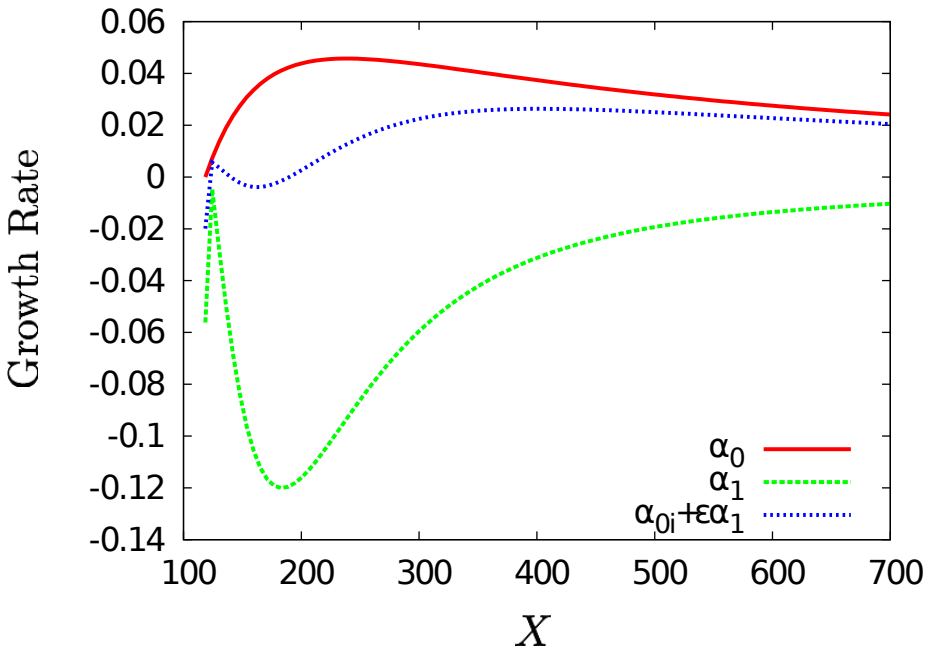

Figure 2.12: Comparison between the inviscid streamwise growth rate (α_{0i}), viscous correction streamwise growth rate (α_{1i}) and the corrected streamwise growth rate (α_i) with the rescaled streamwise coordinate X for $Re = 500$ and $\gamma_0 = 0.4$.

formulated version of unsteady, three-dimensional Navier-Stokes equations in terms of velocity and vorticity equations. The evolution of three-dimensional disturbances in boundary layers can be simulated quite easily with this method. The advantages of VV compared to other methods are that the boundary conditions can be in terms of the vorticity - there is no need for conditions for the velocity since they can be calculated by an integral containing the vorticity. Also, there are only three dependent variables with three governing equations, which can be solved in less time than if other methods were used. Most numerical schemes struggle with a large Reynolds numbers due the matrices becoming larger. The difficulty arises with the large matrices when inversion techniques are applied to them. The most common matrix inversion packages are *Lapack* in Fortran and *eigen* for C++. The non-dimensionalisation for the numerical procedure for pressure and velocities is with respect to the spanwise velocity at infinity, W_∞. Hence the base flow can be defined as

$$u_b = (X/Re)f'(\zeta),\ v_b = (-1/Re)f'(\zeta),\ \text{and}\ w_b = g(\zeta),$$

where $X = x^*/\delta^*$, $\delta^* = \sqrt{\nu/m}$ (which is defined as the thickness parameter), ν is the kinematic viscosity of the fluid and, m is a parameter from the uniform flow field ($U_\infty(\mathrm{X}) = mx^*$). The roughness element is given by the function

$$h(X) = \frac{1}{\sqrt{2\pi}} e^{-\frac{(X-X_f)^2}{2}},$$

where $X_f = 185.5$. We start at this particular location due to the numerical scheme we are using for a comparison of this theory and we use this base flow for our prediction. More details about the roughness element and basic flow can be found in a paper by Thomas,Hall & Davies [96]. We restrict our attention to $Re = 500$ due to constraints of computational power. We notice in figure 2.13 that there is a disagreement

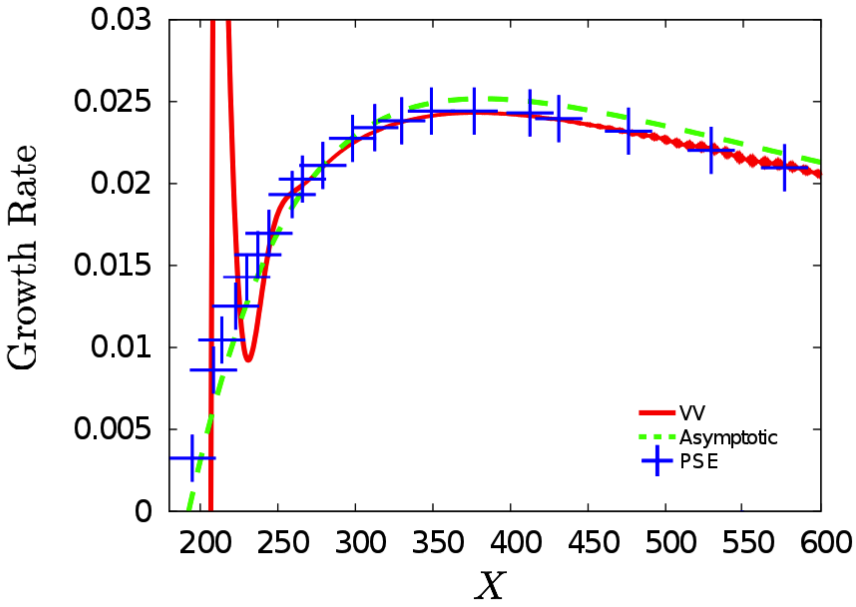

Figure 2.13: Comparison between velocity-vorticity equations [95] (_____) , asymptotic theory (.....), and PSE [58] (+++++) at a Reynolds number of $Re = 500$, and a spanwise wavenumber of $\gamma_0 = 0.4$.

regarding the location of the neutral stability point. It occurs further upstream than expected. The asymptotic result and PSE are in agreement. Initially the VV method does not agree as it is forced at the neutral stability point location. Further ahead the growth rates seem to be in good agreement between the three methods. However for $X > 300$, the asymptotic results agree with the numerical schemes and they provide

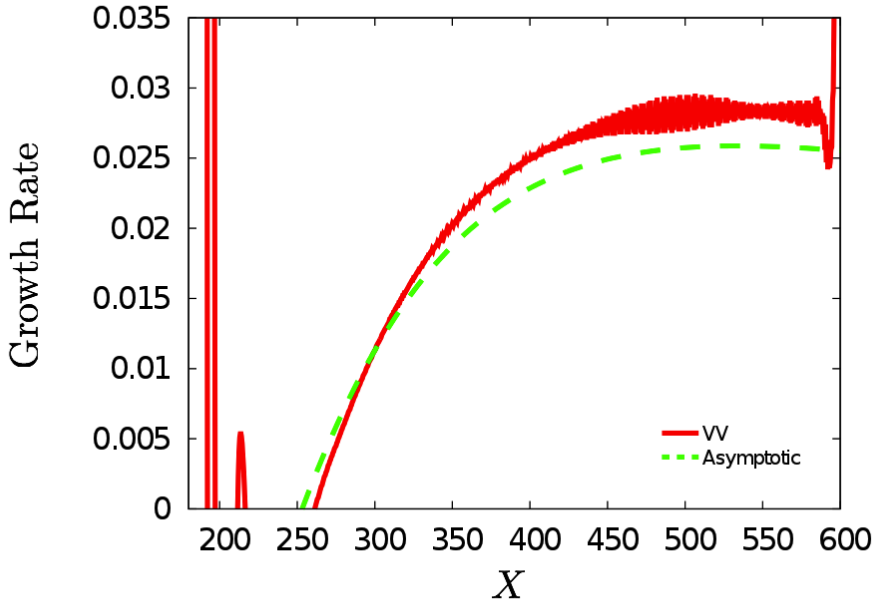

Figure 2.14: Comparison between velocity-vorticity equations (_____) and viscous correction theory (.....), at a Reynolds number of $Re = 750$, and a spanwise wavenumber $\gamma_0 = 0.4$.

a slight over estimation of 0.001. To improve the result we could include the next order in the expansion (α_2) which would give a correction to the growth rate of order $Re^{-1/3} \sim 0.12692$ and this could account for the discrepancy. Nevertheless, there seems to be a good agreement so no further analysis needs to be performed at this point.

Next we will consider a comparison with a different Reynolds number to validate the previous results. We consider a Reynolds number of $Re = 750$ and compare with the asymptotic prediction in figure 2.14. We witness good agreement between the two methods but for this Reynolds number we have a slight under evaluation of 0.002. From $X \sim 400$, the VV results [95] start to develop oscillations due to the oscillating term in $U \sim e^{i(\alpha_r)}$. In figure 2.14 we have changed the Reynolds number compared with the previous study in figure 2.13 and we are using the same spanwise wavenumber as before. Since the contribution from the viscous correction term is $Re^{-1/6}$, this implies that the contribution at $Re = 500$ is $\epsilon \sim 7/20$, whereas for $Re = 750$ we have a contribution of $\epsilon \sim 1/3$. We would expect the examples of different Reynolds numbers to have a similar contribution since the difference between the viscous correction

terms is $\epsilon \sim 0.02$. Whilst there is still some discrepancy between the two methods of VV and the two-term approach these may be accounted for by numerical errors.

Next we considered varying the spanwise wavenumber. Figure 2.15 shows how the downstream growth rate changes with the spanwise wavenumber. Generally, as X increases the growth rate decreases. This demonstrates that as X increases, the extent of the unstable region of spanwise wavenumbers becomes larger. Hence as the crossflow effect decreases, more spanwise wavenumbers corresponding to a positive growth rate are included, as shown in figure 2.10. For instance if we consider $X = 100$ then only the unstable spanwise wavenumbers between $0.1 < \gamma_0 < 0.3$ but for $X = 300$ we have $0.1 < \gamma_0 < 0.8$. In figure 2.15 the most dangerous mode changes with the crossflow effect. This is also inherent in the inviscid dispersion relation where the high crossflow case has the largest growth rate. However for the low crossflow corresponds to the smallest maximum growth rate. Therefore we notice that for small spanwise wavenumbers a maximum growth rate occurs in a high crossflow region, whereas for higher spanwise wavenumbers a maximum growth rate occurs at smaller crossflow values.

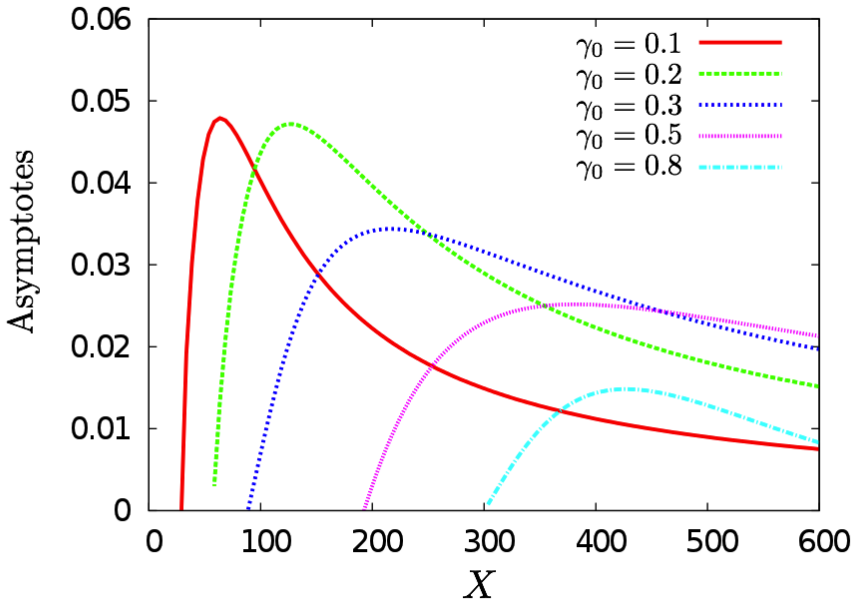

Figure 2.15: Growth rate comparison between different values of spanwise wavenumber at $Re = 500$ calculated using the asymptotic approach.

2.4.6 Travelling Crossflow Vortices

To compare with experimental work it is useful to model travelling crossflow vortices. This is due to most experiments are unable to achieve low turbulence levels associated with stationary crossflow vortices. Furthermore we want to understand the impact that an active or passive mechanism, used for laminar flow control, will have on the crossflow vortices. More specifically, do these control techniques dampen or amplify the initial amplitudes of the travelling crossflow vortices? We shall investigate to find this out, by including the frequency of ω_0 in our analysis. In figure 2.16 as the

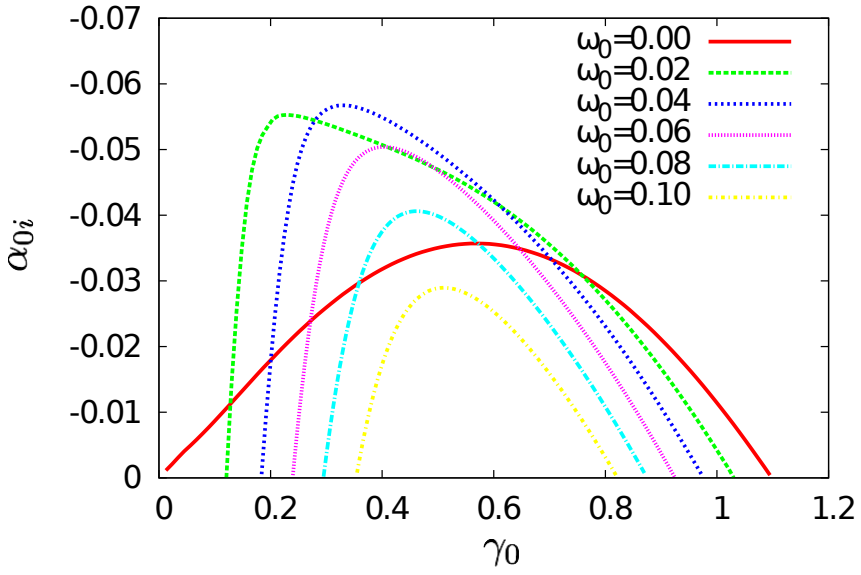

Figure 2.16: Dispersion relation between imaginary part of the streamwise wavenumber, α_{0i}, and spanwise wavenumber, γ_0, for different frequencies, ω_0 for a fixed streamwise position of $x = 1.0$ and a sweep angle of $\theta_{sw} = 45°$.

frequency increases the number of unstable spanwise numbers decreases. However, the most dangerous modes amplify when the frequency has increased. The largest growth rate corresponds to $\gamma_0 = 0.36$ and $\omega_0 = 0.04$ which is almost twice as large as the stationary case for that given spanwise wavenumber. The disturbance is completely stable for any given spanwise number for frequencies $\omega_0 > 0.135$ as shown in figure 2.17. We focus our attention on a particular spanwise mode of $\gamma_0 = 0.5$ and witness the impact of varying the frequency. The dispersion relation can be seen in figure 2.17 and the most dangerous mode occurs for $\omega_0 = 0.04$. Interestingly for frequencies

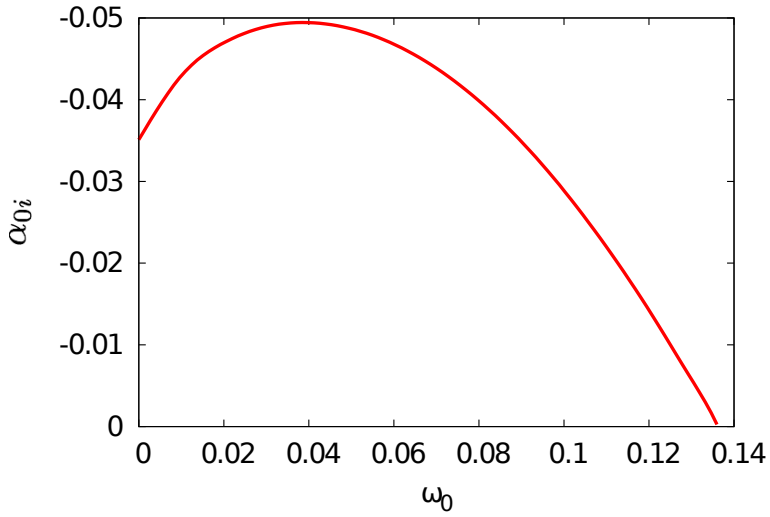

Figure 2.17: Dispersion relation between the imaginary part of the streamwise wavenumber (α_{0i}) and the frequency (ω_0) for a fixed spanwise wavenumber (γ_0=0.5).

$\omega_0 > 0.09$, the growth rates are smaller than for the stationary case. We already know the downstream streamwise behaviour of stationary crossflow vortices for streamwise growth rates from figure 2.12. We now vary the frequencies of the travelling modes and observe the impact on the streamwise growth rates. In figure 2.18 we can observe

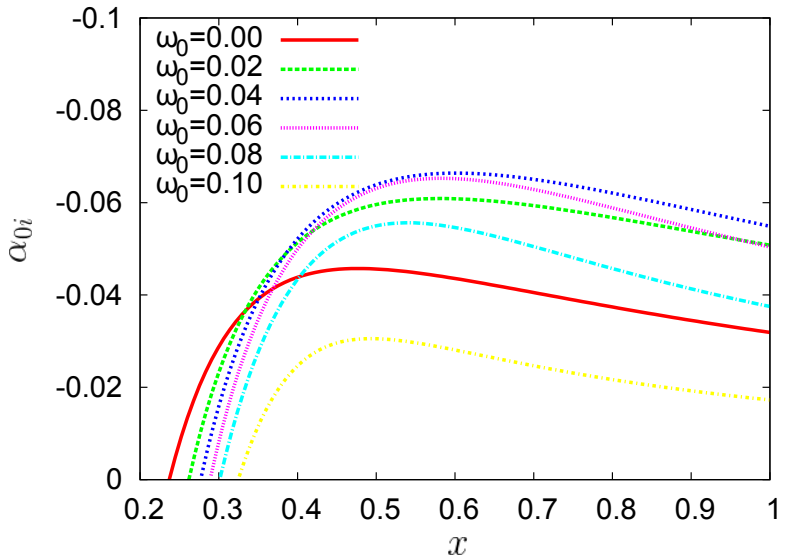

Figure 2.18: Streamwise inviscid growth rate comparison with varying frequency (ω_0) for fixed spanwise wavenumber $\gamma_0 = 0.4$.

that the neutral stability point increases in x as the frequency is increased. The most dangerous mode changes as x changes but we notice that for $0.4 < x < 1$ the most dangerous mode occurs for a frequency of $\omega_0 = 0.04$, as apparent in the dispersion relation of figure 2.16.

The correction term from equation (2.71), α_1, has now been modified by including the frequency. For travelling modes due to the integrals of I_1 and I_2 have been modified because of changes in the 'effective' base flow ($\overline{U}_{0B}$). As with the stationary crossflow vortices, we compare with VV and PSE again. For this certain frequency ($\omega_0 = 7.5 \times$

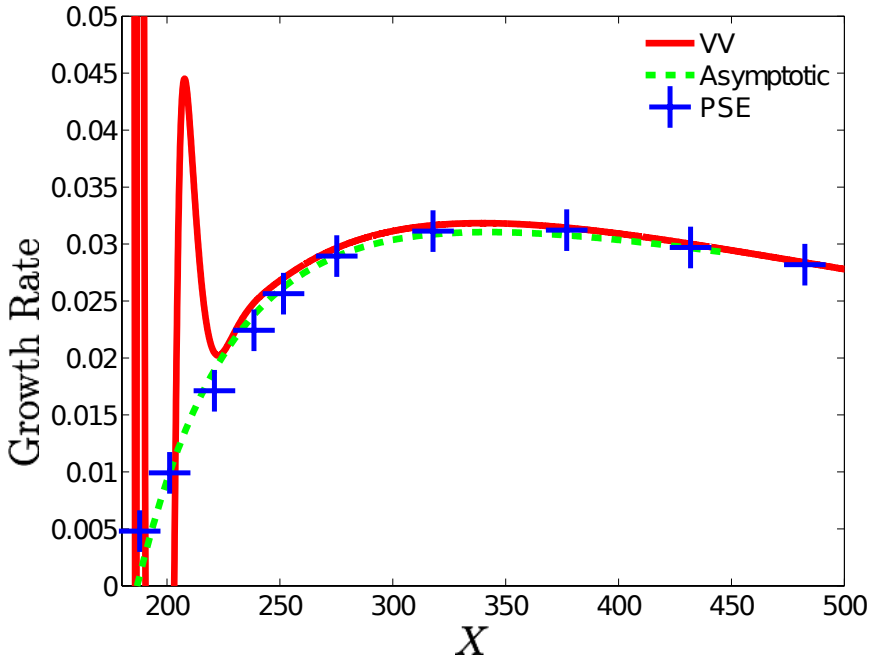

Figure 2.19: Comparison between velocity-vorticity equations [95](_____) , two-term theory (.....), and PSE [58] (+++++) at $Re = 500$, $\gamma_0 = 0.4$ with a frequency $\omega_0 = 7.5 \times 10^{-4}$.

.

10^{-4}) there seems to be excellent agreement with the two numerical methods. There also seems to be a better agreement than seen in the stationary case, which suggests that the method might be sensitive to changes in the frequency.

2.5 The Effects of Curvature on the Stability of Crossflow Vortices

Thus far we have only considered stationary and travelling crossflow vortices on a flat surface. We now turn our attention to curved surfaces and we consider $\kappa \ll 0$ (κ is the local body curvature), since we are only interested in small curvature modifications. We perform the same analysis as for §2.3.4 but now we include the curvature terms. Doing so yields the following

$$i\overline{U}_{0B}u_0 + v_0 {u_b}' = -i\alpha_0 p_0, \tag{2.73a}$$

$$i\overline{U}_{0B}v_0 + \kappa_C u_b u_0 = -{p_0}', \tag{2.73b}$$

$$i\overline{U}_{0B}w_0 + v_0 {w_b}' = -i\gamma_0 p_0, \tag{2.73c}$$

$$i\alpha_0 u_0 + {v_0}' + i\gamma_0 w_0 = 0, \tag{2.73d}$$

with $\kappa_C = -G\kappa(x)$ where G is the Görtler number and defined in the introduction. The disturbance velocity has to be zero at the wall because it has a no-slip boundary condition. We can rearrange (2.73) - with some manipulation we eliminate p_0 and rearranging for v_0, we obtain

$${v_0}'' - \frac{\alpha_0 u_b \kappa_C {v_0}'}{\overline{U}_{0B}} + \left[\frac{\alpha_0 u_b \kappa_C {\overline{U}_{0B}}'}{\overline{U}_{0B}^2} - {\beta_0}^2\left(1 + \frac{u_b {u_b}' \kappa_C}{\overline{U}_{0B}^2}\right) - \frac{\overline{U}''_{0B}}{\overline{U}_{0B}}\right] v_0 = 0, \tag{2.74}$$

subject to the following boundary conditions

$$v_0(0) = 0 \quad \text{and} \quad v_0(\infty) = 0. \tag{2.75}$$

We observe by multiplying by $\overline{U}_{0B}$ and setting $\kappa_C = 0$ we can obtain

$$\overline{U}_{0B}[{v_0}'' - {\beta_0}^2 v_0] - \overline{U}''_{0B} v_0 = 0. \tag{2.76}$$

This is the Rayleigh stability equation which we found earlier (as equation (2.41)).

2.5.1 Results

First we consider the dispersion relation between the streamwise growth rate and the spanwise wavenumber, as in figure 2.7. We are interested is in the curvature modifica-

tions, so we change κ_C accordingly and observe the changes to the dispersion relation.

Inviscid Results

We will see that by varying κ_C, we can stabilise the disturbance with a positive value and destabilise the disturbance when we consider negative values. We shall investigate what impact curvature has on the inviscid results obtained earlier including travelling crossflow vortices. We solve this problem in a familiar fashion to the Rayleigh stability equation, seen earlier in (2.41). Numerically we solve (2.74) using a fourth order Runge-Kutta shooting technique and the boundary conditions of (2.75). By performing this calculation we obtain a dispersion relation - the same relation as in figure 2.7 but we can see the different effects of curvature.

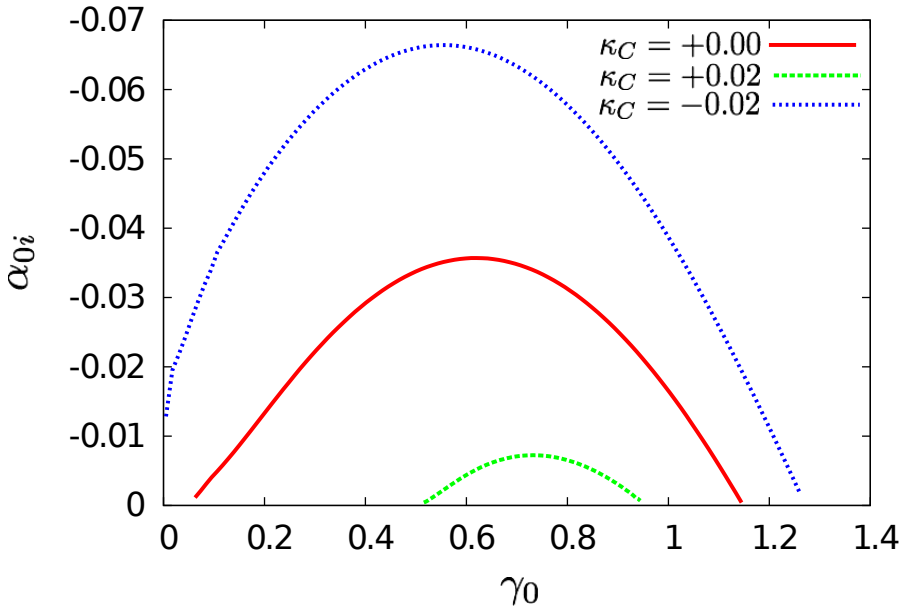

Figure 2.20: Dispersion relation between streamwise growth rate (α_{0i}) and the spanwise wavenumber (γ_0) for convex (.....), flat (_____) and concave surface curvature (- - - - -) for a fixed streamwise position of $x = 1.0$, sweep angle of $\theta_{sw} = 45°$ and for a stationary crossflow mode $\omega_0 = 0.0$.

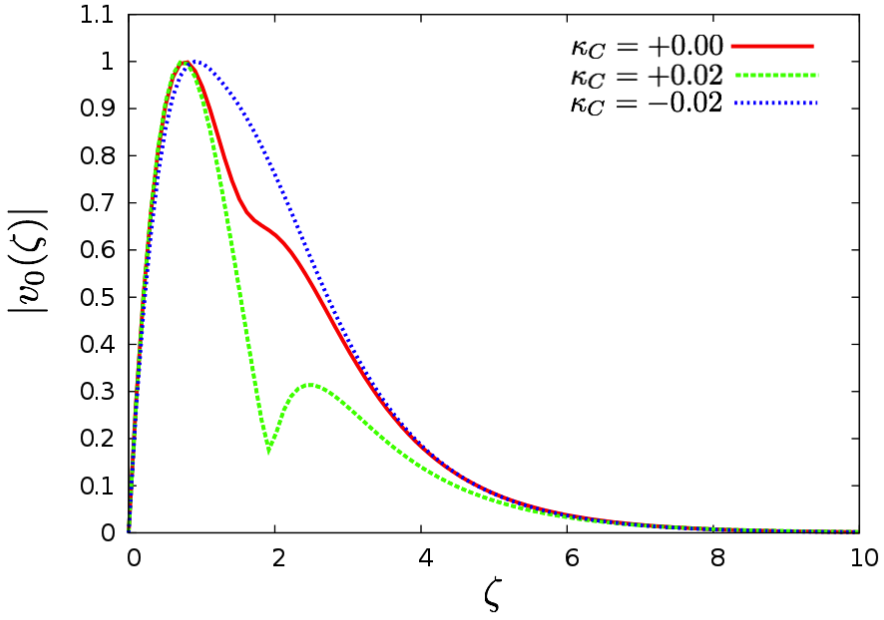

Figure 2.21: Normalised eigenfunction of v_0 with x=1.0 for a fixed spanwise wavenumber $\gamma_0 = 0.6$ with varying κ_C corresponding to convex (.....), flat (_____) and concave surface curvature (- - - - -).

It appears that small positive κ_C stabilises the disturbance and negative κ_C destabilises. This is in agreement with what is already known, that convex curvature stabilises the crossflow vortex disturbance and concave curvature destabilises it [59]. We notice that not only has the most unstable mode been reduced due to κ_C but also the extent of unstable spanwise wavenumbers is been has reduced. We refer the extent of the unstable spanwise wavenumbers as the region of spanwise wavenumbers where $\alpha_{0i} < 0$ as shown in figure (2.20). The most dangerous mode increases with decreasing κ_C. This is not surprising since negative κ_C has a destabilising effect. By observing figure 2.21 we can see the inflexion point in the basic flow as discussed earlier. As we increase κ_C, we can see that a local extrema in the eigenfunction occurs at $\zeta \sim 2$ due to taking the absolute value.

We now look at the effect of surface curvature with travelling modes. It is known that small convex curvature has a stabilising effect on small frequencies [59]. However, this is not the case for larger frequencies - a larger curvature is required to stabilise the disturbance.

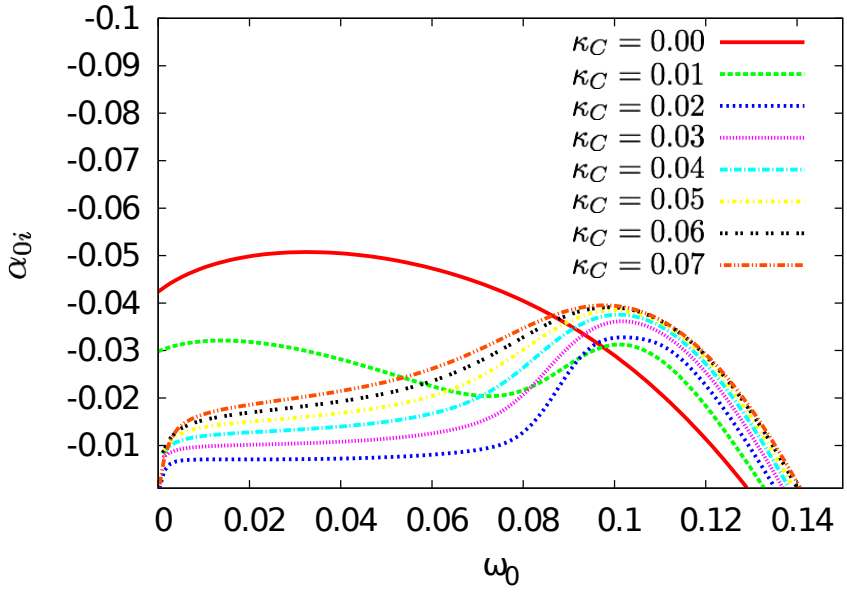

Figure 2.22: Dispersion relation between streamwise wavenumber (α_{0i}) and frequency (ω_0) for a fixed spanwise wavenumber ($\gamma_0 = 0.5$) with varying κ_C, for $\kappa_C \ll 1$.

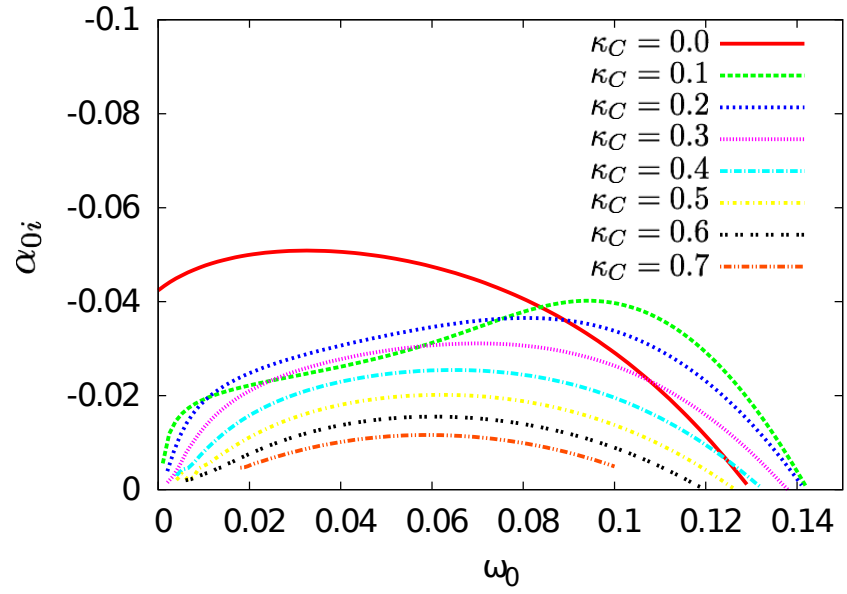

Figure 2.23: Dispersion relation between streamwise wavenumber (-α_{0i}) and frequency (ω_0) for a fixed spanwise wavenumber ($\gamma_0 = 0.5$) with varying κ_C, for $\kappa_C \sim O(1)$.

In figure 2.22 we have a dispersion relation between the streamwise growth rate and the frequency for increasing convex curvature. First we notice that for the disturbance to be stabilised we need a curvature term of $\kappa_C > 0.02$. Any κ_C value greater than this produces a sudden drop in the dispersion relation. As the curvature is increased the maximum unstable frequency increases. From small curvature of $\kappa_C = 0.02$ there is a significant change in the growth rates for frequencies less than $\omega_0 = 0.09$. In fact for this frequency range small convex curvature reduces the growth rate by about five times compared to the stationary case. We notice that for frequency of $\omega_0 > 0.09$ the streamwise growth rates have increased when convex curvature is added. Therefore we observe that as κ_C increases so does $-\alpha_{0i}$, for frequencies greater than $\omega_0 = 0.09$. A frequency of $\omega_0 = 0.08$ onwards appears to destabilise the disturbance. Masad & Malik [59] found that the effect of convex curvature is gradually less stabilising as the frequencies of the disturbance increases. We can also note that highly convex curvature ($\kappa_C > 1$) has a stabilising effect.

The convex curvature is increased further and we see the effects of large curvature with frequency in figure 2.23. As κ_C is increased the growth rates increase for all frequencies and the stabilisation is not effective for these convex curvature values. Also, as κ_C increases, the largest unstable frequency decreases and for $\kappa_C > 1$ there are no longer any unstable frequencies.

Due to the interesting results in figures 2.22 and 2.23, we shall focus on fixing two frequencies of $\omega_0 = 0.05$ and $\omega_0 = 0.10$. From earlier results we already know the impact of convex curvature has on the stability of stationary crossflow vortices - a small amount of convex curvature is needed to stabilise the disturbance ($\kappa_C = 0.037$). We will now focus our attention on the dispersion relation for these two frequencies.

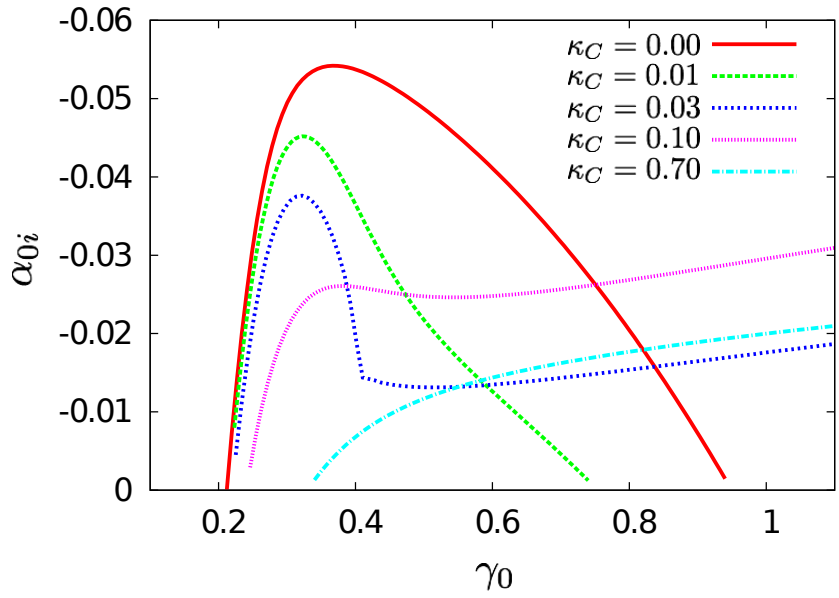

Figure 2.24: Dispersion relation between streamwise wavenumber (-α_{0i}) and spanwise wavenumber (γ_0) for a fixed frequency (ω_0=0.05) with varying κ_C.

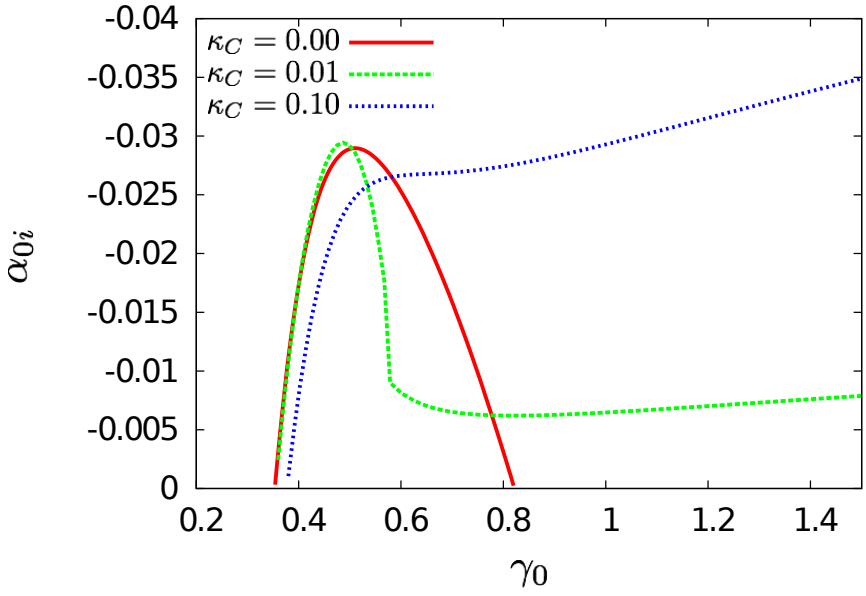

Figure 2.25: Dispersion relation between streamwise wavenumber (-α_{0i}) and spanwise wavenumber (γ_0) for a fixed frequency (ω_0=0.1) with varying κ_C.

We can see that in figure 2.24, as the the convex curvature increases it does have a stabilising effect for small spanwise wavenumbers ($\gamma_0 < 1$) as shown earlier. But we can see that as the convex curvature increases the larger spanwise wavenumbers start to become unstable referring to the unstable streamwise wavenumbers for $\kappa_C > 0.01$. After this point all spanwise wavenumbers from $\gamma_0 = 0.2$ are completely unstable. This is similar to figure 2.25 but from $\gamma_0 = 0.4$. Also note, this effect occurs at a lower κ_C value and this is in agreement with the Masad & Malik results that were discussed earlier. For small convex curvature ($\kappa_C = 0.01$) the amount of unstable spanwise wavenumbers are reduced. The value of the most dangerous mode (the amplification rate) also reduces in this manner. However as κ_C is increased the number of unstable spanwise wavenumbers increases. If we consider a value of the curvature parameter of $\kappa_C = 0.3$ for all the spanwise wavenumbers $\gamma_0 > 0.3$ corresponds to unstable streamwise wavenumbers as shown in figure 2.24. In figure 2.25 a similar behaviour for the dispersion relation occurs but at a much smaller κ_C. For instance, $\kappa_C = 0.01$ all the spanwise wavenumbers $\gamma_0 > 0.3$ are unstable and this is true as κ_C is increased. We also notice that as κ_C increases so does the most unstable mode. From this initial analysis, we have calculated the first term in the streamwise growth rate. We can conclude when considering travelling crossflow vortices in a convex curvature region it does not have the same control of the disturbance as for the stationary crossflow modes. Thus far we have considered the curvature parameter $\kappa_C \ll 1$, so we can perform an asymptotic expansion in terms of this curvature. In hindsight we have found the inviscid growth rate in the absence of curvature and now we shall add to this theory by including a curvature correction term. We redefine the quantities in (2.74) as

$$\alpha_0 = \tilde{\alpha},\ u_0 = \tilde{u},\ v_0 = \tilde{v},\ w_0 = \tilde{w},\ p_0 = \tilde{p}. \tag{2.77}$$

Then performing an expansion of

$$\tilde{\alpha} = \tilde{\alpha}_0 + \kappa_C \tilde{\alpha}_1 + \cdots , \tag{2.78}$$

$$\underline{\tilde{u}} = \underline{\tilde{u}}_0 + \kappa_C \underline{\tilde{u}}_1 + \cdots , \tag{2.79}$$

$$\tilde{p} = \tilde{p}_0 + \kappa_C \tilde{p}_1 + \cdots , \tag{2.80}$$

and substituting into the governing equations of (2.3) the first order terms become

$$\tilde{U}_{0B}[\tilde{v}_0'' - \tilde{\beta}_0^2 \tilde{v}_0] - \tilde{U}_{0B}'' \tilde{v}_0 = 0. \tag{2.81}$$

where $\tilde{U}_{0B} = \tilde{\alpha}_0 u_b + \tilde{\gamma}_0 - \omega_0$. This can be solved quite easily with the method described earlier for equations (2.43). This is the Rayleigh stability equation. The next order we have:

$$i\tilde{U}_{0B}\tilde{u}_1 + \tilde{v}_0 {u_b}' + i\alpha_0 \tilde{p}_1 = -i\alpha_1 u_b \tilde{u}_0 - i\alpha_1 \tilde{p}_0, \tag{2.82a}$$

$$i\tilde{U}_{0B}\tilde{v}_1 + \tilde{p}_1' = -i\alpha_1 u_b \tilde{v}_0 - u_b \tilde{u}_0, \tag{2.82b}$$

$$i\tilde{U}_{0B}\tilde{w}_1 + \tilde{v}_1 {w_b}' + i\gamma_0 \tilde{p}_1 = -i\alpha_1 u_b \tilde{u}_0, \tag{2.82c}$$

$$i\alpha_0 \tilde{u}_1 + \tilde{v}_1' + i\gamma_0 \tilde{w}_1 = i\alpha_1 \tilde{u}_0. \tag{2.82d}$$

This can be simplified to

$${v_1}'' - \left[\tilde{\beta}_0^2 + \frac{\tilde{U}_{0B}''}{\tilde{U}_{0B}}\right] v_1 = 2\tilde{\alpha}_0\tilde{\alpha}_1\tilde{v}_0 + \tilde{\alpha}_1 \left[\frac{u_b''\tilde{U}_{0B} - u_b\tilde{U}_{0B}''}{\tilde{U}_{0B}^2}\right] \tilde{v}_0 + \frac{i\tilde{\beta}_0^2 u_b \tilde{u}_0}{\tilde{U}_{0B}}. \tag{2.83}$$

with $\tilde{\beta}_0^2 = \tilde{\alpha}_0^2 + \tilde{\gamma}_0^2$. We only require the equation in terms of $\tilde{v}_1$ and $\tilde{v}_0$, hence using the $O(1)$ equation we can now write

$${v_1}'' - \left[\tilde{\beta}_0^2 + \frac{\tilde{U}_{0B}''}{\tilde{U}_{0B}}\right] v_1 = 2\tilde{\alpha}_0\tilde{\alpha}_1\tilde{v}_0 + \tilde{\alpha}_1 \left[\frac{u_b''\tilde{U}_{0B} - u_b\tilde{U}_{0B}''}{\tilde{U}_{0B}^2}\right] \tilde{v}_0 \tag{2.84}$$

$$- \frac{\tilde{\gamma}_0 u_b}{\tilde{U}_{0B}^2} \left[\tilde{\gamma}_0 {u_b}' - \tilde{\alpha}_0 {w_b}'\right] \tilde{v}_0 - \frac{\tilde{\alpha}_0 u_b \tilde{v}_0'}{\tilde{U}_{0B}}, \tag{2.85}$$

multiplying by $\tilde{v}_0$ and integrating over ζ we get

$$0 = 2\tilde{\alpha}_0\tilde{\alpha}_1 I_1 + \tilde{\alpha}_1 I_2 - \tilde{\gamma}_0 I_3 - \tilde{\alpha}_0 I_4, \tag{2.86}$$

with

$$I_1 = \int_0^\infty \tilde{v}_0^2 d\zeta, \quad I_2 = \int_1^\infty \tilde{F}(\zeta)\tilde{v}_0^2 d\zeta + \fint_0^1 \left[\tilde{F}(\zeta) - \frac{1}{\zeta}\right] \tilde{v}_0^2 d\zeta,$$
$$I_3 = \int_1^\infty \tilde{G}(\zeta)\tilde{v}_0^2 d\zeta + \fint_0^1 \left[\tilde{G}(\zeta) - \frac{1}{\zeta}\right] \tilde{v}_0^2 d\zeta,$$
$$I_4 = \int_1^\infty \tilde{H}(\zeta)\tilde{v}_0 d\zeta + \fint_0^1 \left[\tilde{H}(\zeta) - \frac{1}{\zeta}\right] \tilde{v}_0 d\zeta,$$

where

$$\tilde{F}(\zeta) = \left[\frac{\overline{u}''(\zeta)\tilde{U}_{0B}(\zeta) - \overline{u}(\zeta)\tilde{U}''_{0B}(\zeta)}{\tilde{U}^2_{0B}(\zeta)}\right], \tag{2.87}$$

$$\tilde{G}(\zeta) = \frac{u_b}{\tilde{U}^2_{0B}(\zeta)} \left[\tilde{\gamma}_0 {u_b}'(\zeta) - \tilde{\alpha}_0 {w_b}'(\zeta)\right], \tag{2.88}$$

$$\tilde{H}(\zeta) = \frac{u_b \tilde{v}_0'}{\tilde{U}_{0B}(\zeta)}. \tag{2.89}$$

The integrals I_2, I_3 and I_4 consist of $u_b/\tilde{U}_{0B}$ and this term is singular at the origin due to the boundary conditions. We use the Hardamard Finite Part Integral to evaluate these integrals. The equation (2.86) now can be rearranged for $\tilde{\alpha}_1$ and this yields

$$\tilde{\alpha}_1 = \frac{\tilde{\gamma}_0 I_3 + \tilde{\alpha}_0 I_4}{2\tilde{\alpha}_0 I_1 + I_2}, \tag{2.90}$$

We can now compare this with the original results of figure 2.20. There seems to be good agreement across most of the spanwise wavenumbers except for three cases; $\tilde{\alpha} \ll 1$, $\tilde{\gamma}_0 \ll 1$ and $\tilde{\gamma}_0 > 1$. The curvature correction term contains the first order inviscid term, hence (2.86) can now be written as

$$\tilde{\alpha} = \tilde{\alpha}_0 \left[1 + \kappa_C \left(\frac{\frac{\tilde{\gamma}_0}{\tilde{\alpha}_0} I_3 + I_4}{2\tilde{\alpha}_0 I_1 + I_2}\right)\right]. \tag{2.91}$$

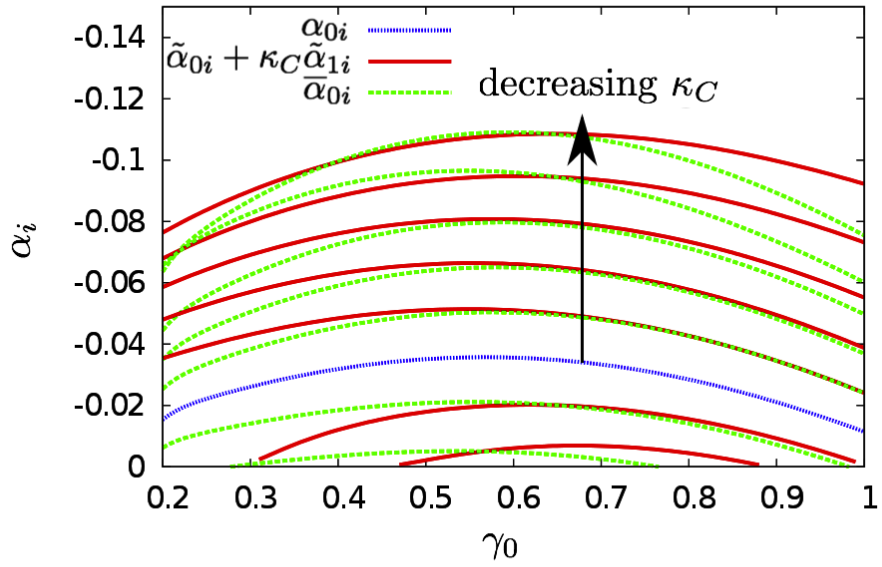

Figure 2.26: Dispersion relation between spanwise wavenumber γ_0 and the streamwise growth rate $-\alpha_i$ comparison between inviscid theory (------) and two-term correction (_____) with X=1.0, $\overline{(\zeta)}$=1.0 and at the values of $\kappa_C = 0.02, 0.01, 0.00$(.....), $-0.01, -0.02, -0.03, -0.04, -0.05$.

We now consider the three situations where there is a clear breakdown between the two results.

1. $\tilde{\alpha}_0 \ll 1 \implies \tilde{\alpha}_1 = \frac{\kappa_C \tilde{\gamma}_0 I_3}{I_2} \sim \mathcal{O}(10^{-1}\kappa_C \tilde{\gamma}_0)$.
2. $\tilde{\gamma}_0 \ll 1 \implies \tilde{\alpha}_1 = \tilde{\alpha}_0 \left[1 + \kappa_C \left(\frac{I_4}{2\tilde{\alpha}_0 I_1 + I_2}\right)\right] \sim \mathcal{O}(10^{1}\kappa_C)$.
3. $\tilde{\gamma}_0 > 1 \implies \tilde{\alpha}_1 = \frac{\kappa_C I_3}{2\tilde{\alpha}_0 I_1 + I_2} \sim \mathcal{O}(10^{-1}\kappa_C)$.

By considering certain limits of $\tilde{\alpha}_0 \ll 1$, $\tilde{\gamma}_0 \ll 1$ and $\tilde{\gamma}_0 > 1$, we can discuss the reasons why we do not have agreement in certain regions of the dispersion relation. For the first case we consider the situation when inviscid streamwise wavenumber is small ($\tilde{\alpha}_0 \ll 1$), this modifies the two-term correction method to only depend on the curvature term and spanwise wavenumber. If we consider convex curvature then this will have a stabilising impact on the streamwise growth rate and thus cause a disagreement to occur. In the second case, we consider when the spanwise wavenumber is small ($\tilde{\gamma}_0 \ll 1$) and this produces the term $\tilde{\alpha}$ to depend only on κ_C. A similar argument to

the first case can be used, that we have $\kappa_C > 0$ will stabilise the growth rate which explains the discrepancy. This is why we notice that for the example of $\kappa_C = -0.04$, the two-term correction is larger than the inviscid growth rate due to $\kappa_C < 0$. Making this contribution more unstable in terms of the inviscid growth rate. However, the reverse argument can be used for $\kappa_C = 0.02$. Since $\kappa_C > 0$, it will have a stabilising impact on the growth rate. For large spanwise wavenumbers ($\tilde{\gamma}_0 > 1$) a similar argument can be used but the contribution from $\tilde{\alpha}_1$ is smaller and has less of an impact.

2.5.2 Numerical Comparison with PSE

We shall compare results with a PSE swept cylinder case for $\theta_{SW} = 65°$ and we will use the base flow data from a boundary-layer solver provided by Mughal [63].

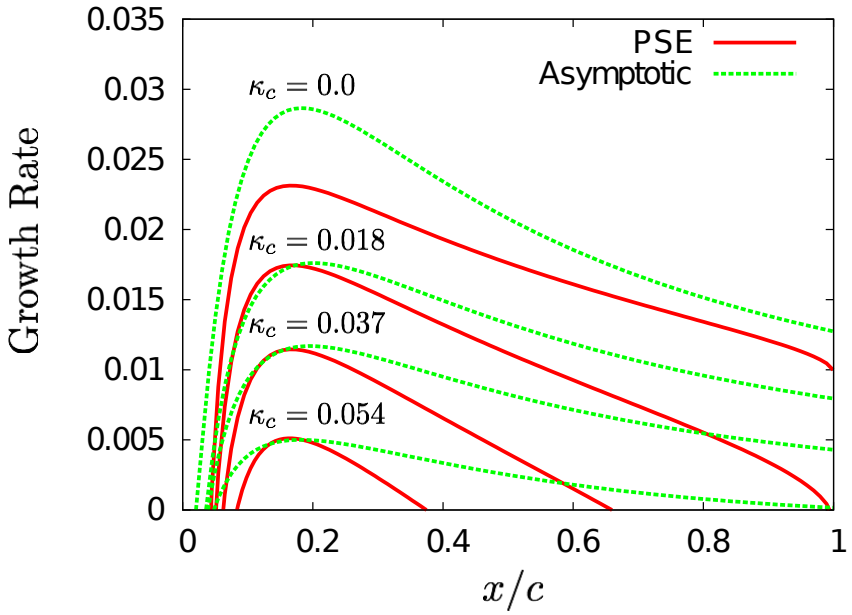

Figure 2.27: Comparison between PSE (_____) and two-term curvature method [$\tilde{\alpha}_0 + \kappa_C\tilde{\alpha}_1$] (.....) for streamwise growth rate downstream, $\gamma_0 = 0.8$.

We next include the viscous term and compare with the same PSE results. From the

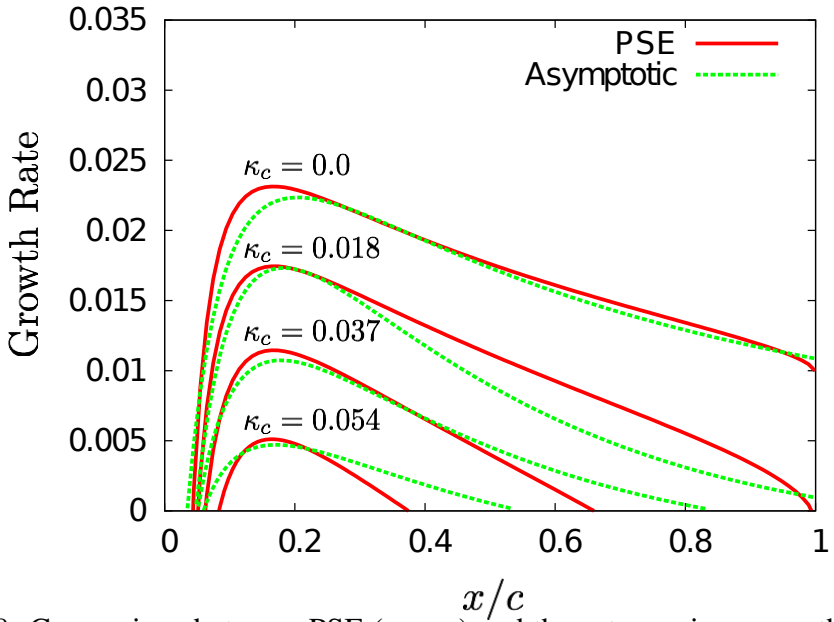

Figure 2.28: Comparison between PSE (_____) and three-term viscous method [$\tilde{\alpha}_0 + \kappa_C\tilde{\alpha}_1 + \epsilon\alpha_1$] (.....) for streamwise growth rate downstream, $\gamma_0 = 0.8$.

inviscid analysis, larger crossflow strength implied that there is a smaller unstable spanwise region and increased maximum streamwise growth rate. There seems to be good agreement between the two methods of PSE and two-term curvature analysis initially. Earlier results indicated good agreement between PSE and asymptotic prediction for a flat surface ($\kappa_C = 0.0$), but clearly since the viscous term has not been included yet we notice a large discrepancy. For comparison purposes a spanwise wavenumber of $\gamma_0 = 0.8$ was used but as we have seen in figure 2.26 there is clearly some discrepancy between the streamwise growth rates. From figure 2.27 for $x/c > 0.4$ a discordance is apparent between PSE and two-term curvature method. As $x/c \to \infty$, $\tilde{\alpha}_0 \to 0$, $\tilde{\alpha}_0$ is getting smaller and taking this limit

$$\lim_{\tilde{\alpha}_0 \to 0} \tilde{\alpha}_1 = \frac{\kappa_C \tilde{\gamma}_0 I_3}{I_2}.$$

As $\tilde{\alpha}_0$ becomes smaller, $\tilde{\alpha}_1$ becomes larger and has a stronger impact on the total streamwise growth rate, since the viscous growth rate is negative than for larger x/c values. Due to κ_C being negative we see that the impact will cause $\tilde{\alpha}_1$ to be negative

and destabilising. We also notice that for higher crossflow effect, more curvature is needed to stabilise the disturbance. This is not surprising due to the results which were obtained earlier. Notice that if κ_C is small this implies that $\kappa(x) \ll 1$. So if the wall curvature is small, it has a large stabilising effect on the streamwise growth rate. This implies that a small amount of wall curvature is needed to stabilise the crossflow disturbance. We can improve this theory by including the viscous correction term from earlier analysis. In the absence of curvature, this impact can be observed in figure 2.28. Since α_1 has a stabilising effect on the overall growth rate, we can observe that there is an improvement on the previous method. But since $\alpha_1 > \tilde{\alpha}_1$, the main contribution corresponds to the viscous correction term.

We can apply the same technique to the travelling crossflow vortices. In figure 2.29

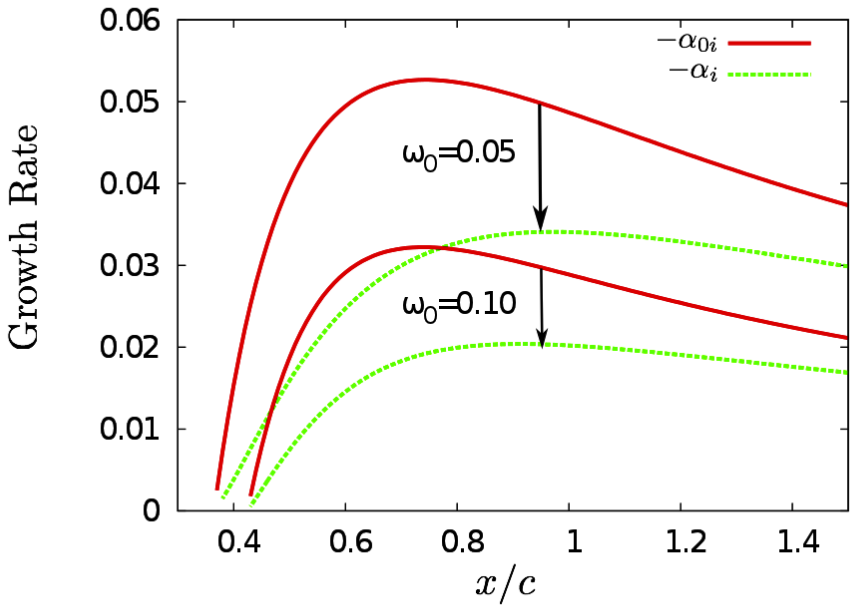

Figure 2.29: Comparison between three-term theory and inviscid growth rate in the absence of curvature at spanwise wavenumber ($\gamma_0 = 0.5$) for frequencies of $\omega_0 = 0.05$ and $\omega_0 = 0.1$.

we have a comparison with earlier, no curvature, inviscid result and three-term correction theory for two different frequencies. This was to observe the effect of the inviscid result, when the frequency increase the amount of curvature has less impact on stabilising the streamwise growth rate. The impact can be seen in figure 2.29, the same

results occur. Furthermore, Masad & Malik [59] discussed that the stabilising effect of the convex curvature on both stationary and travelling crossflow vortices increases as the distance from the leading edge increases. We can therefore verify that these results agree with what was found by Masad & Malik [59].

2.6 Conclusion

The effects of wall curvature on the stability of an incompressible three-dimensional boundary-layer over an infinitely swept wing were addressed here. We considered both stationary and travelling crossflow modes in our analysis. The disturbance equations are formulated with a fixed body curvature framework. This retains the new body curvature terms which introduce convex and concave curvature into the disturbance equations. We addressed the problem with the use of asymptotic methods and viscous theory.

Initially, we investigated this problem in the absence of curvature. The comparison between inviscid results from the stationary and travelling crossflow vortices was made. We found that the most dangerous inviscid mode was the travelling crossflow of $\omega_0 = 0.04$ - the growth rate was almost double compared with the stationary mode for a spanwise wavenumber given by $\gamma_0 = 0.4$. The theoretical procedure in question is the two-term perturbation theory. The first term corresponds to the inviscid theory from which the Rayleigh stability equation is solved and the second term is due to a solvability condition which involved matching the higher order inviscid equations with the viscous wall layer. This theory was first developed by G.S.W [39] and was was extended for a rotating disk by Hall [42].

We can apply this theory to compare results with numerical methods. The numerical methods for comparison were the parabolised stability equations (PSE) provided by Malik [58] & Mughal [63] and velocity vorticity formulation (VV) provided by Thomas [95]. The three methods seem to be in good agreement. It was expected that VV and PSE would agree since comparisons have been made before [95], [63]. There is a slight discrepancy between the two-term viscous theory and the numerical results but this can be corrected by looking at higher order terms. We also have to consider numerical error between the methods, but it seems to be in good agreement with the numerical results provided. Initially the results were for stationary crossflow vortices.

Then we applied the technique to the travelling crossflow vortices and a satisfactory agreement was also found in this case. There was a good agreement for two different Reynolds numbers $Re = 500$ and $Re = 750$ for stationary crossflow vortices and only one Reynolds number was considered $Re = 500$ for the travelling crossflow vortex.

We will now discuss the results which include curvature. The inviscid analysis predicts known results from Malik & Masad [59] when considering convex curvature. The disturbance stabilises and the opposite is true for the concave curvature. In particular, we considered a concave wall and observed the impact of crossflow vortices on the disturbance. This work was similar to the work of Bassom & Hall [4], who investigated the effect of crossflow vortices on the Görtler instability. They found that increasing the crossflow strength has a stabilising effect on the Görtler vortices. For the dispersion relation of streamwise growth rate and spanwise wavenumbers, as the crossflow increased, two unstable regions of spanwise wavenumbers developed corresponding to streamwise growth rates. One close to the origin for small spanwise wavenumbers and another for large spanwise wavenumbers. As the crossflow increased these unstable regions became smaller thus producing less unstable spanwise wavenumbers corresponding to streamwise growth rates. A similar result was found in our inviscid theory in that for small concave curvature, the crossflow had a stabilising effect on the disturbance.

Furthermore, we investigated the situation of convex curvature and its impact on travelling crossflow vortices. The interest was to see if there was control of the streamwise growth rates with different curvature variations. Small convex curvature had a stabilising effect on small frequencies. However, this was not the case for larger frequencies, as the curvature had a destabilising effect on the disturbance. Interestingly Malik & Masad [59] discovered for a small convex curvature, as the frequency increased, the curvature had a less stabilising effect on the overall growth rate of the crossflow mode. By observing the dispersion relation for two different frequencies, we noticed that for a small amount of convex curvature, all spanwise wavenumbers $\gamma_0 \geq 0.2$ for a moderate frequency, $\omega_0 = 0.05$, are unstable whereas for a larger frequency of $\omega_0 = 0.1$ all spanwise wavenumbers $\gamma_0 \geq 0.4$ are unstable. Also we note that a larger convex curvature is needed to stabilise for larger frequency. Since small amounts of curvature was needed to stabilise the stationary crossflow vortex, we performed an asymptotic

expansion in terms of κ_C. From this we used two-term correction and compared with the inviscid curvature results. We found that there was good agreement between the two methods. The curvature method breaks down when the streamwise growth rate wavenumber or the spanwise wavenumber are small and when the spanwise wavenumber is large. This is due to the curvature correction terms becoming highly stabilising within these regions.

We used the curvature perturbation theory to compare with results form PSE method with appropriate changes to the base flow. In general there was initially adequate consistency between the two methods of the two-term curvature theory and PSE but for larger x/c there was a large disagreement. The only discrepancy, other than small numerical errors, occurs when the inviscid streamwise wavenumber tends to zero. This causes the curvature correction term to get larger and have more of a stabilising impact on the overall streamwise growth rate. Adding the viscous term from earlier analysis has a stabilising impact. This new three-term viscous method predicts the disturbance characteristics well and has an improved correction than the two-term curvature method. The travelling mode was also included in this analysis. We compared this to the inviscid analysis for two different frequencies of $\omega_0 = 0.05$ and $\omega_0 = 0.1$. From this comparison we noticed a small convex curvature had a more stabilising effect on the smaller $\omega_0 = 0.05$ frequency than the larger frequency $\omega_0 = 0.1$. No numerical comparison was found for this example but this demonstrates the essence of the results from Malik & Masad [59]. Hence, this suggests that as the frequency increases, more convex curvature is needed to stabilise the disturbance.

Chapter 3

Receptivity Theory of Crossflow Vortices with Surface Curvature Variations and Plasma Actuators.

3.1 Introduction

Morkovin [62] suggested that a mechanism called receptivity might be important when considering surface variations and boundary layers. This mechanism consists of external disturbances penetrating the boundary-layer and converting them into internal instability waves. Numerous disturbances can occur via this process in a two-dimensional or three-dimensional framework. It is important to understand how these instabilities initially evolve. The first theoretical investigation was performed by Ruban [84] and Goldstein [34]. They found that the production of a T-S instability wave could be achieved via streamwise variations in surface geometry coupled with the external acoustic waves. However this study was for a two-dimensional instability - the receptivity mechanism is different for a three-dimensional disturbance such as a crossflow vortex. One of the more recent attempts to understand crossflow receptivity was undertaken by Choudhari & Streett [16]. A method was developed to solve the receptivity problem by introducing a parallel set of equations within the vicinity of the surface and is called Finite Reynolds Number Theory (FRNT). Therefore, using this method, a vast number of problems can be solved for receptivity involving curvature [19], localised surface roughness and vortical disturbances. We will try and understand the effects of

wall curvature on the receptivity of crossflow vortices in this chapter.

3.2 Formulation

The amplitude of the crossflow instability is scaled linearly with the height of the surface roughness. The main feature of the stationary crossflow receptivity problem is that the surface roughness can directly excite the crossflow mode. This is completely different than for TS-waves which are excited via surface vibrations. The crossflow receptivity occurs within a thin viscous sublayer close to the surface. However the crossflow instabilities are concentrated near the main part of the boundary layer and are predominately inviscid. This theory was originally developed by Smith [92] in the context of a hump in a two-dimensional boundary-layer. There are two distinct regions along the normal, an inviscid region and a viscous sublayer. The disturbance has its largest amplitude with the thin viscous layer (with a thickness $\mathcal{O}(Re^{-1/3})$). This region is strongly influenced by viscous diffusion of vorticity away from the surface. The region above this subregion corresponds to the main part of the boundary-layer. Within this region the disturbance is mainly inviscid and is weaker. There is an interesting condition regarding the viscous sublayer, it completely absorbs vertical velocity fluctuations caused by the surface deviations. Therefore the outer region is practically undisplaced due to the viscous sublayer absorbing the displacements. This process causes the displacement of the flow by surface roughness into a velocity flux. This then forces the motion in the outer region and excites the eigenmodes of this region which are the inviscid crossflow modes.

We are investigating the effect of both convex and concave curvature on receptivity of crossflow vortices. In view of this, we use the same body-fitted Navier-Stokes equations and continuity equation as shown in equations (2.3). Crossflow vortices are an inviscid instability so for our receptivity analysis we will start with inviscid modes. Also note we will continue to use the same basic flow; the swept Hiemenz flow. We restrict the disturbance to a periodic one in z and t. Therefore we can Fourier transform the spanwise coordinate and perform a Laplace transform in time. Therefore we can formulate a periodic disturbance in the following way

$$Q(x, y, z, t) = \tilde{Q}(x, y)e^{i\gamma z - i\omega t} + c.c, \tag{3.1}$$

where $c.c.$ means complex conjugate, $\tilde{Q} = (U, V, W, P)$, γ is the spanwise wavenumber and ω is the frequency of the disturbance. With $\tilde{Q}$ denoting the Fourier-Laplace transform in z and t respectively. We seek solutions of the form

$$\tilde{Q}(x, y) = \tilde{Q}_0(x, y) + \kappa_C \tilde{Q}_1(x, y) + \cdots , \tag{3.2}$$

with the small parameter $\kappa_C \ll 1$. Since our interest lies with the impact of curvature and its effect on receptivity, we consider an asymptotic expansion of this form for our analysis. Since we are only concerned with disturbance that amplify downstream $x \to \infty$ we need to perform a Laplace transform for the streamwise coordinate. We can solve for $\tilde{Q}$ by using a Laplace transform of

$$q(y; \alpha) = \int_0^\infty \tilde{Q}(x, y) e^{-i\alpha x} d\bar{\alpha}. \tag{3.3}$$

We are interested in spatial instability hence we expand the streamwise wavenumber, α, as

$$\alpha \;\; = \;\; \alpha_F + \kappa_C \alpha_C + \cdots , \tag{3.4}$$

where α_F corresponds to the flat surface eigenvalue and α_C corresponds to the surface curvature eigenvalue. For the inviscid region we can expand u, v, w, p as

$$\begin{aligned} u &= u_0(y) + \kappa_C u_1(y) + \cdots , \quad v = v_0(y) + \kappa_C u_1(y) + \cdots , \\ w &= w_0(y) + \kappa_C u_1(y) + \cdots , \quad p = p_0(y) + \kappa_C u_1(y) + \cdots . \end{aligned} \tag{3.5}$$

Hence by eliminating p_0 and rearranging for v_0, we obtain

$$\overline{U}_B[{v_F}'' - {\beta_F}^2 v_F] - \overline{U}_B'' v_F = 0. \tag{3.6}$$

with

$$\overline{U}_B = -\omega + i\alpha_F u_b + \gamma w_b \text{ and } {\beta_F}^2 = -{\alpha_F}^2 + \gamma^2. \tag{3.7}$$

This is the stationary form of Rayleigh's equation and it governs the crossflow vortex in the boundary layer. We have boundary conditions of

$$v_F(0) = \overline{\mathcal{H}}(\alpha_F, \gamma), \quad v_F(\infty) = 0. \tag{3.8}$$

The asymptotic matching condition enforces an inhomogeneous boundary condition at the surface. From this arises the crossflow disturbance because of the solution to the inhomogeneous Rayleigh stability problem. We found this equation in Chapter 2 but we have changed some of the definitions regarding our receptivity analysis with the notation "F" indicating a flat surface. We shall solve (3.6) using a fourth-order Runge-Kutta shooting technique which is subject to boundary conditions of (3.8). Relating the forcing due to the roughness element and the boundary layer response is described in terms of a coefficient (magnitude of the function) i.e. the efficiency function. It is also known as a response function.

We can express the entire model since we have used a three-dimensional formulation. We start with a roughness shape of

$$h(x) = \exp\left[\frac{-(x - x_s)^2}{2\sigma}\right]. \tag{3.9}$$

In computing theoretical predictions, the Laplace transform of the bump is required in the chordwise direction.

$$\overline{h}(\alpha) = \sqrt{\pi}\, erfc\left[\sqrt{\frac{2}{\sigma}}\,(\alpha - \sigma x_s)\right] \exp\left[\frac{1}{2\sigma}(\alpha - \sigma x_s)^2\right] \exp\left[-\frac{\sqrt{2\sigma}\, {x_s}^2}{4}\right]. \tag{3.10}$$

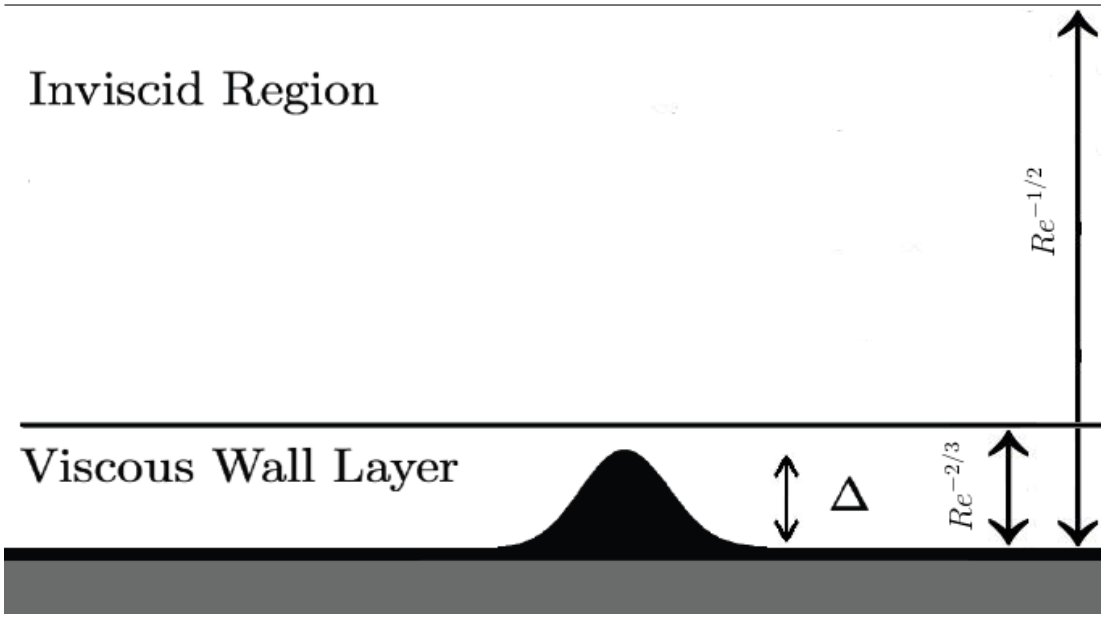

Figure 3.1

3.3 Viscous Sublayer

In the previous chapter we formulated and calculated the growth rates of these crossflow modes using asymptotic analysis. To generate this inviscid instability there needs to be an existence of surface roughness. This produces a boundary condition from the viscous sublayer to drive the crossflow instability. We know from our earlier analysis in chapter 2 that the thickness of the viscous wall layer must be of $\mathcal{O}(\epsilon^4)$. We also note that the surface roughness is contained within this layer, hence $\Delta \ll \epsilon^4$. Rescaling by $\xi = \epsilon^{-4}Y$, the base flow within the wall layer can be expanded as

$$u_b = \epsilon\overline{u_0}\xi + \cdots \text{ and } w_b = \epsilon\overline{w_0}\xi + \cdots \tag{3.11}$$

where

$$\overline{u}_0 = \frac{du_b}{d\xi}(\xi = 0) \text{ and } \overline{w}_0 = \frac{dw_b}{d\xi}(\xi = 0) \tag{3.12}$$

are the slopes at the wall of the velocity profiles of the boundary-layer flow as it approaches the hump and this is calculated via a Taylor expansion. The other components of the base flow v_b and w_b can be expanded in a similar way.

The disturbance velocities and pressure are formulated by

$$\begin{aligned}(u,v,w,p) \quad &= \\ (U_0(\xi)+\epsilon U_1(\xi) \quad &, \epsilon V_0(\xi)+\epsilon^2 V_1(\xi), W_0(\xi)+\epsilon W_1(\xi), \epsilon P_0(\xi)+\epsilon^2 P_1(\xi))+\cdots .\end{aligned} \tag{3.13}$$

Within the viscous wall layer the pressure and wall normal velocity are an order of ϵ smaller than the streamwise and spanwise velocity components because they have a smaller influence. Substituting all of the new scaled disturbance velocities and pressures, and also using the rescaled base flow the leading order quantities are

$$\overline{u}_0\xi\frac{\partial U_0}{\partial x}+V_0\overline{u_0}+\overline{w}_0\xi\frac{\partial U_0}{\partial z} = -\frac{\partial P_0}{\partial x}+\frac{\partial^2 U_0}{\partial \xi^2}, \tag{3.14a}$$

$$0 = -\frac{\partial P_0}{\partial \xi}, \tag{3.14b}$$

$$\overline{u}_0\xi\frac{\partial W_0}{\partial x}+V_0\overline{w_0}+\overline{w}_0\xi\frac{\partial W_0}{\partial z} = -\frac{\partial P_0}{\partial z}+\frac{\partial^2 W_0}{\partial \xi^2}, \tag{3.14c}$$

$$\frac{\partial U_0}{\partial x}+\frac{\partial V_0}{\partial \xi}+\frac{\partial W_0}{\partial z} = 0, \tag{3.14d}$$

Subject to the following boundary conditions

$$U_0 = V_0 = W_0 = 0 \text{ at } \xi = 0 \tag{3.15}$$

$$U_0 \sim \overline{u}_0(\xi+\Delta h)+\mathcal{O}(1/\xi), \quad W_0 \sim \overline{w}_0(\xi+\Delta h)+\mathcal{O}(1/\xi) \tag{3.16}$$

and

$$U_0 \sim \overline{u}_0\xi,\ V_0 \to 0,\ W_0 \sim \overline{w}_0\xi \text{ as } x^2+z^2 \to \infty \text{ at each } \xi \tag{3.17}$$

where

$$\overline{u}_0 = \frac{du_b}{d\xi}(\xi=0) \text{ and } \overline{w}_0 = \frac{dw_b}{d\xi}(\xi=0) \tag{3.18}$$

are the slopes at the wall of the velocity profiles of the boundary-layer flow as it approaches the hump. We know from earlier analysis that the viscous sublayer produces a velocity flux condition, such that we have

$$\overline{\mathcal{H}}(\alpha_F,\gamma) = -3v_0'(0)Ai'(0)([i(\alpha_F\overline{u_0}+\gamma\overline{w_0})]^{2/3}. \tag{3.19}$$

This agrees with the result of Hall [42] (3.13).

3.4 Receptivity Analysis

The original perturbation velocity can be extracted by using

$$V(x,y,z,t) = e^{i\gamma z - i\omega t}\frac{1}{2\pi i}\int_{\Gamma} v_F(y;\alpha)e^{\alpha x}d\alpha, \tag{3.20}$$

where Γ is the inversion contour and is to the above of all singularities of v in the complex plane of α. The inverse Laplace transform integrals can be evaluated by using the residue theorem, which requires us to locate the poles of the integrand in the complex plane of α. We expect all the singularities of our integrand to be located at the eigenvalues of the original homogeneous problem. In the current problem, the Rayleigh stability equation has homogeneous boundary conditions and it can be solved without performing any further analysis. We can rewrite v in terms of the individual components of the residues corresponding to the complete perturbation form (Goldstein [34]) connecting the initial eigenmode to the forced disturbance. Hence (3.20) becomes,

$$V(x,y,z,t) = \frac{1}{2\pi i}\int_{\Gamma} v_F(\alpha;y)\Lambda(\alpha)\bar{h}(\alpha)e^{\alpha x}e^{i(\gamma z-\omega t)}d\alpha, \tag{3.21}$$

where $\bar{h}(\alpha)$ is the Laplace transform of the roughness bump $h(x)$ and $\Lambda(\alpha)$ is denoted as the response function which is given by $\Lambda(\alpha) = |v_F(\alpha;y)|_{\text{MAX}}/\bar{h}(\alpha)$. Note that causality must be considered since we have to be careful of the contour Γ to integrate over. Without any rigorous analysis, the crossflow vortex is assumed to be convective in nature [7], [10]. This assumption has been used by several researchers [14],[21], [19] and applied to Finite Reynolds Number Theory (FRNT). The assumption implies that the contribution of the integral to a particular crossflow mode is given by the residue of the integrand. Problems arise when we have non-homogeneous boundary conditions for a linear eigenvalue problem. From simple examples we can show that the solution to these sets of problems produces a singular solution within the eigenvalue spectrum, this results in solutions blowing up. This motivates us to find a solution to the equation

in the form

$$v_F(y;\alpha) = \frac{1}{\alpha - \alpha_F} v_0(y) + v_1(y) + \cdots \quad \text{as} \quad \alpha \to \alpha_F, \tag{3.22}$$

where α_F is the homogeneous eigenvalue, a solution to (3.6). The eigenmode responses are given by the residues at the poles of the function

$$(v_0(\alpha, y) + \epsilon v_1(\alpha, y) + ...)e^{i\alpha_F x}. \tag{3.23}$$

Since the Rayleigh Stability Equation (RSE) coincides with poles from above then RSE has a simple pole at $\alpha = \alpha_F$. This can be evaluated by $\theta = \alpha - \alpha_F$, $\alpha = \alpha_F + \theta$. Hence,

$$Lv_0 + \theta L v_1 = \theta[2\alpha_0 v_0 + u_b''/u_b] = \theta R_F(v_0) + \mathcal{O}(\theta^2), \tag{3.24}$$

with $L = \frac{d^2}{d\zeta^2} - \beta^2 - \frac{\overline{U}_B{}''}{\overline{U}_B}$ (this operator can be found in (3.6) and the effective baseflow can be located in (3.7)) and

$$v_0(0) + \theta v_1(0) = 0 + \theta v_0'(0)\overline{h} = 0 + \theta S_F \tag{3.25}$$

We have divided by $\overline{U}_B$ to obtain the Rayleigh stability equation in self-adjoint form hence, $L = L_{SA}$. Therefore (3.24) reduces to

$$Lv_0 = 0 \quad v_0(0) = v_0(\infty) = 0 \tag{3.26}$$

$$Lv_1 = R_F(v_0) \quad v_1(0) = S_F, \quad v_1(\infty) = 0 \tag{3.27}$$

where $S_F = v_0(0)\overline{h}$. The eigenvalue problem of (3.27) only exists if a certain solvability condition is applied by the Fredholm alternative. We define the inner product as

$$< f, g >= \int_0^\infty f(x)g(x)dx \tag{3.28}$$

The solvability condition is found by assuming the solution 3.27 and using the lower order solution 3.26 such that

$$< Lv_1, v_0 >=< R_F, v_0 > . \tag{3.29}$$

Now if we integrate by parts we can obtain

$$< Lv_1, v_0 >= [{v_1}'v_0 - v_1{v_0}']_0^\infty + < v_1, Lv_0 > \tag{3.30}$$

but $< v_1, Lv_0 >= 0$ from (3.26) boundary conditions and due to the other boundary conditions we obtain

$$< Lv_1, v_0 >= v_1(0){v_0}'(0) \tag{3.31}$$

Since we have a linear eigenvalue problem with homogeneous boundary conditions we can impose $v_0 = A\hat{v_0}$. Hence, to obtain a solvability condition we need to multiply both sides by the adjoint of v_0 and by the Fredholm alternative we can impose $v_0 = \overline{A}\hat{v}_0$. Hence,

$$\overline{A}\int_0^\infty {v_1}''\hat{v}_0 - \left[{\beta_0}^2 + \frac{{\overline{U}_B}''}{\overline{U}_B}\right] v_1\hat{v}_0 d\zeta = \overline{A}^2\int_0^\infty 2\alpha_0\hat{v}_0^2 d\zeta + \int_0^\infty \left[\frac{{u_b}''}{u_b\overline{U}_B}\right]\hat{v}_0^2 d\zeta,$$

using the inner product results in,

$$\overline{A} = \frac{\int_0^\infty {v_1}''\hat{v}_0 - \left[{\beta_0}^2 + \frac{{\overline{U}_B}''}{\overline{U}_{0B}}\right] v_1\hat{v}_0 d\zeta}{\int_0^\infty 2\alpha_0\hat{v}_0^2 d\zeta + \int_0^\infty \left[\frac{{u_b}''}{u_b\overline{U}_{0B}}\right]\hat{v}_0^2 d\zeta}. \tag{3.32}$$

Therefore we obtain

$$\overline{A} = \frac{-v_1(0)\hat{v}_0'(0)}{2\alpha_0 I_1 + I_2}, \tag{3.33}$$

with

$$I_1 = \int_0^\infty \hat{v}_0^2(\zeta)d\zeta \quad \text{and} \quad I_2 = \int_0^\infty \left[\frac{{u_b}''}{u_b\overline{U}_B}\right]\hat{v}_0^2 d\zeta$$

The integral (3.20) is determined by contributions from the poles and the branch cuts of the integrand,v, which includes the singularities of the forcing function plus the discrete and continuum eigenmodes of the homogenous, steady RS problem. The wavenumber location $\alpha = \alpha_F$ corresponds to a first-order pole singularity of the integrand $v(\alpha, y)$ in (3.20). Whether the residue contribution due to this pole is relevant to upstream/downstream sides depends on whether Γ lies above $\alpha = \alpha_F$. The solution of (3.22) can be evaluated using residue calculus in the following way. Since we have a

simple pole at $\alpha = \alpha_F$, then

$$\int_\Gamma v_F(y;\alpha)e^{\alpha x} = Res(v_0, \alpha_F) = 2\pi i \lim_{\alpha\to\alpha_F} v_0({\alpha_F}^*; y)e^{\alpha_F x}. \tag{3.34}$$

Hence the physical velocity (3.6) becomes

$$V(x, y, z, t) = iK_R(\alpha_F)\bar{h}(\alpha_F)v_0(y;\alpha_F)e^{\alpha_F x}e^{i(\gamma z-\omega t)}, \tag{3.35}$$

where $K_R(\alpha_F)$ is the residue of $\Lambda(\alpha \to \alpha_F)$ with the assumption of a singularity in $\Lambda(\alpha)$ of order 1 and therefore we have

$$K_R(\alpha_F) = \lim_{\alpha\to\alpha_F} [\Lambda(\alpha)]\,. \tag{3.36}$$

This is the receptivity response function for a flat plate, where all curvature effects have been neglected. The response function describes the efficiency of the localised receptivity process and this is independent from information about the surface. We can now observe the response function over certain parameters, for instance streamwise coordinate or spanwise wavenumber. The initial crossflow amplitude can be determined from

$$A_{CF}(Re) = |\Delta K_R(\alpha_F)\bar{h}(\alpha_F)|, \tag{3.37}$$

for a certain Reynolds number, Re and with $\bar{h}$ denoting the Laplace Transform of the surface roughness. Due to the linear characteristics of (3.35) we have

$$\hat{v}_{cf}(\gamma) = \overline{\mathcal{H}}[\alpha_{cf}(\gamma), \gamma]\Lambda(\gamma) \tag{3.38}$$

where the function $\Lambda(\gamma)$ is independent of the hump geometry (i.e. it depends only on the upstream boundary-layer profiles and the wavenumber of the crossflow mode.)

3.5 Receptivity on a Flat Surface

We are going to use a test case of $\sigma = 0.1$, $\Delta = 0.1$ and $x_s = 0.3$ (refer to the roughness description in equation (3.9)) to analyse the response function. We use the same basic flow as we did in the previous chapter, swept Hiemenz flow. First we consider the response function downstream in the streamwise direction and the variation with the

spanwise wavenumber.

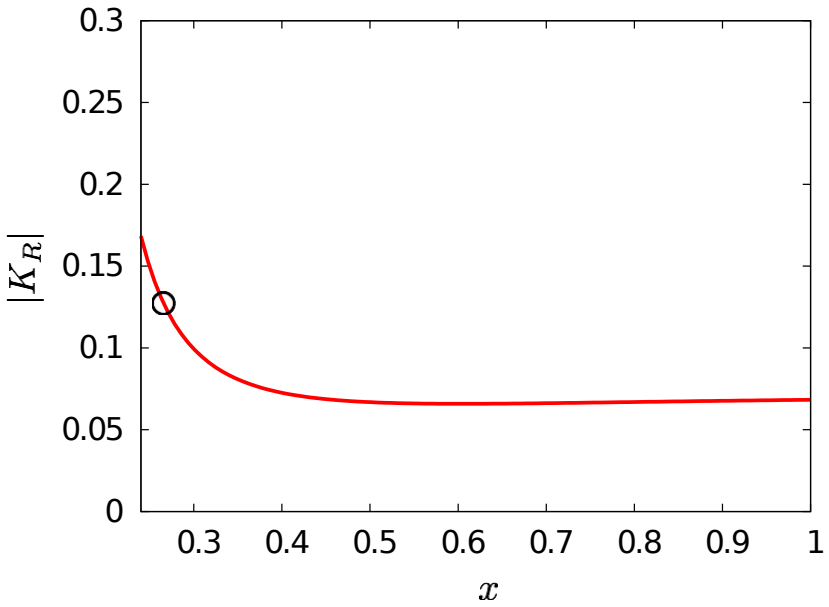

Figure 3.2: Receptivity response function, $|K_R|$, over the streamwise coordinate, x, for a stationary mode, with a spanwise wavenumber of $\gamma = 0.4$ and sweep angle of $\theta_{sw} = 45°$, with the circle referring to the neutral stability point.

We see in figure 3.2 that initially at the leading edge where $x \to 0$, the response function is largest for stationary crossflow vortices. The response function, $|K_R|$, appears to be constant as crossflow strength decreases. Schrader *et al.* [89] produced similar behaviour - the response function decreases downstream such the response function behaves $|K_R(x)| \sim 1/x$. Our response function performs in an analogous manner. As the crossflow decreases the response function decreases and tends to a constant for both stationary crossflow modes. We notice that upstream from the neutral stability point the response function increases rapidly, but this is not a problem. The streamwise growth rates decay after this point as mentioned by Schrader *et al.* [89]. Therefore we only consider analysing the receptivity of crossflow vortices downstream from the neutral stability point. Due to the three-dimensional nature of the crossflow disturbances, we consider the effect of the spanwise wavenumber with receptivity.

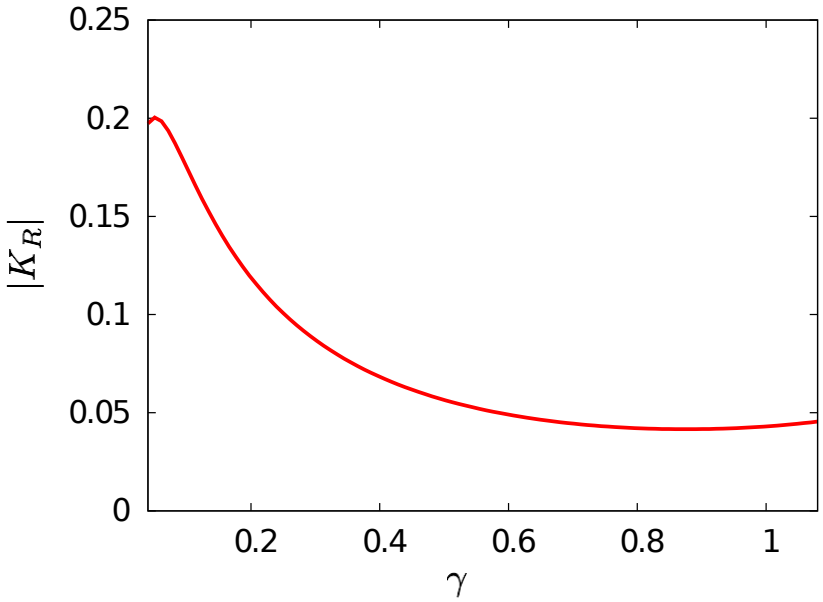

Figure 3.3: Receptivity response function, $|K_R|$, over the spanwise wavenumber, γ, for stationary modes ($x = 1.0$).

In figure 3.3 it appears that the response function is largest at $\gamma = 0.05$. Interesting behaviour occurs for small spanwise wavenumber values - we observe a large response function for small values of γ. We also note that Collis & Lele [19] showed this effect for both flat and convex curvature response functions.

3.6 Influence of surface curvature on the boundary-layer receptivity.

So far we have observed receptivity only for a flat surface. Our main interest lies with the impact of surface curvature and hence we will add the effect of convex curvature by considering $\kappa_C > 0$, for our numerical calculations we have set $\kappa_C = 0.01$. For small convex curvature. We shall perform a similar analysis compared to earlier results and start with the Rayleigh stability curvature equation (2.74). Since curvature effects are small ($\kappa_C > 0$, $\kappa_C \ll 1$) we perform an asymptotic expansion of the form

$$v = v_F + \kappa_C v_C + \cdots , \tag{3.39}$$

where v_F and v_C describe the flat and curvature velocity perturbations respectively. Substituting this expansion of (3.39) into (2.74) and collecting first order terms we have

$$v_F{}'' - \beta^2 v_F - \frac{\overline{U}_B{}''}{\overline{U}_B} v_F = 0, \tag{3.40}$$

where we impose a solution of the form

$$v_F = \frac{v_0(y)}{\alpha - \alpha_F} + v_1(y) + \cdots . \tag{3.41}$$

Now we gather terms of the next order, $\mathcal{O}(\kappa_C)$ and obtain the equation

$$v_C{}'' - \beta^2 v_C - \frac{\overline{U}_B{}''}{\overline{U}_B} v_C = \frac{\alpha u_b}{\overline{U}_B} v_F{}' - \frac{\alpha u_b \overline{U}_B{}'}{\overline{U}_B{}^2} v_F + \frac{\beta^2 u_b u_b{}'}{\overline{U}_B{}^2} v_F. \tag{3.42}$$

As with the flat surface receptivity analysis, we use a Laurent expansion in the form

$$v_C(y;\alpha) = \frac{1}{\alpha - \alpha_C} v_0(y) + v_1(y) + \cdots , \quad \text{as} \quad \alpha \to \alpha_C, \tag{3.43}$$

but when substituting this Laurent expansion of (3.43) into (3.42) we have terms of the order $1/(\alpha_C - \alpha_F)$ and we have the first order solution of the form $Lv_0 = 0$ with

$$L = \frac{d^2}{dy^2} - \alpha_C{}^2 - \gamma^2 - \frac{\overline{U}_{CB}{}''}{\overline{U}_{CB}}, \tag{3.44}$$

and

$$\overline{U}_{CB} = \alpha_C u_b + \gamma w_b - \omega. \tag{3.45}$$

We have already solved the eigenvalue problem $Lv_0 = 0$ earlier in §2.2 and obtained an eigenvalue of α_F, so the first order eigenvalue problem here must have the same eigenvalue due to the same eigenvalue problem, hence $\alpha_C \to \alpha_F$. This implies that our expansion is singular and we need a new form of the Laurent expansion. We now choose v_C of the form

$$v_C(y;\alpha) = \frac{1}{(\alpha - \alpha_F)^2} v_0(y) + \frac{1}{\alpha - \alpha_F} v_1(y) + \cdots \quad \text{as} \quad \alpha \to \alpha_F. \tag{3.46}$$

Since we had an expansion of the form

$$v = v_F + \kappa_C v_C + \cdots , \tag{3.47}$$

we want to find the combined Laurent expansion. Since we have $\alpha = \alpha_F + \kappa_C \alpha_C$ then v becomes

$$v = v_0 \left(\frac{1 + \kappa_C \left[\frac{1-\alpha_C}{\alpha - \alpha_F} \right]}{\alpha - \alpha_F - 2\kappa_C \alpha_C} \right) + O(v_n) + \cdots \quad n \geq 1. \tag{3.48}$$

This is obtained by substituting (3.46) and (3.22) into (3.47). Therefore we can calculate the value of the integrand in equation (3.20) with the residue since we have a simple pole at $\alpha = \alpha^*$, with $\alpha^* = \alpha_F + 2\kappa_C \alpha_C$, therefore the residue theorem yields

$$\int_\Gamma (v_F(y;\alpha_F) + \kappa_C v_C(y;\alpha_C)) e^{i\alpha_F x} = Res(v, \alpha^*) = 2\pi i \lim_{\alpha \to \alpha^*} v_0(\alpha^*; y). \tag{3.49}$$

Hence accounting for curvature, we see that (3.20) becomes

$$V(x, y, z, t) = iK_R(\alpha^*) \bar{h}(\alpha^*) v_0(y; \alpha^*) e^{\alpha^* x} e^{i(\gamma z - \omega t)}, \tag{3.50}$$

where $K_R(\alpha*)$ is the residue of $\Lambda(\alpha \to \alpha^*)$ and with the receptivity response function defined as

$$K_R(\alpha^*) = \lim_{\alpha \to \alpha^*} \left[\Lambda(\alpha) \right]. \tag{3.51}$$

3.6.1 Convex Curvature

We can vary this response function by changing the streamwise coordinate, x, and by the spanwise wavenumber, γ, to witness the impact of the convex curvature effects.

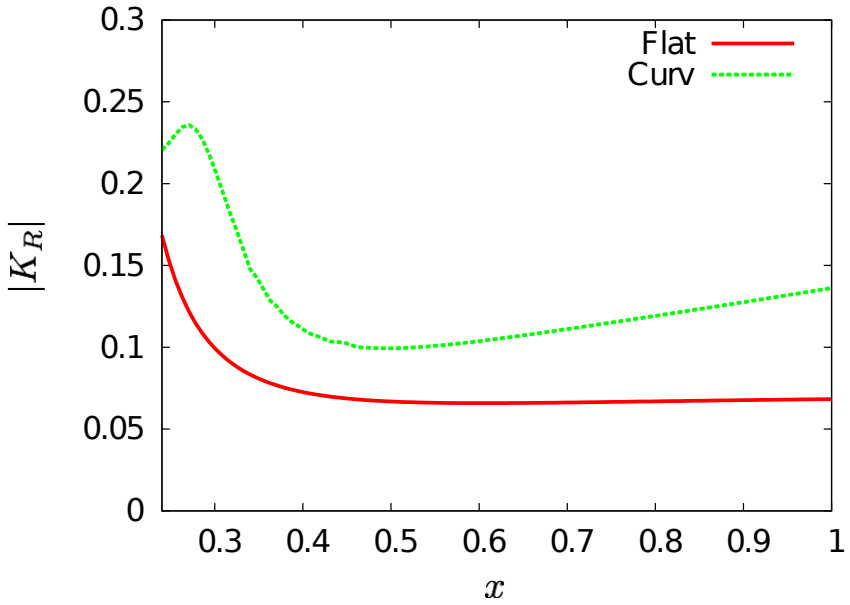

Figure 3.4: Receptivity response function, $|K_R|$, over the streamwise coordinate, x, for a stationary crossflow mode for flat and convex curvature surface with a spanwise wavenumber of $\gamma = 0.4$.

We are also interested in the spanwise wavenumber behaviour with convex curvature.

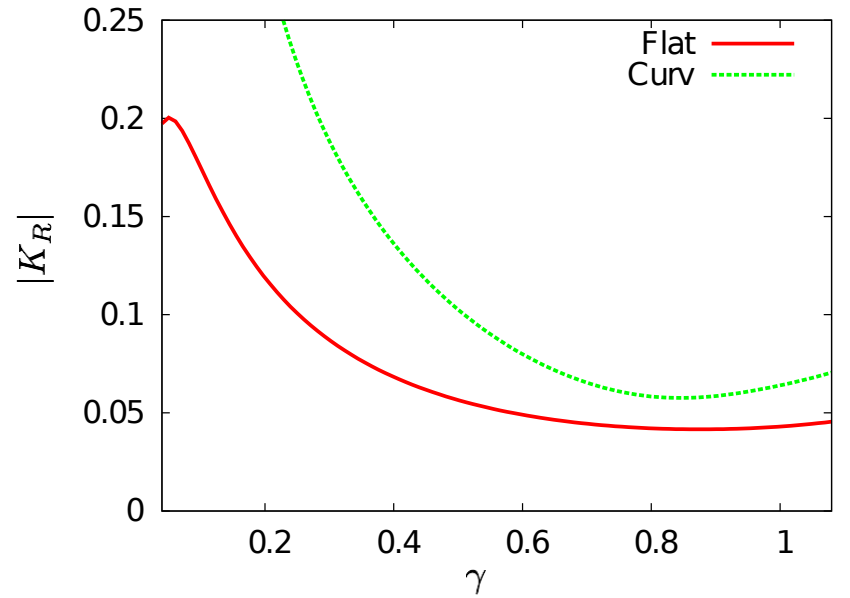

Figure 3.5: Receptivity response function, $|K_R|$, over the spanwise wavenumber, γ, for stationary crossflow modes for flat and convex surface with a streamwise coordinate of $x = 1.0$.

In figure 3.4, we notice that the response function for the flat surface, denoted by K_{RF}, is smaller than the curvature response function, denoted by K_{RC}. We see that K_{RC} is larger than K_{RF} for all values of the streamwise coordinate, x. We notice similar behaviour streamwise downstream such as both flat and convex response functions become constant. This agrees with the results from Schrader *et al.* [89]. There is a peak in the response function for the convex surface near the neutral stability point. We have taken the absolute value of the response function and x_s is situated there. It also implies that for $x = 0.3$, there is a high response from the receptivity. It is known that curvature has a stabilising effect on the disturbance (Masad & Malik[59]) since the convex curvature has a stabilizing impact on the streamwise growth rates. By adding convex curvature we can see that the response function is enhanced for large crossflow but as the crossflow strength decreases the curvature response function becomes closer to the case where curvature is absent. The convex curvature has the largest effect for the response function for high crossflow strength (small x). Hence, even though the convex curvature has a stabilising effect on the disturbance it has a larger response function than for a flat surface. This means that adding convex curvature effects makes the disturbance become more receptive, hence adding small convex curvature is a more efficient mechanism for introducing the stationary crossflow disturbance into the boundary layer. Considering the response function for both convex and flat surfaces with varying spanwise wavenumber, we observe in figure 3.5 that the curvature response function is greater than the flat response function. We witnessed this in figure 3.4. These ideas are in agreement with Collis & Lele [19] - where the convex curvature has a stabilising impact on the streamwise growth rate yet enhances the response function. This indicates that the crossflow vortices are more receptive to convex curvature than to a flat plate. In figure 3.5 for small spanwise wavenumbers the response function is significantly larger when including the effects of curvature than in the case were curvature is absent. Interestingly there is a large difference for small spanwise wavenumbers. When we consider larger spanwise numbers, this difference is smaller in comparison and is almost constant for $0.6 < \gamma < 1.0$. In fact as $\gamma \to \infty$ the difference between the response functions is $\Delta K_R \sim$ constant.

3.6.2 Concave Curvature

We now look at the effects of concave curvature ($\kappa_C < 0$) using receptivity analysis we have done so far. We will compare with the convex curvature for downstream behaviour and the variation for the spanwise wavenumbers of the response function.

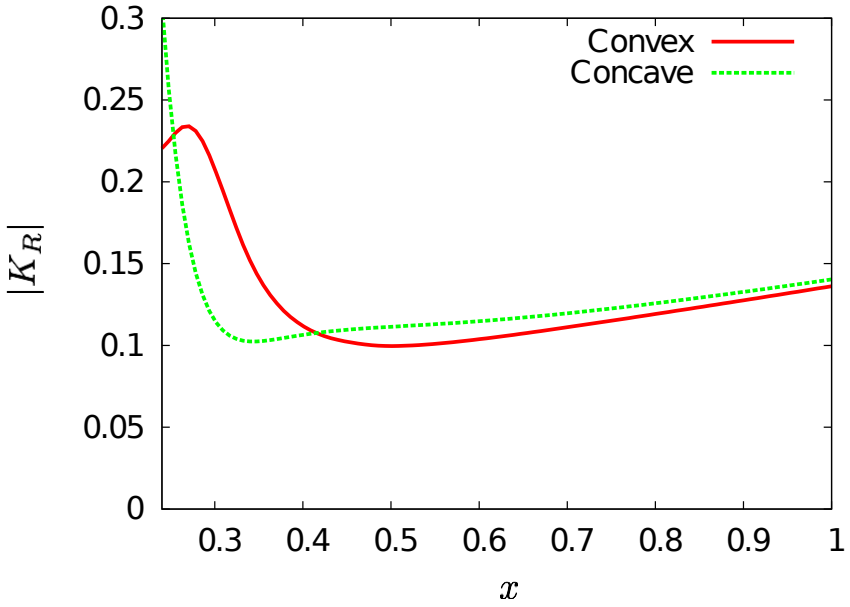

Figure 3.6: Comparing the receptivity response function, $|K_R|$, across the streamwise coordinate, x for stationary crossflow vortices with small convex and concave curvature for a spanwise wavenumber of $\gamma = 0.4$.

In figure 3.6 we see that near the leading edge the response function is largest. We also observe that the concave response function is larger near the leading edge than the convex response function. But as we move further downstream, as crossflow strength becomes smaller, the convex response function is larger than the concave response function. At $x = 0.42$ this changes, the concave response function is larger than the convex response function but we notice that the difference between the response functions reduces as we progress downstream. We notice that the concave response exhibits similar attributes to the flat and convex response functions. As the crossflow effect is reduced, the response function becomes constant. We will now turn our attention to the spanwise wavenumbers and see the impact of concave curvature.

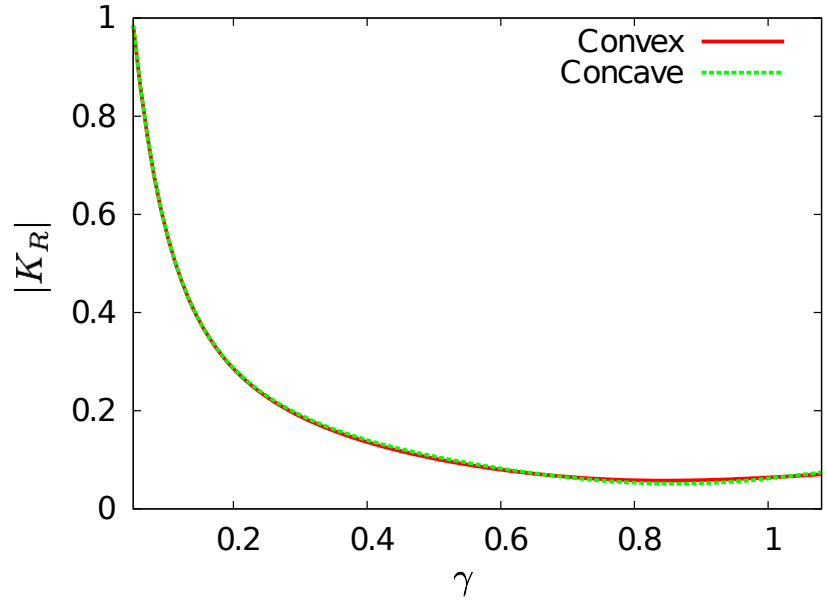

Figure 3.7: A comparison of the receptivity response function, $|K_R|$, across the spanwise wavenumber, γ, for stationary crossflow vortices for small convex and concave curvature for a streamwise coordinate of $x = 1.0$.

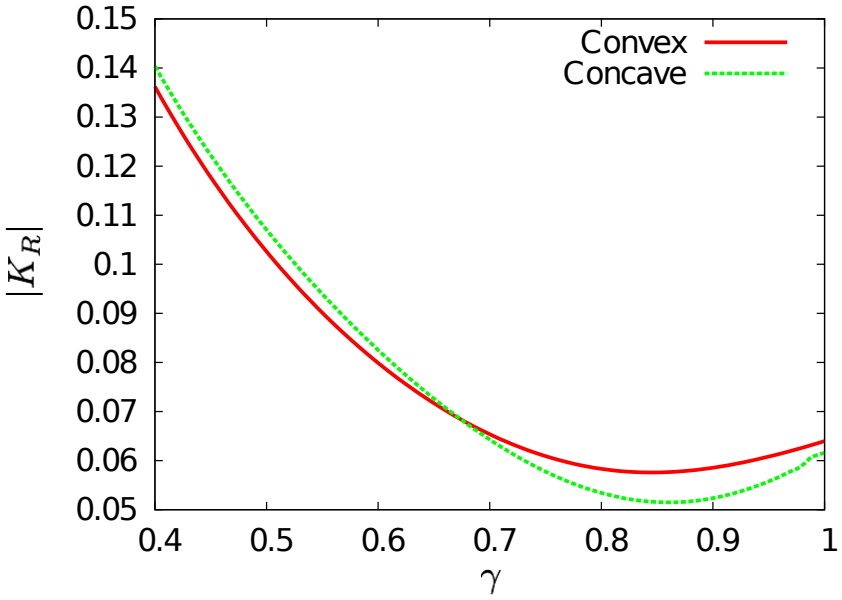

Figure 3.8: A comparison of the receptivity response function, $|K_R|$, across a reduced range of spanwise wavenumber, γ - for stationary crossflow vortices for small convex and concave curvature for a streamwise coordinate of $x = 1.0$.

The initial observation of figure 3.7 shows that there does not seem to be any difference between the two response functions. We will reduce the range in γ in the next figure. We observe the spanwise wavenumber effect in figure 3.7 and can see that the concave response function is larger than the convex response function initially. However this changes for $\gamma > 0.685$ the convex response function is larger than the concave. But we have chosen a small crossflow value ($x = 1.0$), so we would expect this type of stability characteristic based on figure 3.6. We notice the response function have similar values for this range of spanwise wavenumbers.

3.7 Receptivity of Surface Vibrations.

We next see the impact of travelling modes and apply the same analysis as seen previously. The travelling crossflow vortices are generated from the interaction of the flow over the vibrating wing with a roughness element. The vibrations considered are vertical i.e. parallel to the normal coordinate in our system. We consider the downstream behaviour and the impact of the spanwise wavenumbers of the response function with two travelling modes.

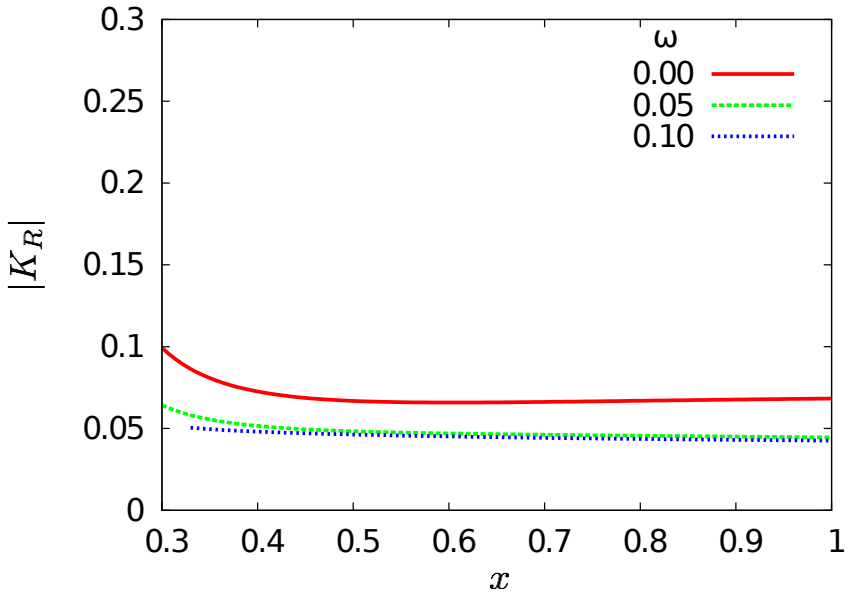

Figure 3.9: Variation of the response function, $|K_R|$, with the streamwise coordinate, x for stationary and travelling crossflow modes for a flat surface with a spanwise wavenumber of $\gamma = 0.4$.

In figure 3.9 it seems that the response function is strongest at the leading edge, as expected since the crossflow vortices are produced near the leading edge. Stationary crossflow vortices have a larger response function than any travelling one. This implies the stationary modes are more receptive that the travelling ones. This has been observed in aircraft environment data; the stationary modes dominate over the travelling modes even though they have larger initial amplitudes compared with stationary ones. By using FRNT Crouch [21] and Choudhari [17] showed this result was correct. We have only considered the impact downstream for the response function for a fixed spanwise wavenumber. Next we shall focus on a particular streamwise coordinate and vary the spanwise wavenumber to see what impact this has on the response function.

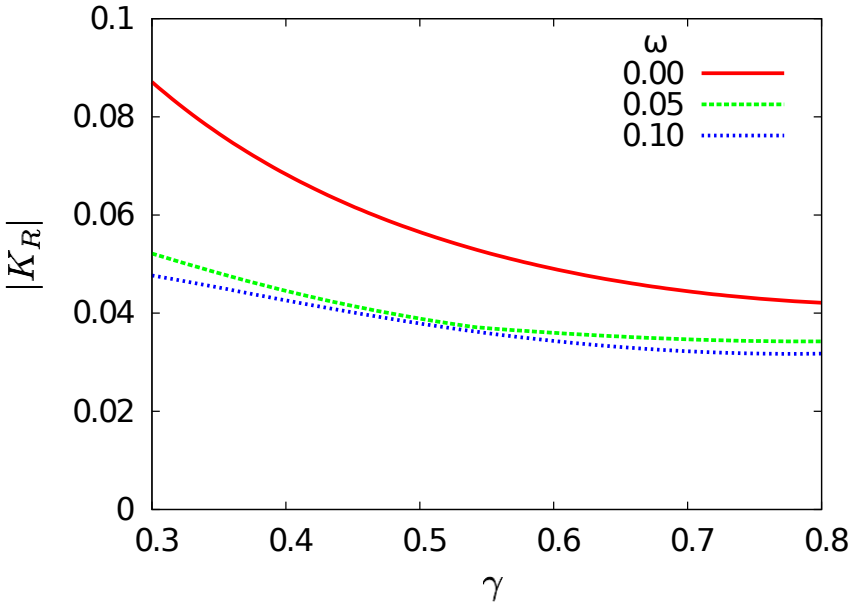

Figure 3.10: Receptivity response function, $|K_R|$, over spanwise wavenumber, γ, for stationary and travelling modes for a flat surface with a streamwise coordinate of $x = 1.0$.

In figure 3.10 it appears that the response function is largest at the smallest value of the spanwise wavenumber. Interesting behaviour occurs for small spanwise wavenumber values - we observe a large response function for small values of γ. We also note that Collis & Lele [19] showed this effect for both flat and convex curvature response functions.

The extent of unstable spanwise wavenumbers decrease as the frequency increases. We

see this effect in figure 2.16 and we are only considering the region were the streamwise growth rates are growing. We notice in figure 3.10, that the stationary crossflow vortices have a larger response function than any travelling one across the spanwise wavenumbers. The response function is largest for small spanwise wavenumbers for both stationary and travelling modes. We are interested in the effects of surface curvature and receptivity. Our analysis is extended to accommodate surface curvature in the following section.

We are interested in the travelling modes and the impact curvature has on receptivity. We analyse travelling modes at moderate frequency ($\omega = 0.05$) and at high frequency ($\omega = 0.1$), due to the intriguing behaviour at each of these modes. First we look at the downstream behaviour of the response function and we observe the impact of the response function with variations in the spanwise wavenumber. We have investigated the impact of travelling modes on a flat plate already. Next we introduce travelling modes for convex curvature receptivity.

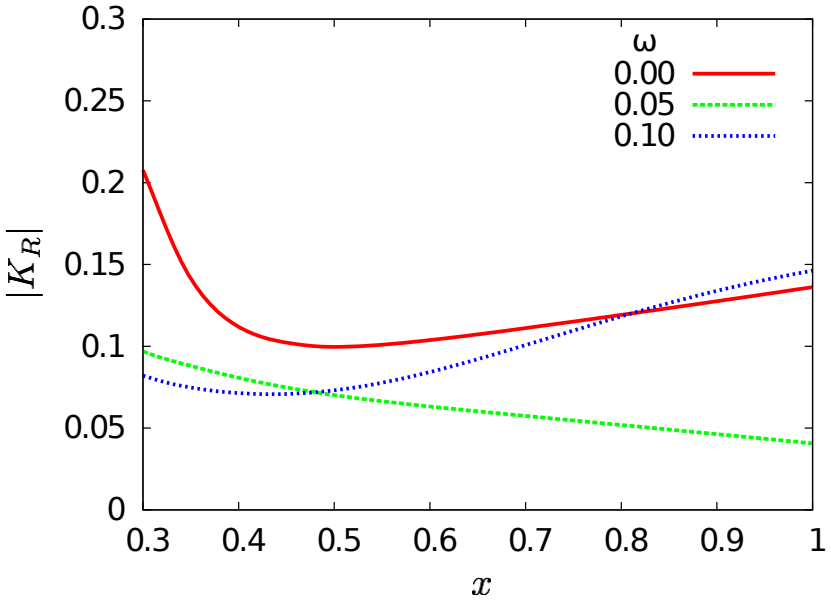

Figure 3.11: Variation of the response function, $|K_R|$, over the spanwise wavenumber, γ, for stationary and travelling crossflow modes for a convex surface with a streamwise coordinate of $x = 1.0$.

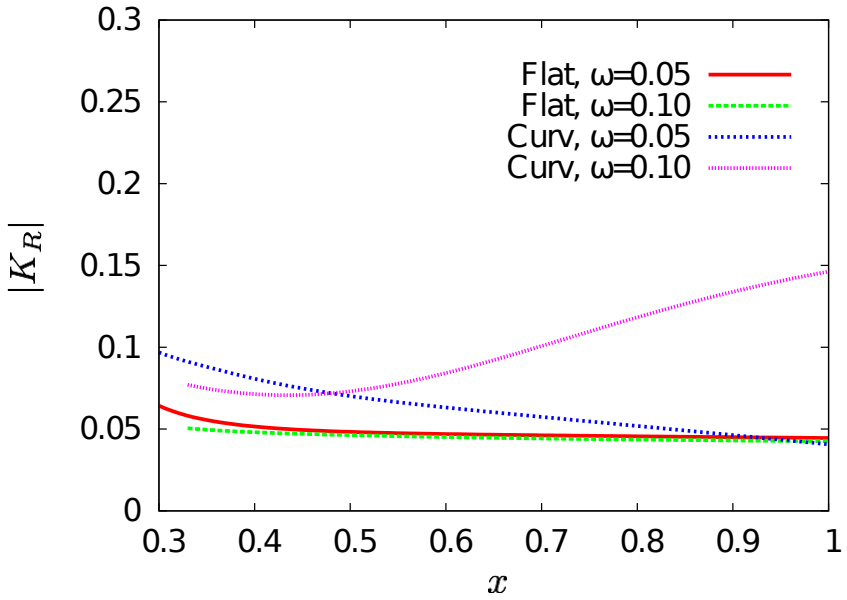

Figure 3.12: Variation of the response function, $|K_R|$, with the streamwise coordinate, x, for two different travelling crossflow modes with and without curvature with a spanwise wavenumber of γ=0.4.

Also notice that as we increase the frequency the response function decreases in figure 3.9 and figure 3.11. Initially a study by Choudhari & Streett [16] suggested that the travelling crossflow modes have larger growth rates than stationary ones but the receptivity mechanism prefers to excite the stationary crossflow vortices. Independently, the analysis performed by Crouch [21] and Choudhari [15] investigating stationary and travelling crossflow modes for receptivity verified this statement. They found that local receptivity mechanisms prefer to excite stationary modes rather than travelling ones. This is also verified here since the response function for stationary crossflow vortices is larger than for any travelling crossflow modes for a flat surface. However this is different when we analyse the response function with curvature. For moderate frequency on a convex surface the response function is always smaller than for a stationary crossflow mode. This is different when we consider higher frequencies, towards the trailing edge of the swept wing the response function is larger than for the stationary crossflow mode. Note that other travelling modes were considered here but not shown, since these two are the most important. The $\omega = 0.05$ mode is at the location of the most unstable streamwise wavenumber and thus the largest growth rate. The mode of $\omega = 0.1$

refers to a large frequency and is useful for understanding these effects.

By looking more closely at figure 3.11, we can observe that the response function asymptotes to a particular value as the streamwise coordinate is increased. As the frequency increases the curvature has less impact on the response function for moderate frequencies. We note that for a high frequency ($\omega = 0.10$), the curvature response function is larger than the flat surface response function ($K_{RC} > K_{RF}$). For moderate frequency, we notice that for high crossflow strength (smaller x) the curvature impact is largest. Whereas when the crossflow effect decreases (x increases) the impact is far less and the higher frequencies have larger response functions . It seems that the effect of convex curvature has the largest impact near the leading edge. However when the frequency is increased the response function increases due to the convex curvature, as seen in figure 3.12. We shall observe the response functions for large streamwise coordinates for stationary and travelling modes, with flat and convex surfaces.

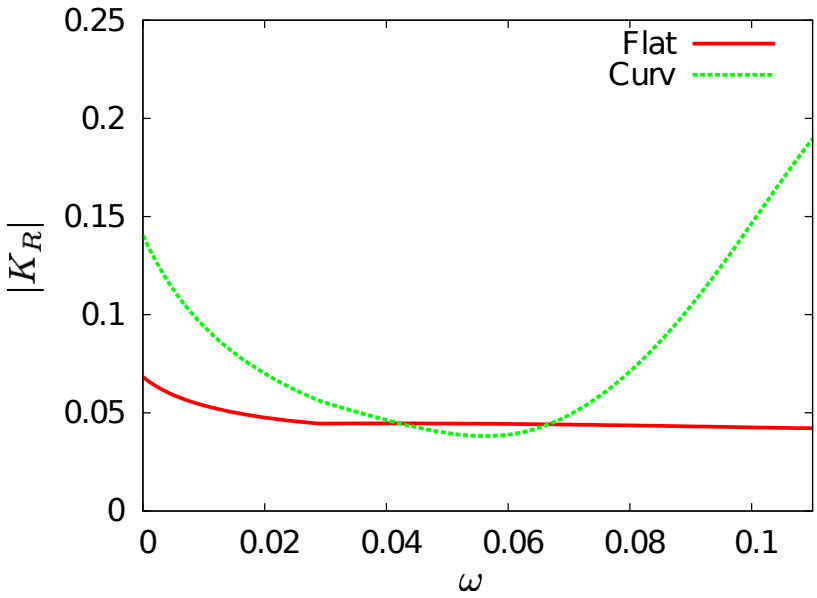

Figure 3.13: Variation of the response function, $|K_R|$, over the frequency, ω, with and without curvature for x=1.0 and γ=0.4.

Due to the interesting behaviour seen in figure 3.12, for moderate frequencies have a larger impact on the response function at high crossflow. This effect reduces when the frequency increases or the crossflow decreases. Therefore we focus on a particular streamwise position and spanwise wavenumber and observe the changes in the

response function with a varying frequency. In figure 3.13 the disparity between the response functions of the flat surface and convex curvature is large, for small frequencies. As we increase the frequency, the difference decreases and at $\omega = 0.41$, $K_{RF} > K_{RC}$ for a short range of the frequency domain. For $\omega > 0.66$, K_{RC} increases and is larger than K_{RF}. If we consider a high frequency the convex response function is larger than the flat response function. Next we focus on the effect of varying the spanwise wavenumber has on receptivity function.

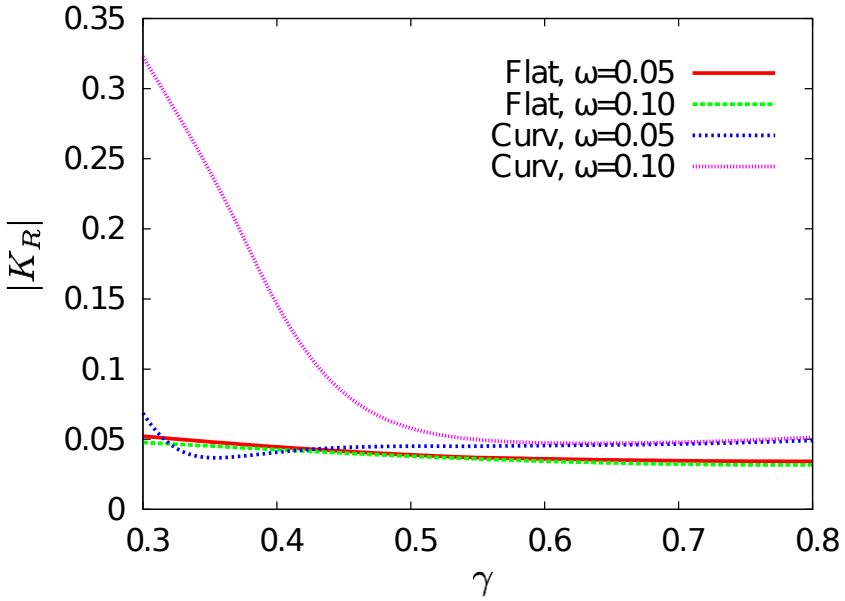

Figure 3.14: Variation of the response function, $|K_R|$, with spanwise wavenumber, γ, for travelling modes for a flat and convex surface with a streamwise coordinate of $x = 1.0$.

For small spanwise wavenumbers both flat and convex surface response functions are similar as we increase the spanwise wavenumber. The difference between the flat and convex curvature becomes very apparent for high frequency ($\omega = 0.1$) due to the disparity between them at small spanwise wavenumbers. As we increase the spanwise wavenumber the difference between all of the response functions is minor. In particular, for large γ the difference between response functions for moderate and high frequency is negligible for both a flat and convex surface. This further suggests what we stated earlier was correct that as the frequency is increased the curvature effects have less impact on the response function for a flat surface. Thus far we have only

discussed the impact of convex curvature on the response function for the travelling modes, we now turn our attention to concave surface variations. We now look at the impact concave curvature has on the response function with the travelling modes and will compare with the results obtained for convex curvature.

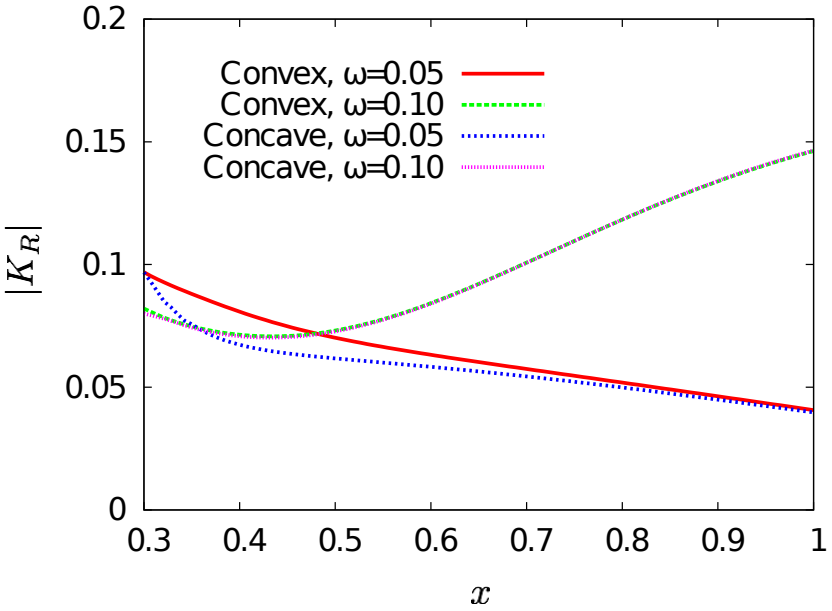

Figure 3.15: Receptivity response function, $|K_R|$, over the streamwise coordinate, x, for travelling modes comparing with convex and concave curvature for a spanwise wavenumber of $\gamma = 0.4$.

In the high frequency limit, the response functions for convex or concave curvature across all crossflow values (seen in figure 3.15) are comparable to each other as seen for larger x. There is a large impact on the response function in both convex and concave regions for large crossflow and high frequency. Therefore both convex and concave surfaces are highly receptive to high frequency crossflow modes at the trailing edge compared to a convex surface curvature.

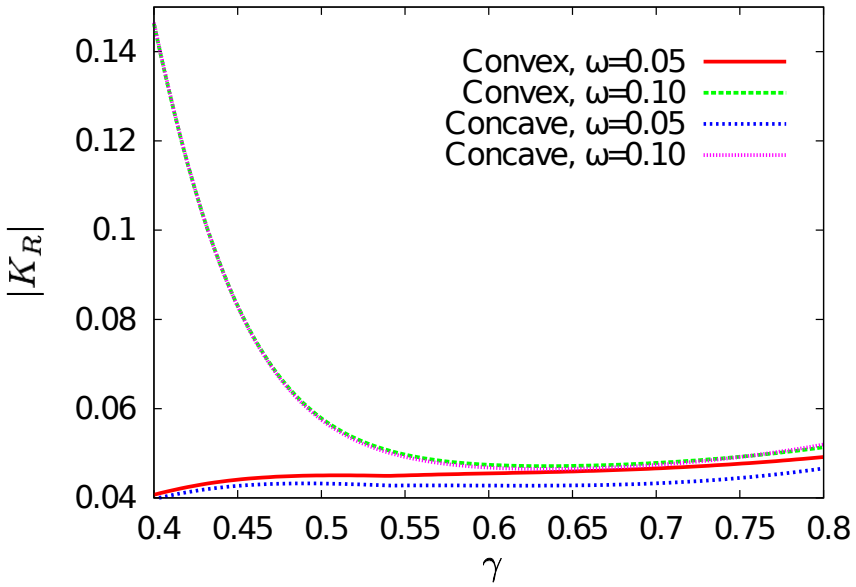

Figure 3.16: Receptivity response function, $|K_R|$, over the spanwise wavenumber, γ, for travelling modes comparing with convex and concave curvature for a streamwise coordinate of $x = 1.0$.

Observing the change in spanwise wavenumbers in figure 3.16 we see that, for large frequency, there is no change in the response function for both concave and convex surfaces. For moderate frequency, we observe for all spanwise wavenumbers within this range, that there is a noticeable difference between them. The convex response function is always larger than the concave response function. However, for larger frequencies there is a minor difference between the convex and concave response functions for all the spanwise wavenumbers within this range. Thus far we have only analysed solid roughness bumps. As mentioned in the introduction, new technologies such as plasma actuators have been used for transition control. We can extend this theory further to include plasma actuators since the analysis is similar to that of a roughness bump.

3.8 Plasma Actuators

For our device and flow consideration we are interested in the DBD plasma actuator which we will discuss shortly.

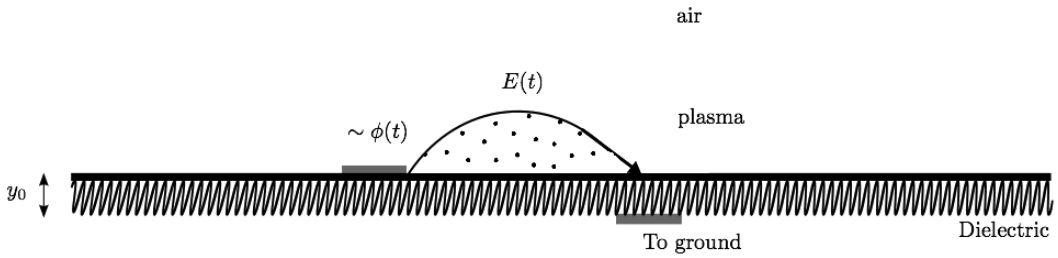

Figure 3.17: Schematic of an asymmetric single dielectric barrier plasma.

A high voltage current is applied to the electrode and this can either be a high frequency applied current or a pulsed direct current depending on certain operating requirements. This creates plasma between the two electrodes. The design of the electrodes on the swept wing can be modified to be embedded within the surface to avoid adding further roughness. The voltage and current of the electrode control the intensity, shape and width of the discharge and modify the induced velocity.

3.8.1 Fluid-Plasma Interaction

We are considering a plasma actuator in place of a roughness bump to induce crossflow vortices via a velocity flux at the leading edge of the aerofoil. Since we have a plasma which is an ionized quasi-neutral gas, we will need to consider electromagnetic effects. Following the work of Orlov [67], the representing equations for the electro-static plasma problem in general are governed by the four Maxwell equations.

For our purpose, these can be written in differential form

$$\nabla \cdot \mathbf{B} = 0, \tag{3.52}$$

$$\nabla \cdot \mathbf{E} = \frac{\rho_c}{\epsilon}, \tag{3.53}$$

$$\nabla \times \mathbf{B} = \mu_0 \left(\mathbf{J} + \epsilon_\mathbf{0} \frac{\partial \mathbf{E}}{\partial \mathbf{t}} \right), \tag{3.54}$$

$$\nabla \times \mathbf{E} = -\frac{\partial \mathbf{B}}{\partial t}, \tag{3.55}$$

where $\mathbf{B}$ is the magnetic field, $\mathbf{E}$ is the electric field, $\mathbf{J}$ is the electric current, ρ_c is the charge density and ϵ is the electric permittivity. We assume that the ion charges within the plasma have an adequate amount of time to redistribute. With this assumption in mind, we can assume that the plasma is quasi-steady. Therefore the only equation remaining is Gauss' law. Next we are interested of the interaction and movement of the different species located within the plasma. The various species involved include electrons, ions and neutral species (meta-stables). The plasma model of the species as used by Colella *et al* [18] is shown below

$$\frac{\partial n_j}{\partial t} + \nabla \cdot (n_j v_j) = \sum_k R_{jk}, \tag{3.56}$$

$$\begin{aligned} \frac{\partial m_j n_j v_j}{\partial t} + \nabla \cdot (m_j n_j v_j v_j) + \overrightarrow{\nabla}(n_j k_* T) &= q_j n_j E - \\ \sum_j R_{jk} \frac{m_j m_k}{m_j + m_k} n_{jk} \upsilon_{jk} (v_j - v_k) &+ \sum_{j|R_{jk}<0} R_{jk} m_j v_j + \sum_{j|R_{jk}>0} R_{jk} m_j v_j. \end{aligned} \tag{3.57}$$

where n is the density of the species, v is the velocity of the species, k_* is the boltzmann constant, T is the temperature of the species, m is the mass of the species, q is the charge of the species, υ the collision frequency and R is the source term. This is a generalised form for the continuity and momentum equations. The right hand side of the momentum equation include all source terms. The source terms include momentum loss terms and Lorentz force. In this model each species denoted by the index j is under the assumption of a Maxwellian distribution. These equations of (3.56) and (3.57) are solved with Maxwell equations. Due to the atmospheric pressure conditions that the plasma exists in and the ion mass is similar to neutral particles the momentum and

continuity equations can be simplified further. Thus (3.56) becomes

$$\frac{\partial n_\alpha}{\partial t} + \nabla \cdot (n_\alpha v_\alpha) = R_{c,\alpha} - R_{d,\alpha}, \tag{3.58}$$

where $\alpha = e, i$ are the subscripts for the electron and ion respectively, R_c is the ionization term sometimes called the creation term, R_d is the recombination term sometimes called the destruction term. An assumption can be made with the source terms such that a velocity distribution function can be used to estimate the ionization and recombination rates. Therefore we have

$$R_{c,\alpha} = f_c n_\alpha, \tag{3.59}$$

$$R_{d,\alpha} = f_d n_\alpha, \tag{3.60}$$

where f_c is the creation frequency and f_d is the destruction frequency. The velocities in (3.58) can be obtained from the following momentum equations

$$\frac{\partial m_\alpha n_\alpha v_\alpha}{\partial t} + \nabla \cdot (m_\alpha n_\alpha v_\alpha v_\alpha) = -\nabla P_\alpha + q_\alpha m_\alpha n_\alpha E - R_{m\alpha}, \tag{3.61}$$

where $R_{m\alpha}$ is the collisional momentum loss of the species and $P_\alpha = n_j k_* T$ is the partial pressure of the species. Due to the isotropic nature of pressure, the collisional momentum loss can be reduced to a form similar to equations (3.59) and (3.59) and yields

$$R_{m\alpha} = m_\alpha n_\alpha v_\alpha f_{m\alpha}, \tag{3.62}$$

where $f_{m\alpha}$ is the frequency of collisions. With some further manipulation (see [49]) by neglecting the electron inertia term (due to the comparison in mass with the ion) and for low pressure we obtain the following momentum and continuity equations

$$\frac{\partial n_\alpha}{\partial t} + \nabla \cdot (n_\alpha v_\alpha) = n_\alpha S_{ie} + r n_i n_e, \tag{3.63}$$

$$n_\alpha \mu_\alpha E - \nabla (n_\alpha D_\alpha) = n_\alpha v_\alpha, \tag{3.64}$$

where n is the density of the species, v is the velocity of the species, e is the electron charge, μ is the electron/ion mobility, D is the electron/ion diffusivity and S_{ie} is creation or ionization source process and r is destruction source process. Considering the

confined region of plasma, the plasma equations are non-linear and therefore are solved numerically which will consist of three stages. Firstly, the Boltzmann equation needs to be solved to gain information for different species involved. Secondly, the transport equations are solved which are given by equations of (3.63) and (3.64). Finally, the Poisson equation is solved for the electric field. The momentum equations are coupled and non-linear, and have sparse temporal and spatial scales. The time scales considered in this problem are dielectric relaxation time, electron drift, ion drift, non-linear source terms (collisions and ionization terms) and the discharge operating environment. Solving the equations of (3.63), (3.64) is the basis of the DBD model. We have considered a dielectric barrier discharge which is operating in conditions with a voltage of kV and a frequency of kHz. It produces a wall jet and creates a large isothermal surface. This device has many applications. We will consider the atmospheric aero-dynamical ones. We are considering control of the crossflow disturbance with the forcing from the DBD. We need to understand the aspects of the flow and plasma interaction. Since the flow and plasma have several molecular properties and behave like different species, the flow feels the plasma as a roughness bump. They act on different time scales, so this is why there is no flow-plasma interaction and only a body force on the flow from the plasma actuator. This is different to a solid roughness bump since we need to consider the electric field and solve the problem for the plasma situated within the DBD. We shall take a slightly different approach which is relevant to the receptivity analysis previously performed. An example of the direct solving of these equations is shown in figure 1.1. As mentioned earlier, there is a significant improvement when the plasma actuator is placed at the trailing edge.

3.8.2 Formulation of DBD model

We rewrite the variables in the following way to avoid confusion with sub/superscripts. We introduce new notation

$$n_e = \overline{n}, \quad n_i = \hat{n}, \quad S_{ie} = S, \quad \mu_e = \overline{\mu}, \quad \mu_i = \hat{\mu}, \quad D_e = \overline{D}, \quad D_i = \hat{D},$$
$$v_e = \overline{v}, \quad v_i = \hat{v}. \tag{3.65}$$

From the equations of (3.63) and (3.64) we have the following set of equations

$$\frac{\partial \overline{n}}{\partial t} + \nabla \cdot (\overline{nv}) = \overline{n}S + r\hat{n}\overline{n}, \tag{3.66}$$

$$\frac{\partial \hat{n}}{\partial t} + \nabla \cdot (\hat{n}\hat{v}) = \hat{n}S + r\hat{n}\overline{n}, \tag{3.67}$$

$$\overline{n\mu}E - \nabla(\overline{n}\overline{D}) = \overline{nv}, \tag{3.68}$$

$$\hat{n}\hat{\mu}E - \nabla(\hat{n}\hat{v}) = \hat{n}\hat{v}, \tag{3.69}$$

$$\nabla \cdot (\epsilon_d E) = \frac{e(\hat{n} - \overline{n})}{\epsilon_0}. \tag{3.70}$$

We notice that we have a nv term in both the continuity and momentum equations for both electrons and ions. We can eliminate the electron momentum equation (3.68) by taking the divergence of it and adding it to the electron continuity equation (3.66). Hence, by performing the following manipulation of (3.66) + $\nabla\cdot$ (3.68) we obtain

$$\frac{\partial \overline{n}}{\partial t} - \overline{n}S - r\overline{n}\hat{n} + \nabla \cdot (\overline{n\mu}E) - \nabla^2(\overline{n}\overline{D}) = 0.$$

We can use a similar process with the ion equations too. In doing this we get the following set of reduced equations

$$\frac{\partial \overline{n}}{\partial t} - \overline{n}S - r\overline{n}\hat{n} + \nabla \cdot (\overline{n\mu}E) - \nabla^2(\overline{n}\overline{D}) = 0, \tag{3.71}$$

$$\frac{\partial \hat{n}}{\partial t} - \hat{n}S - r\overline{n}\hat{n} + \nabla \cdot (\hat{n}\hat{\mu}E) - \nabla^2(\hat{n}\hat{D}) = 0, \tag{3.72}$$

$$\nabla \cdot (\epsilon_d E) = \frac{e(n_i - n_e)}{\epsilon_0}. \tag{3.73}$$

where ϵ_d is the dielectric constant and ϵ_0 is the permittivity value. We have to solve this set of non-linear equations numerically. We shall use a finite difference scheme, in particular the forward time space centre (FTCS) method.

3.8.3 FTCS Discretisation and Implementation

Therefore the equations of (3.71),(3.72) and (3.73) yield

$$
\begin{aligned}
\overline{n}_{i,j}^{n+1} &= \overline{n}_{i,j}^{n}(1+\Delta t(S_{i,j}^{n}+r_{i,j}^{n}\hat{n}_{ij}^{n}) - \frac{\Delta t}{2\Delta x}(\overline{n}_{i+1,j}^{n}-\overline{n}_{i-1,j}^{n})\overline{\mu}E_{i,j}^{n} \\
&- \frac{\Delta t}{2\Delta x}(E_{i+1,j}^{n}-E_{i-1,j}^{n})\overline{n}_{i,j}^{n}\overline{\mu} - \frac{\Delta t}{\Delta x}\left(\frac{1}{\Delta x}\right)(\overline{n}_{i+1,j}^{n}-2\overline{n}_{i,j}^{n}+\overline{n}_{i-1,j}^{n})\overline{D} \\
&- \frac{\Delta t}{2\Delta y}(\overline{n}_{i,j+1}^{n}-\overline{n}_{i,j-1}^{n})\overline{\mu}E_{i,j}^{n} - \frac{\Delta t}{2\Delta y}(E_{i,j+1}^{n}-E_{i,j-1}^{n})\overline{n}_{i,j}^{n}\overline{\mu} \\
&- \frac{\Delta t}{\Delta y}\left(\frac{1}{\Delta y}\right)(\overline{n}_{i,j+1}^{n}-2\overline{n}_{i,j}^{n}+\overline{n}_{i,j-1}^{n})\overline{D}, \\
\hat{n}_{i,j}^{n+1} &= \hat{n}_{i,j}^{n}(1+\Delta t(S_{i,j}^{n}+r_{i,j}^{n}\hat{n}_{i,j}^{n})) - \frac{\Delta t}{2\Delta x}(\hat{n}_{i+1,j}^{n}-\hat{n}_{i-1,j}^{n})\hat{\mu}_{i,j}^{n}E_{i,j}^{n} \\
&- \frac{\Delta t}{2\Delta x}(\hat{\mu}_{i+1,j}^{n}-\hat{\mu}_{i-1,j}^{n})\hat{n}_{i,j}^{n}E_{i,j}^{n} - \frac{\Delta t}{2\Delta x}(E_{i+1,j}^{n}-E_{i-1,j}^{n})\hat{n}_{i,j}^{n}\hat{\mu}_{i,j}^{n} \\
&- \frac{\Delta t}{\Delta x}\left(\frac{1}{\Delta x}\right)(\hat{n}(i,j+1)-2\hat{n}_{i,j}^{n}+\hat{n}_{i,j-1}^{n})\hat{D} \\
&- \frac{\Delta t}{2\Delta y}(\hat{n}_{i,j+1}^{n}-\hat{n}_{i,j-1}^{n})\hat{\mu}_{i,j}^{n}E_{i,j}^{n} - \frac{\Delta t}{2\Delta y}(\hat{\mu}_{i,j+1}^{n}-\hat{\mu}_{i,j-1}^{n})\hat{n}_{i,j}^{n}E_{i,j}^{n} \\
&- \frac{\Delta t}{2\Delta y}(E_{i,j+1}^{n}-E_{i,j-1}^{n})\hat{n}_{i,j}\hat{\mu}_{i,j}^{n} - \frac{\Delta t}{\Delta y}\left(\frac{1}{\Delta y}\right)(\hat{n}_{i,j+1}^{n}-2\hat{n}_{i,j}^{n}+\hat{n}_{i,j-1}^{n})\hat{D}, \\
E_{i+1,j}^{n} &= E_{i-1,j}^{n} + \left(\frac{\Delta x e}{2\epsilon_0\epsilon_d}\right)(\hat{n}_{i,j}^{n}-\overline{n}_{i,j}^{n}) - (\frac{\Delta x}{\Delta y})(E_{i,j+1}^{n}-E_{i,j-1}^{n}),
\end{aligned}
$$

with the following parameters

$$
\begin{aligned}
e &= 1.6022\times10^{-19}\,C, \quad m_e = 9.1094\times10^{-31}\,kg, \quad \nu_{en} = 10^{12}/s, \\
k &= 1.38\times10^{-23}m^2kgs^{-2}K^{-1}, \quad \epsilon_d = 1.055F/m, \quad \epsilon_0 = 8.854\times10^{-12}F/m, \\
p &= 300.0\,\text{torr}, \quad T = 300.0K, \quad \overline{\mu} = \frac{e}{m_e\nu_{en}}\,cm^2/Vs, \quad \overline{D} = (kT/e)\overline{\mu}\,cm^2/s, \\
\hat{D} &= 500.0\,cm^2/s, \quad \hat{\mu}_{ij}^{n} = \frac{8\times10^3}{p}\left(1-8\times10^{-3}\frac{E_{ij}^{n}}{p}\right)\,cm^2/Vs \\
S_{ij}^{n} &= 4.4\times\exp\left(\frac{-14}{E_{ij}^{n}/p}\right)p\overline{\mu}E_{ij}^{n}\,/s, \quad r_{ij}^{n} = 1.09\times10^{20}T^{-9/2}\epsilon_{ij}^{n}\,m^3/s, \\
T_e &= 11,600\,K,
\end{aligned}
$$

where m_e is the electron mass, ν_{en} is the electron-neutral collision frequency, k is the Boltzmann constant, p is the bulk pressure, T is the bulk temperature, r_{ij}^{n} is the recombination coefficient and finally T_e is the electron temperature, which is nearly

uniform. These constants and variables are for helium discharge simulations. The transport and reaction properties are the same as in Jayaraman *et al* [49].

Boundary conditions

The boundary conditions are shown in the following figure We want no species (ions

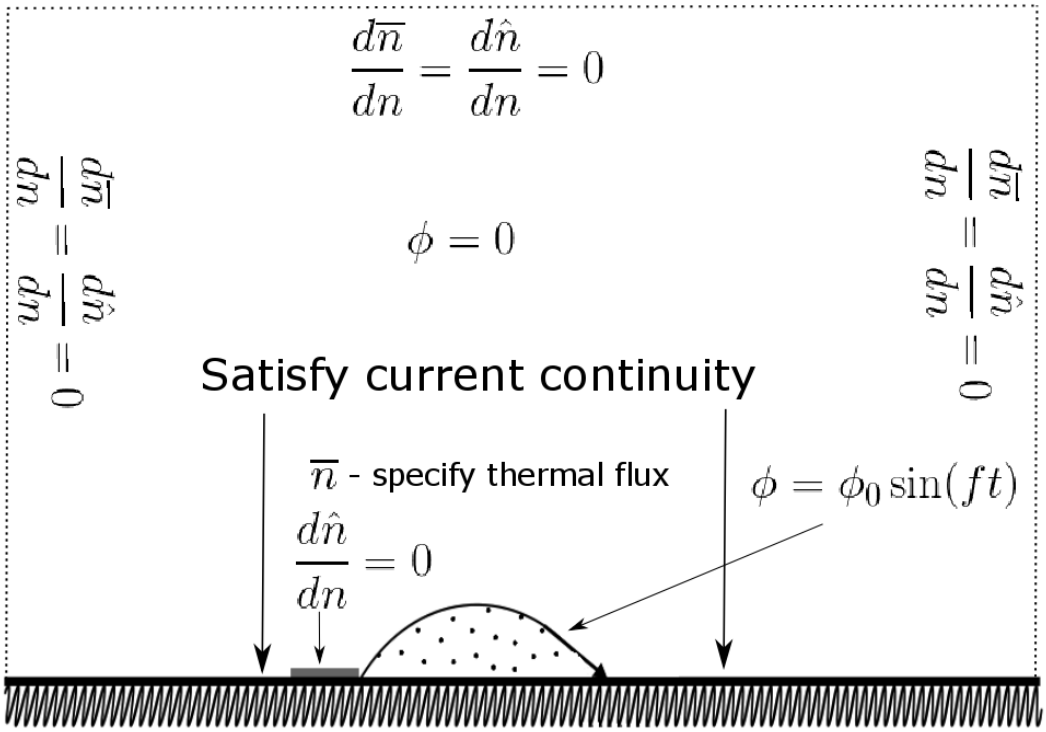

Figure 3.18: Boundary conditions for the 2D plasma actuator

or electrons) existing before the electrode, far from the electrode, nor on the interface, hence

$$\overline{n}(x, y) = \hat{n}(x, y) = 0 \quad \text{for} \quad x < x_a, y \in [0, 1] \tag{3.74}$$

where x_a is the start point location of the electrode in the streamwise direction. We want zero gradient conditions to the density, hence we see this condition in figure 3.18 such that

$$\frac{\partial \overline{n}}{\partial n} = 0. \tag{3.75}$$

We also have a no flux condition around the electrode as well

$$\left.\frac{\partial \overline{n}(x,y)}{\partial x}\right|_{x=x_a} = \left.\frac{\partial \hat{n}(x,y)}{\partial x}\right|_{x=x_a} = 0. \tag{3.76}$$

For the central difference method we have the spatial derivative for the electron defined as

$$\frac{\partial \overline{n}(x,y)}{\partial x} = \frac{\overline{n}^n_{i+1}(x,y) - \overline{n}^n_{i-1}(x,y)}{2\Delta x}.$$

This implies that the no flux condition now becomes

$$\begin{aligned} \left.\overline{n}^n_{i+1}(x,y)\right|_{x=x_a, y\in[0,1]} &= \overline{n}^n_{i-1}(x,y), \\ \left.\hat{n}^n_{i+1}(x,y)\right|_{x=x_a, y\in[0,1]} &= \hat{n}^n_{i-1}(x,y). \end{aligned} \tag{3.77}$$

Parametric Study

We start this study with the following initial conditions

$$\overline{n}^1_{x,y} = e^{-((x-m_x)^2/2+y)}, \quad \hat{n}^1_{x,y} = e^{-((x-m_x)^2/2+y)}, \quad E^1_{x,y} = e^{-((x-m_x)^2/2+y)}$$

where m_x=0.5. We progress through each time step until we reach a steady state solution. We are then interested in the initial conditions for the electric field. We consider the three initial conditions as

$$E^1_{x,y} = e^{-((x-m_x)^2/2+y/10)}, \tag{3.78}$$

$$E^1_{x,y} = e^{-((x-m_x)^2/2)}, \tag{3.79}$$

$$E^1_{x,y} = e^{-(y)}. \tag{3.80}$$

Each initial condition is marched through time until a steady state solution is found.

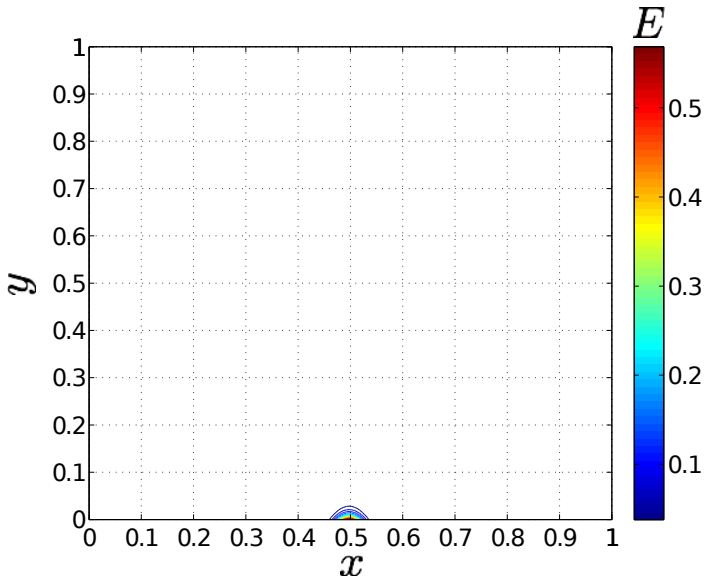

(a)

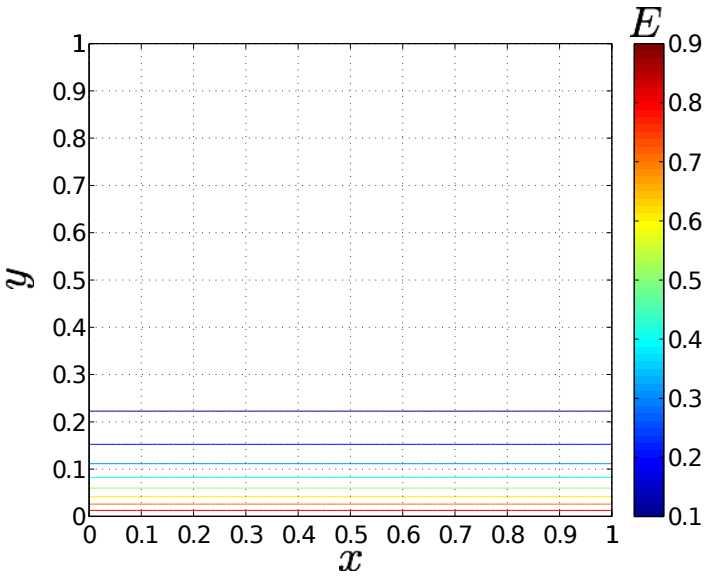

(b)

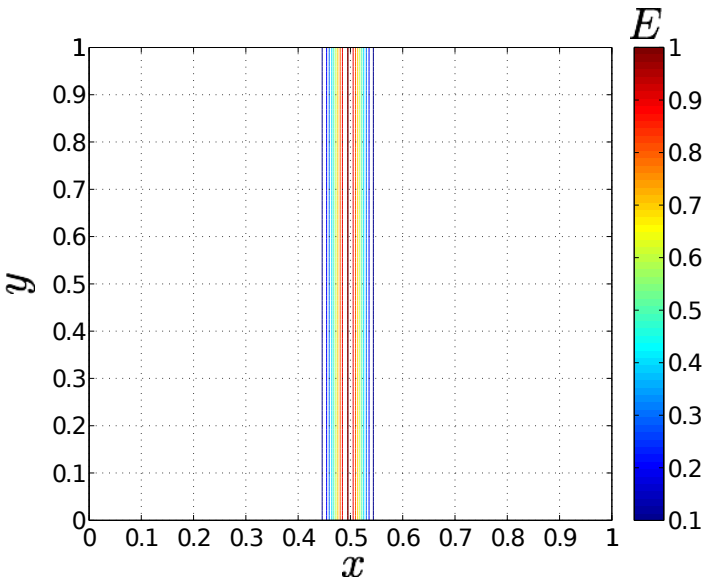

(c)

Figure 3.19: Initial electric fields for parametric study.

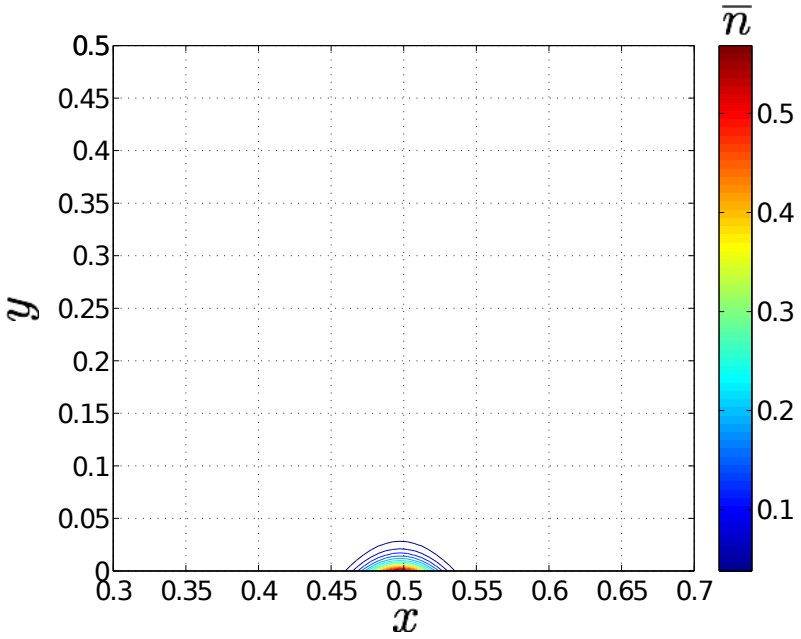

(a) Initial electron density.

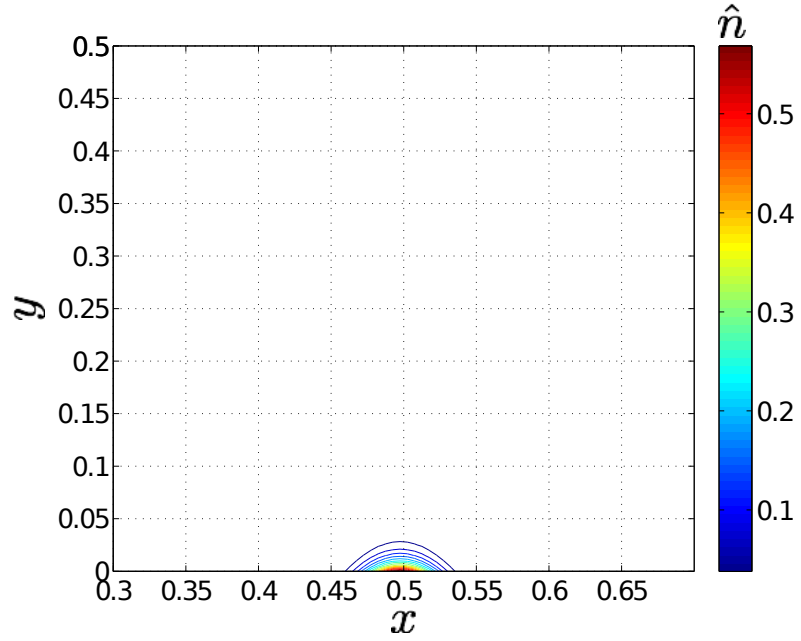

(b) Initial ion density

Figure 3.20: Initial species densities.

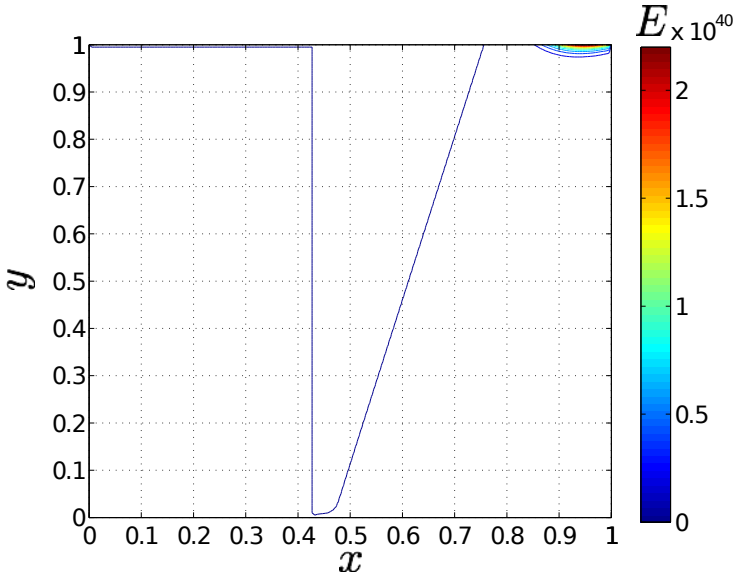

(a) t=1.0×10^{-6}.

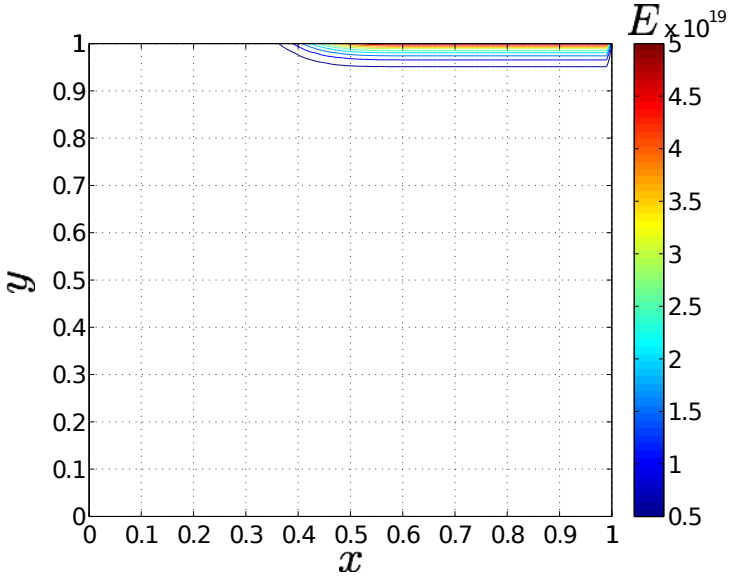

(b) t=1.0×10^{-6}.

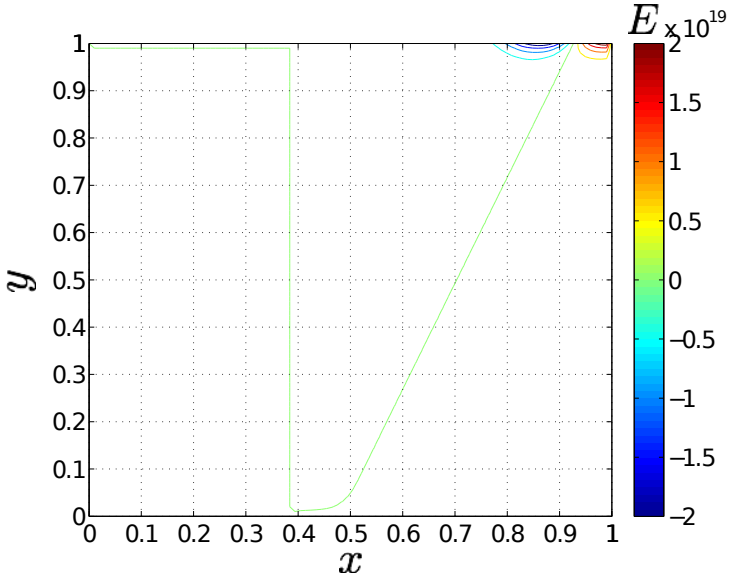

(c) t=1.0×10^{-6}.

Figure 3.21: Electric field for various initial conditions.

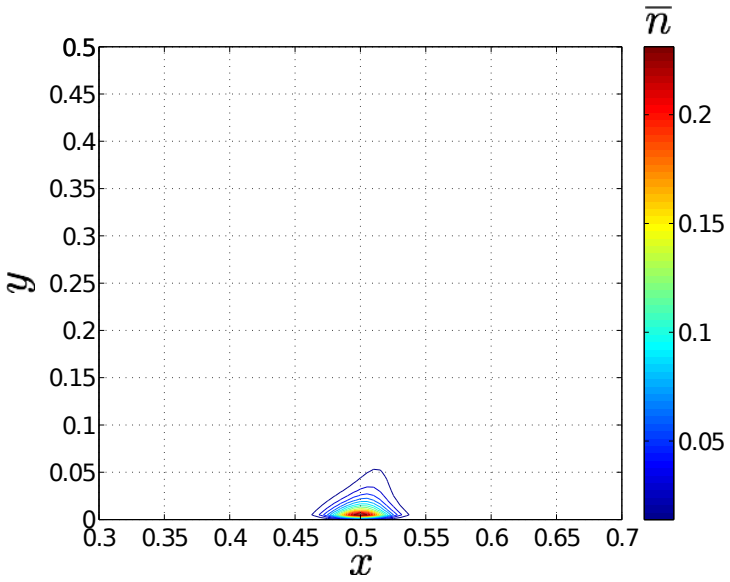

(a) t=1.0×10^{-6}.

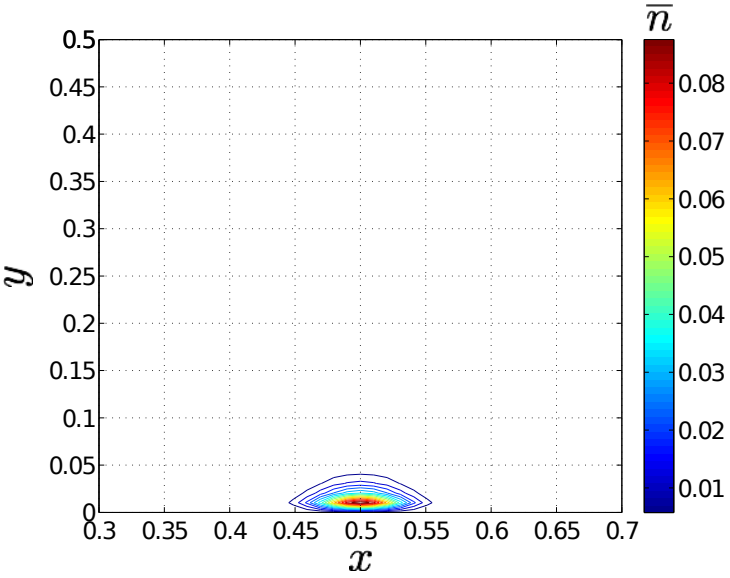

(b) t=1.0×10^{-6}.

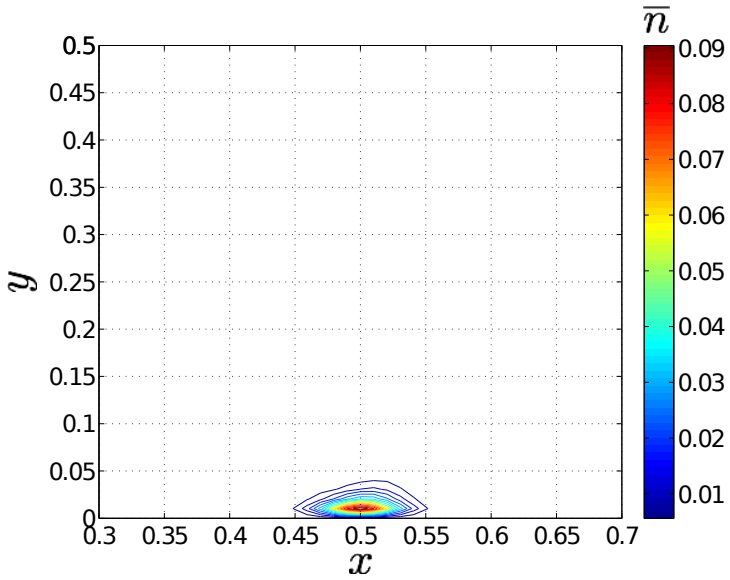

(c) t=1.0×10^{-6}.

Figure 3.22: Electron density for various initial conditions.

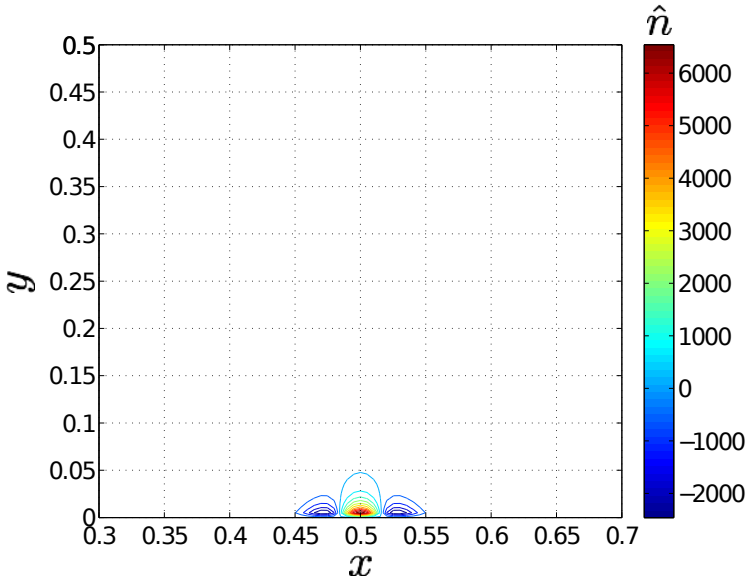

(a) t=1.0×10^{-6}.

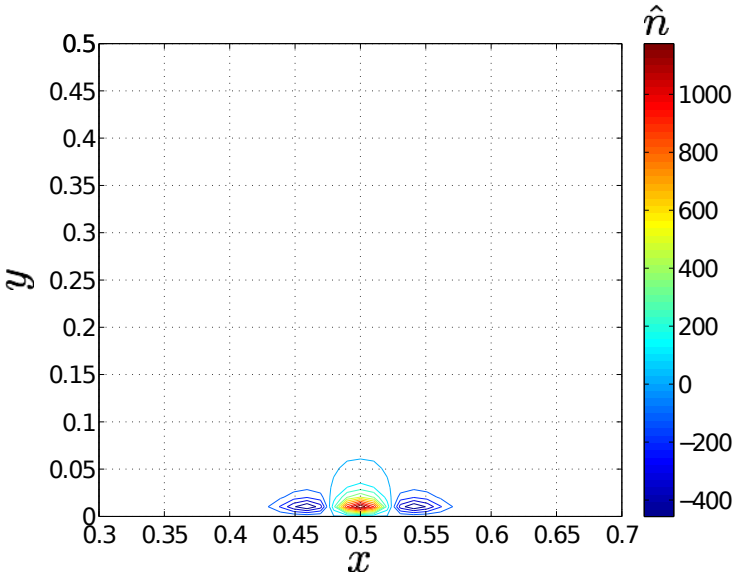

(b) t=1.0×10^{-6}.

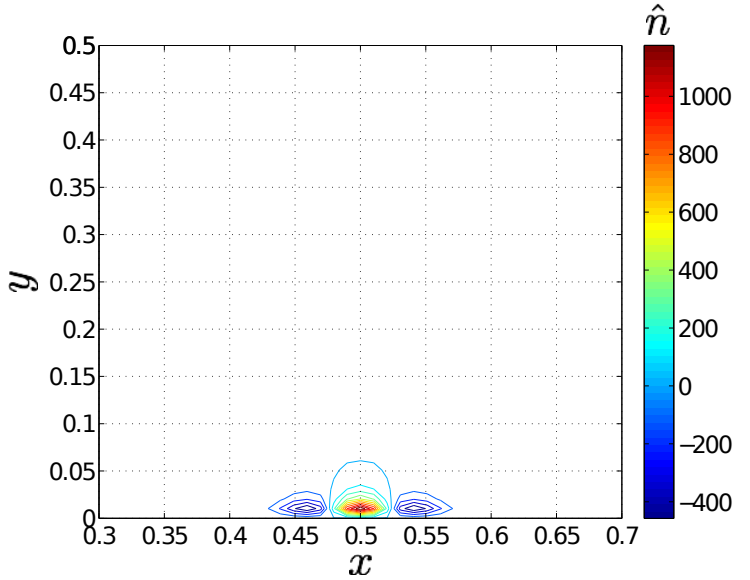

(c) t=1.0×10^{-6}.

Figure 3.23: Ion density for various initial conditions.

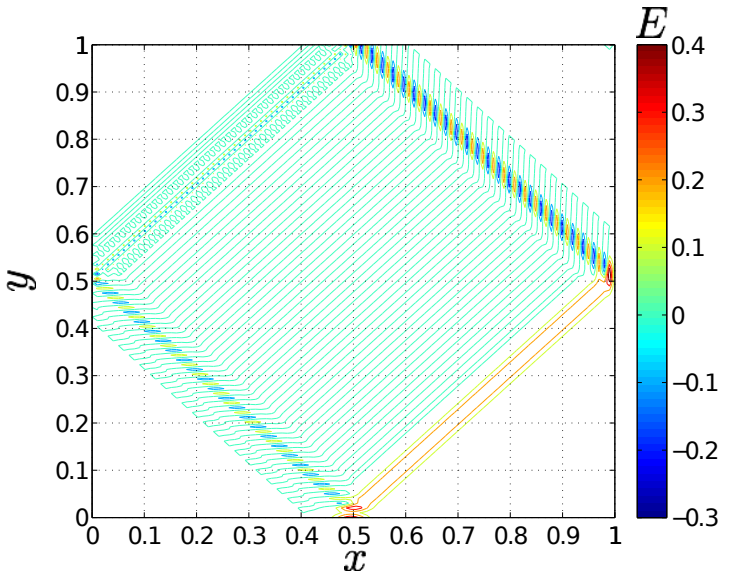

(a)

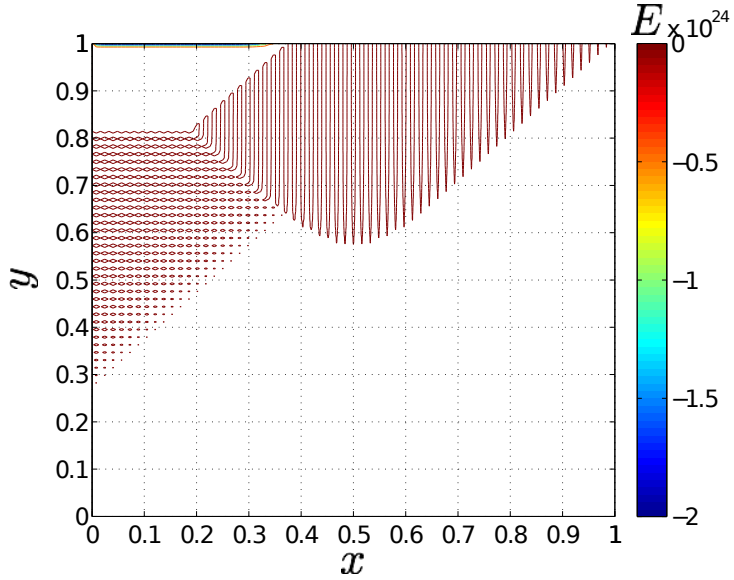

(b)

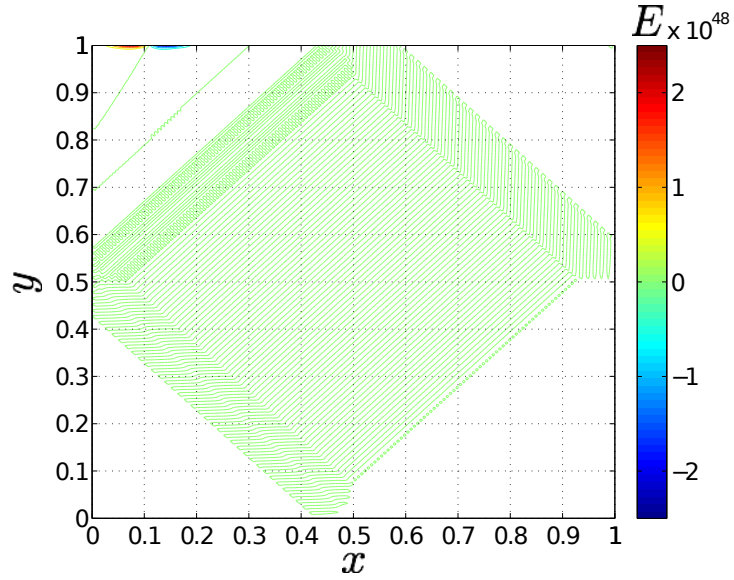

(c)

Figure 3.24: Electric field at t=5.0×10^{-5} for various initial conditions shown in figure 3.19.

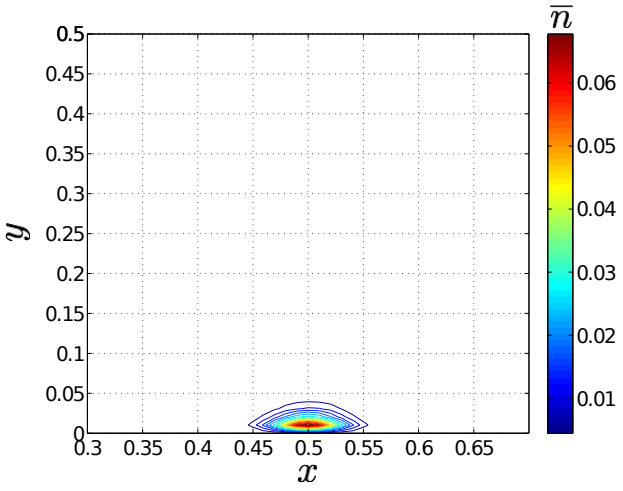

(a)

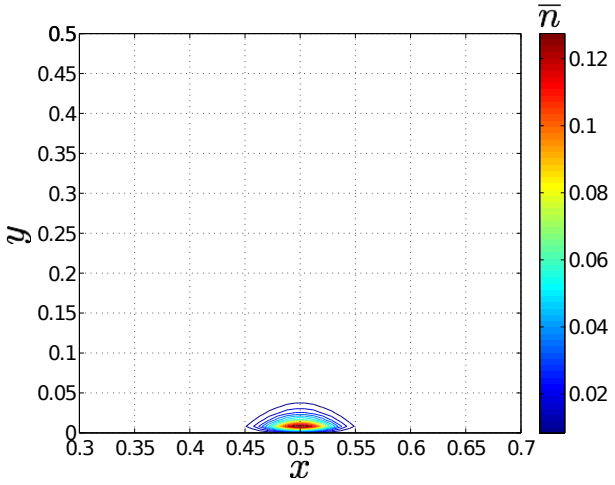

(b)

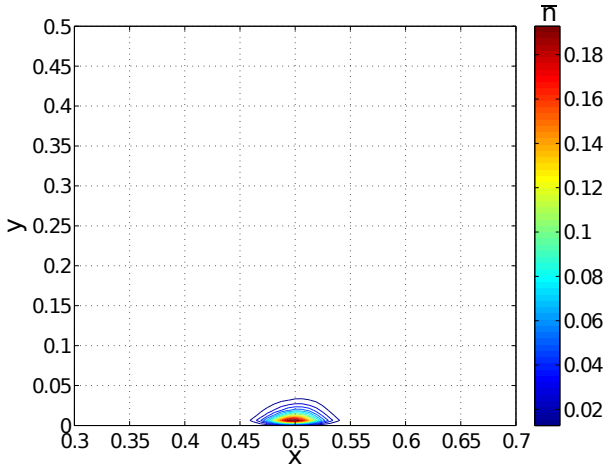

(c)

Figure 3.25: Electron density at t=5.0×10^{-5} for various initial conditions shown in figure 3.19.

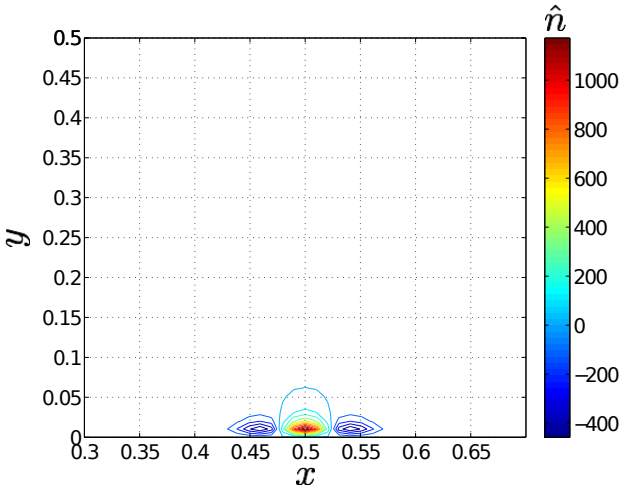

(a)

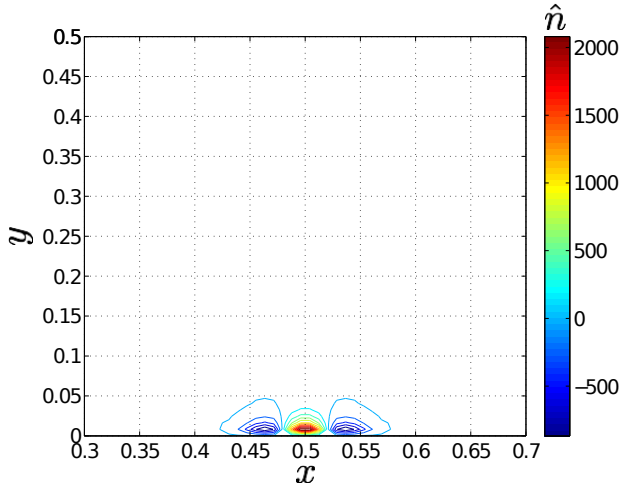

(b)

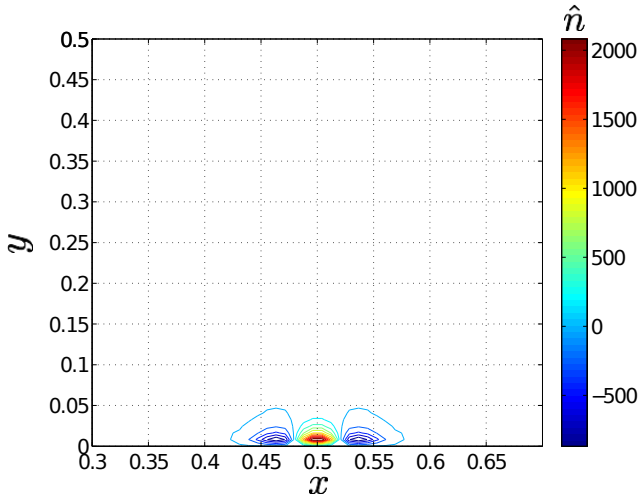

(c)

Figure 3.26: Ion density at t=5.0×10^{-5} for various initial conditions shown in figure 3.19.

In figures 3.25 and 3.26 the corresponding values have converged into a steady state solution. Convergence was obtained after 50 time steps, which is $t = 5.0 \times 10^{-5}$. In figure 3.21c we notice that the electric field is large and non uniform. But as time progresses within our calculation the undefined electric field disappears from the domain and a singularity appears. We can also observe a uniform electric field with no singularities in figure 3.24a. We will inspect changes to the initial imposed electric field. We shall monitor three cases where the electric field is concentrated near the plasma, constant in the wall normal direction, y, and constant in the streamwise coordinate, x. In figure 3.24b and figure 3.24c we see that after 100 time steps the electric field has not converged. This is worrying since we don't want a singularity to occur within the electric field because we want it to be uniform. Therefore we consider case 3 and observe what happens to the electric field after a few more time steps.

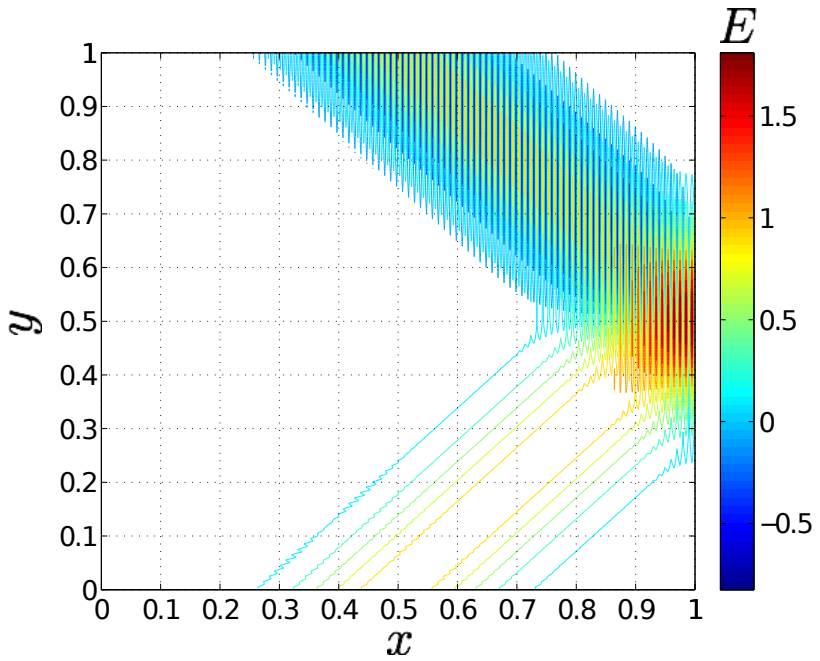

Figure 3.27: Electric field at t=1.0×10^{-3}.

In figure 3.27 the electric field has converged to a uniform field. The electric field is similar to that of figure 3.24a, which is promising. Next we look at starting with different initial conditions for the ion and electron densities. The two cases we consider are

1. $\overline{n}^1_{i,j} = e^{-((i-50)^2/100+j)}$, $\quad \mu^1_{i,j} = e^{-((i-50)^2/100+j)}$ and

2. $\overline{n}^1_{i,j} = e^{-((i-50)^2+j)}, \quad \mu^1_{i,j} = e^{-((i-50)^2+j)}.$

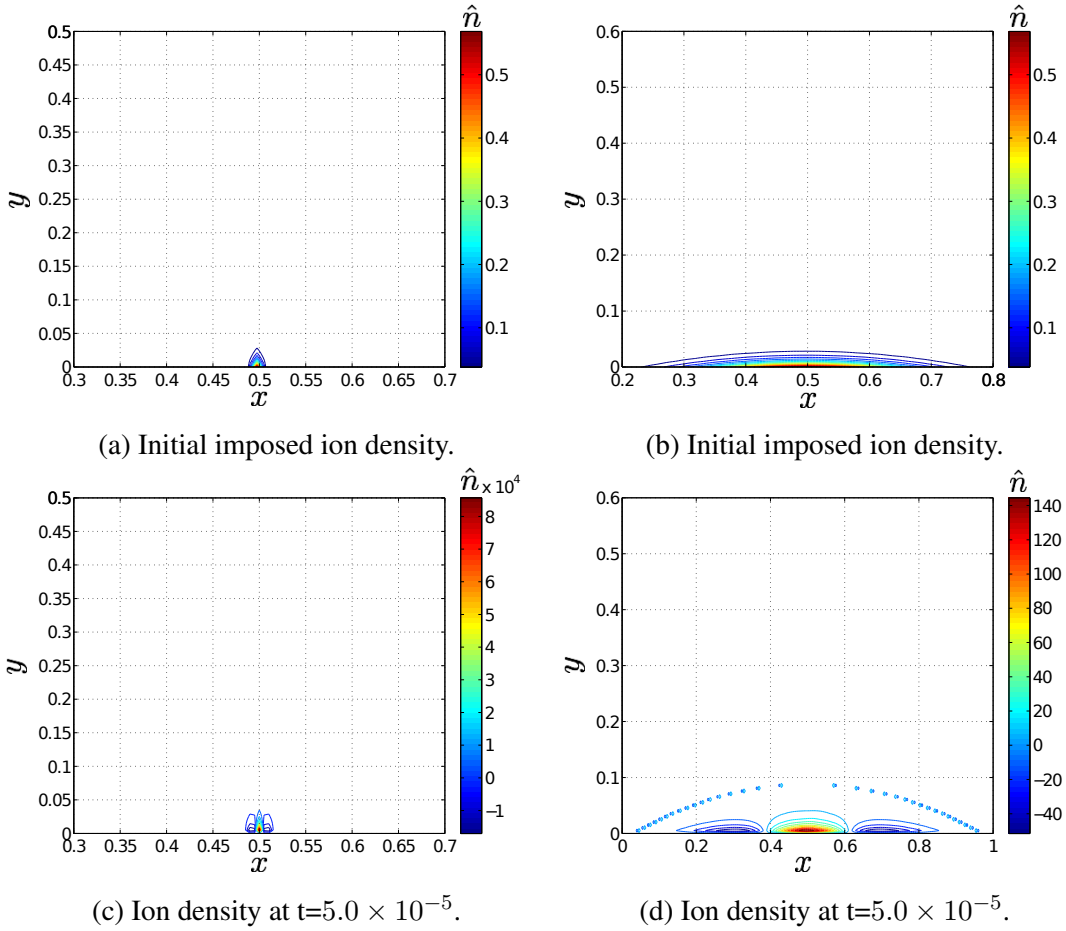

(a) Initial imposed ion density.

(b) Initial imposed ion density.

(c) Ion density at t=5.0×10^{-5}.

(d) Ion density at t=5.0×10^{-5}.

Figure 3.28: Two cases for different widths of the ion density.

First we impose two different lengths for the electrodes for the plasma to exist over its domain. We inspect that figures 3.28a and 3.28b have both converged to a steady-state solution but have different length and height of plasma. We change the no flux condition location, x_a, in equation (3.76) for two different positions of $x_a = 45$ in figure 3.28a and $x_a = 35$ in figure 3.28b, for which we witness the impact of the steady state solution. We are not interested in the densities of the ions or electrons therefore they are not stated. We are only interested in the boundary they create. Next we fix the electrodes at $x = 0.45$ and $x = 0.65$. We change various parameters such as the frequency and applied power. We also observe the change over different points in time. We can find the boundary of the plasma by locating where 99% of the density of both the electrons and ions lie.

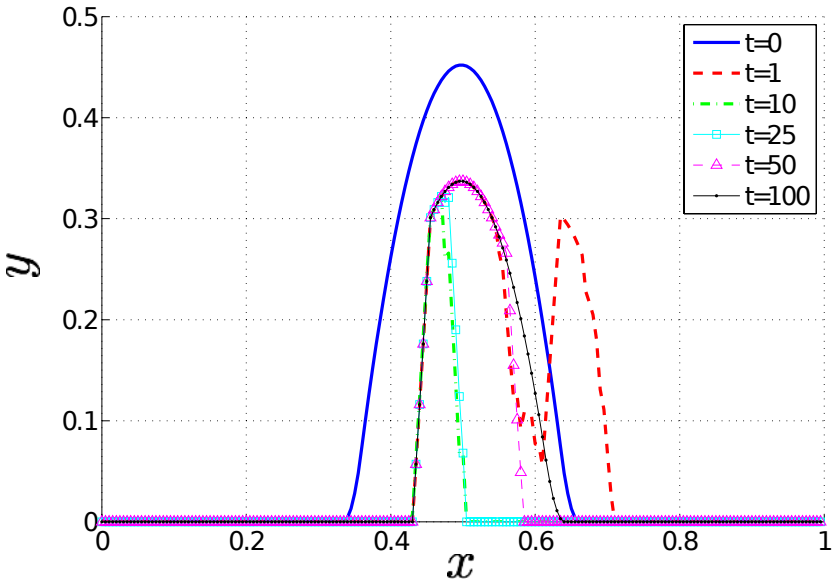

Figure 3.29: Progression of plasma boundary through time.

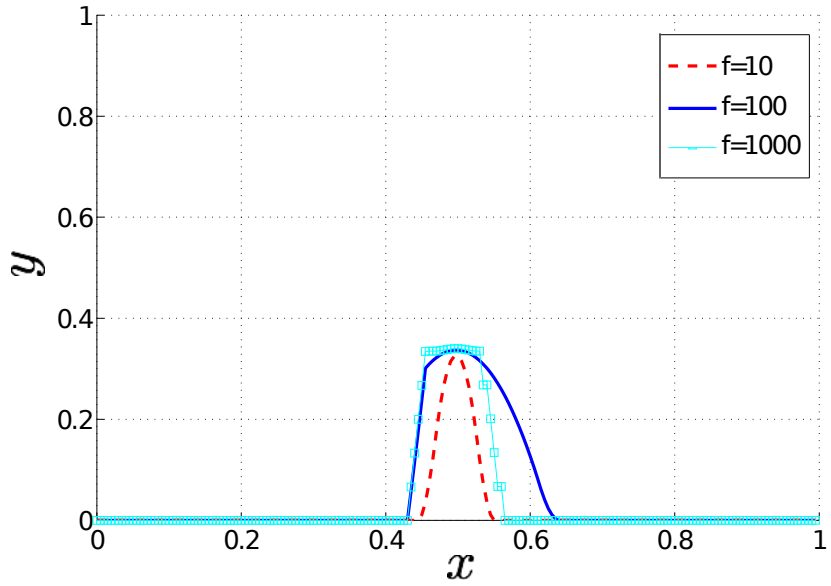

Figure 3.30: Plasma boundary with various different frequencies for a fixed power, $\phi_0 = 1.0$.

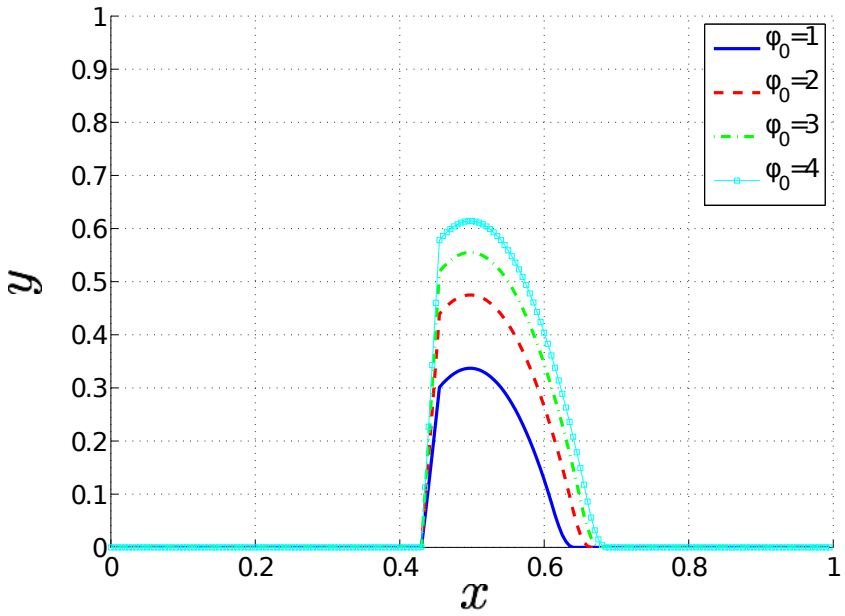

Figure 3.31: Plasma boundary with various different applied power for a fixed frequency, $f = 100$.

We can observe from figure 3.29 that after 50 time steps the solution has converged to a steady state. We are then only concerned with simulations for 50 time steps (depending on the size of the time step) and we use $\Delta t = 10^{-6}$. Next we look at changing the applied frequency of the plasma. In figure 3.30 we see that for certain frequency the width of the plasma formed changes. Note that the height of the plasma is also modified due to the frequency (not observed here). We can change the voltage input too. The impact of the voltage variation applied to the plasma is displayed in figure 3.31. We observe that there is almost a linear relationship between the plasma height and the input voltage. Also note that the width of the plasma has changed as the voltage is increased, such that as the voltage increases the width increases. We need to calculate the Fourier transform of the plasma confinement for our receptivity analysis. We can find y as a function of x by applying an algorithm to find the edge of the plasma.

3.8.4 Receptivity Analysis for Plasma Actuators

We can see that $b_P(X)$ denotes the boundary of the plasma, which defines the shape of the plasma. The Laplace transform of this is given by

$$B_P(\alpha) = \int_0^\infty b_P(X) e^{-\alpha X} dX, \tag{3.81}$$

The same conditions are used for the plasma as for the solid bump. We are going to use a test case of $\sigma = 0.1$, $\Delta = 0.1$ and $x_s = 0.3$ to analyse the response function. As discussed earlier we can calculate the response function in the following way

$$K_{RP}(\alpha_F) = \lim_{\alpha \to \alpha_F} max|v_0(\alpha)|/B_P(\alpha).$$

Since we are interested in changing the shape of the plasma produced we vary the voltage and frequency of the electrode accordingly.

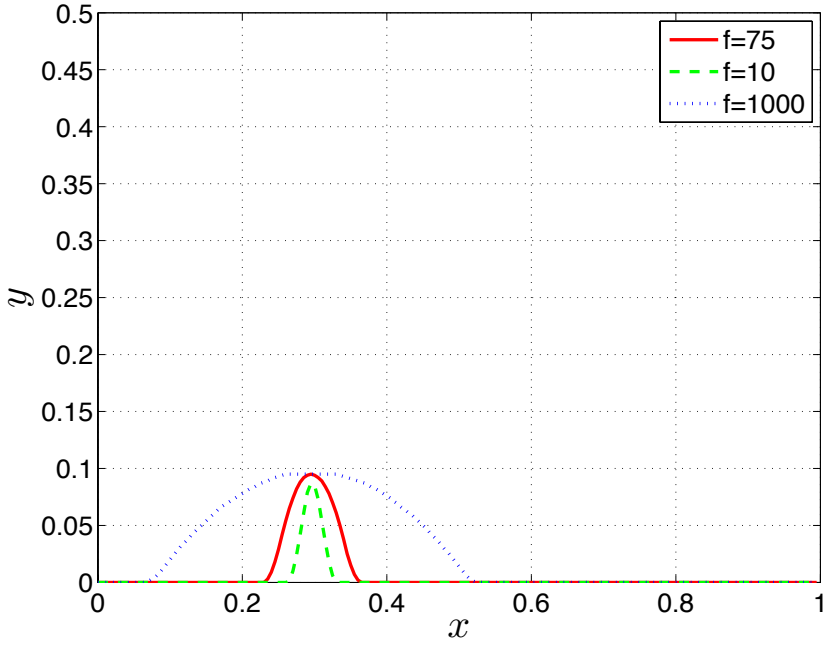

Figure 3.32: Plasma boundary with various different frequencies.

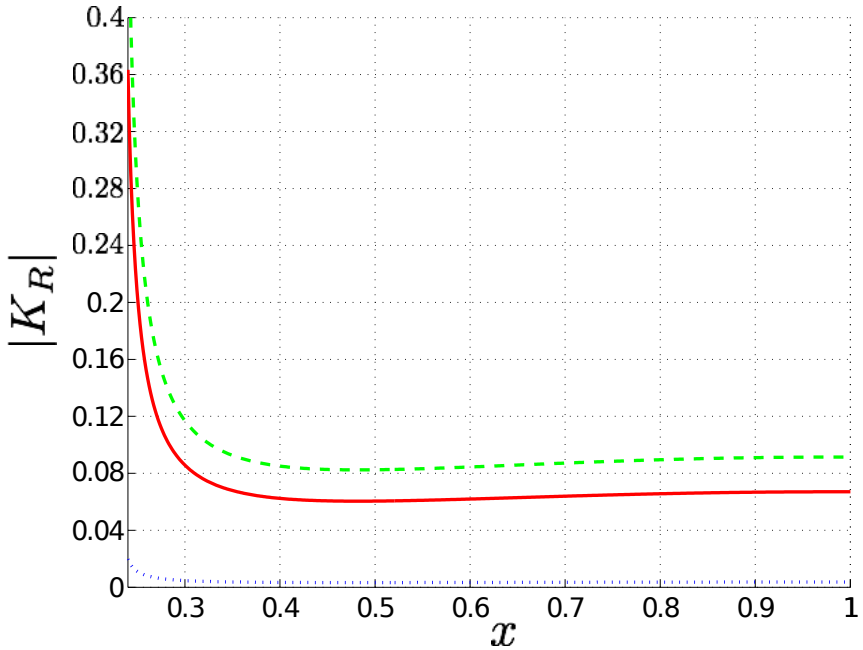

Figure 3.33: Receptivity response function, $|K_R|$, over the streamwise coordinate, x, for stationary modes with a spanwise wavenumber of $\gamma = 0.4$ with various frequencies for a plasma actuator.

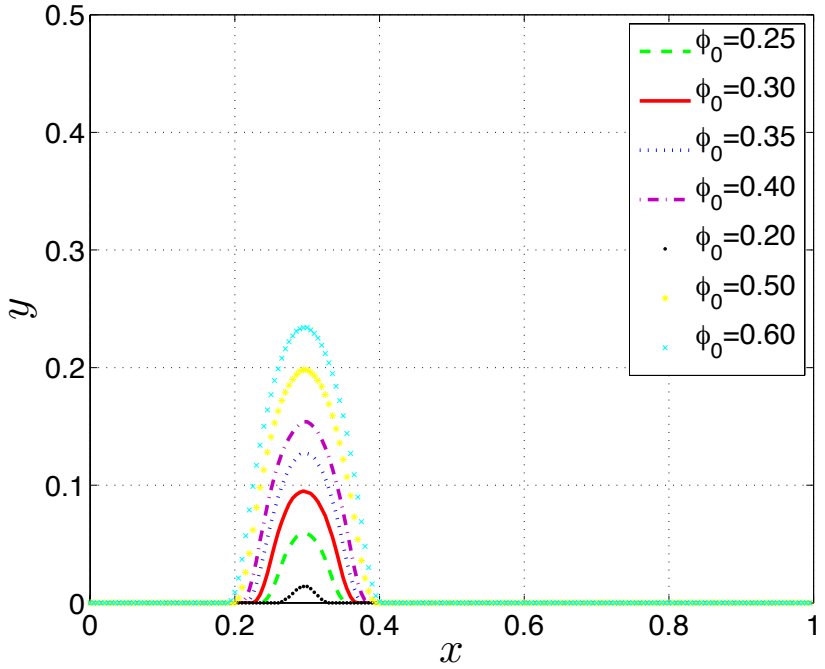

Figure 3.34: Plasma boundary with various different voltages.

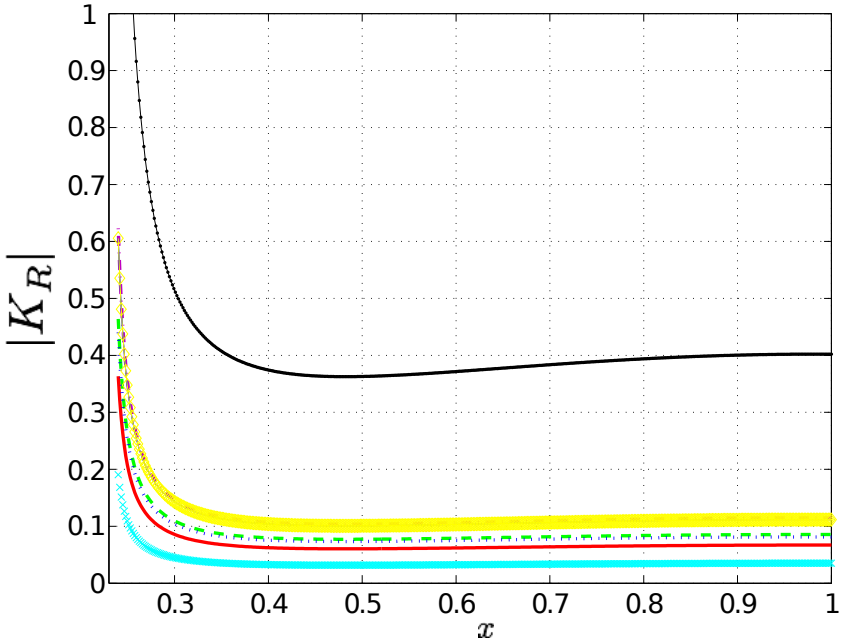

Figure 3.35: Receptivity response function ($|K_R|$) over the streamwise coordinate (x) for stationary modes ($\gamma = 0.4$) with various voltages for a plasma actuator.

We are interested imposing certain conditions for the plasma to generate the boundary of the plasma to provide with information about the response function subject to changes in the frequency or voltage input. Further downstream in x we observe that both plasma and solid bump have the same value for the response function. This is promising, since there is no distinguishable difference physically between the surface roughness and plasma actuator. We can apply the same changes as we did for figures 3.30, 3.31 for this roughness and observe changes in the response function. This can be seen as an optimisation process. We begin by varying the frequency, as we know already that this changes the width of the plasma. As the frequency is increased the width of the plasma is increased. Also the height of the plasma increases slightly as the frequency increases, as shown in figure 3.32. Large frequencies produce a small response function compared with lower frequencies of $f = 10$ and $f = 75$. But it seems that a lower frequency is beneficial since the response function is much larger. So the crossflow disturbance is more receptive to lower frequency plasma actuators.
Next we shall look at various applied voltages. As shown previously, it is known that a linear relationship exists between the plasma height and the applied voltage, ϕ_0. Figure

3.34 gives evidence of this statement. As discussed for figure 3.34, the voltage changes the width of the plasma and this is also the situation here. The result shows that for this voltage ($\phi_0 = 25$) and frequency ($f = 75$) the response function is four times the size of the next largest response function in figure 3.35. This verifies what we know about swept wing transition - that small micron sized roughness elements are more receptive for the crossflow disturbance.

3.9 Conclusion

We performed a similar receptivity analysis that used in the research of Crouch [21], Choudhari [15] and Bertolotti [8]. Firstly, we used receptivity analysis for a flat surface with a Gaussian bump. We used residue calculus to calculate the inverse Fourier transform and to evaluate the poles. From this we calculated the response function, which gave us information about the receptivity and efficiency of the process. The results showed that the response function is largest near the leading edge and, when marching along in x (high crossflow regime to a lower crossflow), it eventually becomes constant. The spanwise wavenumber was also varied and we discovered that the largest value occurred when the spanwise wavenumber was small. This is verified by Collis & Lele [19]. A similar structure across the region of spanwise wavenumbers of the response function was found to agree with Collis & Lele. From a different view, in terms of penetration depth, Schrader *et al.* [89] remarked that a noticeable peak occurred for small spanwise wavenumbers. Some authors prefer to understand receptivity from the context of penetration depth. The penetration depth is a measure of the distance at which the eigenfunction has decayed within 1% of its freestream value and gives an understanding of the receptivity process. Increasing the spanwise wavenumber enhanced the response function, which resembled results from Bertolotti [8].
Next we included curvature effects, which had an interesting impact on the development of the response function. We introduced convex curvature into our analysis. This increased the response function compared with the flat surface. This result, which was first discovered by Collis & Lele [19] numerically. Including effects of convex curvature enhanced the response function compared to a surface with no curvature variations. Collis & Lele [19] used a Gaussian bump to analyse the response function with the addition of curvature, as we did here. They compared convex and flat

surface response function with variation across the spanwise wavenumber and found that the convex curvature enhanced the response function compared to the flat surface. The behaviour was similar to the results obtained here - a minimum value occurred in the centre of the range of spanwise wavenumbers, where as a large response occurred at both small and large values of spanwise wavenumbers. The results obtained agree with the numerical findings and provide further evidence for their discovery. This was interesting because convex curvature is known to have a stabilising effect on the streamwise growth rates [59]. We have already shown theoretically, using a three-term viscous-curvature correction for the streamwise growth rates, that the convex surface did have a stabilizing impact on the streamwise growth rates compared to the flat surface streamwise growth rates. The same result exists for all spanwise wavenumbers - that including convex curvature improves the receptivity efficiency.

Next we considered a response function for concave curvature. Due to the complex dynamics of a swept wing, regions of concave curvature exist, especially on the lower surface of the wing. The results show that concave surface curvature has a greater impact on the enhancement of the response function near the leading edge, whereas the convex surface curvature has more impact further downstream. Hence, for large crossflow strength, the concave response function has greater receptivity efficiency compared with the convex. This is not intuitive since, with reference to the streamwise growth rates, the convex curvature has a stabilizing effect whereas the concave curvature has a destabilizing impact. Therefore, near the leading edge, small concave curvature is the most efficient mechanism for producing stationary crossflow vortices into the boundary-layer.

Finally we observe the travelling modes. First we note that as the frequency increases, the impact of the convex curvature on the response function decreases. For a small crossflow the flat response function and convex response function are very similar. For large frequencies this has little impact on the receptivity efficiency but for moderate frequencies there is a large effect. Masad & Malik [59] found that, for the streamwise growth rates, the curvature impact decreases as the frequency increases. These results have been validated using a three-term viscous-curvature correction for travelling crossflow vortices due to the streamwise growth rate. Next we observe the travelling modes with both convex and concave curvature. The same result occurs for the concave

response function for high frequency as for the convex response function, as they have similar values downstream in x. For large values of spanwise wavenumbers in a high frequency limit, the convex and concave response functions exhibit minor differences between them. A large difference occurs when considering moderate frequency. The concave response function dominates over the convex response function downstream in x - this could lead to some interesting behaviour. Further downstream we see that all the frequencies for both curvatures have become constant and have similar values. Therefore, it seems that far downstream the response function is independent of frequency and curvature. We observe for the different spanwise wavenumbers that the concave response function is larger than the convex response function. In particular, we notice again that for high frequencies that the response function is invariant due to different surface curvature, since they have similar values for the spanwise wavenumbers. For moderate frequencies we see that with concave curvature there is a significant enhancement of the response function compared to convex curvature. Hence, for this spanwise wavenumber range, the concave curvature is a more efficient process for receptivity.

In summary, stationary crossflow vortices have larger values of the response function than travelling ones, and including curvature effects increases the response function further. Both convex and concave curvature enhance the response function for both stationary and travelling crossflow modes. Close to the leading edge, adding concave curvature seems to be the most efficient receptivity mechanism for the stationary and travelling crossflow modes, but only for moderate frequencies. Convex curvature is effective but only compared to a flat surface or further downstream. In the high frequency limit there is a minor change between all three response functions of flat, convex and concave surface curvature. This includes considering both downstream behaviour and spanwise wavenumber variation of the response functions.

We extended this theory further by introducing a plasma actuator near the leading edge. The idea was to replace the solid surface roughness with plasma. We formulated this problem from the Maxwell equations and treated the fluid-plasma problem as separate, such that we are only interested in the steady state shape of the plasma formed. First we started from the Maxwell equations for electromagnetism and derived a set of equations for ions and electrons within the plasma. We began with values and constants

from helium discharge simulations, since there isn't much data available from experiment with other elements [49]. With these values we solved the plasma equations subject to a finite difference scheme. In particular, we used a Forward Time Central difference Scheme (FTCS) method. We marched in time until a steady state solution was achieved. Since the boundary was unclear, a procedure was written to obtain it and this was needed for the receptivity analysis. From this the response function for the plasma actuator was obtained by calculating the Fourier transform of the plasma boundary and the corresponding stationary crossflow wavenumber. We do not consider any travelling modes or curvature effects in the following discussion.

We first changed the frequency of the electrodes of the DBD plasma actuator. As mentioned earlier this changes the width and changes the height of the plasma. We observe three different frequencies of $f = 10, 75$ and 1000 with the response function. Figure 3.32 shows the different plasma boundaries of various frequencies. We then calculated their corresponding response functions of these different applied frequencies. It appears that the smaller the frequency the larger the response function, but there is a minor discrepancy in that the height is modified with frequency. But the main effect is that, if we increase the width of the plasma, the response function decreases.

We can also change the height of the plasma by varying the input voltage. A similar problem occurs for the voltage - the width of the plasma boundary changes with voltage as seen in figure 3.34. We witness the changes of the receptivity response function in figure 3.35 and notice that the largest response function occurs when the voltage is smallest, which produces the smallest plasma height. Also notice that the other response functions have similar response magnitudes for different plasma heights. However, there is still a discrepancy with these results since the width has also changed. To be more consistent a constant factor between the voltage and frequency could be introduced, but it seems from figure 3.35 that the largest effect on the receptivity response function is the height of the plasma. This statement can be justified by that difference between the frequencies of $f = 10$ and $f = 75$. Both have a similar plasma height but in figure 3.33 the difference in the response functions is, $\Delta|K_R| \sim 0.02$. Whereas if we consider the difference between two applied voltages $\phi_0 = 0.5$ and $\phi_0 = 0.6$, the difference in the response function is $\Delta|K_R| \sim 0.05$. But with these two applied voltages produce similar plasma widths. The changes in the frequency seem to appear

have a greater impact on the response function than changing the applied voltage. This is why the height is a more important factor then the width of the plasma for the response function. Taking into account the fact that decreasing the width of the plasma increases the response function, there is a significant change for when the voltage is $\phi_0 = 0.2$ in figure 3.35. It appears that the largest receptivity response function occurs for the smallest plasma height and only increased when the width is decreased. We know that micron sized roughness elements cause a large response from the stationary crossflow vortex.

In summary, we derived the plasma equations from Maxwell equations and solved them using a FTCS method, until a steady state solution was formed, we used an algorithm. To determine the boundary of the plasma to find the Fourier transform of it to evaluate the response function. With this calculation we made a comparison to the surface roughness bump and found good agreement. We then changed the frequency and voltage, and found that small height and small width had the largest response function which corresponds to small voltage and small frequency. We could do a parametric study to find the optimal configuration but this is time consuming and will not be discussed in our study.

Chapter 4

Three-dimensional short-wave instabilities developing on general two-dimensional closed streamlines

4.1 Introduction

Pierrehumbert [70] discovered that a general mechanism exists from which convoluted three-dimensional flows emerge from two-dimensional structures with coherent large scales. Henceforth, we have an inviscid two-dimensional structure with elliptical cores that form a response to three-dimensional instabilities, which can be compared to turbulent studies and large scale secondary instabilities.
This theory applies to a three-dimensional instability where pressure is essential to secondary instabilities of finite amplitudes. It has been shown explicitly that the classical centrifugal instability can be generalised to a large class of two-dimensional flows, namely, those whose streamlines are convex closed curves with the directed outwards. The centrifugal instability does not only exist in flows that are close to being symmetric but also arises for multiple scale systems that are developed from a boundary-layer structure (Görtler vortices). Previous studies show that centrifugal instability is a generic property of a given class of flows, regardless of the symmetry or asymmetry of the flow or its degree of distortion from circularity. A class of short-wave three-dimensional instabilities can be constructed by

1. Closed convex streamlines in some region of the flow.

2. Magnitude of the circulation increases outwards.

If the instability is localised near streamline, the Floquet matrix is maximised, and from this a disturbance will arise. For our analysis we need to find a condition to locate where this instability exists, at some distance away from the centre of the vortex as mentioned by Bayly [6]. We are interested in this disturbance for our analysis.

4.2 Formulation

4.2.1 Flow Configuration

In light of Pierrehumbert [70] and Bayly's [5] work, we consider a new formulation of this short-wave instability problem. We will work with the same framework so we consider an unbounded and incompressible fluid, where the flow acts along closed two-dimensional streamlines accordingly and we consider a temporal disturbance along this streamline. A streamline is given by the streamfunction of

$$\psi = \frac{x^2}{a^2} + \frac{y^2}{b^2} = K, \tag{4.1}$$

such that we have a family of streamlines where a/b is constant and K is a constant variable (a measure of the streamline and is useful for analysis later in this chapter), a is the length of the ellipse in the x-direction and b is the length of the ellipse in the y-direction. First we start with a basic flow which can be determined from

$$u = \frac{\partial \psi}{\partial y} \quad \text{and} \quad v = -\frac{\partial \psi}{\partial x}, \tag{4.2}$$

with u and v satisfying the Euler equations. The speed can be determined by

$$\overline{u} = 2\sqrt{x^2/a^4 + y^2/b^4}. \tag{4.3}$$

This is the basic flow we will consider the the rest of this chapter. Since we have a general two-dimensional closed streamline, for our analytical approach we need to transform into curvilinear coordinates.

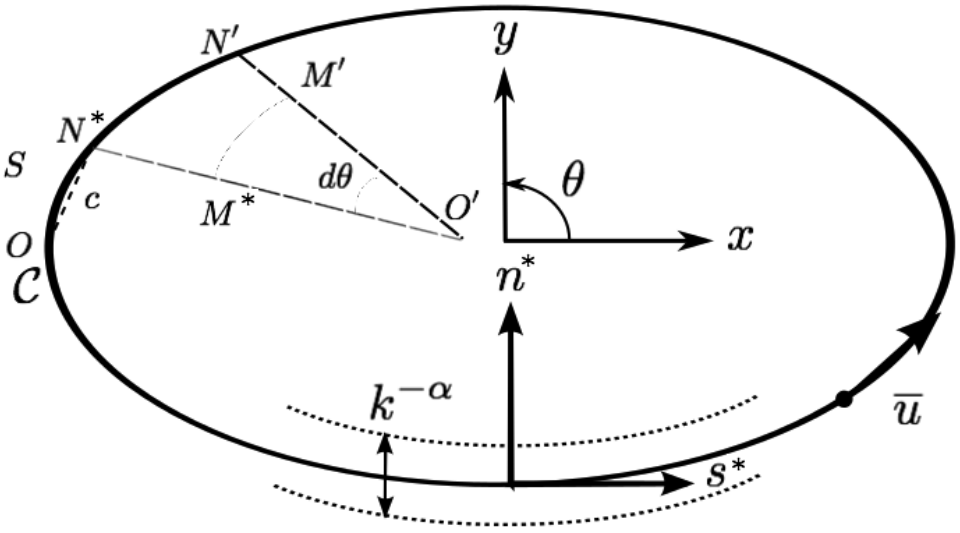

Figure 4.1: Two-dimensional closed streamline with body formed coordinates with n^* as the normal, s^* is situated along it, l^* is normal to the surface (coming out of the page) and the basic flow ($\overline{u}$) is situated along the streamline s^*.

Due to the general approach we are considering, any deformations to the streamline can be incorporated within this analysis as shown in figure 4.1. The region to which the disturbance is confined to $k^{-\alpha}$, with k as the spanwise wavenumber and α is to be determined later with scaling arguments but we note that this is a short-wave instability. We consider a contour (c) along the elliptical streamline, as shown in figure 4.1, and draw a normal at point N^* towards the centre. For our argument we need a point M^* which exists somewhere on this normal. If we speculate that another point exists on the streamline N', there must be a corresponding M' along the normal. This is an unbounded flow, so points M and M' can exist outside the reference streamline. The distance between the points M and M' can be approximated by a small length $\hat{m}$, such that $\hat{m} \approx M^* - M'$. As this length $\hat{m}$ approaches zero, the normals of N^*M^* and $N'M'$ meet at the centre of the curvature O' along the contour c. Let $R(s)$ denote the radius of curvature, which is continuous in s^* with respect to the contour c. This includes derivatives of $R(s^*)$ at point N^*. By calculating the distance in this way, by taking the square of the distance MM', we obtain the following Lamè coefficients values

$$H_1 = 1 + sgn(n^*)\kappa(s^*)n^*, \quad H_2 = 1. \tag{4.4}$$

In our system we have n as positive such that

$$H_1 = 1 + \kappa(s^*)n^*, \quad H_2 = 1. \tag{4.5}$$

In terms of Cartesian coordinates (x, y) can be determined from

$$x = \frac{ab\cos(\theta)}{\sqrt{a^2\sin^2(\theta) + b^2\cos^2(\theta)}}, \quad y = \frac{ab\sin(\theta)}{\sqrt{a^2\sin^2(\theta) + b^2\cos^2(\theta)}}. \tag{4.6}$$

The x and y given in equation (4.6) can be generalised to encompass non-symmetric streamlines or any shape of a two-dimensional streamline. They are in reference to the origin O' which can be seen in figure 4.1. We can calculate s from line integral of

$$s = \int_0^{2\pi} \sqrt{\left(\frac{dx}{d\theta}\right)^2 + \left(\frac{dy}{d\theta}\right)^2} d\theta. \tag{4.7}$$

The curvature κ can be calculated from

$$\kappa = \frac{x'y'' - x''y'}{(x'^2 + y'^2)^{3/2}}, \tag{4.8}$$

hence using the definition of (4.6) yields

$$\kappa = \frac{1}{\sqrt{\frac{x^2}{a^4} + \frac{y^2}{b^4}}} \left(\frac{1}{a^2} + \frac{1}{b^2}\right) - \frac{1}{\left(\frac{x^2}{a^4} + \frac{y^2}{b^4}\right)^{3/2}} \left(\frac{x^2}{a^6} + \frac{y^2}{b^6}\right). \tag{4.9}$$

The terms involving derivatives with respect to s^*, $\overline{u}_{s^*}$ or κ_{s^*}, can be calculated numerically using a finite difference method. An example of this can be demonstrated by

$$\frac{\partial \overline{u}}{\partial s^*} = \frac{\overline{u}_{i+1} - \overline{u}_{i-1}}{2\Delta s^*}. \tag{4.10}$$

Within the elliptical system the unit normal vector is given by

$$\underline{\hat{n}} = \frac{\left(\frac{x}{a^2}, \frac{y}{b^2}\right)}{\sqrt{\frac{x^2}{a^4} + \frac{y^2}{b^4}}}. \tag{4.11}$$

Hence we can calculate $\overline{u}_{n^*}$ in the following way

$$\overline{u}_{n^*} = \nabla\overline{u}\cdot\underline{\hat{n}} = \frac{\left(\frac{x^2}{a^6}+\frac{y^2}{b^6}\right)}{\left(\frac{x^2}{a^4}+\frac{y^2}{b^4}\right)}. \tag{4.12}$$

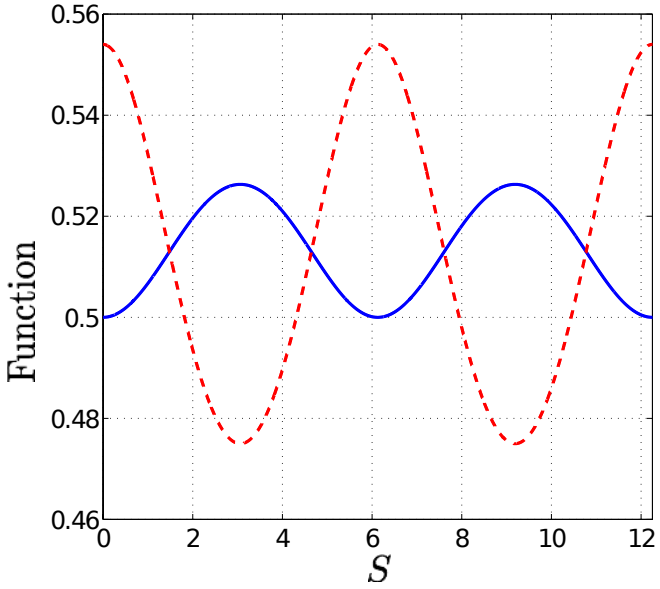

Figure 4.2: Baseflow $\overline{u}$ (solid, blue line) and curvature κ (dashed, red line) changes around the ellipse for different s^* with the associated derivatives of these functions for the values of $a = 2.0, b = 1.9, K = 1.0$.

We now introduce non-dimensional variables $\mathbf{u}$, s, n, l, p, t

$$s = s^*L, \quad n = n^*L, \quad l = l^*L, \quad p = \rho {u^+}^2 p^*, \quad \mathbf{u}{=}u^+\mathbf{u}^*, \quad t^* = \tfrac{tL}{u^+},$$

where u^+ is a reference velocity located away from the streamline such that fluctuations are small, L is the characteristic length scale of the system and the Reynolds number is defined as $Re = u^+L/\nu$. We will now perturb the base flow by

$$\mathbf{u} = (\overline{u}(s,n),0,0){+}\epsilon(U(s,n,l,t),V(s,n,l,t),W(s,n,l,t)) \quad \text{and} \quad p = \epsilon P(s,n,l,t) \tag{4.13}$$

We substitute (4.13) into (1.3) and (1.4) with linearisation around ϵ (where $\epsilon \ll 1$) and

we obtain

$$\begin{aligned}
&\frac{\partial U}{\partial t}+\frac{\overline{u}}{1+\kappa n}\frac{\partial U}{\partial s}+\frac{U}{1+\kappa n}\frac{\partial \overline{u}}{\partial s}+V\frac{\partial \overline{u}}{\partial n}+\frac{\kappa \overline{u}V}{1+\kappa n}\\
&\qquad=-\frac{1}{1+\kappa n}\frac{\partial P}{\partial s}+\frac{1}{Re(1+\kappa n)}\left[\frac{\partial}{\partial s}\left(\frac{1}{1+\kappa n}\frac{\partial U}{\partial s}\right)+\frac{\partial^2 U}{\partial n^2}\right.\\
&\qquad\left.+\kappa\frac{\partial}{\partial n}\left(\frac{V}{1+\kappa n}\right)+\frac{1}{1+\kappa n}\frac{\partial}{\partial s}\left(\kappa\frac{V}{1+\kappa n}\right)+\frac{\partial^2 U}{\partial l^2}\right], \quad (4.14a)\\
&\frac{\partial V}{\partial t}+\frac{\overline{u}}{1+\kappa n}\frac{\partial V}{\partial s}-\frac{2\kappa\overline{u}U}{1+\kappa n}=\\
&\qquad-\frac{\partial P}{\partial n}+\frac{1}{Re(1+\kappa n)}\left[\frac{\partial}{\partial s}\left(\frac{1}{1+\kappa n}\frac{\partial V}{\partial s}\right)+\frac{\partial^2 V}{\partial n^2}\right.\\
&\qquad\left.+\kappa\frac{\partial}{\partial n}\left(\frac{U}{1+\kappa n}\right)+\frac{1}{1+\kappa n}\frac{\partial}{\partial s}\left(\kappa\frac{U}{1+\kappa n}\right)+\frac{\partial^2 V}{\partial l^2}\right], \quad (4.14b)\\
&\frac{\partial W}{\partial t}+\frac{\overline{u}}{1+\kappa n}\frac{\partial W}{\partial s}\\
&\qquad=-\frac{\partial P}{\partial l}+\frac{1}{Re(1+\kappa n)}\left[\frac{\partial}{\partial s}\left(\frac{1}{1+\kappa n}\frac{\partial W}{\partial s}\right)\right.\\
&\qquad\left.+\frac{\partial^2 W}{\partial n^2}+\kappa\frac{\partial}{\partial n}\left(\frac{W}{1+\kappa n}\right)+\frac{\partial^2 W}{\partial l^2}\right], \quad (4.14c)\\
&-\frac{\partial \kappa}{\partial s}\frac{Un}{1+\kappa n}+\frac{\partial U}{\partial s}+\frac{\partial V}{\partial n}-\frac{\kappa V}{1+\kappa n}+\frac{\partial W}{\partial l}=0. \quad (4.14d)
\end{aligned}$$

We impose a disturbance of the form

$$Q(s,n,l,t)=\tilde{Q}(s,n)e^{\sigma t+kl}.$$

where $Q=(U,V,W,P)$ and l is the coordinate perpendicular to the plane of (s,n). We consider the following scalings

$$\begin{aligned}
&\tilde{U}(s,n)=\hat{U}(s,N), \quad \tilde{V}(s,n)=\hat{V}(s,N), \quad \tilde{W}(s,n)=k^{-1/2}\hat{W}(s,N),\\
&\tilde{P}(s,n)=k^{-3/2}\hat{P}(s,N), \quad n=k^{-1/2}N. \quad (4.15)
\end{aligned}$$

The scalings of (4.15) is very similar to that used by Bayly [6], but there is one key difference - the axial velocity is scaled as $k^{-1/2}$, whereas considering the tangential velocity is scaled as $\mathcal{O}(1)$ quantity. Since we are considering high wavenumber, k is assumed to be large. However, the analysis is different and also the coordinate system. However, with this introduction of the scalings to the n-momentum equation, the pres-

sure term is included and, from Bayly's discussion, we only need to acknowledge s and n momentum equations that are absent of pressure terms. Hence we rescale the normal coordinate to the streamline within a thin layer of thickness $k^{-1/2}$ near the streamline such that $n = k^{-1/2}N$ [6]. We take an asymptotic expansion for the disturbance and the temporal wavenumber

$$\hat{Q} = \hat{Q}_0 + k^{-1/2}\hat{Q}_1 + \mathcal{O}(k^{-1}), \tag{4.16}$$

$$\sigma = \sigma_0 + k^{-1}\sigma_2 + \mathcal{O}(k^{-2}). \tag{4.17}$$

This expansion is similar to the one Bayly used [6]. We note that there is no σ_1 term. Bayly also did not consider this term in the analysis. If this term was included we would not find the condition where the instability was located but we could find the value of σ_1. This would not be helpful in this analysis. Notice that there are terms of $1/(1+\kappa n)$ arising in the disturbance equations and they have now been transformed into $1/(1+\kappa N k^{-1/2})$. Since we are interested in terms proportional to k, we need to expand this term and therefore using a binomial expansion yields

$$1/(1+\kappa N k^{-1/2}) = (1+\kappa N k^{-1/2})^{-1} = 1 - \kappa N k^{-1/2} + \frac{1}{2}\kappa^2 N^2 k^{-1} + \cdots . \tag{4.18}$$

Due to the grouping of the disturbance near the streamline, we Taylor expand the base flow in the following way around $(s, 0)$:

$$\overline{u}(s, N) = \overline{u}(s, 0) + \frac{\partial \overline{u}(s,0)}{\partial N} N + \frac{1}{2}\frac{\partial^2 \overline{u}(s,0)}{\partial N^2} N^2 + \cdots . \tag{4.19}$$

4.2.2 Leading Order Problem

By substituting (4.16), (4.17), (4.18) and (4.19) into (4.14) and assuming the flow is inviscid, for leading order we obtain

$$\sigma_0\hat{U}_0 + \overline{u}\frac{\partial\hat{U}_0}{\partial s} + \hat{U}_0\frac{\partial\overline{u}}{\partial s} + \hat{V}_0\frac{\partial\overline{u}}{\partial N} + \kappa\overline{u}\hat{V}_0 = 0, \tag{4.20a}$$

$$\sigma_0\hat{V}_0 + \overline{u}\frac{\partial\hat{V}_0}{\partial s} - 2\overline{u}\hat{U}_0\kappa = 0, \tag{4.20b}$$

$$\sigma_0\hat{W}_0 + \overline{u}\frac{\partial\hat{W}_0}{\partial s} = -\hat{P}_0, \tag{4.20c}$$

$$\frac{\partial\hat{V}_0}{\partial N} + \hat{W}_0 = 0. \tag{4.20d}$$

For convenience we define the following operators

$$\mathcal{D}_{s,m} = \sigma_0\hat{U}_m + \overline{u}\frac{\partial\hat{U}_m}{\partial s} + \hat{U}_m\frac{\partial\overline{u}}{\partial s} + \hat{V}_m\frac{\partial\overline{u}}{\partial N} + \kappa\overline{u}\hat{V}_m, \tag{4.21a}$$

$$\mathcal{D}_{n,m} = \sigma_0\hat{V}_m + \overline{u}\frac{\partial\hat{V}_0}{\partial s} - 2\overline{u}\hat{U}_m\kappa, \tag{4.21b}$$

$$\mathcal{D}_{l,m} = \sigma_0\hat{W}_m + \overline{u}\frac{\partial\hat{W}_m}{\partial s} + \hat{P}_m, \tag{4.21c}$$

$$\mathcal{D}_{c,m} = \frac{\partial\hat{V}_m}{\partial N} + \hat{W}_m, \tag{4.21d}$$

where m has the values of 0, 1, 2. We see that when $m = 0$ differential equations of (4.21) correspond to (4.20). The functions of (4.21a)-(4.21d) will be needed later for our analysis. We notice that both the s-momentum (4.20a) and n-momentum (4.20b) are the only contain $\hat{U}_0$ and $\hat{V}_0$. This means we only need to manipulate these two equations to formulate an eigenvalue problem for either $\hat{U}_0$ or $\hat{V}_0$. This is in agreement with Bayly [6], who states that the reason for the successful analysis was "ignoring" the continuity and l-momentum equations. In our analysis we removed these two equations of l-momentum and continuity via scaling arguments and not by diagonalisation of the inertia operator (see [6]). By rearranging (4.20b) and substituting into (4.20a), we

obtain an equation for $\hat{V}_0$

$$\left[\frac{\partial^2}{\partial s^2}+\left(\frac{2\sigma_0}{\overline{u}}+\frac{1}{\overline{u}}\frac{\partial\overline{u}}{\partial s}-\frac{1}{\kappa}\frac{\partial\kappa}{\partial s}\right)\frac{\partial}{\partial s}+\left(\frac{{\sigma_0}^2}{\overline{u}^2}+\frac{2\kappa}{\overline{u}}\frac{\partial\overline{u}}{\partial N}+2\kappa^2-\frac{\sigma_0}{\overline{u}\kappa}\frac{\partial\kappa}{\partial s}\right)\right]\hat{V}_0 = \hat{L}_0\hat{V}_0 = 0, \tag{4.22}$$

where $\hat{L}_0$ is the leading order operator. We can solve this using a Runge-Kutta fourth order method with appropriate initial conditions. We have to find the initial conditions, since we have no information about them. Due to the streamlines being closed we have the following conditions

$$\hat{V}_0(0) = \hat{V}_0(\mathcal{C}), \tag{4.23a}$$

$$\hat{V}_0'(0) = \hat{V}_0'(\mathcal{C}), \tag{4.23b}$$

where $\mathcal{C}$ indicates the end point of the streamline. We can see this in figure 4.1. Since the eigenfunction $\hat{V}_0$ can be normalised, we can set the initial condition as $\hat{V}_0(0) = (\alpha_*, 0)$ and fix values for α_* and σ_0. We initially set $\hat{V}_0(0)$ to be complex, however this made no difference to the final solution. We define $\hat{V}_0$ in this way since it is composed of real and imaginary parts, due to σ_0 being complex. With $\hat{V}_0'(0) = (\beta_*, 0)$, we use a fourth order Runge-Kutta to solve (4.22) and find the corrected value using a secant method (this method can be found in the appendix E) for β_*

$$\beta_* = \beta_1 - \frac{\alpha_1(\beta_2-\beta_1)}{(\alpha_2-\alpha_1)}. \tag{4.24}$$

We use these conditions and solve the eigenvalue problem for σ_0. The solution is independent of the initial conditions of α_* and β_* to which we can set them to any trivial values. From this we have two initial condition guesses

1. $\hat{V}_0(0) = (\alpha_1, 0), \quad \hat{V}_0'(0) = (\beta_1, 0)$ and
2. $\hat{V}_0(0) = (\alpha_2, 0), \quad \hat{V}_0'(0) = (\beta_2, 0),$

which we used to find β_* in (4.24). As an example of the solution to this eigenvalue problem, we keep b constant and vary a, and we can see some results in figure 4.3. We can see that there are regions of stability existing and notice that for $a = b$ the

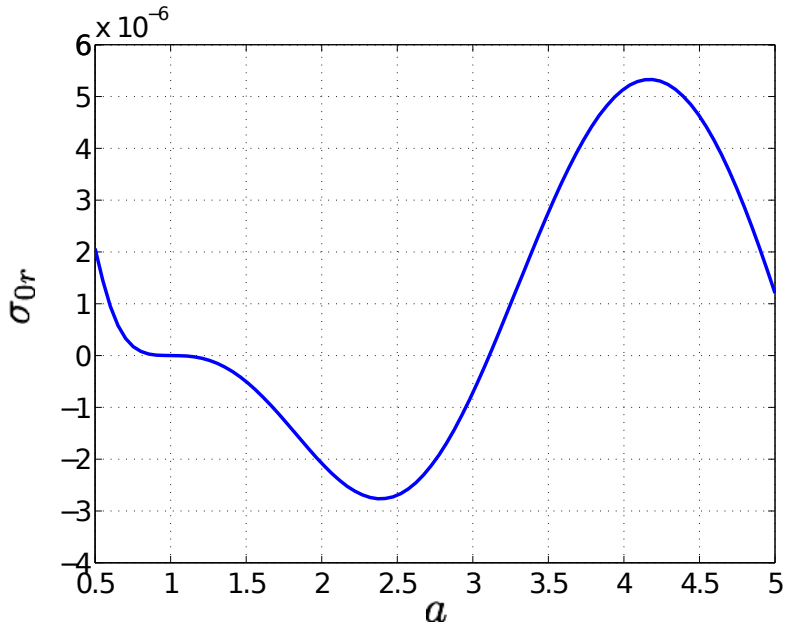

Figure 4.3: Temporal leading order growth rate, σ_{0r}, for a fixed value of $b = 1.0$ with varying a.

growth rate is zero. This implies that if $a = b$ for a circular streamline the disturbance is initially neutrally stable. From figure 4.3 we have found the leading order temporal growth rate for this instability. We observe that there are regions of stability and instability as a varies. We are interested in finding the location where this instability arises and therefore we need to consider the next order term.

4.2.3 Determination of Instability Location.

The momentum and continuity equations for next order, $\mathcal{O}(k^{-1/2})$, are as follows

$$\mathcal{D}_{s,1} = N\left[\mathrm{A}\frac{\partial \hat{U}_0}{\partial s} + \mathrm{B}\hat{U}_0 + \mathrm{C}\hat{V}_0\right], \tag{4.25a}$$

$$\mathcal{D}_{n,1} = N\left[\mathrm{A}\frac{\partial \hat{V}_0}{\partial s} - 2\mathrm{A}\hat{U}_0\kappa\right], \tag{4.25b}$$

$$\mathcal{D}_{l,1} = \overline{u}\kappa N\left[\frac{\partial \hat{W}_1}{\partial s}\right], \tag{4.25c}$$

$$\mathcal{D}_{c,1} = -\kappa\hat{V}_0 - \frac{\partial \hat{U}_0}{\partial s}, \tag{4.25d}$$

where

$$\mathrm{A} = \overline{u}\kappa - \frac{\partial \overline{u}}{\partial N}, \quad \mathrm{B} = \kappa\frac{\partial \overline{u}}{\partial s} - \frac{\partial^2 \overline{u}}{\partial N \partial s}, \quad \mathrm{C} = -\kappa^2\overline{u} + \kappa\frac{\partial \overline{u}}{\partial N} - \frac{\partial^2 \overline{u}}{\partial N^2}. \tag{4.26}$$

As with the (4.20) equations, we can manipulate (4.25) in a similar manner. This yields

$$\hat{L}_0\hat{V}_1 = \hat{R}_1(s, N), \tag{4.27}$$

where

$$\begin{aligned}\hat{R}_1(s,N) = &\left(\frac{2\kappa N}{\overline{u}}\right)\left[\frac{\sigma_0 + \frac{\partial \overline{u}}{\partial s}}{2\kappa\overline{u}}\right]\left(\mathrm{A}\frac{\partial \hat{V}_0}{\partial s} - 2\kappa\mathrm{A}\hat{U}_0\right) \\ &+ \left(\frac{2\kappa N}{\overline{u}}\right)\left(\mathrm{A}\frac{\partial \hat{U}_0}{\partial s} + \mathrm{B}\hat{U}_0 + \mathrm{C}\hat{V}_0\right) \\ &+ 2\kappa N\frac{\partial}{\partial s}\left[\frac{1}{2\kappa\overline{u}}\left(\mathrm{A}\frac{\partial \hat{V}_0}{\partial s} - 2\kappa\mathrm{A}\hat{U}_0\right)\right].\end{aligned} \tag{4.28}$$

Notice that a new term involving the basic flow $\overline{u}_{NN}$ appears in (4.25a) due to the local Taylor expansion. This term can be calculated in a similar way to $\overline{u}_N$ and therefore we have

$$\overline{u}_{NN} = \nabla\overline{u}_N \cdot \underline{\hat{n}} = 2\frac{\left(\frac{x^2}{a^4} + \frac{y^2}{b^4}\right)\left(\frac{x^2}{a^8} + \frac{y^2}{b^8}\right) - \left(\frac{x^2}{a^6} + \frac{y^2}{b^6}\right)^2}{\left(\frac{x^2}{a^4} + \frac{y^2}{b^4}\right)^{5/2}}. \tag{4.29}$$

Now we apply a solvability condition to equation (4.27) by multiplying both sides by the adjoint of leading order eigenfunction and integrating across the domain. This yields

$$\int_0^{\mathcal{C}} \hat{L}_0\hat{V}_1 \cdot \hat{V}_0^{\dagger} ds = \int_0^{\mathcal{C}} \hat{R}_1(s, N) \cdot \hat{V}_0^{\dagger} ds. \tag{4.30}$$

We have the following boundary conditions

$$\hat{V}_0(0) = \hat{V}_0(\mathcal{C}), \quad \hat{V}_0'(0) = \hat{V}_0'(\mathcal{C}), \tag{4.31a}$$

$$\hat{V}_1(0) = \hat{V}_1(\mathcal{C}), \quad \hat{V}_1'(0) = \hat{V}_1'(\mathcal{C}). \tag{4.31b}$$

The operator $\hat{L}_0$ is not in self adjoint form and we will get a contribution of the left hand side. We require that

$$\hat{L}_0\hat{V}_0 = \left[\frac{\partial}{\partial s}\left(e^{\int_0^s c_0(s^*)ds^*}\frac{\partial}{\partial s}\right) + e^{\int_0^s c_0(s^*)ds^*}c_1(s)\right]\hat{V}_0 = L_0^*\hat{V}_0 = 0, \tag{4.32}$$

with $c_0(s) = \left(\frac{2\sigma_0}{\overline{u}} + 2\kappa\frac{\partial\overline{u}}{\partial s} - \frac{1}{\kappa}\frac{\partial\kappa}{\partial s}\right)$, $c_1(s) = \left(\frac{{\sigma_0}^2}{\overline{u}^2} + \frac{2\kappa}{\overline{u}}\frac{\partial\overline{u}}{\partial N} + 2\kappa^2 - \frac{\sigma}{\overline{u}\kappa}\frac{\partial\kappa}{\partial s}\right)$ and hence we have

$$\int_0^{\mathcal{C}} L_0^*\hat{V}_1 \cdot \hat{V}_0^\dagger ds = 0. \tag{4.33}$$

Therefore

$$\int_0^{\mathcal{C}} \hat{R}_1(s,N) \cdot \hat{V}_0^\dagger e^{\int_0^s c_0(s^*)ds^*} ds = I_N = 0. \tag{4.34}$$

For an example of this condition being satisfied we can take a simple elliptical streamline, as shown in figure 4.3. The temporal growth rate for a circular streamline is zero. We change the initial size of the ellipse and find for which value of K the integral condition vanishes (which is found from equation 4.1).

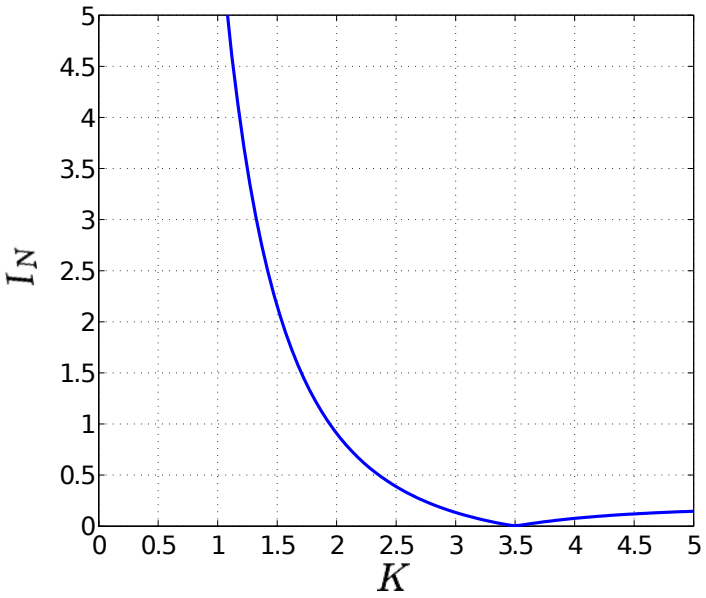

Figure 4.4: The value of the integral condition I_N with varying K for $a = 0.7$ and $b = 1.0$.

We see in figure 4.4 that the condition has been satisfied for a value of $K \simeq 3.5$.

4.2.4 Next Order Eigenvalue Problem

Thus far we have found the leading order temporal growth rate and the location where the disturbances arise, but the behaviour of the normal vector to the streamline needs to be understood. This will give us a correction to the leading order temporal growth rate. We start by scaling $k = Re^{1/2}$ to include viscous terms in the next order, $\mathcal{O}(1/k)$, with

$$\hat{Q} = \hat{Q}_0 + k^{-1/2}\hat{Q}_1 + k^{-1}\hat{Q}_2. \tag{4.35}$$

Hence the next order momentum and continuity equations (4.14a)-(4.14d) for $\mathcal{O}(k^{-1})$ are

$$\mathcal{D}_{s,2} = \mathcal{A}_0 + N\mathcal{A}_1 + N^2\mathcal{A}_2, \tag{4.36a}$$

$$\mathcal{D}_{n,2} = \mathcal{B}_0 + N\mathcal{B}_1 + N^2\mathcal{B}_2, \tag{4.36b}$$

$$\mathcal{D}_{l,2} = -\sigma_2\hat{W}_0 + \frac{\partial^2\hat{W}_0}{\partial N^2} + \mathrm{A}N\frac{\partial\hat{W}_1}{\partial s} + \frac{1}{2}\mathrm{C}N^2\frac{\partial\hat{W}_0}{\partial s} \tag{4.36c}$$

$$\mathcal{D}_{c,2} = -\kappa\hat{V}_1 - \frac{\partial\hat{U}_1}{\partial s} + \frac{\partial\kappa}{\partial s}\kappa^2N^2\hat{U}_0 + \frac{\partial\kappa}{\partial s}\kappa N\hat{U}_1 - \kappa^2N\hat{V}_1 - \kappa^3N^2\hat{V}_0, \tag{4.36d}$$

with

$$\mathcal{A}_0 = -\sigma_2\hat{U}_0 + \frac{\partial^2\hat{U}_0}{\partial N^2}, \tag{4.37a}$$

$$\mathcal{A}_1 = \mathrm{A}\frac{\partial\hat{U}_1}{\partial s} + \mathrm{B}\hat{U}_1 - \mathrm{C}\hat{V}_1, \tag{4.37b}$$

$$\mathcal{A}_2 = \mathrm{C}\frac{\partial\hat{U}_0}{\partial s} - \left(\frac{\partial\mathrm{B}}{\partial N} - \frac{1}{2}\kappa^2\frac{\partial\overline{u}}{\partial s}\right)\hat{U}_0 + \mathrm{D}\hat{V}_0, \tag{4.37c}$$

$$\mathcal{B}_0 = -\sigma_2\hat{V}_0 + \frac{\partial^2\hat{V}_0}{\partial N^2} - \frac{\partial\hat{P}_0}{\partial N}, \tag{4.37d}$$

$$\mathcal{B}_1 = \mathrm{A}\left(\frac{\partial\hat{V}_1}{\partial s} - 2\kappa\hat{U}_1\right), \tag{4.37e}$$

$$\mathcal{B}_2 = \mathrm{C}\left(\frac{\partial\hat{V}_0}{\partial s} - 2\kappa\hat{U}_0\right), \tag{4.37f}$$

$$\mathrm{D} = \kappa^3\overline{u} + \kappa^2\frac{\partial\overline{u}}{\partial N} + \kappa\frac{\partial^2\overline{u}}{\partial N^2} + \frac{\partial^3\overline{u}}{\partial N^3}. \tag{4.37g}$$

We notice a new term $\overline{u}_{NNN}$ appearing in D. This term can be calculated in the same manner as (4.29). With some manipulation this leads to

$$\begin{aligned}\hat{L}_0\hat{V}_2 = &\left(\frac{2\kappa}{\overline{u}}\right)\left\{\mathcal{A}_0 + N\mathcal{A}_1 + N^2\mathcal{A}_2\right\} + \\ &\left(\frac{2\kappa}{\overline{u}}\right)\left\{\left[\sigma_0 + \frac{\partial\overline{u}}{\partial s}\right]\frac{1}{2\kappa\overline{u}}\left(\mathcal{B}_0 + N\mathcal{B}_1 + N^2\mathcal{B}_2\right)\right\} + \\ &\left(\frac{2\kappa}{\overline{u}}\right)\left\{\frac{\partial}{\partial s}\left[\frac{1}{2\kappa\overline{u}}\left(\mathcal{B}_0 + N\mathcal{B}_1 + N^2\mathcal{B}_2\right)\right]\right\}. \end{aligned} \tag{4.38}$$

We can apply a solvability condition to (4.38), as we did with previous order to obtain

$$\begin{aligned}\int_0^{\mathcal{C}} L_0^*\hat{V}_2\cdot\hat{V}_0^\dagger ds = \int_0^{\mathcal{C}}&\left(\frac{2\kappa}{\overline{u}}\right)\left\{\mathcal{A}_0 + N\mathcal{A}_1 + N^2\mathcal{A}_2 + \right. \\ &\left[\sigma_0 + \frac{\partial\overline{u}}{\partial s}\right]\frac{1}{2\kappa\overline{u}}\left(\mathcal{B}_0 + N\mathcal{B}_1 + N^2\mathcal{B}_2\right) + \\ &\left.\frac{\partial}{\partial s}\left[\frac{1}{2\kappa\overline{u}}\left(\mathcal{B}_0 + N\mathcal{B}_1 + N^2\mathcal{B}_2\right)\right]\right\}\cdot\hat{V}_0^\dagger e^{\int_0^s c_0(s^*)ds^*}ds = 0. \end{aligned} \tag{4.39}$$

We observe in (4.39) that there are different powers of N and we can divide the right hand side in this way. As with the previous order, the left hand side disappears such that

$$\int_0^{\mathcal{C}} L_0^*\hat{V}_2\cdot\hat{V}_0^\dagger ds = 0, \tag{4.40}$$

and yields

$$\int_0^{\mathcal{C}}\left(\frac{2\kappa}{\overline{u}}\right)\left\{\left[\sigma_0 + \frac{\partial\overline{u}}{\partial s}\right]\frac{\mathcal{B}_0}{2\kappa\overline{u}} + \frac{\partial}{\partial s}\left[\frac{\mathcal{B}_0}{2\kappa\overline{u}}\right] + \mathcal{A}_0\right\}\cdot\hat{V}_0^\dagger e^{\int_0^s c_0(s^*)ds^*}ds + \tag{4.41a}$$

$$N\int_0^{\mathcal{C}}\left(\frac{2\kappa}{\overline{u}}\right)\left\{\left[\sigma_0 + \frac{\partial\overline{u}}{\partial s}\right]\frac{\mathcal{B}_1}{2\kappa\overline{u}} + \frac{\partial}{\partial s}\left[\frac{\mathcal{B}_1}{2\kappa\overline{u}}\right] + \mathcal{A}_1\right\}\cdot\hat{V}_0^\dagger e^{\int_0^s c_0(s^*)ds^*}ds + \tag{4.41b}$$

$$N^2\int_0^{\mathcal{C}}\left(\frac{2\kappa}{\overline{u}}\right)\left\{\left[\sigma_0 + \frac{\partial\overline{u}}{\partial s}\right]\frac{\mathcal{B}_2}{2\kappa\overline{u}} + \frac{\partial}{\partial s}\left[\frac{\mathcal{B}_2}{2\kappa\overline{u}}\right] + \mathcal{A}_2\right\}\cdot\hat{V}_0^\dagger e^{\int_0^s c_0(s^*)ds^*}ds = 0. \tag{4.41c}$$

We notice that the terms $\mathcal{A}_n$ and $\mathcal{B}_n$, with $n = 0, 1, 2$, contain streamwise velocities and pressure. First we can eliminate the pressure from (4.20c) and (4.20d) which can be simplified to

$$\frac{\partial\hat{P}_0}{\partial N} = \sigma_0\frac{\partial^2\hat{V}_0}{\partial N^2} + \frac{\partial\overline{u}}{\partial N}\frac{\partial^2\hat{V}_0}{\partial s\partial N} + \overline{u}\frac{\partial^3\hat{V}_0}{\partial s\partial N^2}. \tag{4.42}$$

We can replace the $\hat{U}_0$ terms from the n-momentum equation of (4.20b). Hence,

$$\hat{U}_0 = \frac{1}{2\overline{u}\kappa}\left\{\sigma_0\hat{V}_0 + \overline{u}\frac{\partial\hat{V}_0}{\partial s}\right\}, \tag{4.43}$$

and (4.43) derivative with respect to s can be expressed as

$$\frac{\partial\hat{U}_0}{\partial s} = \frac{\partial^2\hat{V}_0}{\partial s^2}\left[\frac{1}{2\kappa}\right] + \frac{\partial\hat{V}_0}{\partial s}\left[\sigma_0 + \frac{\partial\overline{U}}{\partial s} - \frac{\mathrm{E}}{2\overline{u}\kappa^2}\right] - \hat{V}_0\left[\frac{\sigma_0\mathrm{E}}{2\overline{u}^2\kappa^2}\right], \tag{4.44}$$

with $\mathrm{E} = \kappa\frac{\partial\overline{u}}{\partial s} + \overline{u}\frac{\partial\kappa}{\partial s}$. We can replace the $\hat{U}_{0NN}$ term from the s-momentum equation of (4.36a). Hence,

$$\begin{aligned}\frac{\partial^2\hat{U}_0}{\partial N^2} = \frac{1}{2\overline{u}\kappa}&\left\{\sigma_0\frac{\partial^2\hat{V}_0}{\partial N^2} + \frac{\partial^2\overline{u}}{\partial N^2}\frac{\partial\hat{V}_0}{\partial s} + 2\frac{\partial\overline{u}}{\partial N}\frac{\partial^2\hat{V}_0}{\partial s\partial N} + \overline{u}\frac{\partial^3\hat{V}_0}{\partial s\partial N^2}\right\}\\ &-\frac{2\frac{\partial\overline{u}}{\partial N}\kappa}{(2\overline{u}\kappa)^2}\left\{\sigma_0\frac{\partial\hat{V}_0}{\partial N} + \frac{\partial\overline{u}}{\partial N}\frac{\partial\hat{V}_0}{\partial s} + \overline{u}\frac{\partial^2\hat{V}_0}{\partial s\partial N}\right\}\\ &-\frac{\frac{\partial\overline{u}}{\partial N}}{(2\overline{u}^2\kappa)}\left\{\sigma_0\frac{\partial\hat{V}_0}{\partial N} + \frac{\partial\overline{u}}{\partial N}\frac{\partial\hat{V}_0}{\partial s} + \overline{u}\frac{\partial^2\hat{V}_0}{\partial s\partial N}\right\}\\ &+\left(\frac{\frac{\partial^2\overline{u}}{\partial N^2} - \frac{1}{\overline{u}}\left(\frac{\partial\overline{u}}{\partial N}\right)^2}{2\overline{u}^2\kappa}\right)\left\{\sigma_0\hat{V}_0 + \overline{u}\frac{\partial\hat{V}_0}{\partial s}\right\}.\end{aligned} \tag{4.45}$$

We need to eliminate the velocity, $\hat{U}_1$, by rearranging (4.25b) we have

$$\hat{U}_1 = \frac{1}{2\overline{u}\kappa}\left\{\sigma_0\hat{V}_1 + \overline{u}\frac{\partial\hat{V}_1}{\partial s} - \hat{V}_0\sigma_0 N\frac{\mathrm{A}}{\overline{u}}\right\}, \tag{4.46}$$

and (4.46) derivative with respect to s can be expressed as

$$\begin{aligned}\frac{\partial\hat{U}_1}{\partial s} &= \frac{\partial^2\hat{V}_1}{\partial s^2}\left[\frac{1}{2\kappa}\right] + \frac{\partial\hat{V}_1}{\partial s}\left[\sigma_0 + \frac{\partial\overline{U}}{\partial s} - \frac{\mathrm{E}}{2\overline{u}\kappa^2}\right] - \hat{V}_1\left[\frac{\sigma_0\mathrm{E}}{2\overline{u}^2\kappa^2}\right]\\ &- \frac{\partial\hat{V}_0}{\partial s}\left[\frac{1}{2\overline{u}\kappa}\left(\frac{\sigma_0\mathrm{A}N}{\overline{u}}\right)\right] + \hat{V}_0\left[\frac{\sigma_0 N}{2\overline{u}^3\kappa}\left(\mathrm{A}\frac{\partial\overline{u}}{\partial s} - \overline{u}\frac{\partial\mathrm{A}}{\partial s} + \kappa\mathrm{EA}\right)\right].\end{aligned} \tag{4.47}$$

We can then substitute (4.42), (4.43) and (4.45) into (4.41a). We get the following

$$
\begin{aligned}
\mathcal{A}_0 &= -\frac{\sigma_2}{2\overline{u}\kappa}\left\{\sigma_0\hat{V}_0+\overline{u}\frac{\partial\hat{V}_0}{\partial s}\right\}+\frac{1}{2\overline{u}\kappa}\left\{\sigma_0\frac{\partial^2\hat{V}_0}{\partial N^2}+\frac{\partial^2\overline{u}}{\partial N^2}\frac{\partial\hat{V}_0}{\partial s}+2\frac{\partial\overline{u}}{\partial N}\frac{\partial^2\hat{V}_0}{\partial s\partial N}+\overline{u}\frac{\partial^3\hat{V}_0}{\partial s\partial N^2}\right\}\\
&- \frac{2\frac{\partial\overline{u}}{\partial N}\kappa}{(2\overline{u}\kappa)^2}\left\{\sigma_0\frac{\partial\hat{V}_0}{\partial N}+\frac{\partial\overline{u}}{\partial N}\frac{\partial\hat{V}_0}{\partial s}+\overline{u}\frac{\partial^2\hat{V}_0}{\partial s\partial N}\right\}-\frac{\frac{\partial\overline{u}}{\partial N}}{(2\overline{u}^2\kappa)}\left\{\sigma_0\frac{\partial\hat{V}_0}{\partial N}+\frac{\partial\overline{u}}{\partial N}\frac{\partial\hat{V}_0}{\partial s}+\overline{u}\frac{\partial^2\hat{V}_0}{\partial s\partial N}\right\}\\
&+ \left(\frac{\frac{\partial^2\overline{u}}{\partial N^2}-\frac{1}{\overline{u}}\left(\frac{\partial\overline{u}}{\partial N}\right)^2}{2\overline{u}^2\kappa}\right)\left\{\sigma_0\hat{V}_0+\overline{u}\frac{\partial\hat{V}_0}{\partial s}\right\},\\
\mathcal{A}_1 &= \mathrm{A}\left\{\frac{\partial^2\hat{V}_1}{\partial s^2}\left[\frac{1}{2\kappa}\right]+\frac{\partial\hat{V}_1}{\partial s}\left[\sigma_0+\frac{\partial\overline{u}}{\partial s}-\frac{\mathrm{E}}{2\overline{u}\kappa^2}\right]-\hat{V}_1\left[\frac{\sigma_0\mathrm{E}}{2\overline{u}^2\kappa^2}\right]\right.\\
&- \left.\frac{\partial\hat{V}_0}{\partial s}\left[\frac{1}{2\overline{u}\kappa}\left(\frac{\sigma_0\mathrm{A}N}{\overline{u}}\right)\right]+\hat{V}_0\left[\frac{\sigma_0 N}{2\overline{u}^3\kappa}\left(\mathrm{A}\frac{\partial\overline{u}}{\partial s}-\overline{u}\frac{\partial\mathrm{A}}{\partial s}+\kappa\mathrm{EA}\right)\right]\right\}\\
&+ \frac{\mathrm{B}}{2\overline{u}\kappa}\left\{\sigma_0\hat{V}_1+\overline{u}\frac{\partial\hat{V}_1}{\partial s}-\hat{V}_0\left[\sigma_0 N\frac{\mathrm{A}}{\overline{u}}\right]\right\}-\mathrm{C}\hat{V}_1,\\
\mathcal{A}_2 &= \mathrm{C}\left\{\frac{\partial^2\hat{V}_0}{\partial s^2}\left[\frac{1}{2\kappa}\right]+\frac{\partial\hat{V}_0}{\partial s}\left[\sigma_0+\frac{\partial\overline{u}}{\partial s}-\frac{\mathrm{E}}{2\overline{u}\kappa^2}\right]-\hat{V}_0\left[\frac{\sigma_0\mathrm{E}}{2\overline{u}^2\kappa^2}\right]\right\}\\
&- \left(\frac{\partial\mathrm{B}}{\partial N}-\frac{1}{2}\kappa^2\frac{\partial\overline{u}}{\partial s}\right)\frac{1}{2\overline{u}\kappa}\left\{\sigma_0\hat{V}_0+\overline{u}\frac{\partial\hat{V}_0}{\partial s}\right\}+\mathrm{D}\hat{V}_0,\\
\mathcal{B}_0 &= -\sigma_2\hat{V}_0+(1-\sigma_0)\frac{\partial^2\hat{V}_0}{\partial N^2}-\frac{\partial\overline{u}}{\partial N}\frac{\partial^2\hat{V}_0}{\partial s\partial N}-\overline{u}\frac{\partial^3\hat{V}_0}{\partial s\partial N^2},\\
\mathcal{B}_1 &= \mathrm{A}\left(\frac{1}{\overline{u}}\left\{\sigma_0\hat{V}_1-\hat{V}_0\left[\sigma_0 N\frac{\mathrm{A}}{\overline{u}}\right]\right\}\right),\\
\mathcal{B}_2 &= -\frac{\sigma_0\mathrm{C}\hat{V}_0}{\overline{u}}.
\end{aligned}
$$

We notice that only $\hat{V}_0$ and $\hat{V}_1$ velocities remain. From the expansion of the velocity

$$\hat{V}=\hat{V}_0+k^{-1/2}\hat{V}_1+k^{-1}\hat{V}_2, \tag{4.49}$$

we want to split the function $\hat{V}$ into separable functions depending on s or N independently and therefore we impose some amplitude function in N in the following way

$$\hat{V}=d_0(N)\upsilon_0(s)+k^{-1/2}d_1(N)\upsilon_1(s)+k^{-1}d_2(N)\upsilon_2(s). \tag{4.50}$$

Following the work of Papageorgiou [69], this separable form can be substituted into the previous order equations of (4.22) and (4.27) to obtain

$$d_0(N)\hat{L}_0 v_0 = 0, \tag{4.51}$$

$$d_1(N)\hat{L}_0 v_1 = d_0(N)\left[c_2\frac{\partial^2}{\partial s^2} + c_3\frac{\partial}{\partial s} + c_4\right]v_0, \tag{4.52}$$

with

$$\hat{L}_0 = \frac{\partial^2}{\partial s^2} + c_0\frac{\partial}{\partial s} + c_1, \tag{4.53}$$

where

$$c_2 = \frac{\mathrm{A}}{\overline{u}}, \quad c_3 = \frac{1}{\overline{u}}\left(1 + \kappa\frac{\partial \overline{u}}{\partial s} - \frac{\partial^2 \overline{u}}{\partial s \partial N}\right) + \frac{1}{\overline{u}^2}\left(\mathrm{E}\frac{\partial \mathrm{A}}{\partial s} + \mathrm{A}\left[\sigma_0 + \frac{\partial \overline{u}}{\partial s}\right]\right), \tag{4.54}$$

$$c_4 = \frac{2\kappa \mathrm{C}}{\overline{u}} + \frac{\sigma_0}{\overline{u}^2}\left(2\frac{\partial \mathrm{A}}{\partial s} + \kappa\frac{\partial \overline{u}}{\partial s} - \frac{\partial^2 \overline{u}}{\partial s \partial N} + 2\mathrm{EA}\right) + \frac{1}{\overline{u}^3}\left(\sigma_0 \mathrm{E}\frac{\partial \mathrm{A}}{\partial s} - \mathrm{A}\left[\sigma_0 + \frac{\partial \overline{u}}{\partial s}\right]\right). \tag{4.55}$$

Since neither (4.22) and (4.27) are explicitly dependent on N, (apart from the base flow terms) nor are there any terms involving derivatives with respect to N we can include the amplitude functions $d_0(N)$ and $d_1(N)$ and the same set of equations are satisfied. These amplitude functions only change the eigenfunctions in (4.51) and (4.52) by some constant factor and can be easily taken out accordingly. Hence we have $\mathcal{A}_m$, $\mathcal{B}_m$ in terms of their new variables as

$$\mathcal{A}_0 = \overline{a}_0\frac{\partial^2 d_0}{\partial N^2} + \overline{a}_1\frac{\partial d_0}{\partial N} + \overline{a}_2 d_0, \tag{4.56}$$

$$\mathcal{A}_1 = d_1\overline{\mathcal{A}}_1 + N d_0\hat{\mathcal{A}}_1, \tag{4.57}$$

$$\mathcal{A}_2 = d_0\overline{\mathcal{A}}_2, \tag{4.58}$$

$$\mathcal{B}_0 = \overline{b}_0\frac{\partial^2 d_0}{\partial N^2} + \overline{b}_1\frac{\partial d_0}{\partial N} + \overline{b}_2 d_0, \tag{4.59}$$

$$\mathcal{B}_1 = d_1\overline{\mathcal{B}}_1 + N d_0\hat{\mathcal{B}}_1, \tag{4.60}$$

$$\mathcal{B}_2 = d_0\overline{\mathcal{B}}_2, \tag{4.61}$$

where the additional variables can be located in appendix F. Hence (4.39) now becomes

$$\iota_0 \frac{\partial^2 d_0}{\partial N^2} + \iota_1 \frac{\partial d_0}{\partial N} + \left(\iota_2 + \iota_3 N + \iota_4 N^2\right) d_0 = 0, \tag{4.62}$$

where

$$\begin{aligned}
\iota_0 &= \int_0^{\mathcal{C}} \left(\frac{2\kappa}{\overline{u}}\right) \left\{ \left[\sigma_0 + \frac{\partial \overline{u}}{\partial s}\right] \frac{\bar{b}_0}{2\kappa\overline{u}} + \frac{\partial}{\partial s}\left[\frac{\bar{b}_0}{2\kappa\overline{u}}\right] + \overline{a}_0 \right\} \cdot \overline{v_0}\, ds, \\
\iota_1 &= \int_0^{\mathcal{C}} \left(\frac{2\kappa}{\overline{u}}\right) \left\{ \left[\sigma_0 + \frac{\partial \overline{u}}{\partial s}\right] \frac{\bar{b}_1}{2\kappa\overline{u}} + \frac{\partial}{\partial s}\left[\frac{\bar{b}_1}{2\kappa\overline{u}}\right] + \overline{a}_1 \right\} \cdot \overline{v_0}\, ds, \\
\iota_2 &= \int_0^{\mathcal{C}} \left(\frac{2\kappa}{\overline{u}}\right) \left\{ \left[\sigma_0 + \frac{\partial \overline{u}}{\partial s}\right] \frac{(\overline{\mathcal{B}}_2 + \hat{\mathcal{B}}_2)}{2\kappa\overline{u}} + \frac{\partial}{\partial s}\left[\frac{(\overline{\mathcal{B}}_2 + \hat{\mathcal{B}}_2)}{2\kappa\overline{u}}\right] + \overline{\mathcal{A}}_2 + \hat{\mathcal{A}}_2 \right\} \cdot \overline{v_0}\, ds, \\
\iota_3 &= \int_0^{\mathcal{C}} \left(\frac{2\kappa}{\overline{u}}\right) \left\{ \left[\sigma_0 + \frac{\partial \overline{u}}{\partial s}\right] \frac{\overline{\mathcal{B}}_1}{2\kappa\overline{u}} + \frac{\partial}{\partial s}\left[\frac{\overline{\mathcal{B}}_1}{2\kappa\overline{u}}\right] + \overline{\mathcal{A}}_1 \right\} \cdot \overline{v_0}\, ds, \\
\iota_4 &= \int_0^{\mathcal{C}} \left(\frac{2\kappa}{\overline{u}}\right) \left\{ \left[\sigma_0 + \frac{\partial \overline{u}}{\partial s}\right] \frac{\bar{b}_2}{2\kappa\overline{u}} + \frac{\partial}{\partial s}\left[\frac{\bar{b}_2}{2\kappa\overline{u}}\right] + \overline{a}_2 \right\} \cdot \overline{v_0}\, ds,
\end{aligned}$$

with $\overline{v_0} = {v_0}^{\dagger} e^{\int_0^s c_0(s^*)ds^*}$. Equation (4.62) can be reduced further by rearranging ι_1 and ι_3. Therefore (4.62) becomes

$$\frac{\partial^2 d_0}{\partial \eta^2} + \left(\frac{\eta^2}{4} - j\right) d_0 = 0, \tag{4.63}$$

where

$$\eta = \sqrt{\frac{2\iota_4}{\iota_0}}\, N \quad \text{and} \quad j = \frac{\iota_2}{2\sqrt{\iota_0 \iota_4}}. \tag{4.64}$$

As you can see equation (4.63) is in the form of a well known equation called a Weber differential equation. This has solutions called parabolic cylinder functions. We know that these solutions decay for large $\pm N$. The disturbance only exists within a small region around the elliptical streamline. We can find σ_2 by solving the eigenvalue problem of (4.63). If we have an ellipse of size $a = 2.0$ and $b = 1.0$, we have a $\sigma_2 = 3.826 + 0.812i$ with the following eigenfunction.

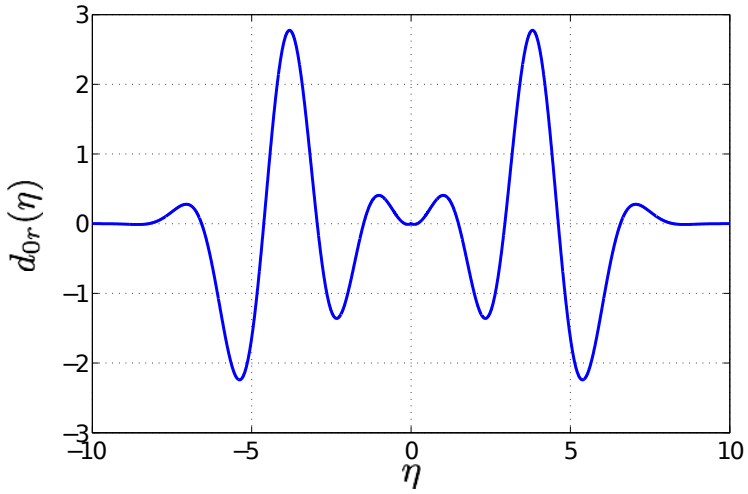

Figure 4.5: An example of the real part of the amplitude function, d_0, with the rescaled normal coordinate, η, for fixed $a = 2.0$ and $b = 1.0$.

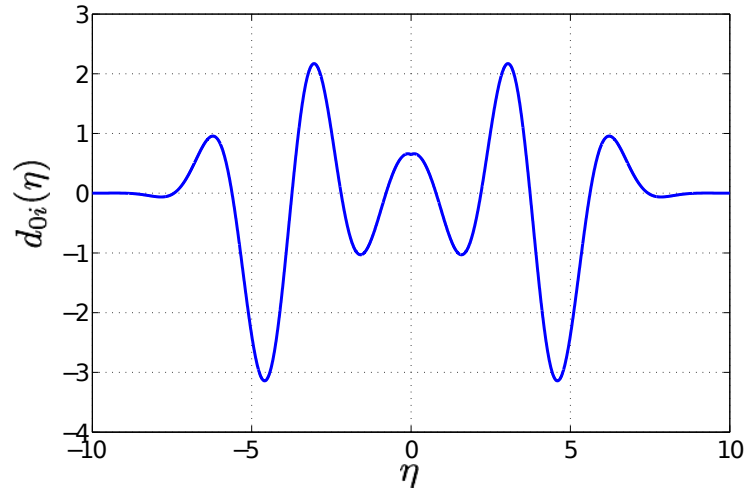

Figure 4.6: An example of the imaginary part of the amplitude function, d_0, with the rescaled normal coordinate (η) for fixed $a = 2.0$ and $b = 1.0$.

A solution has been found for an ellipse of size $a = 2.0$ and $b = 1.0$ which we have found the corresponding amplitude function. Observing figures 4.5 and 4.6, we notice that they both satisfy the boundary conditions and are both symmetric about $\eta = 0$. This is expected since they are solutions of the Weber differential equation. We have the temporal growth rate, the location of the instability and the behaviour of the eigenfunctions in both the streamline and normal to the streamline directions. Once we have obtained an analytical form of the streamlines, the same analysis can

be performed as for the example problem of a circle and an ellipse. A reminder of the steps involved

1. Solve the eigenvalue problem of equation (4.22) to find the leading order temporal growth rate σ_{0r}.

2. Find the value of the integral condition of equation (4.34) is satisfied (i.e $I_N = 0$) - this gives the location of where the disturbance lies.

3. The next order growth rate term (σ_{2r}) is calculated from the eigenvalue problem of equation (4.63), with the total temporal growth rate given by $\sigma_r = \sigma_{0r} + k^{-1}\sigma_{2r}$.

4.3 Localised Streamlines

4.3.1 Circular streamlines

We calculate the value of the integral with different values of K. First we consider the same problem as Bayly for a centrifugal-type instability, which he analysed circularly symmetric streamlines and where the initial interest of this problem arisen.

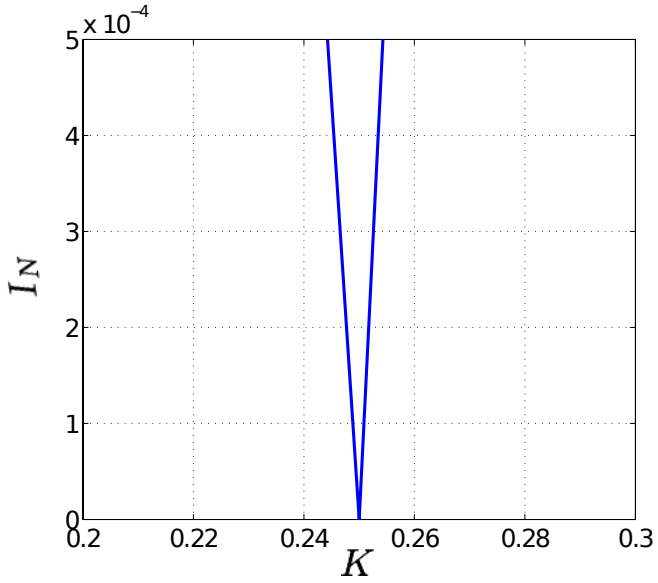

Figure 4.7: The value of the integral I_N with varying K for $a = 2.0$ and $b = 2.0$.

The location in space is shown in figure 4.8, which relates to the previous figure of 4.7, analysing the basic flow streamlines and indicating the location of the disturbance. By applying this new analysis to the same problem which Bayly [6] analysed with

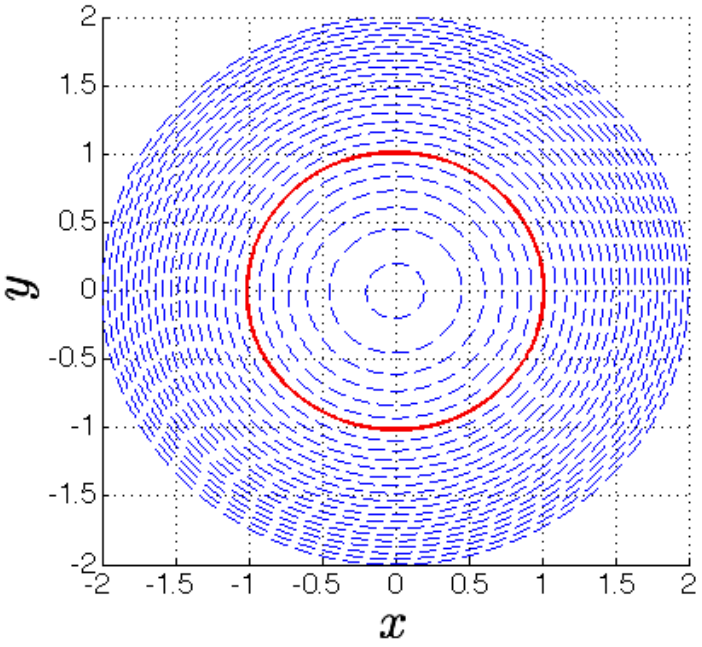

Figure 4.8: The analysed streamlines in blue (.....) lines with the location of the instability represented as the red (_____) line for the circular streamlines with $a = 2.0$ and $b = 2.0$.

Floquet analysis, we have found the location of this instability. In figure 4.1 which is at some distance K away from the centre of the vortex O'. For this example we have $K = 0.25$ for $I_N = 0$ to be satisfied as shown in figure 4.7. We can extend this theory to elliptical streamlines since the circular streamlines are neutrally stable. We can do this by increasing the radius, a, and seeing if we can find a similar region for an ellipse for which this condition is satisfied.

4.3.2 Elliptical streamlines

If we now focus our attention to an ellipse and we vary the parameter K such that we have a family of ellipses, similar to the circular streamlines we can execute the same approach.

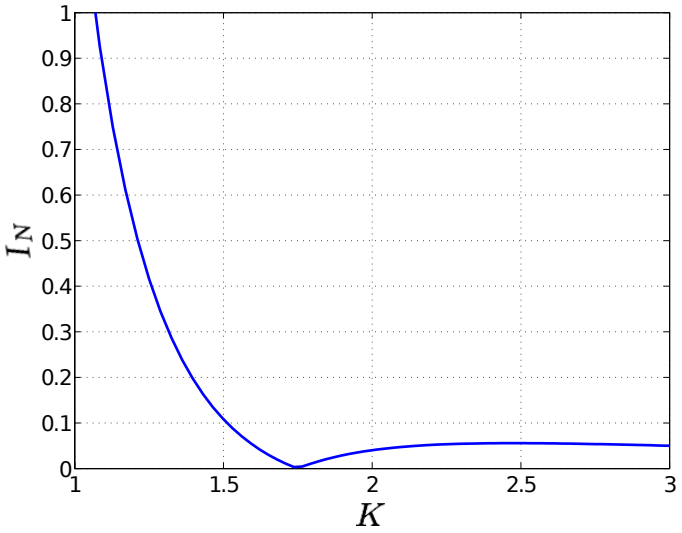

Figure 4.9: The value of the integral I_N with varying K for $a = 2.0$ and $b = 1.15$.

We change the initial size of the ellipse and investigate whether there are more ellipses for which this condition is satisfied. We can see that with $a = 2.0$ and $b = 1.8$ this instability has arisen. We can see if this is the situation for ellipses of other sizes. We focus on keeping the axis fixed at $b = 2.0$, $a = 1.8$ and vary K so we have a family of streamlines with the same a/b ratio. Two examples of different sized ellipses are shown in the following two figures. In figure 4.10a the location of the disturbance is similar to figure 4.8 but we note that they have comparable values for the axes. As we decrease b we notice that the location of the disturbance gets further away from the origin of the vortex, O'.

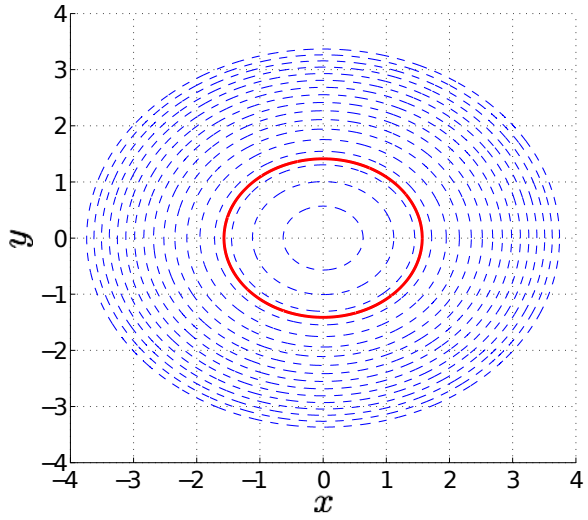

(a) $a = 2.0, b = 1.8$.

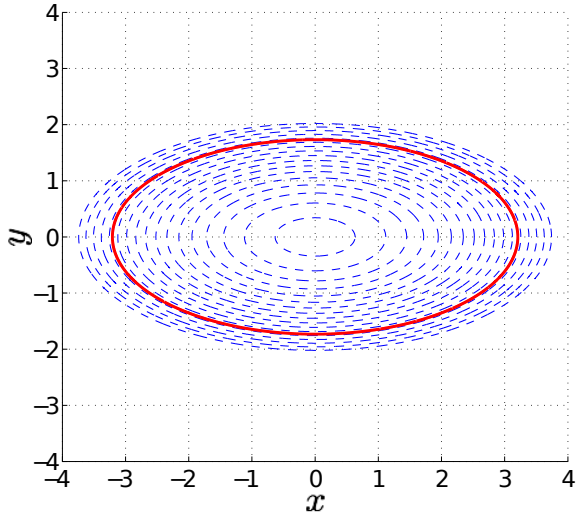

(b) $a = 2.0, b = 1.08$

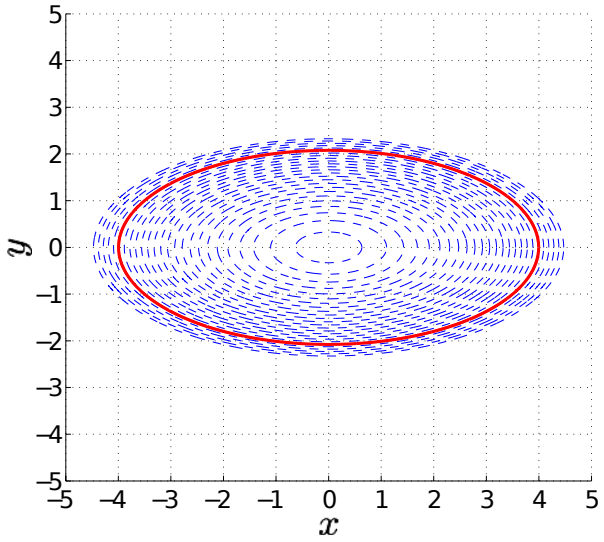

(c) $a = 2.0, b = 1.04$

Figure 4.10: The analysed streamlines in blue (.....) lines with the location of the instability represented as the red (_____) line for ellipses.

We can do this for many sized ellipses. Even if the axes are reversed the same results can be obtained. The location where the disturbance exists can be plotted for various different ellipses as seen in figure 4.11.

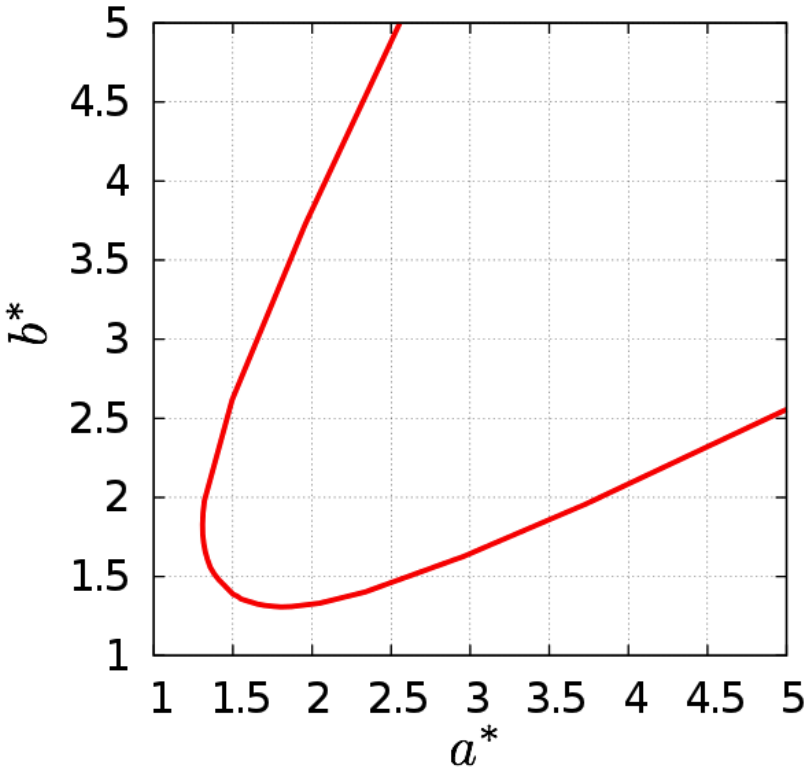

Figure 4.11: Relationship between a^* and b^* for the condition of $I_N = 0$ with $a^* = aK^{1/2}$ and $b^* = bK^{1/2}$.

We have introduced new variables a^* and b^* which determine the location of the disturbance for the minor and major axes, which are given by $a^* = aK^{1/2}$ and $b^* = bK^{1/2}$. Figure 4.11 demonstrates the values at which this condition is satisfied. There is a symmetry between a^* and b^*. We can see that it does not matter which direction the ellipse is stretched - the same location is discovered and hence a and b are interchangeable. The midpoint of the figure 4.11 occurs at $a^* = b^* = 1.41$. This has a circular streamline and is more likely be stable. From figure 4.11 we observe that as a^* or b^* increases in K, we have a linear relationship between them. The gradient of these lines are $2/5$ and $5/2$, respectively. Therefore, there are no isolated regions where the basic flow becomes singular. We use these values of a^* and b^* for our next calculation of the temporal growth rate.

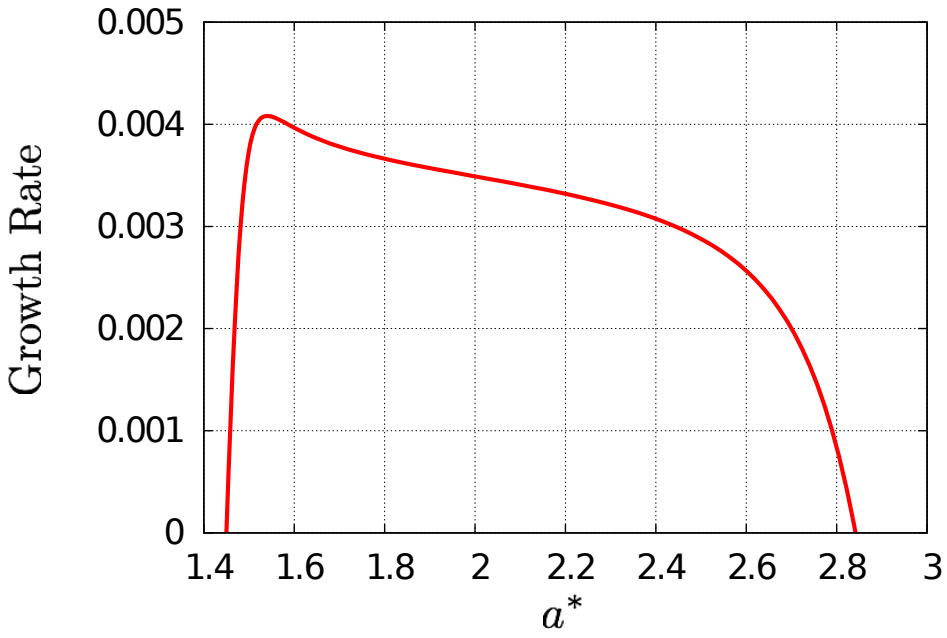

Figure 4.12: Next order growth rate, σ_{2r}, with the major axis, a^*.

We see in figure 4.12 that for $a^* < 1.45$ the disturbance is stable. Then between $a^* = 1.45$ and $a^* = 2.84$ there is an unstable region. Hence, for this family of ellipses the disturbance propagates, whereas for $a^* < 1.45$ or $a^* > 2.84$ no instability arises. As a consequence of this, even though these two constraints on a^* satisfy the integral condition, the disturbance will be stable along the maximised streamline. This agrees with what Bayly stated - that at some distance K away from the centre of the vortex core - there exists some instability.

4.4 Elliptical Instability

Bayly formulated this problem from a theoretical standpoint by using a mathematical approach to this hypothesis. Following the work of Bayly the ensuing elliptical core vortex flow is considered

$$\underline{u}(x, y, z) = \Omega(Ey, E^{-1}x, 0), \quad \Omega > 0, \quad E \geq 1, \tag{4.65}$$

where E is defined as the eccentricity. In this definition, if $E = 1$ then we have a circular streamline. Implementing this definition into our analysis using equation (4.17), we can compare results with Bayly and Pierrehumbert.

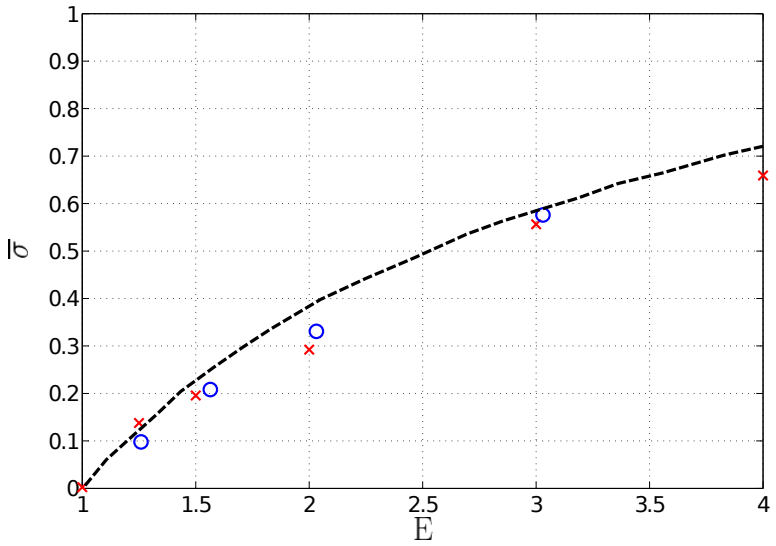

Figure 4.13: Maximum instability growth rate as a function of E. The curve, E, is defined by equation (4.68) from Bayly's paper [5] with ($\circ$) the results of Pierrehumbert's spectral calculation [70] and ($\times$) our calculation with $k = 1000$.

There appears to be relative agreement between the three methods in figure 4.13. From our earlier analysis we observed that as the a axis was stretched the instability become more unstable as seen in figure 4.10. The situation is the same here. The key result is that a relation exists between the eccentricity and temporal growth rate as shown in figure 4.13. This isn't the same as starting from a circular streamline and stretching one of the axes. If one axis increased at a rate of E and the other one decreased by an amount E^{-1}, eventually this disturbance would be highly localised towards the centre. This is a different disturbance, as mentioned before, because we have these highly localised elongated elliptical streamlines to which the largest temporal growth rate occurs for the longest and thinnest elliptical streamlines. It is reassuring that for $E = 1$, which corresponds to a circular streamline, the temporal growth rate is zero - a result that was found earlier. The difference between our theory and Bayly's anaylsis is that he imposed a perturbation of the form

$$(\underline{u}', p') = (\underline{v}(y), \tilde{p}(t))exp(i\underline{k}(t)\underline{x}), \tag{4.66}$$

By performing some manipulation, one can obtain a Floquet problem and the general solution is of the form

$$\underline{v}(t) = e^{\sigma t} f(\Omega(t - t_0)), \tag{4.67}$$

where $f(\phi)$ is periodic with period 2π and consists of a superposition of Floquet modes. By performing some linear algebra and matrix manipulation, Bayly found the temporal growth rate (σ) to be given by

$$\sigma(E, \theta) = \frac{\Omega}{2\pi} \ln \mu(E, \theta). \tag{4.68}$$

This disturbance is known as the elliptical instability, which originates when a vortex exists within a strain field and then the streamlines become elliptical. The linear growth rates scale with the strain rate for this three-dimensional instability to which the flow becomes convoluted due to the small scales involved. This mechanism is related to the understanding of turbulence because it can represent a simple model for secondary instabilities, since the elliptical instability acts on a two-dimensional vortex. Therefore a process has been generated whereby large scale coherent two-dimensional structures propagate via complex three-dimensional mechanisms. This provides an explicit transfer which contributes to transition of flows such as wakes and vortex pairs. A more detailed discussion about elliptical instabilities can be found in [51].

4.5 Generalised Two-Dimensional Closed Streamlines

We are not limited to simple streamlines such as circular or elliptical ones, which we have used for our analysis thus far. We can extend this theory to include any symmetric closed streamline. The meaning of symmetry, in this case, is that the streamline is symmetric about one axis.

4.5.1 Symmetrical Two-Dimensional Closed Streamlines

We first look at a few examples of symmetrical streamlines and what impact they have on the temporal growth rate.

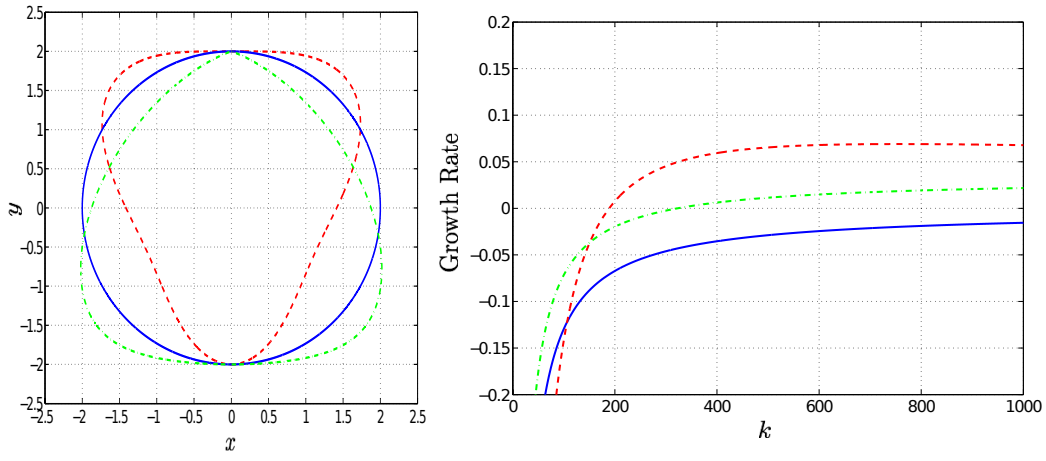

(a) (b)

Figure 4.14: (a) Two-dimensional symmetrical (about $x = 0$) closed streamlines. (b) Corresponding symmetrical streamline growth rates with spanwise wavenumber k.

4.5.2 Non-symmetrical Two-Dimensional Closed Streamlines

We can also see the effect of non-symmetrical streamlines by considering a few examples. This can be shown below.

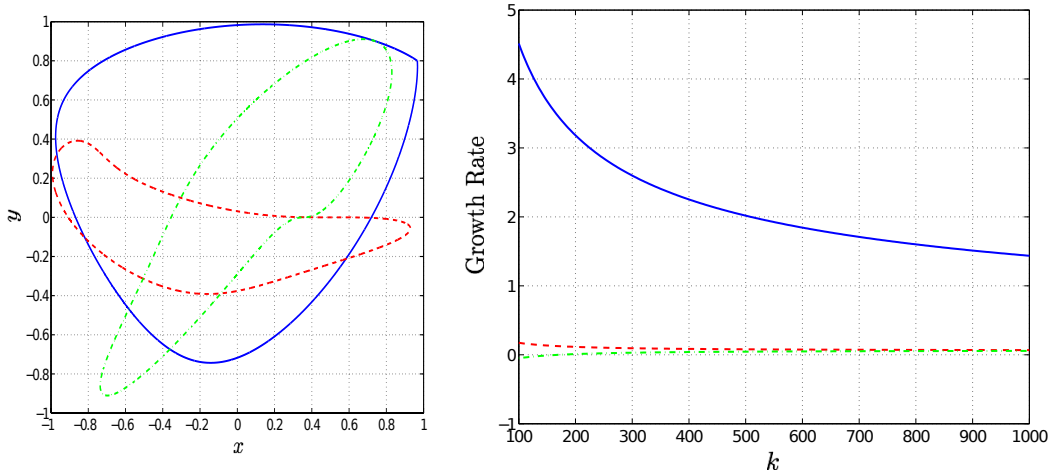

(a) (b)

Figure 4.15: (a) Two-dimensional non-symmetrical closed streamlines. (b) Corresponding non-symmetrical streamline growth rates with spanwise wavenumber k.

In figure 4.14a we have imposed a circular streamline, which is shown as the solid line for a reference to compare with other symmetrical streamlines in figure 4.14a. In our

earlier analysis for any spanwise wavenumber the disturbance is stable for a circular streamline as displayed in figure 4.14b. The structure of the streamline can change accordingly to a tear function - we see this in figure 4.14a - and we see the impact of the temporal growth rate of this streamline in figure 4.14b. The growth rate becomes positive when the spanwise wavenumber is around 300. Therefore, taking this into account the high wavenumber asymptotic disturbance is unstable for this streamline. Another example of a symmetric streamline is given in figure 4.14a, a triangular shaped streamline. This new streamline increases the growth rate compared with the other streamlines, and the growth rate becomes positive for smaller spanwise wavenumbers. It is clear that the temporal growth rate changes with different shaped streamlines and is very sensitive to these changes.

We have only discussed symmetric streamlines thus far but what would happen if non-symmetric streamlines could be analysed in the same manner? It is possible to achieve this in our framework - we consider a few examples of these as seen in figure 4.15a. In figure 4.15a we see a variety of different streamlines producing very different growth rates shown in figure 4.15b. As with the symmetric streamlines, it seems that the growth rate is very sensitive to subtle changes in the streamline. By comparing figures 4.14b and 4.15b we see that the non-symmetric streamlines have larger temporal growth rates than symmetric ones, however, this might not be true for all streamlines. But we must note that the streamline represented by the solid line in figure 4.15a has a discontinuity that possibly makes the temporal growth rate to be large. This might be a numerical instability and we need to be aware of this to minimise any discrepancies. Therefore we need to eliminate any discontinuities that might occur. We can model any two-dimensional closed streamline in this way as long as an analytical form can be obtained, which we now consider a streamline within a cavity.

4.6 Flow inside a Cavity.

We are interested in the global stability properties of streamlines within the cavity with a prescribed imposed flow (for an open cavity). An example would be for instance a shear flow, over a cavity which produce vortices inside inside the cavity. The maximised streamline can be modelled in a similar way to the elliptical instability - this streamline refers to the location where the instability exists. The distance between the wall and streamline needs to be considered as well as the imposed velocity. We can apply this theory to any streamline, as seen in figures 4.14a and 4.15a (both symmetric and antisymmetric streamline). Therefore we can extend this analysis to examine the streamlines generated within the cavity.

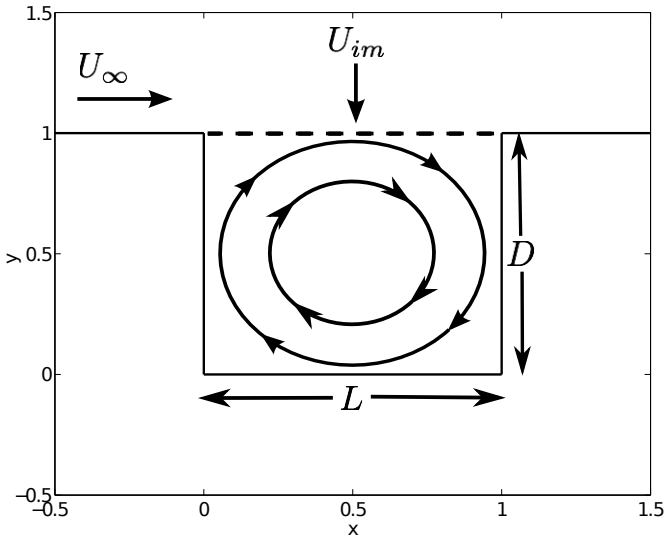

Figure 4.16: Frame of reference and flow configuration of a square cavity. Consisting of the recirculating flow inside the cavity and the shear layer above, there is an imposed velocity, U_{im}, and the cavity has a depth D and length L.

First we consider a closed cavity with no imposed flow conditions.

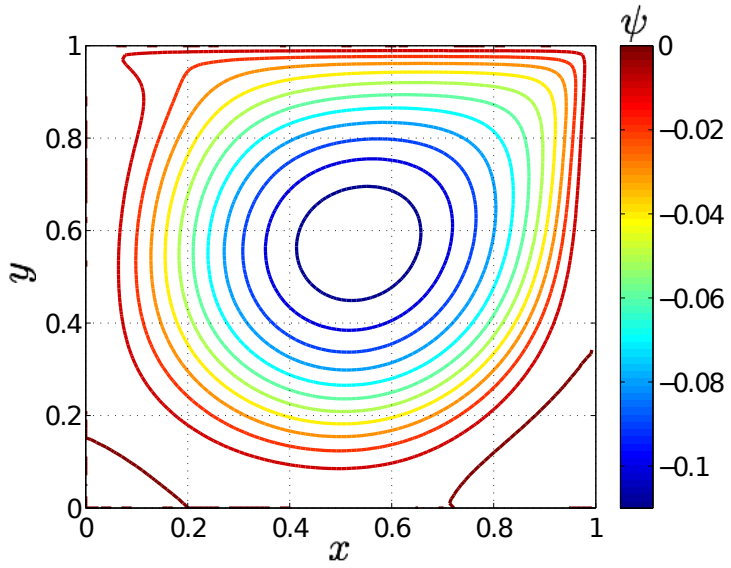

Figure 4.17: Streamlines within a square cavity. The DNS data was provided by Qadri [74] at $Re = 787$.

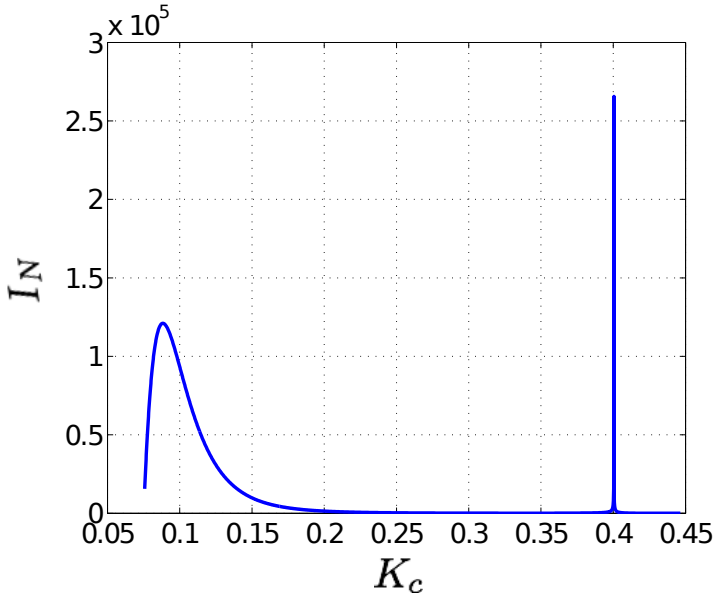

Figure 4.18: The value of the integral I_N with varying K_C for closed square cavity.

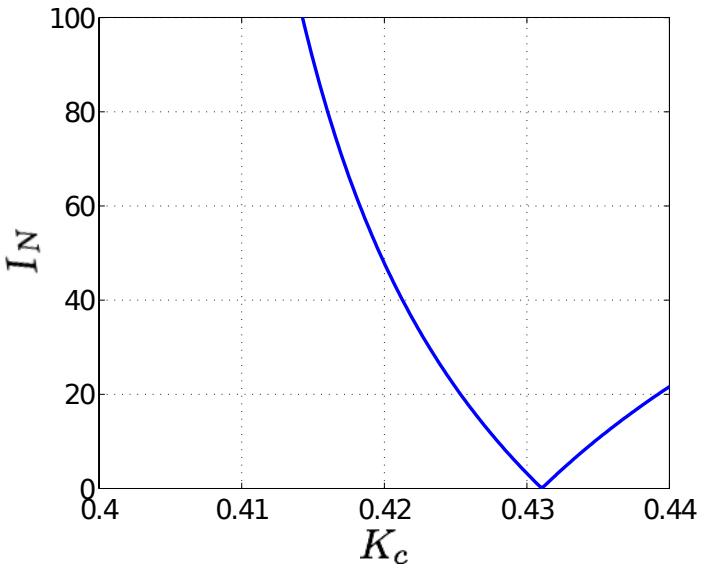

Figure 4.19: The value of the integral I_N with varying K_C for closed square cavity for a smaller range of K_C.

In figure 4.18 we see initially that I_N values are quite large to what we have experienced before and we observe I_N rapidly decreasing.. We decrease the range for I_N and see that the condition is satisfied for $K_c = 0.43103$ in figure (4.19). We can see this location in space with the basic flow streamlines, as we did for the previous analysis.

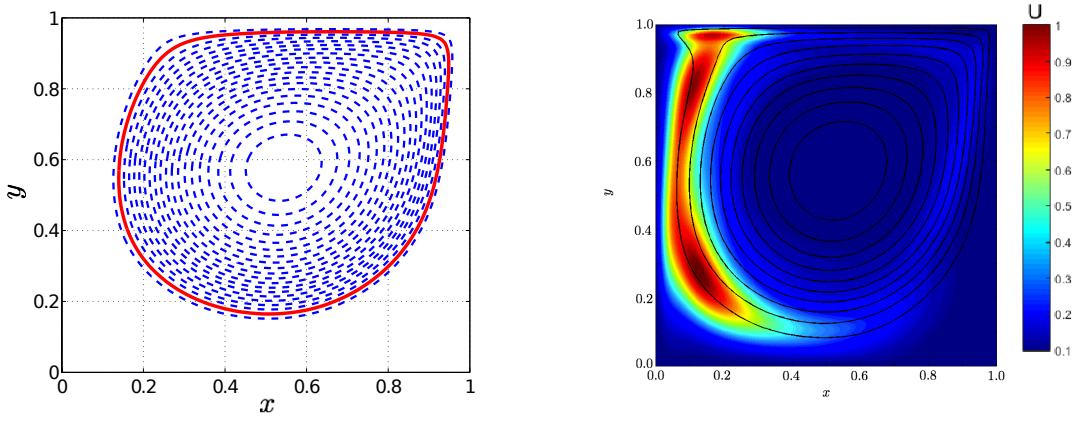

(a) (b)

Figure 4.20: (a)The analysed streamlines in blue (------) lines with the location of the instability as the red (_____) line for the square cavity streamlines. (b)Wavemaker with superimposed base flow streamlines at $Re = 787$ obtained with DNS provided by Qadri [74].

We have found the location of the disturbance as seen in figure 4.20a. By comparing figure 4.20a with figure 4.20b we see that there is agreement with regarding location of the instability. It does not predict the location where the disturbance is most dangerous. This could be due to discrepancies between the methods, since we have a high wavenumber asymptotic method and the numerical approach considers wavenumbers of several magnitudes smaller. We note in figure 4.20b that the streamlines do not represent the streamlines of the actual flow - this could be slightly misleading. As discussed before these streamlines are the basic flow which we are analysing. The idea was to compare with the location of the theoretical prediction. We are interested in the magnitude of the temporal growth rate, therefore we solve (4.63) to find σ_2.

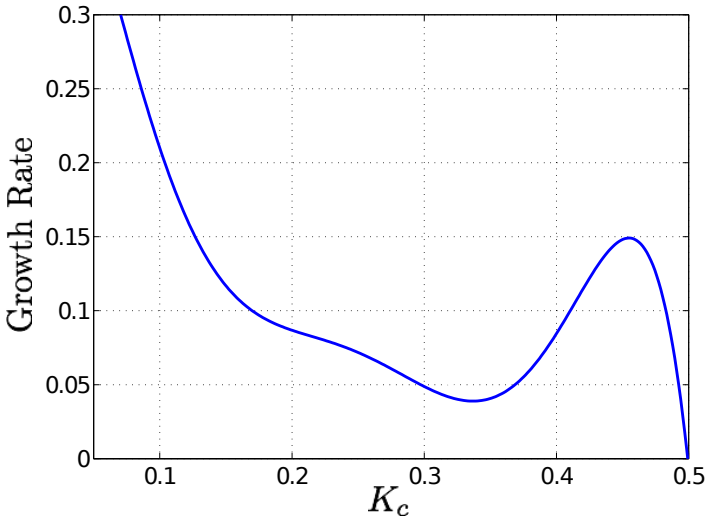

Figure 4.21: The temporal growth rate σ_r with different streamlines.

Observing figure 4.21 we notice that a turning point occurs for $K_c \simeq 0.45$. For any streamline $K_c > 0.49$ is stable since $\sigma_{2r} < 0$ and therefore has a stabilising impact on the total growth rate. We notice that the location of the disturbance doesn't correspond to the maximum growth rate but it appears that the maximum growth rate is near the location of the most dangerous instability mode within the cavity. This seems to be in qualitative agreement with the DNS results. Therefore the asymptotic theory can correctly predict the location of this instability and how dangerous it can be within the cavity. The most dangerous mode refers to the mode with the largest temporal growth rate. We are interested in how the eigenfunctions ($\hat{V}_0(s)$) change for these different streamlines, in particular, this location of the instability. We note that the point at we

start our analysis is shown in figure 4.1.

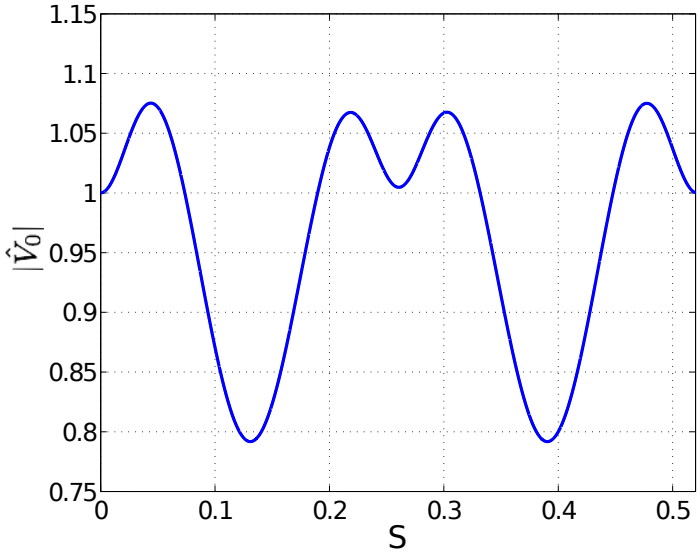

Figure 4.22: Absolute value of the streamwise eigenfunction $\hat{V}_0$ with the streamwise coordinate at $K_c = 0.1$.

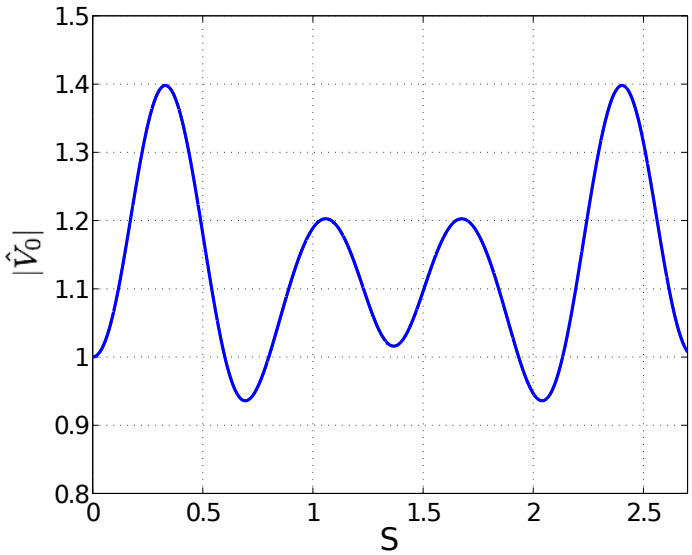

Figure 4.23: Absolute value of the streamwise eigenfunction $\hat{V}_0$ with the streamwise coordinate at $K_c = 0.40$.

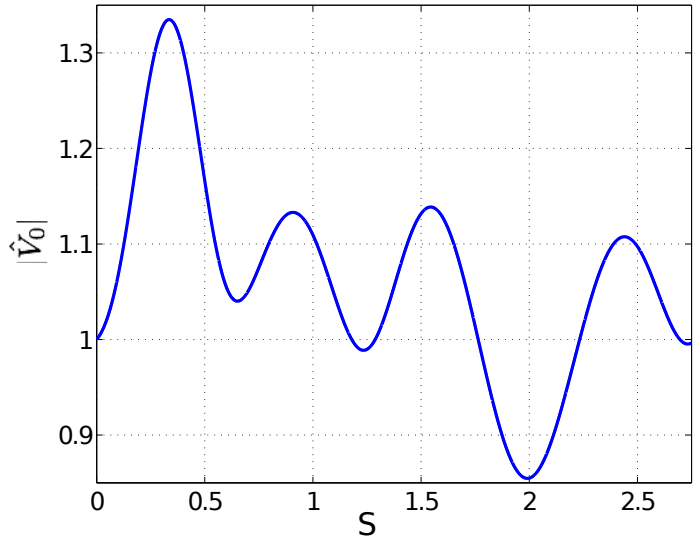

Figure 4.24: Absolute value of the streamwise eigenfunction $\hat{V}_0$ with the streamwise coordinate at $K_c = 0.414$.

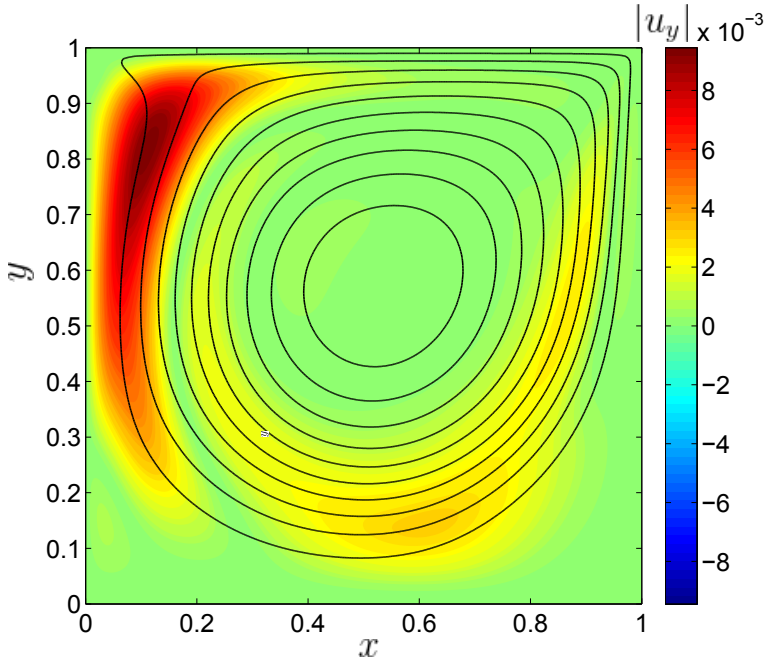

Figure 4.25: Absolute value of the eigenfunction in y for the square cavity with superimposed basic flow streamlines in the cavity from DNS results.

In figure 4.22 we see that there is symmetry about the midpoint in s. We would expect this behaviour since the core is similar to an elliptical streamline. As we change the streamline location, the streamlines develop a pinch point in the corner and therefore

dissociate with an elliptical streamline shape. However, in figure 4.23 the eigenfunction is still symmetric about the mid point. Symmetry breaks when $K_c \simeq 0.41$, which corresponds to non-symmetrical streamlines appearing. We see that the behaviour of the eigenfunction in figure 4.24 resembles that of the DNS results in figure 4.20b. We start at the same location is shown in figure 4.1 which quality agrees with the DNS results. However, the only difference is where the maximum instability occurs. It does predict where the disturbance lies, just not the location of largest growth of the cavity mode. It indicates the locations of the maximum and minimum temporal growth rates. As we move anti-clockwise we see in figure 4.20b that the disturbance lies close to the left wall of the cavity and on the right hand side there is no activity. Figure 4.24 isn't an exact representation of the instability that is propagating along the streamline but gathers the nature of the behaviour inside the cavity. We see that there is an initial increase in the eigenfunction near where the disturbance is located and as we move along the streamline the eigenfunction decreases in amplitude.
We can see the amplitude function at the streamline. We take the absolute value and see that the disturbance decays far away.

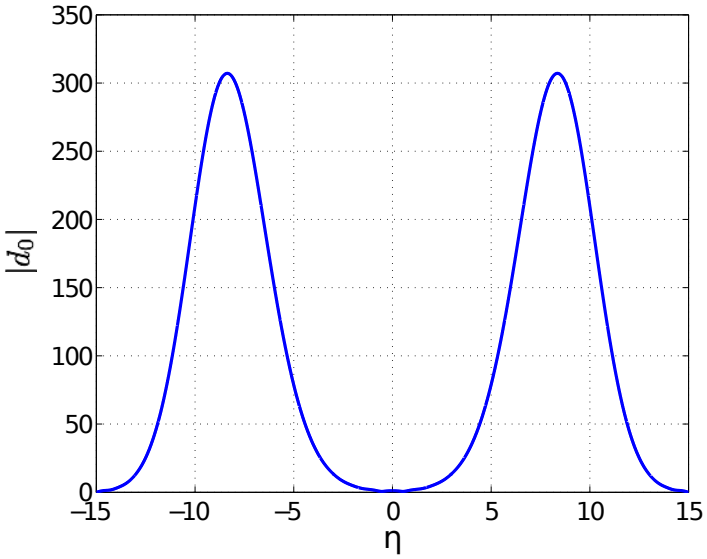

Figure 4.26: Absolute value of the amplitude function, d_0, along the normal coordinate to the streamline.

In figure 4.26 we observe the behaviour of the disturbance away from the streamline and we also see that it satisfies the far-field condition, where the disturbance has the

decay near the cavity wall. We can extend the length by four such that we have at a closed cavity of $L/D = 4$.

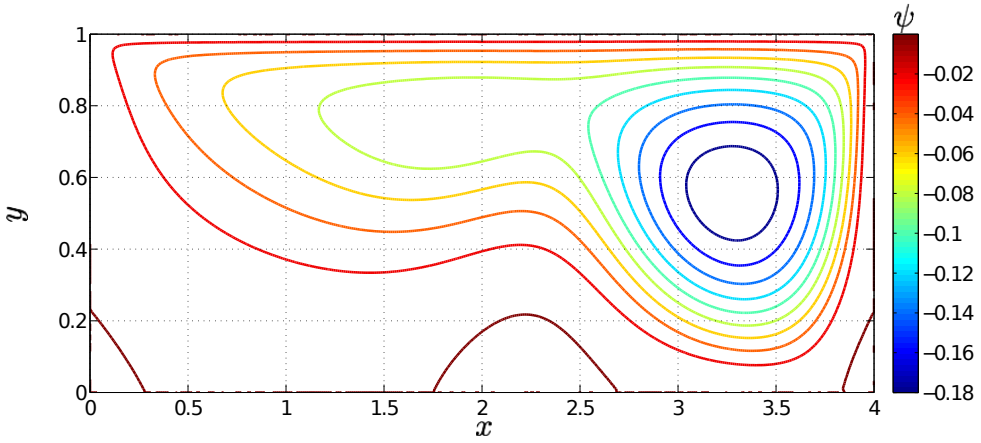

Figure 4.27: Basic flow streamlines within a rectangular cavity at $Re = 289$ with $L/D = 4$. The DNS results were provided Qadri [74].

From figure 4.27 we see that there is a large vortex similar to the square cavity streamlines but regions of recirculation exists at several locations near the wall at $x \sim 0$. We notice that this vortex lies close to the right wall of the cavity. The main vortex is stretched so the streamlines are very different to the square cavity, therefore we should expect very different results. We perform the same calculation as we did for the square cavity and observe the I_N condition for different streamlines.

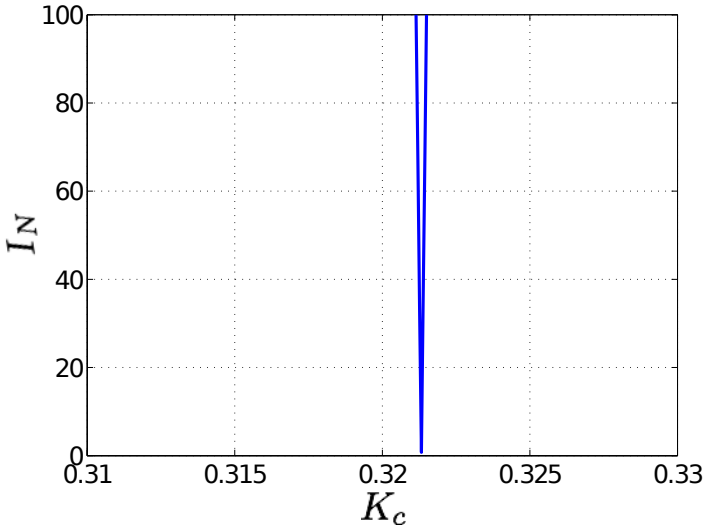

Figure 4.28: The value of the integral I_N with varying K_C for a rectangular cavity for a smaller range

Observing figure 4.28 the condition has been satisfied for $K_c = 0.32132$. We can now plot the streamlines and highlight the neighbourhood of the disturbance as we did for the square cavity. We observe in figure 4.29 that this location is situated far closer to

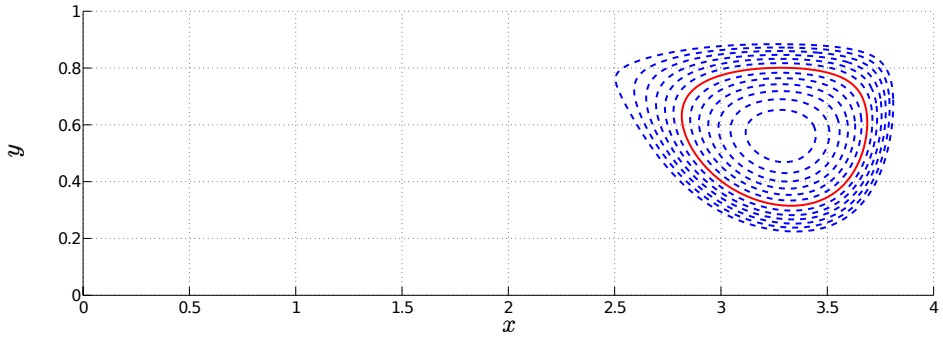

Figure 4.29: The analysed streamlines in blue (------) lines with the location of the instability as the red (_____) line for the rectangular cavity streamlines.

the centre of the vortex than the previous result. This is due to the different streamlines involved producing a different structure.

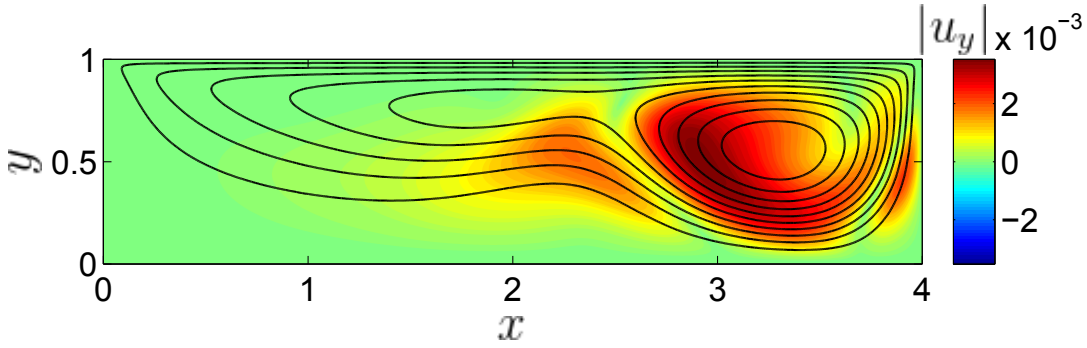

Figure 4.30: Absolute value of the eigenfunction in y for the rectangular cavity with superimposed basic flow streamlines in the cavity from DNS results.

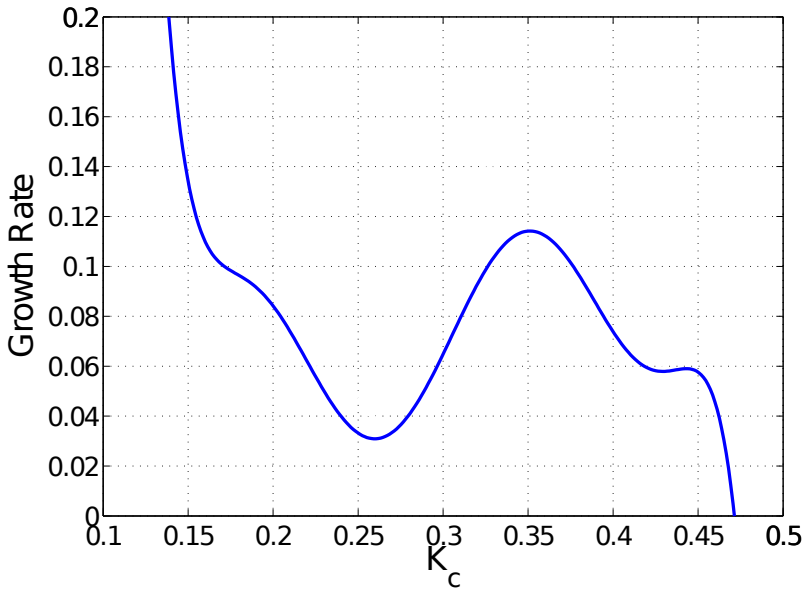

Figure 4.31: The temporal growth rate, σ_r, with different streamlines.

Observing figure 4.31 we notice that a turning point occurs for $K_c \simeq 0.35$. For any streamline $K_c > 0.47$ is stable since the growth rate is negative. We notice that the location of the disturbance doesn't correspond to the maximum growth rate but it appears the maximum is near the location of the most dangerous instability mode within the cavity. This seems to be in qualitative agreement with the DNS results and therefore the asymptotic theory can correctly predict the location of this instability and how dangerous it can be within the cavity. All disturbance activity is concentrated near the right wall of the cavity as we see the vortex situated there.

Thus far we have only discussed cavities that are closed. We next consider an open cavity with the dimensions of $L/D = 2$. The open cavity will have a developing boundary layer over the top which will prescribe some flow condition at the top layer. However, we are only interested in the structure of the streamlines that develop for this situation.

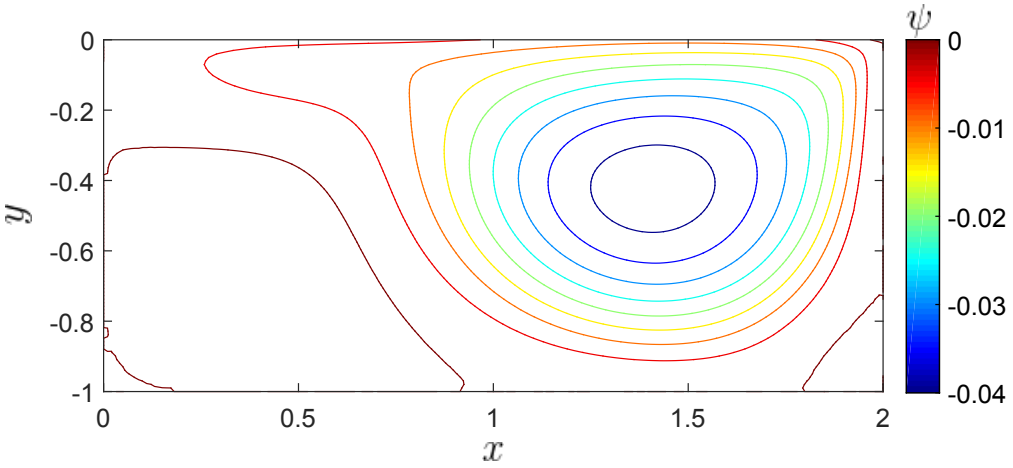

Figure 4.32: Streamlines within an open cavity at $Re = 1500$. The DNS data was provided by Qadri [74].

We notice that figure 4.32 appears to resemble streamlines to a closed square cavity streamlines, with a small recirculation region near the wall at $x \sim 0$. We can now find the location of the disturbance.

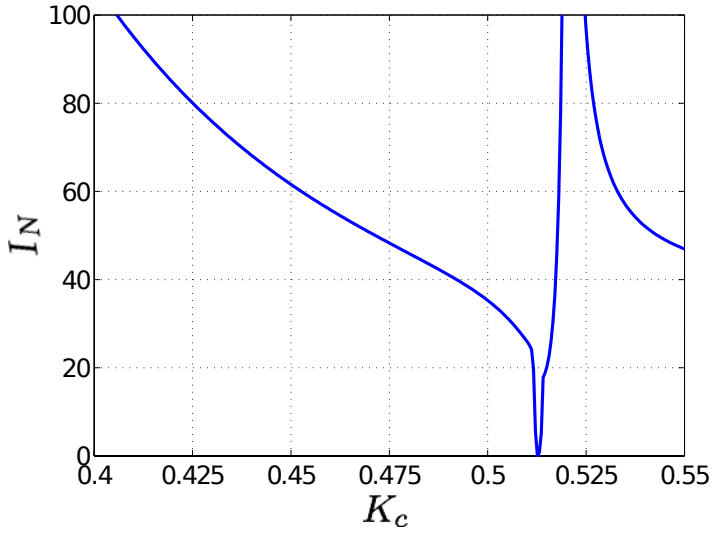

Figure 4.33: The value of the integral I_N with varying K_C for an open cavity for a smaller range

In figure 4.33 where the condition has been satisfied for $K_c = 0.51262$ as with previous analysis.

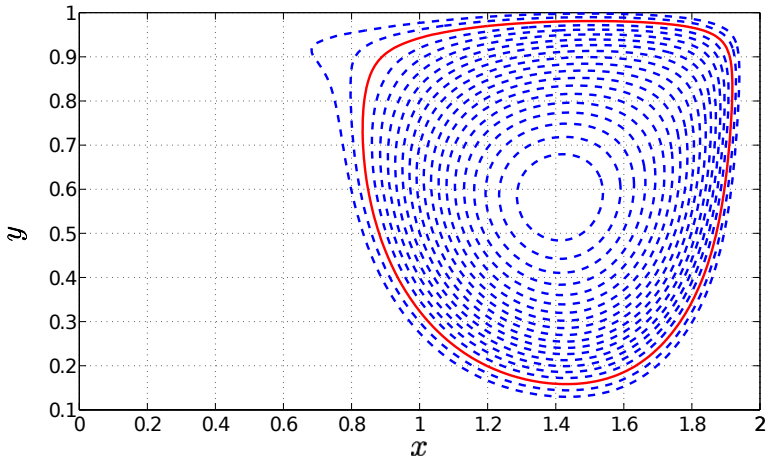

Figure 4.34: The analysed streamlines in blue (------) lines with the location of the instability as the red (——) line for the open cavity streamlines.

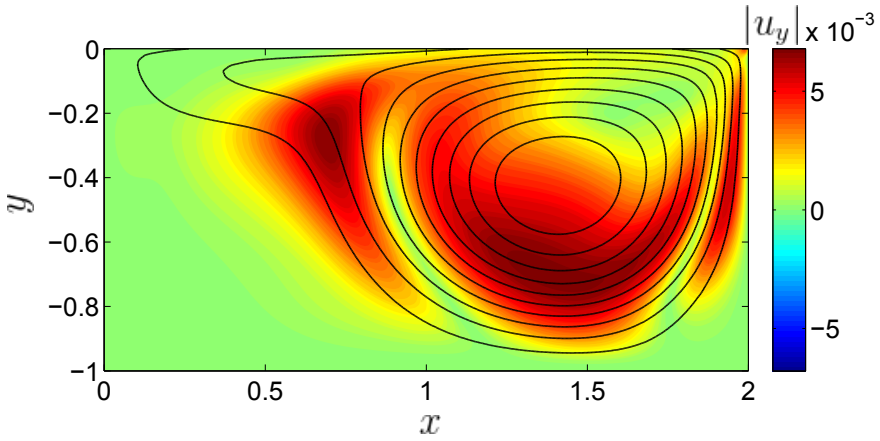

Figure 4.35: Absolute value of the eigenfunction in y for the open cavity with superimposed basic flow streamlines in the cavity from DNS results.

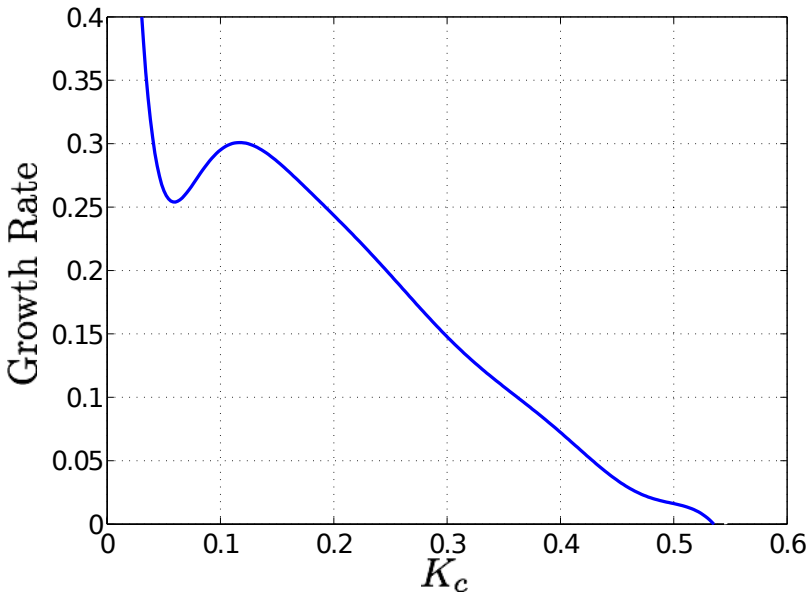

Figure 4.36: The temporal growth rate (σ_r) with different streamlines.

We notice in figure 4.36 that the growth rate is smaller than for the closed cavities. The behaviour is different than for the previous two studies due to the area of where the instability is located. There is a turning point near the centre, $K_c \simeq 0.1$, but there is no indication from the analysis that the disturbance is within that region. There could be several reasons for this difference. The first is that the Reynolds numbers are different for each cavity. The open cavity has a much larger Reynolds number compared to the closed cavities studied here. We notice the streamline becoming quite flat near the top of the cavity due to the imposed velocity. This is promising since we have located the instability (in the region to similar to the square cavity) and is located near the outer streamlines within the cavity.

4.7 Conclusion

The initial interest in this problem was due to the creation of a general framework for analysis of two-dimensional streamlines, which are subject to a temporal instability. There are many problems that occur for these types of flow, such as modelling turbulence or separation bubbles. Here we formulate this problem in a more general formulation, where we consider curvilinear coordinates acting along and normal to the streamline. We considered a high wavenumber limit in our prescribed expansion. We used the same assumptions as Bayly [6] which are that the flow is unbounded and incompressible fluid with a temporal disturbance propagating near the streamline. We addressed this problem by using asymptotic analysis and used an asymptotic expansion for the temporal wavenumber. By solving the various order equations to find the temporal wavenumbers we could obtain an overall growth rate, which depended on the spanwise wavenumber.

Years later Bayly [6] studied the classical Rayleigh instability theory applied to general two-dimensional flows, in particular, a centrifugal-type instability with closed convex streamlines. Due to certain conditions where the Floquet exponent is maximised around some localised streamline K, away from the centre of the vortex, is obtained and a range of short-wave three-dimensional instabilities arise. We construct similar arguments but with our general curvilinear framework. The condition we conceive depends on minimising an integral which has been derived from our analysis. Due to this condition in our approach, results show that there is a class of streamlines at a distance K away from the centre of the vortex O' where the disturbance exists on this streamline. However, the results indicate only a certain number of these elliptical streamlines exist where the disturbances are unstable.

For our analysis we typically started with a circular streamline and extended one axis to create an elliptical streamline. We considered the stability of a circular streamline for validation purposes since studies of the flow are well documented. We analysed these streamlines and found that they are neutrally stable, which was already known [70], [5]. We were then interested in elliptical streamlines because of intrigue in closed two-dimensional streamlines for secondary instabilities, and one particular interest is the elliptical instability. This disturbance re-emerged in the 1980s in light of studies by Pierrehumbert [70] and Bayly [5]. Pierrehumbert provided an eigenvalue solver

approach to relate the eccentricity of the ellipse and temporal growth rate. Whereas Bayly approached this problem via Floquet analysis and obtained results that agreed with Pierrehumbert's numerical findings. They found that a relation exists between the eccentricity and temporal growth rate - as the eccentricity increases then so does the temporal growth rate. But we note that as one axis increased at a rate of E and the other one decreased by an amount of E^{-1} (where E is the eccentricity), eventually this disturbance would be highly localised towards the centre. Therefore the largest growth rate would correspond to a long thin vortex. For a circle the temporal instability is neutrally stable, however, as E increases so does the growth rate. In figure 4.13 we observe the all three methods are in agreement. Interestingly our results tend to lie closer to Pierrehumbert's numerical findings than Bayly's result. Bayly [6] demonstrated this in terms of eccentricity of a circle is equal to 1 and the temporal growth rate is $\overline{\sigma} = 0$, featured in figure 4.13. Therefore we know our approach is consistent with previous studies.

Thus far we have only discussed elliptical streamlines, but our theory can be extended to any two-dimensional closed streamline. We can study streamlines existing within a cavity for aero-dynamical purposes. We demonstrated that this analysis could work for non-elliptical streamlines, as featured in figure 4.14a, and the growth rates can be easily calculated, as shown in figure 4.14b. We aren't just limited to symmetrical streamlines about $x = 0$ or $y = 0$, non-symmetrical streamlines can be studied too. By inspecting figure 4.15b we see that the growth rates of the corresponding non-symmetrical streamlines of figure 4.15a can be determined. Therefore we can develop this theory to encompass any two-dimensional closed streamline. We can analyse the streamlines in the same way as we did previously. First we start with a simple square closed cavity with $Re = 787$. The DNS results were provided by Qadri [74] and from the data provided for our analysis an algorithm was created in order to read the DNS data to select a certain streamline to analyse. Once this data was collected, a spline between the points was used to apply the theory. We discovered a similar inherent structure, that an instability exists at some distance K, from the centre of the vortex/cavity O'. We discovered the location where the instability arises and agrees with the numerical results, as shown in figure 4.20a compared to figure 4.20b. Qadri performed bi-global analysis with $Re = 787$ for the square cavity and we notice that the location where the

instability is most unstable. This corresponds to the streamline which we have found which the result can be shown in figure 4.20b. The agreement where the instability lies isn't exact, since for our analysis we have a high wavenumber limit and the numerical approach uses $O(1)$ wavenumber. The eigenfunctions in figure 4.24 indicate the region where the disturbance propagates and qualitatively agrees with the DNS results. This work was be extended to encompass different cavity sizes and numerous imposed velocities. Firstly, a rectangular cavity with the dimensions of $L/D = 4$ and $Re = 289$ was considered. The instability was predicted to be in the correct area of the cavity and seemed to be in qualitative agreement. An open cavity was analysed next with the dimensions of $L/D = 2$ and with $Re = 1500$. Again, using this theoretical approach, the streamline where the instability lies was envisaged in the precise region. Further analysis could be performed to create a family of different cavities and imposed velocity, but we have demonstrated that the theory correctly predicts where this instability will occur.

Chapter 5

Conclusion

We developed a good prediction method for calculating the streamwise growth rate and stability characteristics of crossflow vortices with surface curvature variations. The asymptotic theory correctly predicts the growth rates which were determined from the PSE & VV methods. This includes both stationary and travelling crossflow vortices. For a flat surface, a two-term asymptotic prediction was used and with curvature effects an additional term is included in this theory. A comparison with PSE with a small amount of convex curvature was made and streamwise growth rates were correctly predicted. We analysed both forms of surface curvature, convex and concave. Our results will show that a crossflow vortex over a concave surface destabilises and vice versa for the convex curvature, as noted by Malik & Masad [59]. We were not interested in concave curvature due to the destabilisation it causes to the crossflow disturbance, nonetheless, we found some interesting stability properties with convex curvature. First, we found that small convex curvature was enough to stabilise the stationary modes. This had the same impact for small to moderate frequencies for travelling modes. However, for high frequencies the addition of small convex curvature has little impact on stabilising this disturbance. Interestingly, as the curvature term, κ_C, is increased it causes destabilisation for all high frequencies, but eventually for $\kappa_C \gg 1$ all travelling modes are stable. Another interesting result showed the stability characteristics of two travelling modes. We considered a moderate frequency and a high frequency in a dispersion relation between the streamwise growth rate and the spanwise wavenumber. In the case of stationary crossflow vortices we have a limited number of spanwise wavenumbers corresponding to positive growth rates, whereas for

travelling modes when including small convex curvature in the analysis the amount of spanwise wavenumbers corresponding to the streamwise growth rate increases. As the frequency increased this region of spanwise wavenumbers expanded for smaller curvatures.

Therefore it seems that you can calculate a few integrals in the three-term method and it will be enough to capture the effects of PSE with little computational time. In summary, we show that small positive curvature relating to a convex surface stabilises the crossflow disturbance on a swept wing using three-term viscous-curvature theory. This method has been validated with PSE [63] and VV [95] methods.

We understand how the crossflow disturbance grows downstream with various curvatures but how effective are certain mechanisms in producing an instability within the boundary-layer. We performed receptivity analysis to analyse flat and curved surfaces with a roughness bump. We used residue calculus to calculate the inverse Laplace transform and to evaluate the poles. From this we calculated the response function which gave us information about the receptivity and efficiency of the process. We found that stationary crossflow vortices have larger values of the response function than travelling modes for a flat surface. This is also true for both convex and concave surfaces but with one exception, towards the trailing edge of the wing the response function with a high frequency is larger than the stationary one. Close to the leading edge adding concave curvature seems to be the most efficient receptivity mechanism for the stationary and travelling crossflow modes. However, further downstream convex curvature is a more effective mechanism compared to concave curvature.

Interestingly, for moderate frequencies there is a minor change between all three response functions of flat, convex and concave surface curvature. This includes considering both downstream streamwise behaviour and the range of spanwise wavenumbers of the response functions. In the high frequency limit the largest response is from the convex and concave response functions . Both convex and concave curvatures enhanced the response function compared to the flat surface case, but the largest response is due to convex and convex curvatures with small spanwise wavenumbers and a high frequency. This particular case has not been mentioned in the literature and could give some insight into travelling modes with surface deviations. This would be especially useful for experiments. Most experiments cannot achieve flight-like conditions

because of the high turbulence levels due to the environment they are performed in. Therefore when considering a geometry with concave surface variations a careful approach needs to be considered if travelling crossflow modes are active within the flow, due to the large response function for moderate spanwise wavenumbers.

The interest in new technology is ever growing within the business of aerodynamics. There are always new ways to improve efficiency of the current devices. We extend our previous analysis to include and understand one of these new technologies, the plasma actuator. The plasma acts as a roughness bump on the surface of the wing and we find the shape of this plasma for our analysis. For this new problem we derived the plasma equations from Maxwell equations and solved them using a FTCS method, until a steady state solution was formed. We then used an algorithm to determine the boundary of the plasma in order to find the Fourier transform of it to evaluate the response function. We then changed the frequency and voltage and found that small height and small width had the largest response function (corresponding to small voltage and small frequency). We did a parametric study to find the optimal configuration but this is time consuming and was not be discussed in this study. This could not be feasible in the next few years due to the heights of the plasma at which experiments have achieved, they would trigger separation at the leading edge. However, the point of this study was to understand if this could be possible to control the crossflow disturbance in this way. This has not been studied in the context of the crossflow vortex. The control aspects of the plasma actuator could benefit the laminar-turbulent transition location if the heights were a few orders of magnitude smaller.

Thus far we have only discussed primary instabilities. Next we turn our attention to secondary instabilities subject to temporal disturbances. We formulated a problem to analyse two-dimensional streamlines of secondary instabilities. This can encompass many areas within fluid dynamics but we first discuss our primary interest that is in the elliptical instability, which has been linked to turbulent studies over the years. We formulate this problem using general curvilinear coordinates and study the temporal stability of the two-dimensional streamlines. We used the same assumptions as Bayly [6] used: the flow is unbounded and incompressible fluid with a temporal disturbance propagating along the streamline. We developed an asymptotic method to understand the behaviour of the disturbance along and across this closed streamline in a high

wavenumber limit, since we were analysing short-wave instabilities.

The initial interest in this problem came from a paper by Bayly [6], who analysed a centrifugal-type instability with closed convex streamlines. Our analysis indicates that a range of short-wave three-dimensional instabilities arise at some distance K away from the centre of the vortex on a streamline, due to certain conditions of the Floquet exponent is maximised at this location. With a different analytical approach we were able to obtain the location of this disturbance analogous to Bayly's [6] result. The existence of these instabilities occurs in a location where this condition is minimised and a class of closed streamlines at this distance are found.

Due to the interest in turbulence Pierrehumbert [70] found this instability from a strained vortex, which was inviscid and unbounded. A relationship between the temporal growth rate and eccentricity of the ellipse was discovered using an eigenvalue solver. In a different paper, Bayly [5] quantified this using Floquet analysis and found agreement with Pierrehumbert's results. Using a more general approach with a change of coordinates on the streamlines and with the use of asymptotic analysis, we obtain results that agree with Pierrehumbert [70] and Bayly [5]. The results indicate that the asymptotic approach lies closer to Pierrehumbert's[70] results than Floquet analysis.

With this framework, we can make predictions for similar problems in order to find where the instability is located. This can be helpful for many situations such as separation bubbles or steps where closed two-dimensional streamlines are formed. However, for our study we are interested in deviations along a swept wing and a common surface imperfection is a cavity. Within a cavity two-dimensional closed streamlines can develop with some imposed velocity conditions. It is helpful to know where the most dangerous mode occurs within the cavity for aero-dynamical purpose. We found that they grow and interact with the boundary-layer. We analysed a closed square cavity at $Re = 787$ and $L/D = 1$. We investigated applying this asymptotic method to the basic flow cavity streamlines, which we compared with numerical results. The theoretical prediction provides a qualitative location of the region where the disturbance was most dangerous as indicated by the DNS results provided [74]. We observe the behaviour of the eigenfunction along the streamline at which the disturbance is located and notice good agreement with the numerical findings, but there is some discrepancy where the disturbance is at a maximum within the cavity. The differences occur due to the

asymptotic theory using a high wavenumber limit $k \gg 1$, whereas the numerical approach uses an order one wavenumber. Due to the disturbances being short-wave, the only analysis that can be performed is a high wavenumber approach and therefore the differences are unavoidable. We were not just limited to a square cavity and this can be extended further by looking at two examples. The first was a cavity with $L/D = 4$ and $Re = 289$ and a similar prediction was made. The final one was to consider an open cavity with $Re = 1500$ and $L/D = 2$. As with previous cases, the asymptotic theory correctly predicts the location of the instability. The theory exists to give an indication as to where this disturbance is located. To understand the underlying mechanism that there exists short-wave three-dimensional instabilities arise at some distance K away from the centre of the vortex for closed two-dimensional streamlines. Hence this approach can be extended to include a wide range of two-dimensional streamlines subject to three-dimensional short-wave instabilities.

References

[1] Alonso JJ. and Chirayath V. Plasma Actuated Unmanned Aerial Vehicle. `http://www.vedphoto.com/pauavpaperdraft.pdf`, 2014. [Online; accessed 30-July-2014].

[2] Anderson JD. *Introduction to Flight*. McGraw-Hill series in aeronautical and aerospace engineering. McGraw-Hill Higher Education, 2005.

[3] Arnal D., Casalis G., and Juillen JC. Experimental and theoretical analysis of natural transition on infinite swept wing. In *Laminar-Turbulent Transition*, pages 311–325. Springer, 1990.

[4] Bassom AP. and Hall P. Vortex instabilities in three-dimensional boundary-layers: The relationship between Görtler and crossflow vortices. *J. Fluid Mech.*, 232:647, 1990.

[5] Bayly BJ. Three-dimensional instability of elliptical flow. *Physical Review Letters*, 57:216063, 1986.

[6] Bayly BJ. Three-dimensional centrifugal-type instabilities in inviscid two-dimensional flows. *Physics of Fluids*, 31:56–64, 1988.

[7] Bers A. *Linear Waves and Instabilities*. in Physique des Plasmas, (C. DeWitt and J. Peyraud eds.), Gordon and Breach, pp. 117-215, 1975.

[8] Bertolotti FP. Receptivity of three-dimensional boundary layers to localized wall roughness and suction. *Annu. Rev. Fluid Mech.*, 35:413–440., 2000.

[9] Bertolotti FP., Herbert Th., and Spalart PR. Linear and nonlinear stability of the blasius boundary layer. *Journal of Fluid Mechanics*, 242:441–474, 1992.

[10] Briggs RJ. *Electron-Stream Interactions with Plasmas*. MIT Press, Cambridge, MA,, 1964.

[11] Brown GL. and Roshko A. On density effects and large structure in turbulent mixing layers. *Journel of Fluid Mechanics*, 64:775816, 1074.

[12] Cayley G. On aerial navigation. *A Journal of Natural Philosophy, Chemistry and the Arts*, 24:164–174, 1809.

[13] Childress S. *An Introduction to Theoretical Fluid Mechanics*. Courant lecture notes in mathematics. Courant Institute of Mathematical Sciences.

[14] Choudhari M. Boundary-layer receptivity due to distributed surface imperfections of a deterministic or random nature. *Theor. Comp. Fluid Dyn.*, 4:101–17, 1993.

[15] Choudhari M. Roughness-induced generation of crossow vortices in three-dimensional boundary layers. *Theor. Comput. Fluid Dyn.*, 6, 1994.

[16] Choudhari M. and Streett CL. Boundary layer receptivity phenomena in three-dimensional and high-speed boundary layers. In *AlAA Second International Aerospace Pleanes Conference*, 1990.

[17] Choudhari M. and Streett CL. Theoretical prediction of boundary-layer receptivity. In *AIAA, Fluid Dynamics Conference, 25 th, Colorado Springs, CO*, 1994.

[18] Colella P., Dorr MR., and Wake DD. A conservative finite difference method for the numerical solution of plasma fluid equations. *Journal of Computational Physics*, 149(1):168–193, 1999.

[19] Collis SS and Lele SK. Receptivity to surface roughness near a swept leading edge. *J. Fluid Mech.*, 380:141–168, 1999.

[20] Cooke JC. The boundary layer of a class of infinite yawed cylinders. In *Mathematical Proceedings of the Cambridge Philosophical Society*, volume 46, pages 645–648. Cambridge Univ Press, 1950.

[21] Crouch JD. Receptivity of three-dimensional boundary layers. *AIAA Pap.*, 93, 1993.

[22] Crouch JD. Theoretical studies on the receptivity of boundary layers. In *AIAA, Fluid Dynamics Conference, 25 th, Colorado Springs, CO*, 1994.

[23] Crow SC. Stability theory for a pair of trailing vortices. Technical Report Pap. No. 8 2172-79, AIAA, 1970.

[24] Dagenhart J., Stack J., Saric W., and Mousseux M. Crossflow-vortex instability and transition on a 45 deg swept wing. In *20th Fluid Dynamics, Plasma Dynamics and Lasers Conference*, Fluid Dynamics and Co-located Conferences. American Institute of Aeronautics and Astronautics, June 1989.

[25] Dallmann U. *Zur Stabilität dreidimensionaler Scherströmungen: Kriterien für reibungsfreie Störungsanregung*. Dt. Forschungs-u. Versuchsanst. f. Luft-u. Raumfahrt, Inst. f. Theoret. Strömungsmechanik62 1980., 1980.

[26] Davies C. and Carpenter PW. A novel velocity-vorticity formulation of the Navier-Stokes equations with applications to boundary layer disturbance evolution. *Journal of Computational Physics*, 172:119–165, 2001.

[27] Deyhle H. and Bippes H. Disturbance growth in an unstable three-dimensional boundary layer and its dependence on initial conditions. *J. Fluid Mech.*, 316:73113, 1996.

[28] Drazin PG. and Reid WH. *Hydrodynamic Stability Second edition*. Cambridge University Press, January 31, 2004.

[29] Falkner VK. and Skan SW. Some approximate solutions of the boundary-layer equations. *Aero. Res. Coun. Rep. and Mem. no*, 1314, 1930.

[30] Gaster M. A note on the relation between temporally-increasing and spatially-increasing disturbances in hydrodynamic stability. *Journal of Fluid Mechanics*, 14(02):222–224, 1962.

[31] Gaster M. A simple device for preventing turbulent contamination on swept leading edges. *J. Royal Aero. Soc.*, 69:788789, 1965.

[32] Gledzer EB., Dolzhansky FV., Obukhov AM., and Ponomarev VM. An experimental and theoretical study of the stability of a liquid in an elliptical cylinder. *Isv. Atmos. Ocean. Phys.*, 11:61722, 1975.

[33] Gledzer EB., Novibov YV., Obukhov AM., and Chusov MA. An investigation of the stability of liquid flows in a three-axis ellipsoid. *Isv. Atmos. Ocean. Phys.*, 10:6971, 1974.

[34] Goldstein ME. Scattering of acoustic waves into Tollmien-Schlichting waves by Small Streamwise Variations in Surface Geometry. *J. Fluid Mech.*, 154:509–529, 1985.

[35] Görtler H. Instabilita-umt laminarer Grenzchichten an Konkaven Wänden gegenber gewissen dreidimensionalen Störungen. *ZAMM*, 21:250–52, 1941.

[36] Görtler H. Dreidimensionale Instabilität der ebenen Staupunktströmung gegenubër wirbelartigen Störungen. *In 50 Jahre Grenzschichtforschung, H. Görtler and W. Tollmien*, page 304, 1955.

[37] Görtler H. Dreidimensionales zur Stabilitätstheorie laminarer Grenzschichten. *Journal of Applied Mathematics and Mechanics*, 35:362363, 1955.

[38] Gray WE. The effect of wing sweep on laminar flow. Technical Report 255, RAE, 1952.

[39] Gregory N., Stuart JT., and Walker WS. On the Stability of Three-Dimensional Boundary layers with Application to the Flow Due to a Rotating Disk. *Phil. Trans. R. Soc. Lond.*, 248:155–199, 1955.

[40] Grundmann S. and Tropea C. Active cancellation of artificially introduced Tollmien-Schlichting waves using plasma actuators. *Experiments in Fluids*, 44:795–806, 2008.

[41] Hall P. The linear development of Görtler vortices in growing boundary layers. *Journal of Fluid Mechanics*, 130:41–58, 1983.

[42] Hall P. An Asymptotic Investigation of the Stationary Modes of Instability of the Boundary layer on a Rotating Disk. *Proc. Roy. Soc. London Ser.*, 406:93–106, 1986.

[43] Hall P., Malik MR., and Poll DIA. On the stability of an infinite swept attachment line boundary layer. *Proceedings of the Royal Society of London. A. Mathematical and Physical Sciences*, 395(1809):229–245, 1984.

[44] Hämmerlin G. Zur Instabilitätstheorie der ebenen Staupunktströmung. *In 50 Jahre Grenzschichtforschung, H. Görtler and W. Tollmien*, page 315, Symposium Freiburg, 1955.

[45] Heisenberg W. On stability and turbulence of fluid flows. *Tech. Mem. Natl Adv. Comm. Aeor., Wash.*, 1291, 1924.

[46] Hiemenz K. Die Grenzschicht an einem in den gleichförmigen Flüssigkeitsstrom eingetauchtengeraden Kreiszylinder. Technical Report PhD thesis, Gottingen, 1911.

[47] Hoffman JD.and Frankel, S. *Numerical Methods for Engineers and Scientists, Second Edition,*. Taylor & Francis, 2001.

[48] Hadamard J. *Lectures on Cauchy's problem in linear partial differential equations*. Courier Dover Publications, 2003.

[49] Jayaraman B. and Shyy W. Modeling of dielectric barrier discharge-induced fluid dynamics and heat transfer. *Progress in Aerospace Sciences*, 44(3):139–191, 2008.

[50] Johnson RW. *Handbook of fluid dynamics*. Crc Press, 1998.

[51] Kerswell, R. Elliptical instability. *Annual review of fluid mechanics*, 34(1):83–113, 2002.

[52] Kriegseis J., Möller B., Grundmann S., and Tropea C. Capacitance and power consumption quantification of dielectric barrier discharge (dbd) plasma actuators. *Journal of Electrostatics*, 69(4):302–312, 2011.

[53] Krishnamurty KS. Acoustic radiation from two-dimensional rectangular cutouts in aerodynamic surfaces. Technical Report NACA-TN-3487, 1955.

[54] Landau, L.D. and Lifshitz, E.M. *Electrodynamics of Continuous Media*.

[55] Lemon GW. *English Etymology*. G. Robinson, 1783.

[56] Malik MR. The neutral curve for stationary disturbances in rotating disk ow. *J. Fluid Mech.*, 164:275, 1986.

[57] Malik MR. and Li F. Technical Report 93-0077, AIAA, 1993.

[58] Malik MR., Li F., and Chang CL. Crossflow disturbances in three-dimensional boundary layers: nonlinear development, wave interaction and secondary instability. *J. Fluid Mech.*, 268:136, 1994.

[59] Masad JA. and Malik MR. Effects of body curvature and non-parallelism on the stability of flow over a swept cylinder. *Phys. Fluids*, 6:2363–2379, 1994.

[60] Moore DW. and Saffman PG. Structure of a line vortex in an imposed strain. In *Aircraft wake turbulence and its detection*, pages 339–354. Springer, 1971.

[61] Moreau E. Airflow control by non-thermal plasma actuators. *Journal of Physics D: Applied Physics*, 40(3):605, 2007.

[62] Morkovin MV. *On the many faces of transition, In Viscous Drag Reduction ed. CS Wells*. New York: Plenum, 1969.

[63] Mughal S. Personal Communication, 2012.

[64] Müller B. and Bippes H. Experimental study of instability modes in a three-dimensional boundary layer. *Fluid Dyn. Three-Dimens. Turbul. Shear Flows Transit. AGARD CP*, 438, 1989.

[65] Nield DA. On the inviscid solutions of the OrrSommerfeld equation. *Math. Chronicle*, 2:43, 1972.

[66] Obukhov AM. Three-mode interaction in an incompressible fluid. *Radiophysics and Quantum Electronics*, 19(6):614–620, 1976.

[67] Orlov D. Technical Report Modelling and Simulation of Single Dielectric Barrier Discharge Plasma Actuators, University of Notre Dame, 2006.

[68] Orr WMF. The stability or instability of the steady motions of a perfect liquid and of a viscous liquid. part ii: A viscous liquid. In *Proceedings of the Royal Irish Academy. Section A: Mathematical and Physical Sciences*, pages 69–138. JSTOR, 1907.

[69] Papageorgiou D. Stability of the unsteady viscous flow in a curved pipe. *Journal of Fluid Mechanics*, 182:209–233, 1987.

[70] Pierrehumbert RT. Universal short-wave instability of two-dimensional eddies in an inviscid fluid. *Phys. Rev. Lett.*, 57:215759, 1986.

[71] Poll DIA. Some observations of the transition process on the windward face of a long yawed cylinder. *Journal of Fluid Mechanics*, 150:329–356, 1985.

[72] Prandtl L. Über flussigkeits bewegung bei sehr kleiner reibung. *Verhaldlg III Int. Math. Kong*, pages 484–491, 1904.

[73] Press WH. *Numerical Recipes 3rd Edition: The Art of Scientific Computing*. Cambridge University Press, 2007.

[74] Qadri U. Personal Communication, 2014.

[75] Radeztsky RH Jr. , Reibert MS., and Saric WS. Development of stationary crossow vortices on a swept wing. *AIAA Pap. No.*, 94-2373, 1994.

[76] Radeztsky RH Jr., Reibert MS., and Saric WS. Effect of micron-sized roughness on transition in swept-wing ows. Technical Report Paper 93-0076, AIAA, 1993.

[77] Radeztsky RH Jr., Reibert MS., and Saric WS. Effect of isolated micron-sized roughness on transition in swept-wing flows. *AIAA J.*, 37(11):1370–77, 1999.

[78] Lord Rayleigh. The theory of sound, 1894. *Republished by Dover Publications, New York*, 1945.

[79] Reed HL. and Saric WS. Stability of three-dimensional boundary layers. *Annu. Rev. Fluid Mech.*, 21:23584, 1989.

[80] Reynolds O. An experimental investigation of the circumstances which determine whether the motion of water shall be direct or sinuous, and of the law of resistance in parallel channels. *Trans. R. Soc. London*, 174:935, 1883.

[81] Ronald HE. Transient growth instability cancelation by a plasma actuator array. *Experiments in Fluids*, 49:1339–1348, 2010.

[82] Rosenhead L. *Laminar Boundary Layers*. [Fluid Motion Memoirs.]. Oxford, 1963.

[83] Rowley CW. and Williams DR. Dynamics and control of high-reynolds number flow over open cavities. *Annu. Rev. Fluid Mech.*, 38:251–276, 2006.

[84] Ruban AI. On the Generation of Tollmien-Schlichting Waves by Sound. *Fluid Dynamics*, 19:709–716, 1985.

[85] Saric WS., Gladden R., Gabet P., and White EB. Control of transition in 3-d boundary layers with streamwise vortices in the presence of freestream turbulence and random surface roughness. proc. workshop on organized vortical motion as a basis for boundary layer control. *Ukrainian Academy of Sciences*, September 20-22, 2000.

[86] Saric WS., Reed HL., and White EB. Stability and transition of three-dimensional boundary layers. *Ann. Rev. of Fluid Mech.*, 35:413–440, 2003.

[87] Schlichting H. *Boundary-Layer Theory*. McGraw-Hill, 1979.

[88] Schlichting L. Zur Entstehung der Turbulenz kleiner Plattenströmung , Mitteilung Nachr. *Math. Phys*, 1933a:181–208, 1933.

[89] Schrader LU., Brandt L., and Henningson DS. Receptivity mechanisms in three-dimensional boundary layer flows. *J. Fluid Mech.*, 618:209241, 2009.

[90] Simen M. Local and non-local stability theory of spatially varying flows. In *Instability, Transition, and Turbulence*, pages 181–201. Springer, 1992.

[91] Simen M. and Dallmann U. The linear stability equations of compressible, parallel, three-dimensional flow along curved surfaces. *DLR Gottingen, Germany.*, A 13:IB 221–90, 1990.

[92] Smith FT., Sykes RI., and Brighton PWM. A two-dimensional boundary layer encountering a three-dimensional hump. *Journal of Fluid Mechanics*, 83(01):163–176, 1977.

[93] Sommerfeld A. Ein Beitrag zur hydrodynamischen Erklärung der turbulenten Flüssigkeitsbewegungen. *Atti del*, 4:116–124, 1908.

[94] Taylor GI. Stability of a viscous liquid contained between two rotating cylinders. *Philosophical Transactions of the Royal Society of London. Series A, Containing Papers of a Mathematical or Physical Character*, pages 289–343, 1923.

[95] Thomas C. Personal Communication, 2012.

[96] Thomas C., Hall P., and Davies C. Nonlinear effects on the receptivity of crossflow in the swept hiemenz flow. *Journal of Fluid Mechanics*, 763:433–459, 2015.

[97] Tollmien W. Über die Entstehung der Turbulenz, Mitteilung Nachr. Ges. Wiss. *Math. Phys.*, pages 21–44., 1929.

[98] Townsend AA. Flow patterns of large eddies in a wake and a boundary layer. *J. Fluid Mech.*, 95:51537, 1979.

[99] Waleffe FA. . The 3d instability of a strained vortex and its relation to turbulence. phd thesis. Technical report, MIT.

[100] White A. Personal Communication, 2014.

[101] White EB. and Saric WS. Secondary instability of crossflow vortices. *Journal of Fluid Mechanics*, 525:275–308, 2005.

[102] Whittle F. *The Early History of the Whittle Jet Propulsion Gas Turbine*. Institution of Mechanical Engineers, 1945.

[103] Wilson SDR. and Gladwell I. The stability of a two-dimensional stagnation flow to three-dimensional disturbances. *Journal of Fluid Mechanics*, 84(03):517–527, 1978.

[104] Zavol'Skii NA., Reutov VP., and Rybushkina GV. Excitation of tollmien-schlichting waves by acoustic and vortex disturbance scattering in boundary layer on a wavy surface. *Journal of Applied Mechanics and Technical Physics*, 24(3):355–361, 1983.

Appendix A

Boundary-layer equations

From the equation (1.4) we have

$$\frac{\partial u}{\partial x}+\frac{\partial v}{\partial y}+\frac{\partial w}{\partial z}=0 \implies \frac{U_\infty}{L}\sim\frac{\epsilon U_\infty}{\delta L} \implies \epsilon=\delta^{-1}.$$

By substituting the non-dimensional quantities of (1.10) and (1.11) into (1.3) and (1.4) we obtain the following set of equations:

$$\begin{aligned}
u^*u^*_{x^*}+v^*u^*_{y^*}+w^*u^*_{z^*} &= -p^*_{x^*}+R^{-1}(u_{x^*x^*}+u_{z^*z^*})+u_{y^*y^*}, && \text{(A.1)}\\
0 &= -p^*_{y^*}, && \text{(A.2)}\\
u^*w^*_{x^*}+v^*w^*_{y^*}+w^*w^*_{z^*} &= -p^*_{z^*}+R^{-1}(w_{x^*x^*}+w_{z^*z^*})+w_{y^*y^*}, && \text{(A.3)}\\
u^*_{x^*}+v^*_{y^*}+w^*_{z^*} &= 0, && \text{(A.4)}
\end{aligned}$$

with boundary conditions of

$$u^*(0)=v^*(0)=0 \quad u^*(Re^{1/2})=1. \tag{A.5}$$

Due to the scalings involved, the pressure is independent from the normal coordinate. In dimensional form for which Prandtl formulated his problem we have

$$uu_x + vu_y + wu_z = -\frac{1}{\rho}p_x + \nu(u_{xx} + u_{zz}) + u_{yy}, \tag{A.6}$$

$$0 = -\frac{1}{\rho}p_y, \tag{A.7}$$

$$uw_x + vw_y + ww_z = -\frac{1}{\rho}p_z + \nu(w_{xx} + w_{zz}) + w_{yy}, \tag{A.8}$$

$$u_x + v_y + w_z = 0, \tag{A.9}$$

with boundary conditions of

$$u(0) = v(0) = 0, \quad u(Re^{1/2}) = U_\infty. \tag{A.10}$$

These are the steady Prandtl boundary layer equations in three dimensions. We can eliminate the pressure with the aide of Bernoulli's equation such that

$$-\tfrac{1}{\rho}\tfrac{\partial p}{\partial x} = u_e\tfrac{\partial u_e}{\partial x} + w_e\tfrac{\partial w_e}{\partial x},$$
$$-\tfrac{1}{\rho}\tfrac{\partial p}{\partial z} = u_e\tfrac{\partial u_e}{\partial z} + w_e\tfrac{\partial w_e}{\partial z},$$

with u_e and w_e denoted as the freestream velocities in the streamwise and spanwise directions, respectively. The freestream spanwise velocity is approximately constant ($w_e \sim W_\infty$) but the streamwise velocity is dependent on the streamwise coordinate such that $u_e = U_e(x)$. With these assumptions in mind, we are left with

$$uu_x + vu_y + wu_z = u_e\frac{\partial u_e}{\partial x} + \nu(u_{xx} + u_{zz}) + u_{yy}, \tag{A.11}$$

$$uw_x + vw_y + ww_z = \nu(w_{xx} + w_{zz}) + w_{yy}, \tag{A.12}$$

$$u_x + v_y + w_z = = 0. \tag{A.13}$$

These are the boundary-layer equations.

Appendix B

Shooting Method

We consider an ODE of the form

$$\mathcal{U}'' = \mathcal{F}(\mathcal{X},\mathcal{U},\mathcal{U}'), \quad \mathcal{X} \in (\mathcal{A},\mathcal{B}). \tag{B.1}$$

with the following boundary conditions

$$\mathcal{U}(\mathcal{A}) = \alpha, \qquad \mathcal{U}(\mathcal{B}) = \beta. \tag{B.2}$$

The function $\mathcal{U}(\mathcal{X})$ is unknown and is called a two-point boundary value problem. This problem of (B.1) is difficult to solve because of the separate boundary conditions. A method of finding a solution to this problem, we can write it in the form of a coupled pair of nonlinear first order ODEs such as

$$\mathcal{U}' = \mathcal{V}, \mathcal{V}' = \mathcal{F}(\mathcal{X},\mathcal{U},\mathcal{U}'), \tag{B.3}$$

with the following boundary conditions

$$\mathcal{U}(\mathcal{A}) = \beta, \qquad \mathcal{V}(\mathcal{A}) = \mathcal{U}'(\mathcal{A}) = ?. \tag{B.4}$$

The problem of (B.3) cannot be solved since the boundary conditions are unknown for $\mathcal{V}$, as seen in (B.4). Therefore we consider the initial value problem (IVP) of

$$\underline{\mathcal{U}}'' = \mathcal{F}(\mathcal{X},\underline{\mathcal{U}}), \quad \mathcal{X} \in (\mathcal{A},\mathcal{B}), \tag{B.5}$$

with

$$\underline{\mathcal{U}}(\mathcal{A}) = \underline{\alpha}, \tag{B.6}$$

where

$$\underline{\mathcal{U}}(\mathcal{A}) = (\mathcal{U}(\mathcal{A}, \mathcal{V}(\mathcal{A}) \quad \text{and} \underline{\alpha} = (\alpha, \mathcal{S}). \tag{B.7}$$

We let $\mathcal{U}_1(\mathcal{X})$ be a solution of IVP (B.5) then we have the following conditions

$$\mathcal{U}(\mathcal{A}) = \alpha, \qquad \mathcal{U}'(\mathcal{A}) = 0. \tag{B.8}$$

Similarly, we let $\mathcal{U}_2(\mathcal{X})$ be a solution of IVP (B.5) then we have the following conditions

$$\mathcal{U}(\mathcal{A}) = 0, \qquad \mathcal{U}'(\mathcal{A}) = 1. \tag{B.9}$$

The original BVP problem now has a solution in the form (B.1)

$$\mathcal{U}(\mathcal{X}) = \mathcal{U}_1(\mathcal{X}) + \mathcal{S}\mathcal{U}_2(\mathcal{X}), \tag{B.10}$$

hence

$$\mathcal{U}(\mathcal{B}) = \mathcal{U}_1(\mathcal{B}) + \mathcal{S}\mathcal{U}_2(\mathcal{B}) = \beta, \tag{B.11}$$

therefore

$$\mathcal{S} = \left(\beta - \frac{\mathcal{U}_1(\mathcal{B})}{\mathcal{U}_2(\mathcal{B})}\right), \tag{B.12}$$

for a linear ODE [47].

Appendix C

Long-wave Approximation

By observing the dispersion relation for α_0 and γ_0 we notice that α_0 approaches zero but never reaches it. This is due to the Newton method not converging as α_0 approaches zero. We need to investigate the behaviour of the dispersion relation as $\alpha_0 \to 0$. Hence we need to perform long wave analysis across the domain. Notice that the numerics do not span the domain of figure 2.7 because they cannot be started at $(\alpha_{0i}, \gamma_{0R}) = (0, 0)$. The far-field boundary condition is $v_0(\infty) \sim e^{-\beta\zeta}$ ($\beta^2 = {\alpha_0}^2 + {\gamma_0}^2$) and will never approach zero due to the inflexion point in the crossflow disturbance. Some analysis is needed to understand the behaviour near $\alpha_0, \gamma_0 \to 0$ as discussed previously. For clarification some renaming is needed such that $v_0 = \tilde{v}$, to make the analysis more comprehensive. We impose that $\alpha_0 = k\gamma_0$ and let $\zeta = Y$ such that (2.41) becomes

$$\overline{U}[\tilde{v}'' - {\gamma_0}^2(k^2+1)\tilde{v}] - \overline{U}''\tilde{v} = 0, \tag{C.1}$$

where $\overline{U}$=$ku_b + w_b$ and k is a constant. Since the wavenumbers are small, there will be a triple matching an outer inviscid layer, inner inviscid layer and the viscous wall layer.

Outer

In this layer Y has to be rescaled such that $Y = O(1)$. This implies $\xi = \gamma_0 Y$. Observing (C.1) as $\xi \to \infty$, $\overline{U}'' \to 0$, since this is from the base flow as discussed earlier. Hence, we now have

$$\tilde{v}_{\xi\xi} - (k^2+1)\tilde{v} = 0, \tag{C.2}$$

The solution to (C.2) is

$$\tilde{v} = a_1 e^{(\sqrt{k^2+1})\xi} + a_2 e^{-(\sqrt{k^2+1})\xi}, \tag{C.3}$$

since we want the disturbance to decay as $\xi \to \infty$ then $a_1 = 0$. As the solution of (C.2) tends towards the inner solution (i.e., approaches zero), a Taylor expansion can be used so that matching can be performed. Hence,

$$\tilde{v} \sim a_2 \left[1 - \left(\sqrt{k^2+1}\right)\xi + \left(k^2+1\right)\xi^2/2 - \cdots\right]. \tag{C.4}$$

Main

Since $\gamma_0 \ll 1$ we can then use an asymptotic expansion of the form

$$\tilde{v} = \tilde{v}_0 + \gamma_0 \tilde{v}_1 + \cdots .$$

Substituting the expansion into (3.10) and collecting ordered terms to get the following,

$$\begin{aligned}
&\underline{O(1)}: && \overline{U}\tilde{v}_0'' - \overline{U}''\tilde{v}_0 = 0,\\
&\underline{O(\gamma_0)}: && \overline{U}\tilde{v}_1'' - \overline{U}''\tilde{v}_1 = 0,\\
&\underline{O({\gamma_0}^2)}: && \overline{U}\tilde{v}_2'' - \overline{U}''\tilde{v}_2 = (k^2+1)\overline{U}\tilde{v}_0.
\end{aligned}$$

There has to be a careful choice regarding the solutions to $O(1)$, $O(\gamma_0)$ and $O({\gamma_0}^2)$ equations due to the matching between the regions. Since $b\overline{U}$ is a solution to both $O(1)$ and $O(\gamma_0)$ then another solution needs to be found for $O(\gamma_0)$ equation such that there is some Y dependence to match up with the outer solution. Hence the following solutions are proposed

$$\begin{aligned}
&\underline{O(1)}: && \tilde{v}_0 = b_1\overline{U} \sim \text{constant as} \quad Y \to \infty,\\
&\underline{O(\gamma_0)}: && \tilde{v}_1 = b_2\overline{U}\int_0^Y \frac{1}{\overline{U}^2}dY^1 \sim Y \quad \text{as} \quad Y \to \infty,\\
&\underline{O({\gamma_0}^2)}: && \tilde{v}_2 = b_4(k^2+1)\overline{U}\int_0^Y \frac{1}{\overline{U}^2}dY \int_0^Y \overline{U}^2 dY^1 \sim Y^2 \quad \text{as} \quad Y \to \infty.
\end{aligned}$$

Wall layer

As demonstrated by Nield [65] $\tilde{v}$ can be expanded in a different way near a critical layer such that if

$$(U-c)[\phi''-\alpha^2\phi]-U''\phi=0, \tag{C.5}$$

then a solution to the Rayleigh equation is a modified Heisenberg expansion of,

$$\phi_j(z;\alpha^2,c)=\frac{U-c}{U_c'}\sum_{n=0}^{\infty}\alpha^{2n}q_{jn}(z;c)\ \ (j=1,2),$$

where

$$q_{10}=1,\quad q_{20}=\int\frac{1}{(U-c)^2}dz,\quad q_{j,n+1}=\int\frac{1}{(U-c)^2}dz\int(U-c)^2q_{j,n}dz,$$

with $\alpha^2=\gamma_0$, $z=Y$, $c=0$ and $U=\overline{U}$. Nield redefines the coefficients q_{jn} in the following way (near the critical layer),

$$q_{10}=1,\quad q_{20}=\frac{1}{z-z_c}+\frac{U_c''}{U_c}ln(z-z_c)-\frac{U_c''}{2U_c'}-\int_{z_c}^{z}\left[\left(\frac{U_c'}{U-c}\right)^2-\frac{1}{(z-z_c)^2}+\frac{U_c''}{U_c'(z-z_c)}\right]dz,$$

$$q_{j,n+1}=\int_{z_c}^{z}\frac{1}{(U-c)^2}dz\int_{z_c}^{z}(U-c)^2q_{j,n}(z)dz.$$

Now we just have to map the constants which are found via the viscous wall layer problem. There is a critical layer within the inner inviscid layer near the wall therefore we have,

$$\tilde{v}=\frac{\overline{U}}{\overline{U}'(0)}+\frac{\overline{U}}{\overline{U}'(0)}\sqrt{(k^2+1)}\,\gamma_0\left\{\frac{1}{Y}-\frac{\overline{U}''(0)k\ln(Y)}{\overline{U}(0)}-\right.$$
$$\left.\frac{k}{2\overline{U}'(0)}-\int_0^Y\left(\frac{\overline{U}'(0)^2}{\overline{U}}-\frac{1}{Y^2}-\frac{k}{\overline{U}'(0)Y}\right)dY\right\}+O({\gamma_0}^2).$$

[1]From integration by parts, $\rightarrow\int_0^Y\frac{1}{\overline{U}^2}dY=|_0^Y\frac{Y}{\overline{U}^2}-\int_0^Y\frac{Y}{\overline{U}}dY+O(Y^2)+...$ and $b_1b_3=b_4$

We want to understand the behaviour as $Y \to 0$. We note from the base flow that $\overline{U}(0) = 0$. Therefore there exists a critical layer within the wall. Hence,

$$\tilde{v} = \frac{\overline{U}(0)}{\overline{U}'(0)} + \frac{\overline{U}(0)}{\overline{U}'(0)}\sqrt{(k^2+1)}\,\gamma_0 \left\{ \frac{1}{Y} - \frac{\overline{U}''(0) k \ln(Y)}{\overline{U}(0)} - \frac{k}{2\overline{U}'(0)} - \int_0^Y \left(\frac{\overline{U}'(0)^2}{\overline{U}(0)} - \frac{1}{Y^2} - \frac{k}{\overline{U}'(0) Y} \right) dY \right\} + O({\gamma_0}^2). \tag{C.6}$$

Now we just have to map the unknown constants which are found via the viscous wall layer problem. There is a critical layer within the inner inviscid layer near the wall, therefore the following expansion from Nield [65] can be used;

$$\tilde{v} = \frac{\overline{U}}{Ak+B}\left[1 + \gamma_0 \left\{ \frac{1}{Y} - \frac{klnY}{Ak+B} - \frac{k}{2(Ak+B)} - \int_0^Y \left(\frac{Ak+B^2}{\overline{U}} - \frac{1}{Y^2} - \frac{k}{(Ak+B)Y} \right) dY \right\} \right] + O({\gamma_0}^2), \tag{C.7}$$

where A, B are constants from the base flow boundary conditions of $f''(0) = A \sim 1.23$ and $g'(0) = B \sim 0.57$. Hence the solution to match onto the viscous layer is

$$\tilde{v} = b_1\overline{U} + b_2\overline{U}\int_0^Y \frac{1}{\overline{U}^2} dY + b_2\overline{U}\int_0^Y \frac{1}{\overline{U}^2} dY + b_4(k^2+1)\overline{U}\int_0^Y \frac{1}{\overline{U}^2} dY \int_0^Y \overline{U}^2 dY, \tag{C.8}$$

with $b_1 = a_2$, $b_2 = a_2\sqrt{k^2+1}$ and $b_4 = a_2/2$. Since $\gamma_0 = k\alpha_0$ then using the velocity matching condition, we obtain $k = -0.9654 + 0.08745i$. The comparison between the long wave analysis and the Rayleigh stability solution is shown below.

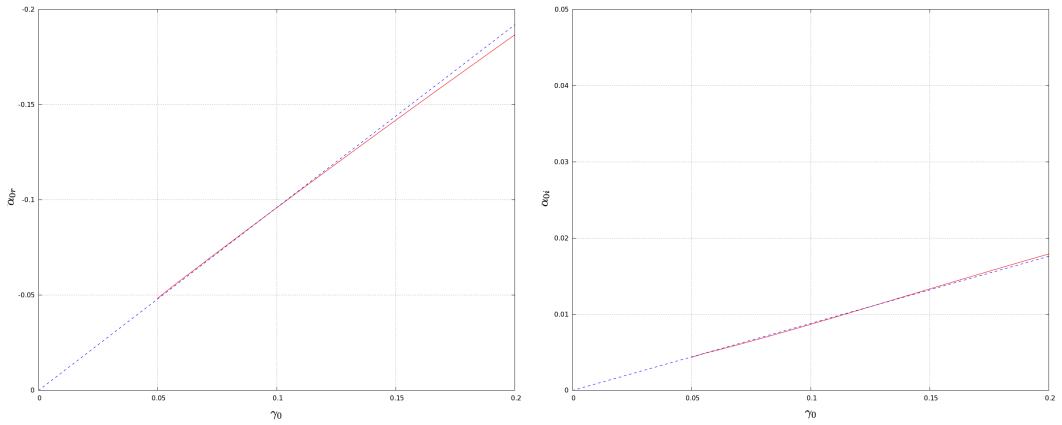

(a) (b)

Figure C.1: Dispersion relation for streamwise wavenumber, α_0, and spanwise wavenumber, γ_0, with $\gamma_0 \ll 1$.

Appendix D

Hadamard Finite Part Integral.

If we consider the following Cauchy's principle integral for $\mathcal{N} < \mathcal{Z} < \mathcal{M}$

$$\mathcal{P}\int_{\mathcal{N}}^{\mathcal{M}} \frac{\mathcal{F}(\mathcal{T})}{(\mathcal{T}-\mathcal{Z})} d\mathcal{T}, \tag{D.1}$$

where $\mathcal{P}$ as the Cauchy principle value and with the assumption that $\mathcal{F}(\mathcal{T})$ is well defined over the region of $\mathcal{N} < \mathcal{T} < \mathcal{M}$. We say that this integral exists and is differential with respect to $\mathcal{Z}$ then

$$\frac{\partial}{\partial \mathcal{Z}}\left(\mathcal{P}\int_{\mathcal{N}}^{\mathcal{M}} \frac{\mathcal{F}(\mathcal{T})}{(\mathcal{T}-\mathcal{Z})} d\mathcal{T}\right) = \oint_{\mathcal{N}}^{\mathcal{M}} \frac{\mathcal{F}(\mathcal{T})}{(\mathcal{T}-\mathcal{Z})^2} d\mathcal{T}, \tag{D.2}$$

Hence the Hardamard finite part integral has the following definition

$$\oint_{\mathcal{N}}^{\mathcal{M}} \frac{\mathcal{F}(\mathcal{T})}{(\mathcal{T}-\mathcal{Z})^2} d\mathcal{T} = \tag{D.3}$$

$$\lim_{\hat{\epsilon}\to 0^+}\left[\int_{\mathcal{N}}^{\mathcal{Z}-\hat{\epsilon}} \frac{\mathcal{F}(\mathcal{T})}{(\mathcal{T}-\mathcal{Z})^2} d\mathcal{T} + \int_{\mathcal{Z}+\hat{\epsilon}}^{\mathcal{M}} \frac{\mathcal{F}(\mathcal{T})}{(\mathcal{T}-\mathcal{Z})^2} d\mathcal{T} - \frac{2}{\hat{\epsilon}}\mathcal{F}(\mathcal{T})\right], \tag{D.4}$$

for $\mathcal{N} < \mathcal{Z} < \mathcal{M}$ [48].

Appendix E

Secant Method.

The secant method is a root finding algorithm and is determined by the definition of the derivative of a function $\mathcal{F}$ such that

$$\mathcal{F}'(\mathcal{X}_{n-1}) \approx \frac{\mathcal{F}(\mathcal{X}_{n-1}) - \mathcal{F}(\mathcal{X}_{n-2})}{\mathcal{X}_{n-1} - \mathcal{X}_{n-2}}, \tag{E.1}$$

hence

$$\mathcal{F}(\mathcal{X}_n) \approx \mathcal{F}(\mathcal{X}_{n-1}) + \mathcal{F}'(\mathcal{X}_{n-1})(\mathcal{X}_n - \mathcal{X}_{n-1}) = 0, \tag{E.2}$$

then we have

$$\mathcal{F}(\mathcal{X}_{n-1}) + \frac{\mathcal{F}(\mathcal{X}_{n-1}) - \mathcal{F}(\mathcal{X}_{n-2})}{\mathcal{X}_{n-1} - \mathcal{X}_{n-2}}(\mathcal{X}_n - \mathcal{X}_{n-1}) = 0, \tag{E.3}$$

therefore

$$\mathcal{X}_n = \mathcal{X}_{n-1} - \frac{\mathcal{F}(\mathcal{X}_{n-1})(\mathcal{X}_{n-1} - \mathcal{X}_{n-2})}{\mathcal{F}(\mathcal{X}_{n-1}) - \mathcal{F}(\mathcal{X}_{n-2})}. \tag{E.4}$$

This is the secant method [73].

Appendix F

Variables for Weber differential equation

$$
\begin{aligned}
\overline{a}_0 &= \frac{\sigma_0 \upsilon_0}{2\overline{u}\kappa} + \frac{\frac{\partial \upsilon_0}{\partial s}}{2\kappa}, \\
\overline{a}_1 &= -\frac{\frac{\partial \overline{u}}{\partial N}}{\overline{u}^2\kappa}\left(2\sigma_0\upsilon_0 + \overline{u}\frac{\partial \upsilon_0}{\partial s}\right), \\
\overline{a}_2 &= -\frac{\sigma_2}{2\overline{u}\kappa}\left\{\sigma_0\upsilon_0 + \overline{u}\frac{\partial \upsilon_0}{\partial s}\right\}, \\
&\quad + \frac{1}{\overline{u}\kappa}\left\{\frac{\partial^2 \overline{u}}{\partial N^2}\frac{\partial \upsilon_0}{\partial s}\right\} - \frac{3\frac{\partial \overline{u}}{\partial N}}{2\overline{u}^2\kappa}\left\{\frac{\partial \overline{u}}{\partial N}\frac{\partial \upsilon_0}{\partial s}\right\} + \left(\frac{\frac{\partial^2 \overline{u}}{\partial N^2} - \frac{1}{\overline{u}}\left(\frac{\partial \overline{u}}{\partial N}\right)^2}{2\overline{u}^2\kappa}\right)\{\sigma_0\upsilon_0\} \\
\overline{\mathcal{A}}_1 &= \frac{\partial^2 \upsilon_1}{\partial s^2}\left[\frac{\mathrm{A}}{2\kappa}\right] + \frac{\partial \upsilon_1}{\partial s}\left[\sigma_0\mathrm{A} + \mathrm{A}\frac{\partial \overline{u}}{\partial s} - \frac{\mathrm{AE}}{2\overline{u}\kappa^2} + \frac{\mathrm{B}}{2\kappa}\right] + \upsilon_1\left[-\frac{\sigma_0\mathrm{AE}}{2\overline{u}^2\kappa^2} + \frac{\sigma_0\mathrm{B}}{2\overline{u}\kappa} - \mathrm{C}\right], \\
\hat{\mathcal{A}}_1 &= \frac{\partial \upsilon_0}{\partial s}\left[\frac{\sigma_0\mathrm{A}^2}{2\overline{u}^2\kappa}\right] + \upsilon_0\left[\frac{\sigma_0}{2\overline{u}^3\kappa}\left(\mathrm{A}\frac{\partial \overline{u}}{\partial s} - \overline{u}\frac{\partial \mathrm{A}}{\partial s} + \kappa\mathrm{EA} - \overline{u}\mathrm{AB}\right)\right], \\
\overline{\mathcal{A}}_2 &= \frac{\partial^2 \upsilon_0}{\partial s^2}\left[\frac{\mathrm{C}}{2\kappa}\right] + \frac{\partial \upsilon_0}{\partial s}\left[\mathrm{C}\sigma_0 + \mathrm{C}\frac{\partial \overline{u}}{\partial s} - \frac{\mathrm{CE}}{2\overline{u}\kappa^2} - \frac{1}{2\kappa}\left(\frac{\partial \mathrm{B}}{\partial N} - \frac{1}{2}\kappa^2\frac{\partial \overline{u}}{\partial s}\right)\right] \\
&\quad + \upsilon_0\left[-\left(\frac{\partial \mathrm{B}}{\partial N} - \frac{1}{2}\kappa^2\frac{\partial \overline{u}}{\partial s}\right)\frac{\sigma_0}{2\overline{u}\kappa} - \frac{\sigma_0\mathrm{CE}}{2\overline{u}^2\kappa^2} + \mathrm{D}\right], \\
\overline{b}_0 &= (1-\sigma_0)\upsilon_0 - \overline{u}\frac{\partial \upsilon_0}{\partial s}, \\
\overline{b}_1 &= -\frac{\partial \overline{u}}{\partial N}\frac{\partial \upsilon_0}{\partial s}, \\
\overline{b}_2 &= -\sigma_2\upsilon_0, \\
\overline{\mathcal{B}}_1 &= -\sigma_0\mathrm{A}\upsilon_1, \\
\hat{\mathcal{B}}_1 &= \frac{\sigma_0\mathrm{A}\upsilon_0}{\overline{u}^2}, \\
\overline{\mathcal{B}}_2 &= -\frac{\sigma_0\mathrm{C}\upsilon_0}{\overline{u}}.
\end{aligned}
$$

Appendix G

Cavity Spline Examples

As mentioned earlier we need the basic flow in an analytical form for our analysis. Since the numerical data given is not in the structure we require, we create an algorithm to read the DNS data for information about the streamlines. To select a certain streamline we establish a parameter to control the thickness of the streamline in question, denoted τ. The optimum parameter range for the thickness was for $\tau = 0.002$, initially. Using these points we can generate a spline for our basic flow and execute the same approach as were done previously.

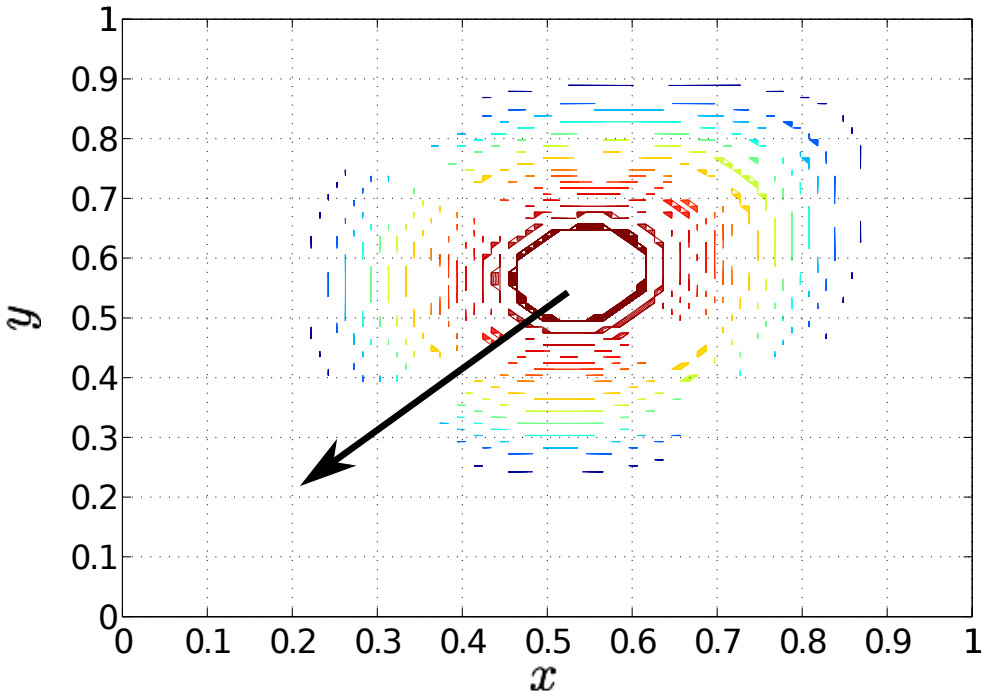

Figure G.1: The points used for the streamlines with a thickness of $\tau = 0.002$.

We use the points in figure G.1 and create a two-dimensional spline through them as seen in appendix G. This method needs to be used due to the basic flow, $\overline{u}$, and curvature, κ, terms are in analytical form, which causes issues with the solution as we shall outline here. An array was created for points from the DNS streamlines in terms of x and y. Solving the eigenvalue problem of (4.22) did not resolve and a suitable value for the eigenvalue σ_0 was not found. There was no convergence of the eigenvalues due to the $\partial\kappa/\partial s$ term becoming singular at certain locations in s. Hence, using these splines for the streamlines we can apply the same approach and see the results of these streamlines. We use the points in figure G.1 and create a two-dimensional spline through them as shown below.

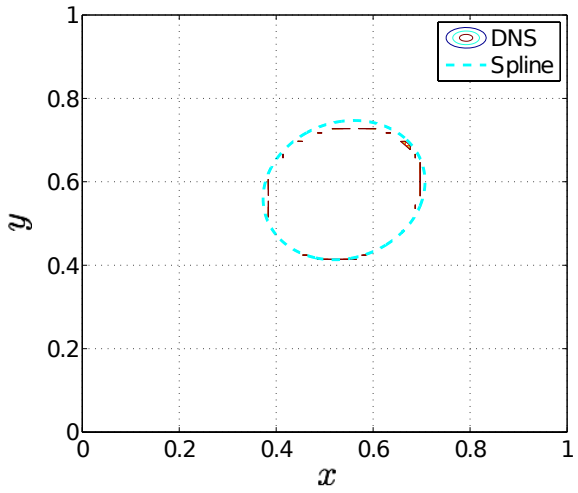

Figure G.2: First spline example.

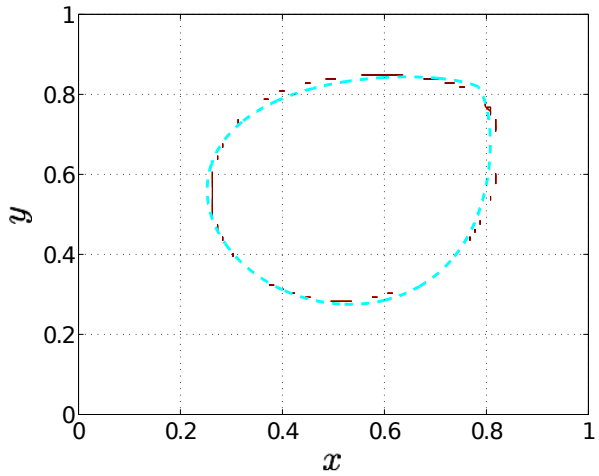

Figure G.3: Second spline example.

Appendix H

DNS eigenfunctions in x for a variety of cavities

Examples of the DNS eigenfunctions for various cavities considered in Chapter 4.

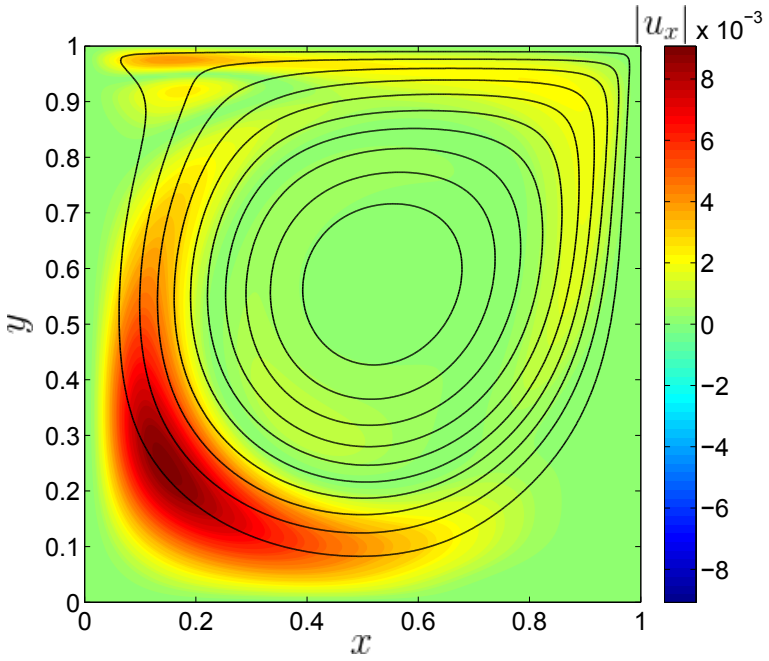

Figure H.1: Absolute value of the eigenfunction in x for the square cavity with superimposed basic flow streamlines in the cavity from DNS results.

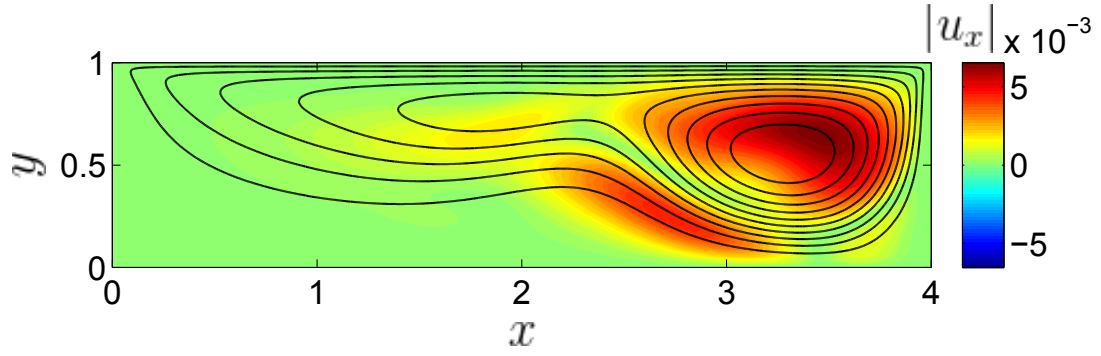

Figure H.2: Absolute value of the eigenfunction in x for the rectangular cavity with superimposed basic flow streamlines in the cavity from DNS results.

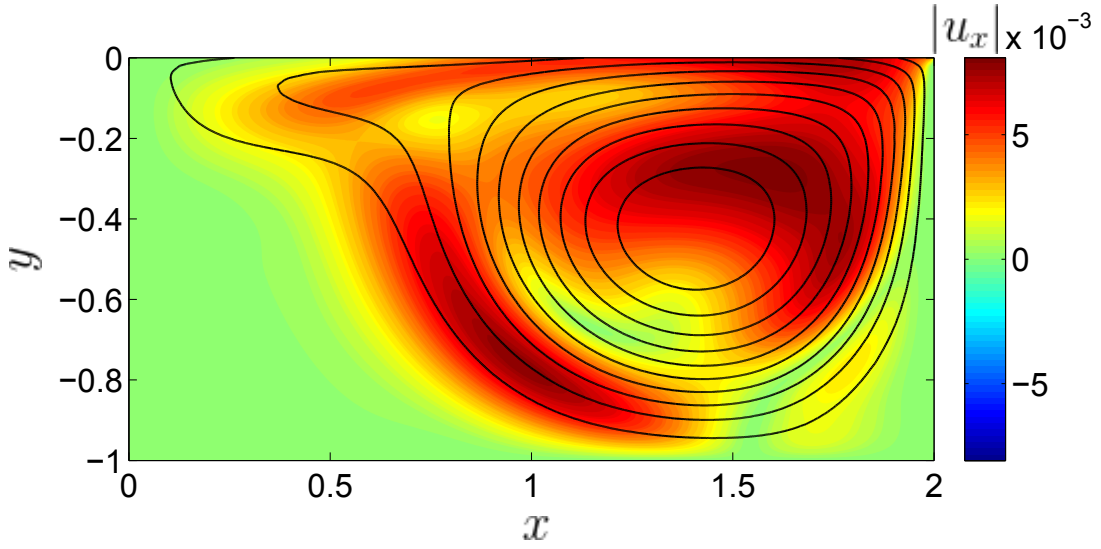

Figure H.3: Absolute value of the eigenfunction in x for the open cavity with superimposed basic flow in the cavity from DNS results.